AFIT/DS/ENP/97D-08

Shock Waves in Nonequilibrium Gases and Plasmas

DISSERTATION

Presented to the Faculty of the School of Engineering
of the Air Force Institute of Technology
Air University
In Partial Fulfillment of the
Requirements for the Degree of
Doctor of Philosophy

William M. Hilbun, B.S., M.S.
Major

October 1997

Approved for public release; distribution unlimited

AFIT/DS/ENP/97D-08

Shock Waves in Nonequilibrium Gases and Plasmas

William M. Hilbun, B.S., M.S.

Major

Approved:

Wm. F. Bailey 24 Oct 97

Dr. William F. Bailey, Chairman

Philip S. Beran 22 Oct 97

Dr. Philip S. Beran

Richard F. Deckro 23 Oct 97

Dr. Richard F. Deckro

Dennis W. Quinn 22 Oct 97

Dr. Dennis W. Quinn

David E. Weeks 22 Oct 97

Dr. David E. Weeks

Robert A. Calico, JR.

Dean

Acknowledgements

Throughout the course of this research, a number of individuals have been a great help to me, without whom this dissertation could not have been written. I would like to express my thanks to Dr. Alan Garscadden and Dr. Joseph Shang, both of Wright Laboratory, for their continual encouragement of this work. Dr. Biswa Ganguly (WL/PO) and Dr. Peter Bletzinger (Mobium Enterprises, Inc.) were extremely generous to me, providing both access to their plasma/shock data and details on their experimental apparatus. I would like to thank Dr. Charlie DeJoseph (WL/PO) for providing the basic vibrational kinetics code used in this work. Mr. Lee Bain (WL/PO) provided funding for travel and Lt Brandon Wood (WL/PO) was extremely helpful in providing information on issues relating to various aspects of the research. I would also like to express my gratitude to Mr. Eswar Josyula (WL/FIMC) for his assistance and patience in the early stages of the research, particularly with regard to the computational fluid dynamic aspects of the problem. I wish I knew as much about CFD as Eswar has forgotten. I also wish to express my thanks to my fellow classmates Major Jim Shoemaker and Captain Eric Bennett, for acting as a sounding board and a reality check throughout this research, as well as providing many LaTex tricks along the way. The Major Shared Resource Center (MSRC) at Wright-Patterson AFB, OH, provided the computer time required for the calculations in this research and are a tremendous asset to the Air Force with their computer hardware and technical personnel. I would also like to thank my adviser, Dr. W.F. Bailey (AFIT/ENP) for his encouragement, support, suggestions and insight throughout my graduate studies at AFIT. He always came up with good ideas when I needed them most. Finally, I must express my deep appreciation to my wife and children for their endless support and encouragement. Without them, none of this would have been possible.

William M. Hilbun

Table of Contents

List of Figures

Abstract

An analysis and assessment of three mechanisms describing plasma/shock wave interaction processes was conducted under conditions typically encountered in a weakly ionized glow discharge. The mechanisms of ion-acoustic wave damping, post-shock energy addition and thermal inhomogeneities are examined by numerically solving the Euler equations with appropriate source terms adapted for each mechanism. Ion-acoustic wave damping is examined by modelling the partially ionized plasma as two fluids in one spatial dimension using the Riemann problem as a basis. Post-shock energy addition in the form of nonequilibrium vibrational energy relaxation is also examined in one spatial dimension using the Riemann problem as a basis. The influence of thermal inhomogeneities on shock wave propagation is examined in two spatial dimensions for both a Riemann shock and a shock generated by a spark discharge. The use of realistic thermal profiles allowed the comparison of measured and numerically predicted shock parameters. Results from time-dependent calculations of the two-fluid plasma under typical weakly ionized conditions, although similar to steady-state results previously reported in the literature, indicate that ion-acoustic wave damping has an insignificant effect on shock propagation. Under strongly ionized conditions, however, ion-acoustic wave damping can increase shock speed and shock front width and reduce the shock strength, each of which is consistent with experimental observation. Results from the analysis of post-shock vibrational relaxation indicate that although this process can lead to increases in the shock speed, the final magnitude of the increase is too small and the time scale for the increase is too large to explain the experimental observations. An analysis of the effects of thermal inhomogeneities reveals that many of the observed plasma/shock anomalies can be explained based solely on this mechanism.

Shock Waves in Nonequilibrium Gases and Plasmas

I. Introduction

1.1 Motivation

Since World War II, the U.S. military has had a keen interest in supersonic and hypersonic aerodynamics. It was in this period that the first discoveries were made regarding the build up of shock waves along the leading edges of wings and control surfaces of aircraft. As fighter aircraft reached their terminal velocities in steep dives at high altitudes, pilots experienced control freezeup, leading to stability problems. It was later recognized that this phenomena was related to shock waves [119:93]. In the late 1940s Chuck Yeager became the first person to fly faster than the speed of sound, a feat many thought impossible, due to the build up of shock waves in front of the aircraft. Interestingly, the design of his aircraft, the Bell X-1, was based on the .50 caliber bullet, a projectile that was known to be stable in supersonic flight [119]. Just two years after the sound barrier was broken for the first time, the first man-made object to reach hypersonic velocities was launched from the New Mexico desert, as a V-2/WAC rocket reached speeds of more than 5000 mph [5:2]. In the 1950s and 1960s the Air Force's interest in shock waves progressed from intellectual curiosity to serious weapon design. The problems of atmospheric re-entry, including the high heat loading on nuclear-tipped re-entry vehicles, the planned X-20 Dynasoar and the manned space flight programs of Mercury, Gemini and Apollo spawned high levels of shock wave research [5:4-8].

This research continued into the 1970s and 1980s with the design and construction of the Space Shuttle and the preliminary design of the National Aerospace Plane (NASP). Through these and many other developments, man's knowledge of high-speed aerodynamics increased dramatically. Throughout this history, shock wave

research has been primarily limited to shock propagation through media initially in a state of thermodynamic equilibrium. However, propagation through media initially in a state of thermodynamic nonequilibrium raises new possibilities and highlights interesting effects not encountered in the equilibrium case. A.I. Osipov and A.V. Uvarov, well-known Russian researchers in the field of molecular vibrational physics, have stated that "The study of the laws of propagation of shock waves and other hydrodynamic perturbations in nonequilibrium gases essentially constitute a new field in hydrodynamics" [93].

The field of plasma-aerodynamics offers new research opportunities for a number of reasons. First, it is apparent that this area represents an intersection of two academic disciplines: aeronautical engineering and plasma physics. The efforts of aeronautics has largely been concentrated in the area of neutral gases, that is, gases with no ionization present. Although some aeronautical researchers have treated weakly ionized flows, they have done so principally from an energy balance point of view, neglecting the collective plasma behavior that would be present in such flows. On the other hand, while plasma physicists have studied wave and shock behavior in ionized gases, such studies were primarily limited to highly ionized states, where the role of neutrals was insignificant. Secondly, the study of shocks in aeronautics has been primarily limited to flows in gas initially in an equilibrium state. With this view, any ionization in the shock front region must arise through kinetic reactions driven by the temperature increase across the shock layer. Ionization is then confined to the relaxation layer downstream of the shock. The study of aerodynamic shocks in gas initially in a state of nonequilibrium has largely been neglected. In nonequilibrium flows it is possible for ionization to be present in the upstream region even before the gas passes through the shock layer. This nonequilibrium state within the plasma may be characterized by an electron temperature that is much higher than the gas temperature. Such a situation can arise in a plasma generated by an electric discharge, for example, or perhaps by creating a plasma zone in front of an aircraft

by a laser or microwave device, as suggested by Myrabo [71]. For these reasons, the study of waves and shocks in weakly ionized gas flows characteristic of possible flight conditions provides a fruitful area of research.

1.2 Shocks in a Neutral Gas

Shocks are regions of gas flow where very large gradients in density, pressure, temperature and velocity exist. They are formed under certain conditions as a result of nature satisfying the equations of continuity of mass, momentum and energy. In a neutral gas, a shock can be divided into four regions, as depicted in Figure 1. Region 1 represents the undisturbed gas in front of the shock and is in complete thermodynamic equilibrium. Region 2 represents the shock front, in which there are rapid changes in the temperature, density, pressure and velocity of the flow. This part of the shock is also called the viscous shock, due to the dissipative process of viscosity which is present in this region. Region 3 represents that part of the

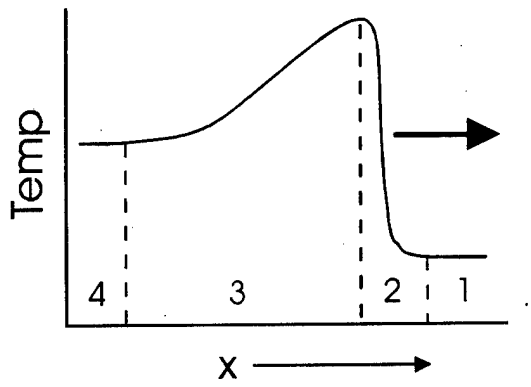

Figure 1. Typical variation in gas temperature with distance in a shock.

shock in which equilibration of the various internal degrees of freedom takes place. In region 4 complete thermodynamic equilibrium is re-established. In an idealized shock, the shock front region is infinitely thin. However, in reality the viscous shock is usually a few mean free paths thick, which under typical flight conditions (60.000

feet, standard atmosphere [4] may be of the order of 10^{-4} cm. If the temperature rise across region 2 is high enough, thermal energy can be coupled into the internal degrees of freedom, resulting in various relaxation processes occurring in region 3. Vibrational and electronic states may be excited, dissociation and ionization may proceed, and many chemical reactions are possible. These relaxation mechanisms increase the thickness of region 3, and can cause structure to appear in the flow variables. As used here, the total shock thickness is defined as the region extending from the point of rapid rise in flow parameters (at the shock front) to the point at which equilibrium is re-established (in the downstream region).

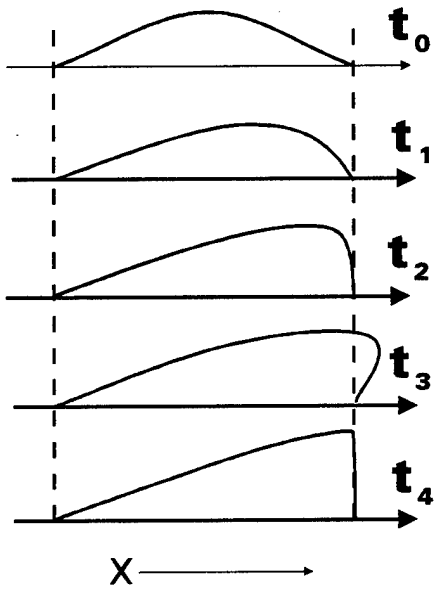

Figure 2. Temporal evolution of the pressure in a large amplitude wave leading to the formation of a shock.

1.2.1 How Do Shocks Develop? Shock formation can be understood by considering the nonlinear terms in the fluid equations. These nonlinear terms cause portions of the wave with a larger amplitude to travel at a higher velocity than portions of the wave with a smaller amplitude. Thus the wave front steepens until it becomes multi-valued and "breaks", as shown figuratively in Figure 2. In reality, this

steepening process continues only until it is balanced by dissipative mechanisms, such as viscosity and thermal conductivity. Since the characteristic distance associated with these processes is a mean free path [123:83], the shock front thickness is of the order of a few mean free paths.

1.2.2 Typical Scale Lengths. As mentioned previously, region 3 of Figure 1 represents that part of the shock in which various relaxation processes occur. Figure 3 explicitly shows some of these processes for a real gas. Here, the gas temperature rises sharply at the shock front then decreases gradually in the post-shock region as the various thermal relaxation processes occur.

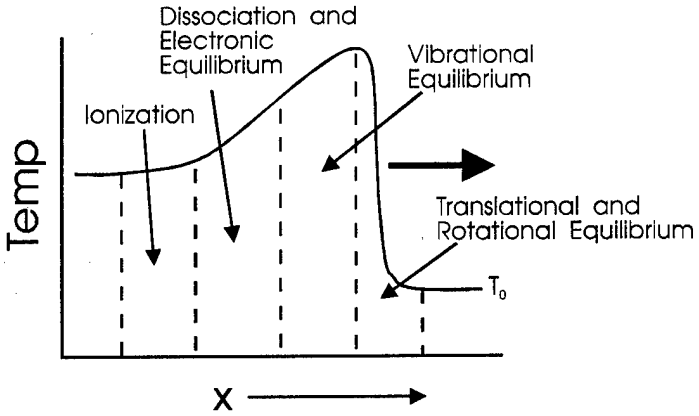

Figure 3. Typical temperature relaxation processes in a shock.

If the gas particles are molecules, then rotational relaxation will play a role in establishing equilibrium in the downstream region. That is, in order to reach equilibrium, the rotational temperature must become equal to the translational temperature, which requires collisions. If the translational temperature in the post-shock region is high enough, then vibrational modes can become excited. For air, this point is reached at a temperature of approximately $800K$ [5:19]. Thus in order to reach a final state of equilibrium the translational, rotational and vibrational temperatures must all be the same, which may require on the order of 20,000 collisions. If the

temperature is higher still, say about $2000 - 4000K$ for air, dissociation of molecules is possible, taking as many as 200,000 collisions to equilibrate [5:483]. Electronic degrees of freedom are excited next and at a temperature of about $9000K$ ionization begins to occur in air, with this process typically requiring more collisions than any other.

1.3 Shocks in a Weakly Ionized Nonequilibrium Plasma

1.3.1 What's New? In a weakly ionized gas, charged particles exist in addition to the neutral particles present in an unionized gas. These charged particles can introduce modes of wave propagation nonexistent in neutral shocks [36]. In addition, in a nonequilibrium weakly ionized gas the electron temperature may be fifty times (or more) higher than the heavy particle temperature. This nonequilibrium can lead to energy transfer from electrons to the ions and neutrals, as well as dissociation and ionization as a result of electron impact collisions. The presence of the high temperature electrons may excite the vibrational modes of molecules, leading to a vibrational temperature much higher than the gas temperature. In some cases this vibrational temperature (whose definition here is based on the relative populations of the ground state and first excited state) may be ten times the gas temperature. These nonequilibrium conditions can exist in the upstream ambient gas even without a shock present (e.g., in a gas discharge). This is in sharp contrast to the ambient equilibrium conditions normally encountered in aerodynamics.

When a shock is present in an ionized gas, large density gradients arise in all plasma constituents (electrons, ions and neutrals) at the shock front. As a result of these gradients, there is a diffusion of particles in the upstream direction. Since the mobility of the electrons is much higher than that of either the ions or neutral particles, they will diffuse faster. The resulting charge separation gives rise to an electrical double layer (as shown in Figure 4), which ultimately equilibrates the fluxes of ions and electrons. The difference in the charged particle densities leads to an

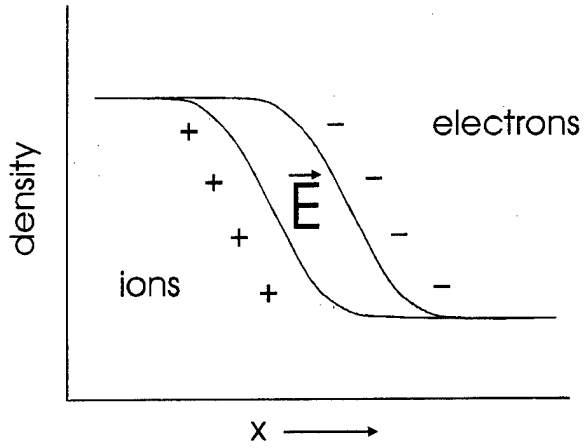

Figure 4. Electric double layer resulting from diffusion of electrons and ions at the shock front.

electric field and potential variation at the shock front, both of which are absent from a shock in a neutral gas.

1.3.2 Typical Scale Lengths. As in neutral gases, shocks in weakly ionized gases have a neutral shock front width which is typically a few neutral-neutral mean free paths thick. However, the shock front width associated with the ions and electrons may be many times this distance. In fact, it will be shown later that under nonequilibrium conditions, the charged particle shock front thickness is greater than the ion-neutral mean free path by a factor of approximately T_e/T_n, which may be as high as 80 or more under typical glow discharge conditions. This charged particle precursor may be able to interact with the neutral flow in front of the shock and significantly affect flow parameters before crossing the neutral shock itself.

The Debye length is an important parameter in a plasma. It is a general characteristic of a plasma that quasi-neutrality is maintained; that is, the plasma reacts in such a way that nearly equal electron and ion number densities are always maintained. A weakly ionized plasma is a quasi-neutral assembly of charged and neutral particles, exhibiting a collective behavior due to the Coulomb interaction. In a collisionless plasma, each charged particle moves according to the local value of

the electric field and, in turn, the electric field is determined by the entire plasma. The Debye length is simply a measure of the spatial extent of charge separation in a quiescent plasma. When the ratio of the Debye length to the mean free path of a charged particle is small, then the particle spends most of its time in a region without a macroscopic electric field. In such a case it would be expected that charged particle effects would be very small in comparison to neutral interactions. Conversely, if the ratio is large, then the charged particle spends most of its time in a region in which there is an electric field. In this case it would be expected that the motion of the charged particle would be greatly determined by the collective behavior of the plasma as a whole.

1.4 Experimental Anomalies of Shocks in Weakly Ionized Plasma

Since the early 1950s, numerous experiments (conducted mostly by Russian researchers) have been carried out in the field of shock propagation in nonequilibrium plasmas. In these experiments, a number of interesting phenomena have been observed involving plasma/shock interactions. These can be summarized by noting that a shock in a plasma is different from a shock in a neutral gas. In a plasma:

- the shock velocity increases [74], [12], [85], [11], [27], [77], [34], [33]
- the shock front spreads and disperses [75], [51], [89], [14]
- a shock precursor may appear [13], [27], [76], [14]
- the shock strength is reduced or even (apparently) eliminated in some cases [10], [87], [85], [51], [88]
- the aerodynamic drag is modified [16], [88], [48], [86]
- the heat flux to the aerodynamic surface is reduced [105]
- the shock standoff distance increases [90], [57], [88]

As a shock propagates, it is seen to accelerate as it enters a region containing a nonequilibrium plasma. This acceleration has been observed in both molecular

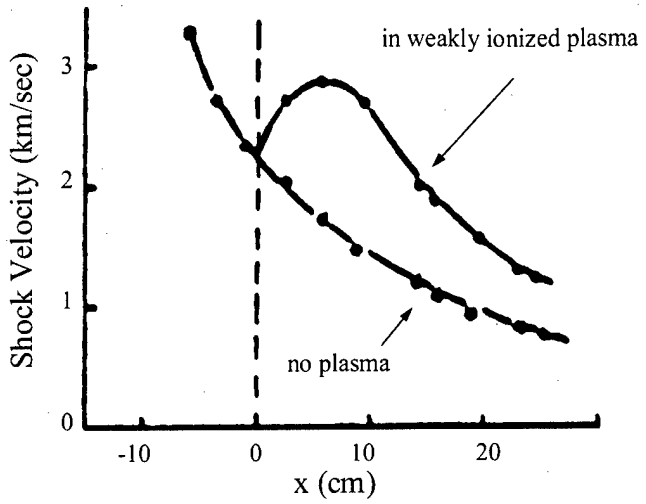

Figure 5. Shock velocity measured in N_2 in the absence of a plasma and in a weakly ionized plasma. [Ref: [34]].

and rare gases. An example of this acceleration is shown in Figure 5, taken from [34]. Here, the measured shock speed in N_2 in the absence of a plasma and in a weakly ionized plasma are shown. The origin is with respect to the beginning of the plasma region, with the plasma located in the region $x > 0$. In each case, the shock was generated by a spark discharge. In the absence of a plasma, the shock speed decreases monotonically as the shock propagates away from the spark source. As the shock enters a plasma region, the shock speed is observed to first increase, then decrease as it propagates further down the shock tube.

When a shock enters a plasma, the shock front region appears to disperse, resulting in significant shock front broadening and attenuation. The dispersion can be quite severe and can result in the nonmonotonic behavior of some of the flow parameters (density and pressure) in the shock front region [89]. Figure 6 (taken from [75]) shows an experimentally measured pressure profile obtained in air and in a weakly ionized plasma in air. The signal arrives earlier in the plasma, reflecting a higher shock velocity in this medium. Furthermore, the shock front width in unionized air is much narrower than the shock front width in weakly ionized air.

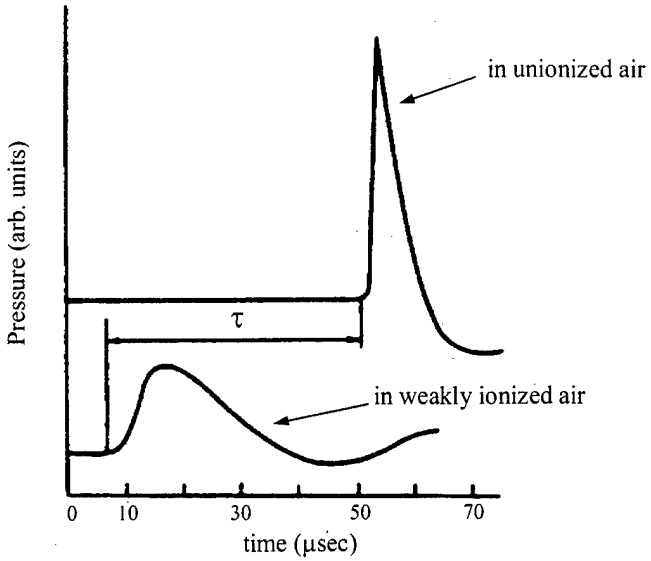

Figure 6. Variation in pressure (arbitrary units) with time for a shock in air and in a weakly ionized plasma in air measured at a fixed point in the flow. The nominal shock velocity is 740 m/sec through air at a pressure of 30 torr. The time shift between the signals is τ [Ref: [75]].

A region of elevated density and temperature, called a precursor, can exist in front of the shock wave. Sometimes this precursor is observed to break apart from the main shock and propagate with a steady waveform. Spreading of the shock front, along with the apparent appearance of a precursor is shown in Figure 7, taken from [77]. The structure of the shock in the presence of a plasma is given as curve 1, while the shock structure in the absence of a plasma is given as curve 2. In this example, the nominal shock travels through air at a pressure of 2 torr with a velocity of 1250 m/sec.

Another anomaly of shocks in a plasma is the reduction of the pressure jump at the shock front when compared to shocks in a neutral gas. That is, the ratio of the pressure just behind the shock front (P_2) to the pressure just in front of the shock (P_1) is lower in plasma than in air for a shock propagating at the same velocity [87], as shown in Figure 8.

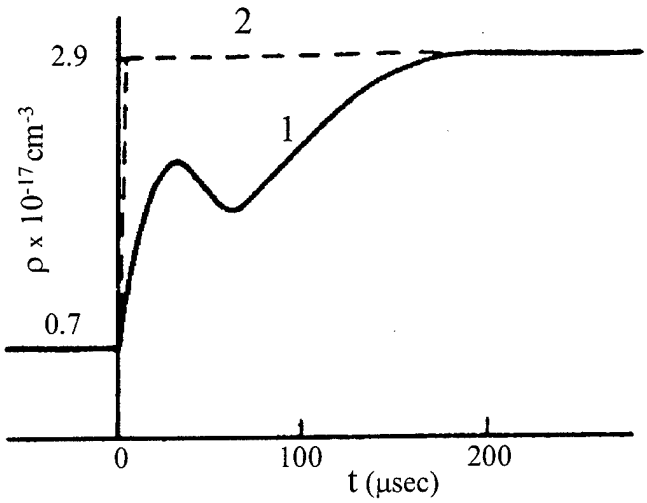

Figure 7. Variation of the density in a shock wave in air in the presence of a plasma (curve 1) and in the absence of a plasma (curve 2). The unperturbed shock wave is traveling at a velocity of 1250 m/sec in air at a pressure of 2 torr [Ref: [77]].

Perhaps the most intriguing phenomena involves the influence of a plasma on the flow of air around an aerodynamic structure. In a recent experiment conducted at the A.F. Ioffe Physicotechnical Institute, located in St. Petersburg, Russia, small spheres were shot down a ballistic range through both air and weakly ionized plasma in air [16]. The spheres, constructed of polyethylene, were 15 mm in diameter and traveled through air at a pressure of 15 torr. The experimentally determined coefficient of drag in the presence of a plasma is significantly altered from that in air, as shown in Figure 9.

In another experiment conducted at the same facility, but by different researchers, a spherical Duralumin model was launched from a ballistic cannon at a velocity of 2.5 km/sec through air at a pressure of 40 torr [105]. The projectile was shot through both unionized air and a uniform glow discharge in air. The projectile had an ablation coating of NaCl, which was used to determine the heat flux to the

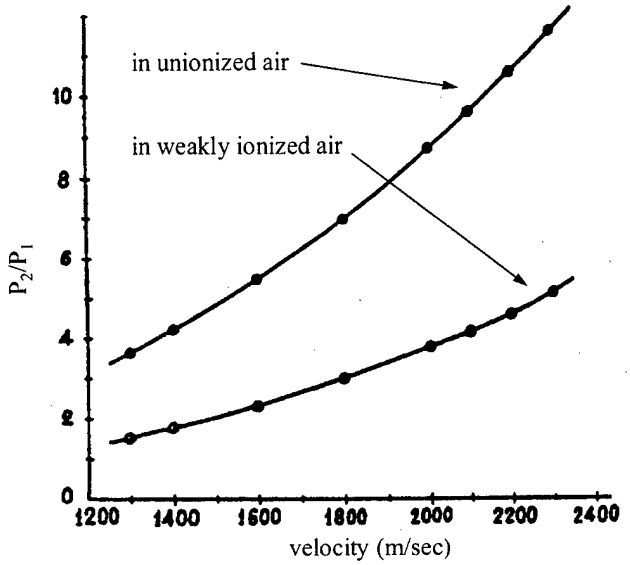

Figure 8. Variation of the pressure jump at the shock front in air and in a weakly ionized plasma in air [Ref: [87]].

model's surface. The experimentally determined heat flux to the model's surface was found to be a factor of 4 lower in the plasma than in unionized air.

Finally, the standoff distance of the shock from a projectile has been reported to be anomalously large as the projectile passes through a plasma. This increase in shock standoff distance has been postulated to be the cause of the reduction in the heat flux mentioned previously [105]. Recent experiments conducted in a ballistic range at the Arnold Engineering and Development Center (AEDC), Arnold AFS, TN [117], appear to confirm the anomaly in the shock standoff distance reported in the Russian literature (Figure 10). Here, the shock boundary measured in unionized gas (diamonds) agrees well with a steady-state fluid calculation for gas at $300K$ (light solid curve). However, the measured shock boundary in a plasma, with a temperature of $1200K$, (triangles and boxes) is much different than the steady-state calculation for gas at $1200K$. This indicates that the plasma effects may be over and above the thermal effects arising due to the presence of the hot gas in the plasma region.

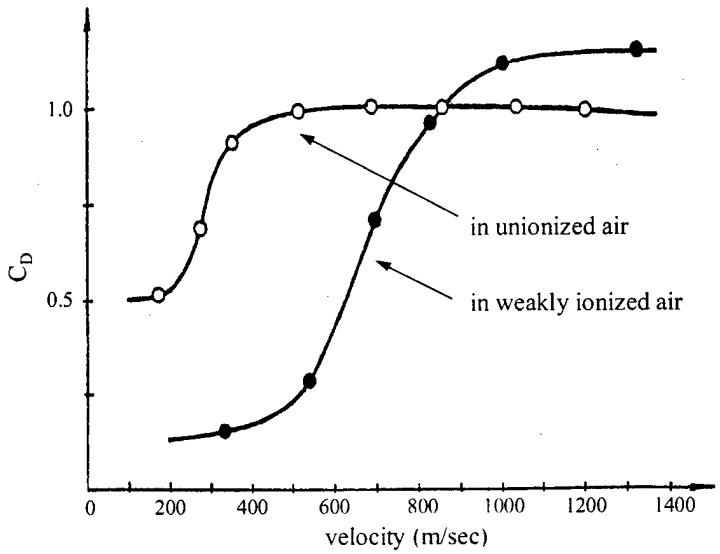

Figure 9. Experimentally determined variation in the aerodynamic drag coefficient (C_D) with velocity for a sphere in unionized air and in weakly ionized air [Ref: [16]].

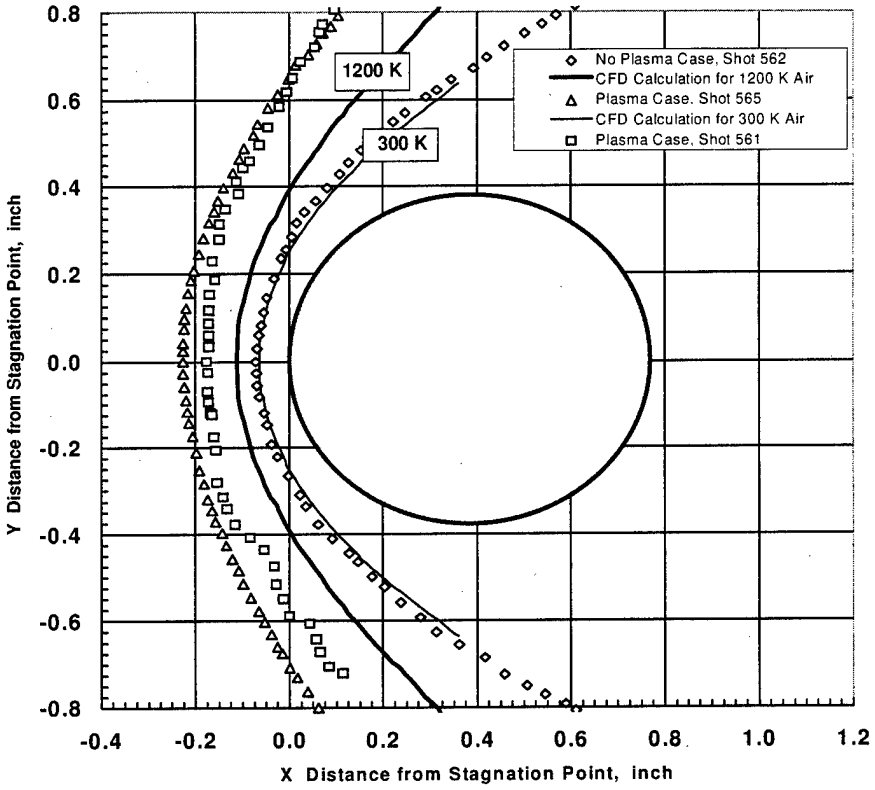

Figure 10. Shock standoff distance measured in weakly ionized plasma (triangles, boxes) and in unionized gas (diamonds). The shock standoff from steady-state fluid calculations (solid curves) are also shown. [Ref: [117]]

1.5 Possible Applications of Plasma-Aerodynamics

In the previous paragraphs, some examples of the plasma/shock phenomenology observed in recent years has been given. If the experimental measurements are accurate, then the implications for the future of aerodynamics are enormous. While the plasma effects have been confined to the laboratory at present, the real pay-off for plasma aerodynamics lies with the flight vehicles of the future.

A number of possible applications using nonequilibrium plasma flows have been offered. These include reducing aircraft radar cross-section, maintaining RF communication with spacecraft during re-entry (when RF blackout is typically experienced) ([29], [92]) and boundary layer control ([29], [25], [94]). Other proposed applications include a control surface-less aircraft, which creates control moments by using magnetic fields to exert forces on the fluid [81].

In this last category are envisioned such ideas as prolonging laminar flow and delaying fluid separation thus allowing flight into very high angle-of-attack regimes. To test these possibilities, North American/Boeing has proposed modifying an existing F-15 fighter aircraft to include a plasma generator in the nose section [58], as shown in Figure 11.

Perhaps even more futuristic is a Russian concept for a revolutionary hypersonic vehicle, designated AJAX, which recently appeared in an American Institute of Aeronautics and Astronautics paper [57]. In this design (Figure 12) plasma aerodynamic effects are reportedly used to create "a nonequilibrium cold plasma adjacent to the vehicle, to reduce shock strength, drag and heat transfer" [57:1].

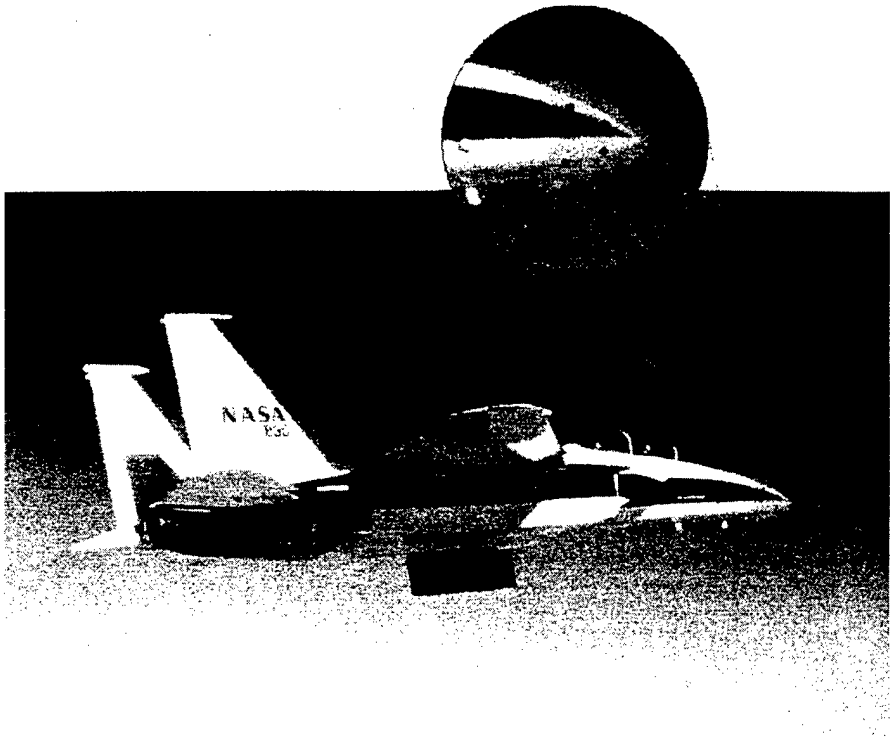

Figure 11. Proposed modification to an existing F-15 aircraft to flight-test plasma-aerodynamic effects. The plasma generating device is shown in the nose section. (photo courtesy of North American/Boeing)

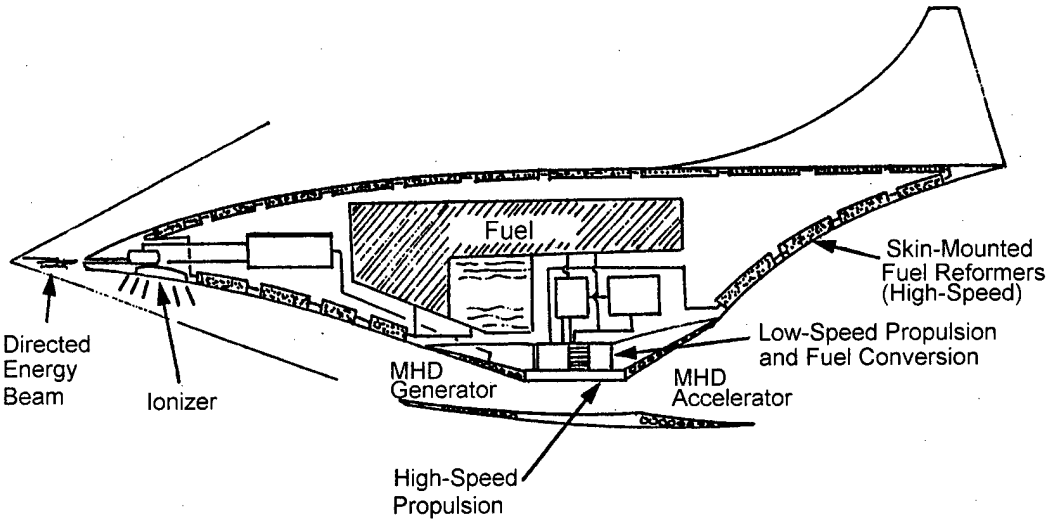

Figure 12. AJAX hypersonic vehicle concept [Ref: [57]].

1.6 Research Objectives

In this chapter, the concept of gasdynamic shocks has been introduced, along with some of the basic differences between shocks in a neutral gas and shocks in a weakly ionized plasma. Experimental anomalies observed in plasma/shock experiments have also been introduced, along with some possible aerodynamic applications which attempt to exploit these anomalies. Obviously, an understanding of the physical processes at work in plasma/shock interactions is critical in exploiting the effects to advantage in an aerodynamic vehicle. While many experiments have been performed on the propagation of shock waves through nonequilibrium plasmas, the theoretical analysis which has been brought to bear on understanding the phenomenology appears to be rather limited. Although a variety of mechanisms have been offered as possible explanations of the observed anomalies, a complete analysis of any such mechanism appears to be lacking. The present research explores three of the most prominent of the proposed plasma/shock mechanisms:

- charged particle/neutral particle interactions
- post-shock energy addition
- thermal inhomogeneities in the flow

Charged particle/neutral particle interactions arise due to the presence of charged particles in the predominantly neutral gas flow, where fractional ionizations as low as 10^{-6} are considered typical. Some have proposed that it is the presence of these interactions in a weakly ionized nonequilibrium plasma (specifically, ion-acoustic wave damping) which lead to the observed structures and anomalies ([11], [12], [13], [51], [75], [85]). In the exploration of this mechanism, parameters typical of weakly ionized plasmas will be used in a fluid analysis to determine the resulting shock structure.

Post-shock energy release involves the addition of energy into the translational degrees of freedom behind the shock front. The energy release is largely confined to

the region behind the shock front due to the higher temperature and density there, both of which tend to increase the relevant collisional rates. The actual method of this energy addition may occur in a number of ways. The de-activation of internal energy stored in both excited electronic states [121] and excited vibrational states [9] has been suggested, as well as the dissociative recombination [121] of electrons and ions. In this study, vibrational relaxation will be adopted as the model describing the addition of energy to the flow in the post-shock region, although the other processes should yield similar qualitative results under the proper conditions.

Finally, the presence of thermal inhomogeneities in the weakly ionized plasma region has been suggested as the cause of the observed plasma/shock anomalies ([41], [115], [2]). In this mechanism, the shock flows into a region of gas which has been previously heated by the plasma. The resulting shock structure is proposed to be a result of neutral particle interactions only, with no need for charged particle/neutral particle interactions or excited state de-activations. Although it is the presence of the charged particles, along with any internal energy release, which heat the gas, the important distinction here is that this heating was accomplished before the shock entered the plasma, not as the shock propagates through the plasma, as is the case in the other two mechanisms.

1.7 Previous Work

In this section, a brief summary of previous work in the area of plasma/shock interactions will be given. Since the literature is full of various descriptions, aspects and proposed mechanisms of this problem, the focus of the current section will be limited to the three mechanisms given previously.

1.7.1 Charge Particle/Neutral Particle Interactions. Interactions between charged and neutral particles encompasses the field of partially ionized plasma physics. Since this field is far too broad a subject for the present undertaking, with the many

wave modes possible in both magnetized and unmagnetized plasmas, the focus must be further limited. To that end, the work of Sessler [106] will be used to identify the plasma wave modes which are believed to be important in the present investigation. The contributions of other researchers to the field will then be briefly mentioned.

According to Sessler, there are three modes of wave propagation in a weakly ionized, unmagnetized plasma. Only one of these wave modes, however, can propagate. This mode is the acoustic mode, so named due to its close relationship to a sound wave propagating in a neutral gas. It is characterized by a propagation speed very nearly equal to the neutral sound speed. This mode also describes wave action in which the electrons, ions and neutral particles move with very nearly the same phase and amplitude. As such, only weak attenuation would be expected with this mode, which Sessler determined was primarily due to neutral particle viscosity effects. Linearizing the fluid equations, which is applicable for small amplitude waves, Sessler obtained a dispersion relation describing this mode of propagation.

Another important mode of wave propagation in a plasma is the ion-acoustic wave. In this mode, ions and electrons move in phase with each other and with almost the same amplitude, while the neutrals can be considered to be at rest [63]. Although the ion-acoustic mode in a plasma travels faster than an acoustic wave in a neutral gas, the ion-acoustic waves are strongly damped for $\omega < \nu_{in}$, where ω is the wave frequency and ν_{in} in the ion-neutral collision frequency. Although this strong damping effectively prevents this mode from propagating long distances, the ion-acoustic mode may nevertheless be an important process in the neutral shock front region and has been frequently mentioned in the literature as such.

Ingard and Schulz [64] improved Sessler's representation of the dispersion relation for the acoustic mode by including an energy equation that treated thermal conduction as well as energy coupling between the different components of the plasma. The viscosity effect of the interaction of the plasma wave with the walls of the shock tube was also treated, in addition to the bulk viscosity of each component. They

found that under conditions representative of a glow discharge, a small-amplitude wave may either be attenuated or amplified. The attenuation is primarily due to viscous and thermal conduction effects, while any growth is due to energy transfer to the neutrals from the electrons.

Hasegawa [60] derived similar results, although he treated only the neutrals in the plasma. He also pointed out that the energy transfer from the electrons to the neutrals affects the wave in two ways. First, the energy is transferred selectively at the compression stage of the wave, and secondly, the velocity of the wave should increase as a result of the heating of the neutrals.

Ingard and Schulz applied their acoustic mode dispersion relation, obtained assuming small amplitude waves, to the problem of a shock in a weakly ionized plasma [65]. Although the application of a dispersion relation (derived from linearized fluid equations) to a shock wave (which requires nonlinear terms for its development) is generally improper, the shocks considered by Ingard and Schulz were weak, with density jumps at the shock front corresponding to shock speeds of approximately Mach 1.06. In this case, the dispersion relation may still be able to accurately describe the motion of the plasma components. Ingard assumed the neutral density, $N_n(x,t)$, of an ideal shock traveling at a velocity of c could be represented by a step function:

$$\frac{N_n(x,t)}{N_{n0}} = \begin{cases} 1 & t > x/c \\ N_{n1}/N_{n0} & t < x/c \end{cases} \tag{1}$$

where N_{n0} is the ambient density in front of the shock ($t < x/c$) and N_{n1} is the density behind the shock front ($t > x/c$). Combining the acoustic mode dispersion relation with Equation 1 resulted in an ion density profile given by

$$\frac{N_i(x,t)}{N_{i0}} = \begin{cases} 1 + (N_{n1}/N_{n0} - 1)\exp\left[-\omega^*(x/c - t)\right] & t < x/c \\ N_{n1}/N_{n0} & t > x/c \end{cases} \tag{2}$$

where N_{i0} is the ambient ion number density far upstream of the shock and ω^* is a characteristic frequency defined as

$$\omega^* = \gamma_n \frac{T_n}{T_e} \omega_{in}. \tag{3}$$

From Equation 2, it is apparent that an ion precursor is present in the region in front of the neutral shock. In a reference frame attached to the neutral shock front, this precursor has a characteristic length of c/ω^*, which can be shown to be approximately equal to $T_e/T_n \, \lambda_{in}$, where λ_{in} is the mean free path of an ion in the neutral gas.

In addition to the perturbation in the ion number density, the dispersion relation can be used to determine the resulting perturbation in the electric field. Ingard's result for the electric field (given in SI units) is

$$E(x,t) = \begin{cases} \gamma_n \, P_n \, \sigma_{in}/q \, (N_{n1}/N_{n0} - 1) \exp\left[-\omega^* \, (x/c - t)\right] & t < x/c \\ 0 & t > x/c \end{cases} \tag{4}$$

where q is the elementary unit of charge and P_n is the ambient pressure in the unperturbed neutral gas. Thus, an electric field is present in the ion precursor region, which points in the direction of shock propagation.

Using a different approach, Avramenko, et al. [6] obtained results nearly identical with those of Ingard. Instead of linearizing the fluid equations to obtain a dispersion relation, which was then applied to the plasma shock problem, Avramenko solved a simplified set of fluid equations directly. Whereas Ingard and Schulz's development started with a three fluid plasma (ions, electrons and neutrals), Avramenko assumed the plasma could be adequately described using a two fluid approximation, in which the charged particles were lumped together and treated as a single fluid, with the neutrals comprising the second fluid. The appearance of a charged component precursor leading the neutral shock was again found. Further details regarding Avramenko's development of a set of fluid equations using the two fluid approxima-

tion will be presented in Chapter II. This development will be extended to include the neutral and ion energy equations in Chapter III.

Although both Ingard and Avramenko found a charged component precursor leading the neutral shock wave, the precursor was not able to influence the neutral shock due to the nature of both derivations (in each case, the neutral density was assumed to follow a given function, rather than being determined as part of the solution to the problem). However, the plasma-based mechanism commonly proposed to explain plasma/shock interactions (ion-acoustic wave damping) requires the energy and momentum contained in the precursor to be transferred to the neutral flow. This is not possible in the analyses of Ingard and Avramenko. Therefore, an approach different from Ingard and Avramenko must be used, in which the neutral flow is not specified but is determined self-consistently.

1.7.2 Vibrational Energy Relaxation. The relaxation of vibrational energy behind the shock front was proposed by Baksht, et al. [9] as a means of explaining observed shock behavior in a weakly ionized plasma. In there theoretical analysis, Baksht, et al. showed that shock wave acceleration as well as the variations in density, pressure and temperature could be attributable to this mechanism. However, it is unclear by what method Baksht determined the characteristic time over which these variations in the flow parameters occurred.

The propagation of a weak shock wave into a region of vibrationally excited N_2, with the subsequent relaxation of vibrational energy behind the shock front, was examined by Rukhadze, et al. [101]. They found that the characteristic vibrational relaxation times determined under nonequilibrium conditions can be many orders of magnitude shorter than the relaxation times under equilibrium conditions (this will be addressed in Chapter II). Using these nonequilibrium relaxation times in a fluid calculation, Rukhadze reported that, in certain cases, very rapid changes in shock velocity and flow parameters could occur. The time scale of these changes

($\approx$ 20 μsec) is of the same order as that observed in experiments. However, the exact manner in which the relaxation time was determined and incorporated into the numerical solution is unclear from the published work.

A similar study was performed by Vstovskii, et al. [116]. However, in this analysis, the shortened relaxation time was obtained by consideration of an impurity (water vapor) in the N_2 gas, rather than vibrational relaxation under nonequilibrium conditions. This impurity served to shorten the vibrational relaxation time in comparison to the relaxation time of pure N_2 under equilibrium conditions. Again, shock wave acceleration and variations in the flow parameters were found.

A study of vibrational relaxation in a shock wave of constant velocity was reported by Evtyukhin, et al. [42]. Here, the flow parameters behind the shock front were determined based on relaxation times determined under equilibrium conditions. Since a constant shock velocity was assumed, Evtyukhin could not examine the velocity increase resulting from vibrational relaxation.

Finally, an examination of the relaxation of vibrational energy in the post-shock region based on a kinetic description of the vibrational levels was made by Gureev, et al. [56]. In this study, the master equations describing the time evolution of the vibrational kinetics were coupled to the steady-state fluid equations. The solution of this coupled set of equations resulted in the determination of how the vibrational distribution function varied with distance throughout the shock. Although his approach is unique and interesting, Gureev could not determine the effect that vibrational relaxation had on the shock velocity, since steady-state fluid equations were used.

Although the literature discussing vibrational relaxation behind a shock front is plentiful, with varying degrees of complexity, several basic questions seem to remain unanswered. These are: 1) what is the final shock velocity in the nonequilibrium region and how does it depend on the initial shock velocity?; 2) how much vibrational energy can be delivered to the gas flow in the post-shock region under realistic

conditions?, and 3) how fast can the store of excess nonequilibrium vibrational energy be delivered to the flow under realistic conditions?

Although the purpose of this section was to review previous work on the plasma/shock interaction mechanism of post-shock energy addition in the form of nonequilibrium vibrational relaxation, one cannot ignore the fact that the shock phenomena which have been observed in molecular gases have been observed in atomic gases as well ([33], [12] and [41], for example). Since such gases obviously lack vibrational degrees of freedom, some other mechanism must be at work in them. Nevertheless, nonequilibrium vibrational relaxation has been a mechanism often proposed in the literature and will be addressed in the present research.

1.7.3 Thermal Inhomogeneities. In examining shock wave interaction with a decaying laser plasma, Aleksandrov, et al. [2] was one of the first to suggest that the observed variations in shock parameters in a plasma might be due to the presence of thermal inhomogeneities. In their experiment, a shock interacted with a hot plasma produced by a laser pulse. By comparing the shock velocity in the plasma region to the shock velocity just outside the plasma, they were able to estimate the gas temperature within the plasma. These estimates correlated well with plasma temperatures measured independently from the shock motion, indicating the higher gas temperature in the plasma was responsible for the higher shock velocity in this same region.

Shock velocities were also measured by Evtyukhin, et al. [41], both inside and outside a plasma region. By estimating the gas temperature in the plasma under known discharge conditions, they were able to predict the velocity increase as the shock propagated from the neutral gas into a plasma region. Their predictions also correlated well with measurements.

A more detailed analysis by Voinovich, et al. [115] reached the same conclusion. In their experiments, the measured temperature in the glow discharge was used in a

two-dimensional fluid calculation to predict the change in the shock velocity as the shock propagated from the neutral gas into a plasma region. The measured velocity increase was within the predicted range of values based on the uncertainties in the experimental measurements.

Taken together, these results offered convincing evidence that thermal effects play a dominant role in plasma/shock interactions. However, a series of other papers offers conflicting evidence with regard to the role of thermal inhomogeneities. Barkhudarov, et al. [10] simulated the temperature within a plasma by use of special equipment, which he claimed closely replicated the temperature. Results obtained by passing a shock through the heated region compared to results obtained by passing the shock through a plasma region led them to conclude that the observed dissipation of the shock front is not due to thermal effects. Basargin, et al. ([12], [13]) also reported no correlation between the gas temperature and the measured shock velocity as a shock propagates through a plasma region. Many other experimenters reach the same conclusion regarding the inability of thermal effects to fully explain the measured data ([27], [77], [75], [55], [52], [53], [46], [85]).

In light of such disagreement among the various researchers with regard to the role of thermal effects in plasma/shock interactions, an independent study of thermal inhomogeneities is warranted.

1.8 Research Approach

The approach to the present problem will be to address each of the proposed plasma/shock mechanisms independently, as shown in Figure 13. That is, although an actual laboratory plasma may have charged particle/neutral particle interactions, vibrational energy relaxation and thermal inhomogeneities present and at work simultaneously, this research will examine the effect of each independent from the other. In each case, the gas modeling the plasma will be treated as an inviscid fluid, which neglects the processes of viscosity and thermal conductivity. Neglecting

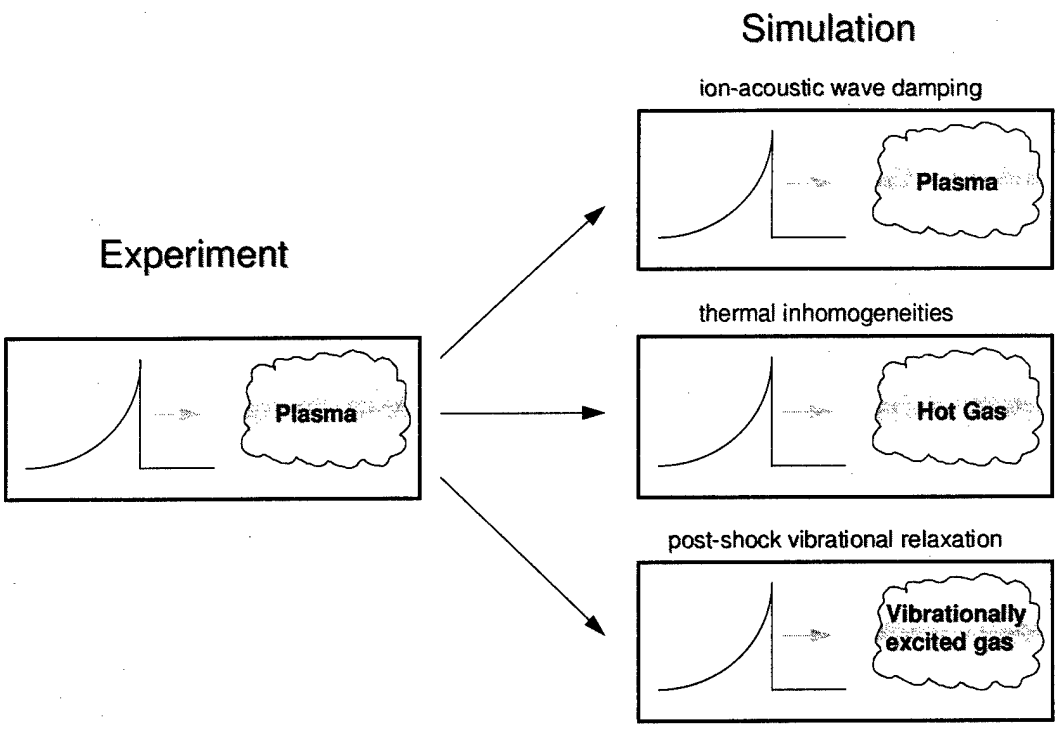

Figure 13. Research Approach.

these physical processes allows the Euler equations to be used, which are simpler to solve than the full Navier-Stokes description of a viscous, thermally conducting fluid. Therefore, the present research will focus on the numerical solution of the Euler equations for each of the cases shown in Figure 13. The basic numerical algorithm to be used in this research is an explicit MacCormack scheme [82]. Flux corrected transport [23] will be used as a means of controlling any numerical oscillations which might arise in regions of the domain where sharp gradients in the flow parameters are present. In order to examine each of these cases, three separate computational codes will be developed. Although each of these will use the MacCormack/FCT algorithm as a foundation, the exact algorithm implemented will be selected and modified as

required based on the the individual aspects of the physical processes present in each case. Specific details regarding each code can be found in the chapter corresponding to the appropriate case or in the appendices.

Two methods of shock generation have been used in the plasma/shock interaction experiments reported in the literature. These are the Riemann shock tube and the spark discharge. In the absence of a plasma, the former produces a shock of constant velocity with flow parameters which are uniform for some distance behind the shock front. The latter produces a shock of varying velocity with nonuniform flow parameters behind the shock front. Since each produces a shock waveform that is distinct from the other and since the experimental observations depend, to some extent, on the type of shock, both types of shocks will be examined in this research.

The influence of charged particles on neutral shock propagation will be examined within the framework of a two-component fluid approximation, in which the plasma (composed of ions, electrons and neutral particles) will be represented as two interacting fluids: neutrals and a charged component. In this approximation, the electrons and ions are assumed to move together as a single fluid, essentially strongly linked to each other by the electrodynamic force. Momentum and energy coupling between the neutral component and charged component will allow the two species to interact. Conditions in the plasma will be typical of those normally encountered in weakly ionized glow discharges. The gas pressure will be 30 torr, with a gas temperature of $300K$ and an electron temperature of 2 eV. A fractional ionization of 10^{-6} will be considered nominal, although higher fractional ionizations will also be examined. In this study, the degree of ionization will remain fixed; i.e., there are no production or loss terms in the conservation of mass equations for either the neutral or charged particles.

The influence of vibrational energy relaxation on shock propagation will be examined with the aid of the Euler equations, augmented by a conservation of vibrational energy equation. The transfer of energy from the vibrational manifold to the

translational and rotational modes will be described by a standard Landau-Teller coupling term [78]. The plasma will be represented by a region of gas containing a nonequilibrium store of vibrational energy. As the shock enters this nonequilibrium region, the vibrational energy contained in the gas will be allowed to relax behind the shock front to equilibrium levels, with the resulting flow parameters examined. This fluid treatment approach to vibrational relaxation will be supplemented with a kinetic treatment of energy relaxation. Here, the temporal evolution of the populations of the various vibrational states of N_2 will be examined under nonequilibrium conditions simulating the density and temperature behind a shock front. The purpose of this study is to determine how much energy can be extracted from the nonequilibrium vibrational manifold and added to the gaseous flow in a given time under realistic conditions.

The influence of thermal inhomogeneities on shock propagation will be examined with the aid of a two-dimensional fluid dynamics code. In this study, the gas in front of the shock will be heated to temperatures representative of those found in weakly ionized gas discharges. The pressure in this heated region will remain constant, which is typical of steady-state gas discharges. A shock will be propagated into the heated region and the resulting flow parameters examined.

The remaining chapters in this report expand on the concepts introduced here. Chapter II reviews pertinent background material that will lay the foundation for the research. This section discusses the basic theory of shocks as it relates to each of the three mechanisms mentioned previously. Each of these areas will be examined in detail in Chapters III through V. In each of these chapters, the model equations describing each proposed physical process will be given, validations of the relevant computer codes will be offered and the plasma/shock interactions from the numerical simulations will be presented and discussed. Overall conclusions of the present research and recommendations for future efforts are contained in Chapter VI.

In addition to the chapters mentioned previously, a number of appendices are offered that treat the specifics of the present research in further detail, beginning with a List of Symbols, which comprises Appendix A. The two-dimensional computational fluid code used to examine thermal inhomogeneities is detailed in Appendix B. The two-fluid plasma code used to examine ion-acoustic wave damping is discussed in Appendix C. The examination of the effects of thermal inhomogeneities required the development of a self-consistent solution of the heat conduction problem as it applies to the weakly-ionized plasmas typical of a glow discharge. The details of the method used to achieve this solution are found in Appendix D. The thermal profiles obtained were then used in the two-dimensional fluid code in order to simulate previously reported experiments. Finally, a short tutorial of optical shock tube diagnostics is offered in Appendix E. These diagnostic methods were also used in the two-dimensional simulations.

II. Background Theory

2.1 Introduction

The current research is focussed on three mechanisms that have been proposed in the literature as being responsible for the observed plasma/shock anomalies. In this chapter, the basic theory of each mechanism will be addressed in sufficient detail to permit an understanding of the discussions contained in the later chapters, where each mechanism is addressed individually in greater detail. First, however, it is necessary to explain the underlying framework upon which this investigation will rest.

2.2 Shock Analysis Approaches

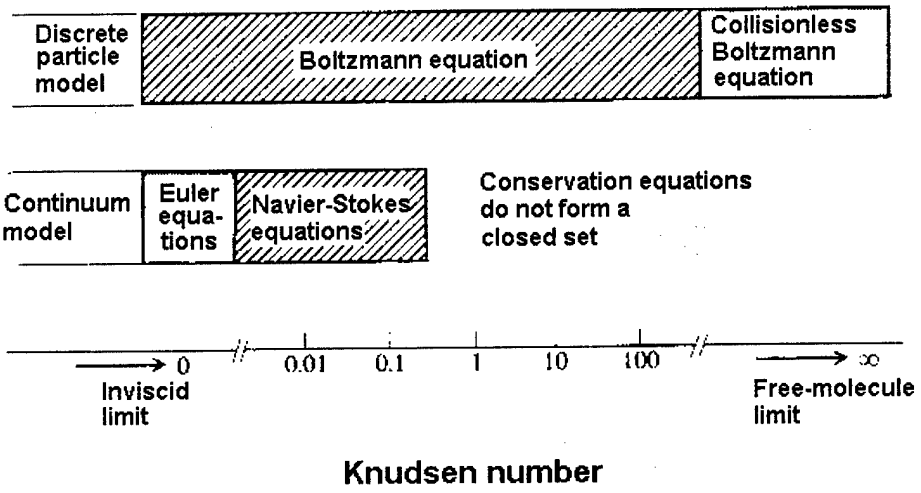

Figure 14. Regimes of applicability for the kinetic and fluid equations. [Ref: [5]]

There are two general approaches that can be used in the study of gasdynamic flows: kinetic based and fluid based. The kinetic approach is based on a discrete

particle model of the flow in which the Boltzmann equation is solved for the particle distribution function. The fluid approach is based on a continuum model for the flow in which either the Euler equations (for inviscid flow) or the Navier-Stokes equations (where viscosity and thermal conductivity are treated) are solved. These equations simply describe the principles of conservation of mass, momentum and energy for the fluid. The selection of the proper approach can be guided by the value of the Knudsen number, as shown in Figure 14. If the Knudsen number (the ratio of the mean free path of a particle divided by the characteristic distance over which the macroscopic variables change appreciably) is much less than one, then the fluid approach is appropriate. If the Knudsen number is of the order of one or greater, the kinetic approach is appropriate.

2.2.1 Kinetic Approach. The kinetic approach is based directly on the Boltzmann equation and treats the flow of gases as distributions of particles. This method yields the particle distribution function as the solution to the Boltzmann equation, from which all the macroscopic variables (density, temperature, velocity, pressure). can be determined. A number of researchers have used the kinetic approach in the study of both unionized [91] and ionized ([111], [1], [80], [113]) gas flows. It should be pointed out that the ionized studies referenced here assumed the plasma in front of the shock to be in an equilibrium state. That is, the electrons, ions and neutrals in front of the shock all had the same temperature. This is in contrast to the conditions relevant to the current research, in which the gas in front of the shock is assumed to be in a nonequilibrium state.

2.2.2 Fluid Approach. The fluid equations can be derived from the more complete Boltzmann equation by taking different moments of the latter. The first moment yields the continuity of mass equation, the second moment yields the continuity of momentum equation and the third moment yields the continuity of energy equation. It should be noted that each moment introduces another unknown, thus

there will always be one more unknown than the number of equations. For example, the continuity of mass equation introduces the mean velocity. The continuity of momentum equation includes this velocity, but also introduces the pressure tensor, which includes the scalar pressure as well as viscosity components. The energy equation contains the pressure tensor, but also introduces the heat flux vector, etc. Such an equation set is impossible to solve exactly. However, in practice the set of equations is usually terminated at some level and an additional constraint imposed. A common practice is to terminate the equation set at the energy equation and close the set with an assumed equation of state.

The fluid or continuum approach is based on the assumption that energy distributions of the individual species which comprise the flow always maintain forms of local thermodynamic equilibrium. That is, the energy distribution of each species is assumed to be a drifting Maxwellian (in the case of the Euler equations) or a slightly perturbed drifting Maxwellian (in the case of the Navier-Stokes equations). However, differences in temperature between species are allowable in this approach, permitting nonequilibrium conditions to be considered.

The fluid equations can be divided into two basic versions. The Euler equations assume that the distribution of particles in velocity space is a true drifting Maxwellian. As such, the coefficients of viscosity and thermal conductivity, which can be determined based on the distribution function, are identically zero. The Navier-Stokes equations assume that there are enough collisions in the flow to keep the distribution of particles in velocity space close to a Maxwellian (and hence describable by a fluid approach), yet not so many collisions that the distribution is a pure drifting Maxwellian. In this case the coefficients of viscosity and thermal conductivity will not be zero.

In the study of processes in and around shock fronts, it would appear that the kinetic approach is the appropriate choice, since the characteristic distance of the shock width is (classically) a few mean free paths, resulting in a Knudsen number

greater than one in this region. However, the kinetic approach is made difficult due to complications arising from the collision term contained within the Boltzmann equation. As a result, many researchers have adopted the fluid treatment as the method of choice. In spite of the apparent short comings this method might have when used to analyze shock structure, it has, in practice, enjoyed considerable success. Experience has shown that the fluid equations are an excellent model and give reasonably good estimates of the mean flow quantities [69].

The fluid approach was also adopted in the present research, with the assumption that the physical mechanisms to be studied are amenable to such a method. However, in the event some portion of these mechanisms is kinetic based, the fluid approach will be incapable of resolving the effect and a kinetic treatment must be used. In the remaining sections of this chapter, the fluid equations will be used to outline the basic concepts of plasma effects, vibrational energy relaxation effects and the effects of thermal inhomogeneities on shock propagation.

2.3 Plasma Effects

2.3.1 Small-Amplitude Wave Propagation in Weakly Ionized Plasma. In a neutral gas, all frequencies of small-amplitude waves travel at the same speed (to an approximation), the speed of sound. Thus a small-amplitude wave packet that is composed of a mixture of frequencies will travel without dispersion at the speed of sound. In a weakly ionized plasma, on the other hand, a number of modes are possible. Each of these modes has its own characteristic speed of propagation and dispersion properties. These modes can be determined by first linearizing the fluid equations for each species, which are the equations describing conservation of mass, momentum and energy, along with an appropriate equation of state. Assuming small-amplitude waves, the nonlinear portions of these equations, which lead to the development of shocks, can be neglected. Following this linearization procedure, the fluid equations can be represented by a system of homogeneous equations, which

can be written in matrix form. Setting the determinant of the coefficient matrix to zero results in a dispersion relation. Once the dispersion relation is known, it can be used to determine how a small amplitude wave will propagate, including the speed of the wave. According to Sessler [106], there are three modes of wave propagation in a weakly ionized, unmagnetized plasma. These modes describe the acoustic wave (neutral-particle wave), the ion-acoustic mode (the ion wave) and the Langmuir mode (electron wave).

The last two of these modes do not normally propagate. In the ion-acoustic mode, ions and electrons move in phase with each other and with almost the same amplitude, while the neutrals can be considered to be at rest [63]. Although the ion-acoustic mode in a plasma travels faster than an acoustic wave in a neutral gas, the ion-acoustic waves are strongly damped for $\omega < \nu_{in}$, where ω is the wave frequency and ν_{in} in the ion-neutral collision frequency. Such strong damping effectively prevents this mode from propagating. In the Langmuir wave the neutrals are approximately stationary and the electrons and ions move in opposite directions [63]. Normally, this mode does not propagate either, due to the very rapid attenuation of the wave with distance (on the order of a Debye length).

A wave mode that can propagate, however, is the acoustic mode, so named due to its close relationship to a sound wave propagating in a neutral gas. It is characterized by a propagation speed very nearly equal to the neutral sound speed. This mode also describes wave action in which all of the components move with very nearly the same phase and amplitude. As such, only weak attenuation would be expected with this mode, which Sessler determined was primarily due to neutral particle viscosity effects.

2.3.2 Shock Propagation in Weakly Ionized Plasma. In the previous section, the propagation modes for small-amplitude waves in an ionized gas were discussed. Since the waves were of small amplitude, the nonlinear terms in the fluid

equations could be neglected. When the amplitude of a wave is not small these nonlinear terms must be retained. It is exactly the nonlinear term in the momentum equation which leads to a steepening of the wave's profile as it propagates. As in a neutral gas, this steepening process leads to the development of shocks in a partially ionized gas as well, which is the subject of the present section. Shocks in nonequilibrium partially ionized gases exhibit different features than shocks in neutral gases. For example, the large disparity between the electron and heavy particle temperature leads to the generation of ion-acoustic waves. Since these waves travel at the ion-acoustic sound speed (approximately seven times the neutral sound speed under typical glow discharge conditions), they are able to propagate out in front of a neutral shock (as long as the neutral shock is traveling less than the ion-acoustic speed). As a result, ion-acoustic waves are able to create a region in front of the neutral shock in which the charged particle densities and velocities are perturbed from their ambient values. The width of this region is large compared to the typical width of the neutral shock. Through ion-neutral collisions, these waves are damped, with their momentum and energy being transferred to the neutral gas.

In this section, the derivation of a simplified set of equations based on the two fluid approximation used by Avramenko, et al. [6] will be used to provide the background theory regarding shocks in weakly ionized plasmas. Since a two fluid approximation will be used to describe the plasma in the present research, it is advantageous to present Avramenko's development here. In this approximation, the electrons and ions are assumed to behave as a single component, with the mean velocity of the electrons assumed to be equal to the mean velocity of the ions. In addition, the plasma is assumed to be quasi-neutral, wherein the ion and electron number densities are very nearly the same. With these assumptions, the ion mass conservation equation can be solved in lieu of the electron mass conservation equation. Avramenko further assumed that the electron temperature was much higher than the ion or neutral gas temperature, which is appropriate in the case of the weakly

ionized glow discharges commonly used in plasma/shock interaction experiments. Furthermore, energy transfer between the different components was neglected. The neutral particle density and velocity profiles were assumed known and modeled by appropriate step functions, as in Ingard's development [65].

Avramenko's approach begins by considering the electron and ion momentum equations, which can be written in one dimension as

$$\frac{\partial}{\partial t}(\rho_e V_e) + \frac{\partial}{\partial x}(\rho_e V_e^2) = -\nabla P_e - \frac{\rho_e q E}{M_e} - \rho_e \nu_{ei}(V_e - V_i) - \rho_e \nu_{en}(V_e - V_n) \quad (5)$$

$$\frac{\partial}{\partial t}(\rho_i V_i) + \frac{\partial}{\partial x}(\rho_i V_i^2) = -\nabla P_i + \frac{\rho_i q E}{M_i} - \rho_i \nu_{ie}(V_i - V_e) - \rho_i \nu_{in}(V_i - V_n) \quad (6)$$

where ρ is the mass density, V is the mean flow velocity, P is the pressure, M is the particle mass, E is the electric field, q is the elementary unit of charge and ν is a collision frequency. The subscripts i, e, n denote the ions, electrons and neutral fluid, respectively. The electron momentum equation can first be simplified by neglecting the electron inertia term (first term on the left hand side of Equation 5). For cases in which the electron thermal speed is much greater than the electron mean flow velocity, the second term on the left hand side of this equation can also be neglected. In conditions typical of weakly ionized glow discharges, this requirement is met for shock Mach numbers of the order of 20 or less. The third term on the right hand side of both of these equations is zero, since V_e has been assumed to be equal to V_i. The three remaining terms in Equation 5 allow the electric field to be approximated as

$$E \approx -\frac{k_B T_e}{\rho_e q}\nabla \rho_e - \frac{M_e \nu_{en}}{q}(V_i - V_n), \quad (7)$$

where T_e has been assumed constant. The first term on the right hand side of this equation represents the gradient in the electron pressure, while the second term represents the electron-neutral collision term. It will be shown in Chapter III that the contribution of the collision term to the electric field is small. For the moment, however, it will be retained. Using Equation 7 to represent the electric field and

assuming the plasma to be quasi-neutral ($n_e \approx n_i$), the ion momentum equation can be rewritten as

$$\frac{\partial}{\partial t}(\rho_i V_i) + \frac{\partial}{\partial x}(\rho_i V_i^2) = -\nabla P_i - \frac{k_B T_e}{M_i}\frac{\partial \rho_i}{\partial x} - \rho_i (V_i - V_n)\nu_{in}\left[1 + \frac{M_e}{M_i}\frac{\nu_{en}}{\nu_{in}}\right]. \quad (8)$$

The first term in the brackets on the right hand side represents ion-neutral collisions while the second term is the electron-neutral collision term retained in the electric field approximation (Equation 7). It can be shown that for conditions typical of a weakly ionized plasma in Argon, the second of these terms is very small compared to one and will be neglected. Under these simplifying assumptions, the ion equations become

$$\frac{\partial \rho_i}{\partial t} + \frac{\partial}{\partial x}(\rho_i V_i) = 0 \quad (9)$$

$$\frac{\partial}{\partial t}(\rho_i V_i) + \frac{\partial}{\partial x}\left(\rho_i V_i^2\right) = -\frac{k_B T_\epsilon}{M_i}\frac{\partial \rho_i}{\partial x} - \rho_i \nu_{in}(V_i - V_n). \quad (10)$$

The ion-neutral collision frequency, ν_{in}, is defined as [110:88]

$$\nu_{in} = \frac{2\sigma_{in}}{\sqrt{\pi}} n_n (2k_B)^{1/2}\left(\frac{T_i}{M_i} + \frac{T_n}{M_n}\right)^{1/2}, \quad (11)$$

where σ_{in} is the ion-neutral collision cross-section. The first term on the right hand side of Equation 10 represents the momentum gained by the ions due to the electric field (from Equation 7), while the second term represents the time rate of change of ion momentum due to collisions with neutral particles. Note the lack of a term representing the gradient of the ion pressure on the right hand side of this equation. Neglecting this term is justifiable in a weakly ionized plasma, in which T_e is typically one to two orders of magnitude greater than T_i.

Avramenko did not use an energy equation for either the neutrals or the ions, assuming instead that the heavy particle temperatures were constant throughout the shock front region. This appears to be a serious omission, especially in light of the

obvious temperature rise across the shock front. However, truncating the equation set at the momentum equation simplifies the problem considerably, and results in a solution nearly identical with Ingard, who retained the energy equations for all the plasma components.

The assumption of a steady-state form of the solution allows Equations 9 and 10 to be transformed into a coordinate system attached to the shock front. This is accomplished by defining a new spatial coordinate, ξ , defined as

$$\xi = x - V_{shock}t \tag{12}$$

where V_{shock} is the shock front velocity. This transformation essentially changes the partial differential equations into ordinary differential equations. Accordingly, Equations 9 and 10 are transformed into

$$-V_{shock}\frac{d\rho_i}{d\xi} + \frac{d}{d\xi}(\rho_i V_i) = 0 \tag{13}$$

$$\frac{d}{d\xi}\left[\frac{\hat{V}_i^2}{2} - V_{ia}^2 \ln\left(\frac{\hat{V}_i}{V_{shock}}\right)\right] - \nu_{in}(\hat{V}_i - \hat{V}_n) = 0 \tag{14}$$

where $\hat{V}_i$ and $\hat{V}_n$ are the ion and neutral flow velocities, now in the shock front frame, defined as

$$\hat{V}_{i,n} = V_{shock} - V_{i,n}. \tag{15}$$

Note that the ion velocity in the transformed conservation of mass equation (Equation 13) is defined with respect to the laboratory frame. The ion-acoustic velocity, V_{ia} , appearing in Equation 14 is the velocity of small disturbances in the plasma and is defined as

$$V_{ia} = \left(\frac{\gamma_i k_B T_i + \gamma_e k_B T_e}{M_i}\right)^{1/2} \tag{16}$$

where γ_i and γ_e is the ratio of specific heats for the ions and electrons, respectively. With $T_e >> T_i$, which is usually the case in weakly ionized plasmas, the ion-acoustic

velocity can be approximated as

$$V_{ia} \approx \left(\frac{\gamma_e k_B T_e}{M_i} \right)^{1/2} . \tag{17}$$

In general, the neutral component would be described by equations analogous to Equations 9 and 10 (lacking, of course, the electric field term). However, in the simplified case considered by Avramenko, the density and velocity of this component were given by step functions:

$$\hat{V}_n(\xi) = V_{n1} \, H(-\xi) \tag{18}$$

$$\rho_n(\xi) = \rho_{n0} + (\rho_{n1} - \rho_{n0}) \, H(-\xi) \tag{19}$$

where ξ is greater than zero in front of the neutral shock front and less than zero behind the neutral shock front. The subscripts 0 and 1 denote regions in front of and behind the shock front, respectively. Thus, ρ_{n0} and ρ_{n1} are the neutral mass densities in the ambient and perturbed regions of the flow, respectively, and V_{n1} is the neutral velocity behind the shock front. $H(\xi)$ is the Heaviside step function, defined as

$$H(\xi) = \begin{cases} 1, & \xi > 0 \\ 0, & \xi < 0 \end{cases} \tag{20}$$

Solving Equation 13 analytically yields an equation relating the ion mass density, ρ_i, to the ion velocity in the laboratory frame, V_i:

$$\rho_i = \rho_{io} \left(1 - \frac{V_i}{V_{shock}} \right)^{-1} . \tag{21}$$

Assuming the ion-acoustic velocity to be much greater than the neutral shock velocity ($V_{ia} >> V_{shock}$) allows the first term in the brackets of Equation 14 to be neglected in comparison to the second term. This is equivalent to neglecting the nonlinear term in the ion momentum equation, which in effect limits any resulting solution to

small amplitudes. However, neglecting this nonlinear term allows Equation 14 to be integrated analytically, resulting in

$$V_i(\xi) = \begin{cases} \frac{V_{shock}}{1+\exp\left(\frac{\xi}{\xi_0}\right)\left(\frac{\rho_{n1}}{\rho_{n0}}-1\right)^{-1}} & \xi > 0 \\ V_{n1} = V_{shock}\left(1 - \frac{\rho_{n0}}{\rho_{n1}}\right) & \xi < 0 \end{cases} \tag{22}$$

where the ion velocity has been transformed back into the laboratory frame of reference. In this equation, ξ_0 is a characteristic length defined as

$$\xi_o = \frac{V_{ia}^2}{V_{shock}\ \nu_{in}^{(o)}} \tag{23}$$

where $\nu_{in}^{(o)}$ is the ion-neutral collision frequency in the unperturbed (upstream) region of the flow. It can be shown that this expression for the characteristic length can be approximated (to within a constant of the order of unity) as

$$\xi_o = \frac{T_e}{T_n}\lambda_{in}^{(0)} \tag{24}$$

where $\lambda_{in}^{(o)}$ is the ion-neutral mean free path in the upstream flow. This characteristic length is nearly identical to Ingard's result.

Using the ion velocity profile of Equation 22 in Equation 21 yields the ion density profile,

$$\frac{\rho_i(\xi)}{\rho_{i0}} = \begin{cases} 1 + \left(\frac{\rho_{n1}}{\rho_{n0}} - 1\right)\exp\left(-\frac{\xi}{\xi_0}\right) & \xi > 0 \\ \frac{\rho_{n1}}{\rho_{n0}} & \xi < 0 \end{cases} \tag{25}$$

which is nearly identical to Ingard's result (Equation 2).

The chief results of Avramenko's derivation are Equations 22 and 25. These approximate analytic expressions describe the motion of the charged particles as a shock propagates through a weakly ionized plasma. As an example of the structures predicted using these results, the case of a Mach 2 shock in weakly ionized Argon is considered. Here, plasma parameters typical of a weakly ionized glow discharge will

be used:

$$\begin{aligned} T_\epsilon &= 2\text{ eV} \quad P_n = 30\text{ torr} \quad \alpha = 10^{-6} \\ T_n &= 400K \quad \sigma_{in} = 10^{-19}\text{m}^2 \end{aligned} \tag{26}$$

where α is the fractional ionization, defined as

$$\alpha = \frac{n_i}{n_i + n_n}. \tag{27}$$

Under these conditions, the characteristic length ξ_o evaluates to approximately 0.23 mm.

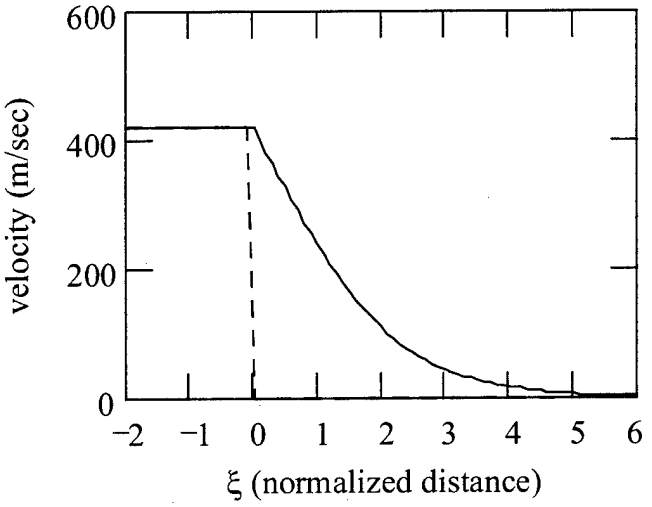

Figure 15. Velocity profiles of the ions (solid) and neutrals (dashed) in the laboratory frame of reference, according to Avramenko's approximate analytic solution (Equation 22). The distance has been normalized by ξ_o.

Avramenko's approximate analytic solution for the ion velocity is shown in Figure 15. The neutral velocity profile is given by the dashed line. The ionic precursor extends out to approximately $5\xi_o$ (or 80 ion-neutral mean free paths) which is just over 1 mm under the present conditions. If the neutral-neutral mean free path and the ion-neutral mean free path are of the same order of magnitude, then the precursor shock front width is approximately 20 times the neutral shock front width. The velocity in the downstream region is consistent with the Rankine-Hugoniot re-

lations for a Mach 2 shock in Argon. The approximate solution is valid for the case in which $V_{in}/V_{shock} >> 1$. In this calculation, this ratio was slightly less than four. The spatial axis has been normalized according to the characteristic length ξ_o.

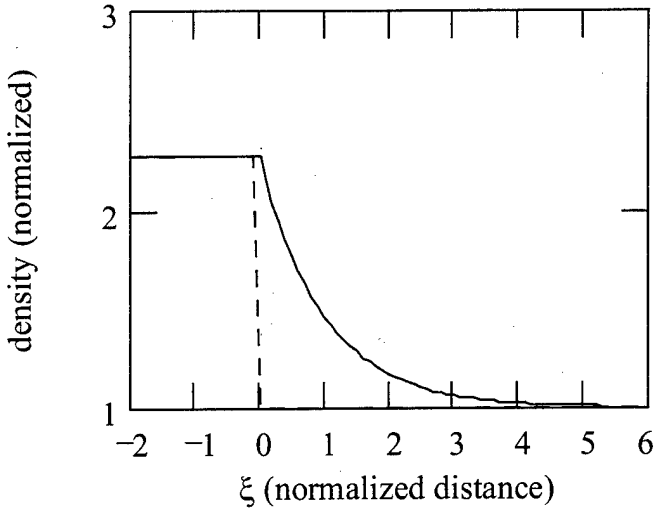

Figure 16. Density profiles of the ions (solid) and neutrals (dashed), according to Avramenko's approximate analytic solution (Equation 25). The distance has been normalized by ξ_o.

The ion (solid) and neutral (dashed) density profiles are shown in Figure 16. The post-shock value of each is consistent with a Mach 2 shock in Argon. Again, an ionic precursor is present, extending approximately $5\xi_o$ in front of the neutral shock. In this figure, the densities have been normalized to their respective upstream values. Thus, although the precursor appears dramatically here, it must be remembered that the ions constitute only a very small fraction of the total mass of the gas at any point in the flow.

Up to the present, no discussion has been given regarding the electron density profile. In the two fluid plasma approximation, the electron and ion motion was assumed to be closely linked to each other, allowing the solution of the ionic equations (density, velocity) to be the approximate solution for the electrons. However, small deviations from charge neutrality will exist in the plasma in certain regions,

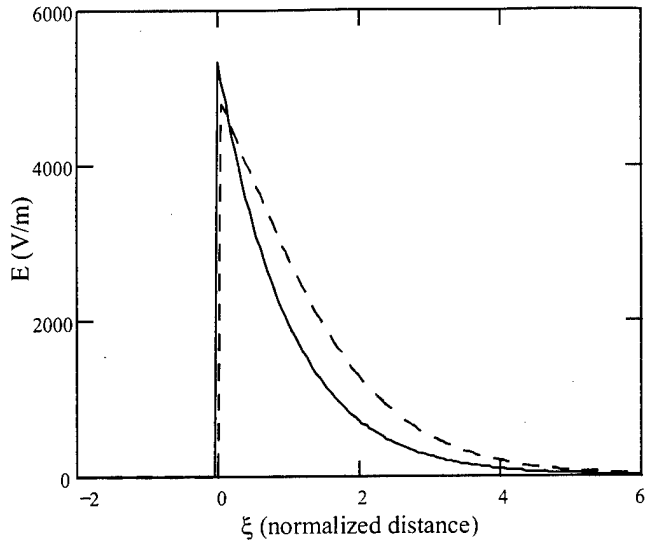

Figure 17. Approximate electrical field calculated by a linearized dispersion relation (Equation 4) (solid) and by balancing the electric force with the electron pressure gradient (Equation 7) (dashed).

resulting in an electric field. This electric field can be calculated in at least two ways. First, there is Ingard and Schulz's approximate analytic solution based on the acoustic mode dispersion relation applied to a neutral shock in weakly ionized plasma (Equation 4). Second, there is Equation 7, which was used in Avramenko's derivation of the ion momentum equation in the two fluid plasma approximation. Here, the electric field was determined by essentially requiring the electric force to be balanced by the electron pressure gradient (the electron-neutral collision term was shown to be small). Ingard's estimate is shown in Figure 17 as the solid curve, while the result of applying Equation 7 to the ion density profile in Figure 16 is shown as the dashed line. Although there are noticeable differences between the curves, the peak values and the spatial extent in front of the neutral shock are very similar.

In this section, the influence of charged particles on the shock profile has been examined using approximate solutions to the fluid equations. A precursor (comprised of charged particles) has been shown to exist upstream of the neutral shock with a width of approximately T_e/T_i times the ion-neutral mean free path. This precursor

arises due to the generation and subsequent dampening of ion-acoustic waves in the shock front region. Alternatively, one can view the precursor as arising from diffusion of charged particles from behind the shock front due to the high electron mobility and the plasma's inherit property to maintain charge neutrality. An electric field has also been shown to be generated in the region of the precursor.

In both Ingard's [65] and Avramenko's [6] development of the ion precursor, the influence of the charged particles on the neutral gas was not examined. By using an assumed form for the neutral density and velocity profile, the neutrals were allowed to influence the charged particles, but the reverse process was prevented. However, it is exactly the reverse process which has been suggested in the literature as a major contributor to the observed experimental anomalies, under the auspices of ion-acoustic dampening ([11], [12], [13], [51], [75], [85]). That is, as the ion-acoustic wave is damped, its momentum and energy are transferred to the neutral gas, heating the neutral fluid in the process. To examine this process, an analysis must be adopted in which no assumptions are made with respect to the form of the neutral component. This analysis will be undertaken in Chapter III.

2.4 Post-Shock Energy Addition: Vibrational Relaxation

The addition of energy into the flow behind the shock front has been proposed as a process responsible (at least in part) for the observed shock phenomena in plasma, particularly the anomalously high shock speed. Physical mechanisms that could lead to post-shock energy addition include electron-ion recombination [75], de-excitation of electronic states [54], atomic association [75] and vibrational energy relaxation [74]. The present section will address the last of these processes, focusing on the relaxation of vibrational energy under nonequilibrium conditions.

A brief introduction to Hugoniot shock adiabatics, used to both understand vibrational relaxation effects and provide analytic calibration points for computational models, will be presented first. This introduction will be followed by the application of shock adiabatics to the cases of both equilibrium and nonequilibrium vibrational energy relaxation, highlighting the essential differences present in the nonequilibrium case. Finally, a discussion of the nonequilibrium vibrational relaxation time will be given. Here, it will be shown that the characteristic time for nonequilibrium vibrational relaxation can be many orders of magnitude faster than that encountered under equilibrium conditions, providing the opportunity for vibrational relaxation to play a relevant role in plasma/shock interactions.

2.4.1 Shocks and Hugoniot Shock Adiabatics. Since both Landau [79:319] and Zel'Dovich [123:5] extensively discuss shock adiabatics, they will not be derived here. Briefly, however, the equations that express the continuity of mass, momentum and energy in a reference frame attached to the shock front can be combined to give a relation between the density and pressure just behind the shock to the density and pressure in front of the shock. This relation is given by Landau [79:320] as

$$\epsilon_1 - \epsilon + P_1 V_1 - PV + \frac{1}{2}(V_1 + V)(P - P_1) = 0 \tag{28}$$

where P is the pressure, V is the specific volume $(1/\rho)$ and the subscript 1 denotes the upstream ambient values. The specific internal energy (thermal, rotational, vibrational, chemical, etc.) is represented by ϵ and is defined as

$$\epsilon = \frac{1}{\gamma - 1}\frac{k_B T}{M}, \tag{29}$$

where γ is the ratio of the specific heats (C_p/C_v). Landau calls Equation 28 the 'shock adiabatic' or the 'Hugoniot adiabatic'. It will be the principal analytical tool used in predicting the values of 1) the jumps in the flow parameters across the viscous shock 2) the equilibrium values of the flow parameters in the downstream region and 3) the shock front velocity in a nonequilibrium gas.

As an example of a shock adiabatic, consider a calorically perfect gas with $\gamma = 7/5$. Such a gas would be representative of a nitrogen molecule with 3 translational degrees of freedom and 2 rotational degrees of freedom (for the moment, vibrational degrees of freedom will be neglected). The shock adiabatic for this gas can be drawn in the P-V (pressure, specific volume) plane by finding the solution to Equation 28 with $\epsilon = \frac{5}{2}\frac{kT}{M}$. Assuming a perfect gas, Equation 28 can be written as

$$\frac{7}{2}P_1V_1 - \frac{7}{2}PV + \frac{1}{2}(V_1 + V)(P - P_1) = 0 \tag{30}$$

The solution to Equation 30 is shown in Figure 18, where the pressure and specific volume have been normalized by their initial values. Thus, a fluid element in the ambient gas is represented by the point (1,1).

A shock can be defined in the P-V plane by a line drawn from the initial point, with the slope specifying the shock speed. This line represents the conservation of mass flux, j, which is defined as

$$j = \rho v, \tag{31}$$

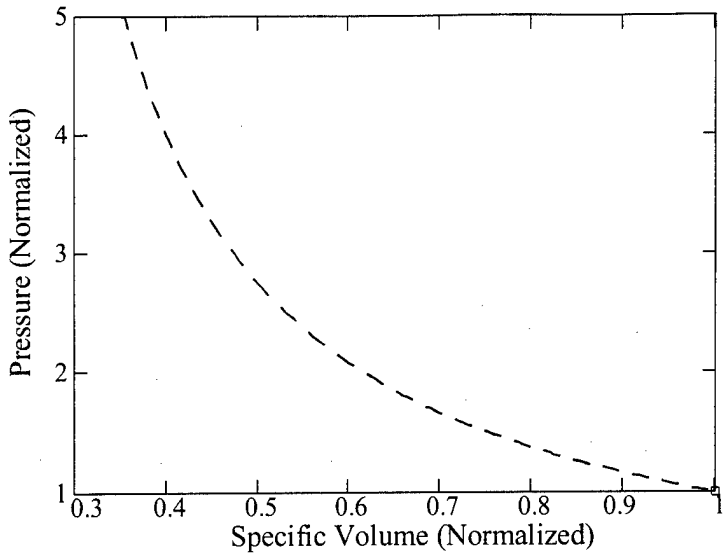

Figure 18. Shock adiabatic for a gas with γ=7/5.

where ρ is the density and v is the flow velocity in the shock front frame. According to Landau [79:320], the square of the mass flux defines the slope of a line drawn from the initial point (P_1, V_1), which intersects the shock adiabatic at some other point (P,V):

$$j^2 = \frac{P - P_1}{V_1 - V}. \tag{32}$$

Thus, the shock speed and the slope of the constant mass flux line are related by

$$\rho_1^2 V_{\text{shock}}^2 = \frac{P - P_1}{V_1 - V}. \tag{33}$$

In Figure 19, the same $\gamma = 7/5$ shock adiabatic as in Figure 18 is shown, together with a mass flux line corresponding to a shock traveling at a speed of 706 m/sec (Mach 2). The coordinates of the intersection of these two curves (point 'A') yields the jump values in pressure and density across the shock front. These are the same values that would have been obtained using the standard Rankine-Hugoniot shock relations [5:33-35] under identical conditions.

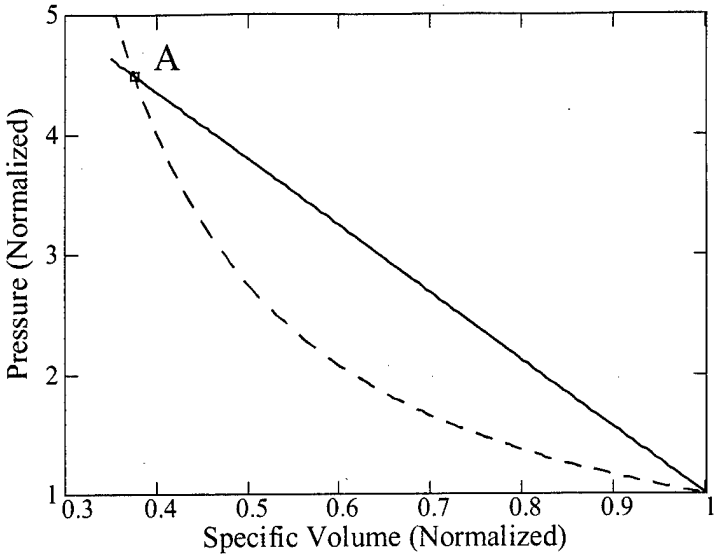

Figure 19. Shock adiabatic for a gas with γ=7/5 and a mass flux line for a shock propagating with a velocity of 706 m/sec.

2.4.1.1 Equilibrium Vibrational Relaxation. Now consider a gas with vibrational degrees of freedom. For simplicity, the specific vibrational energy will be modeled as

$$\epsilon_{vib}(T_{vib}) = \frac{k_B T_{vib}}{M}. \tag{34}$$

It is noted that this representation of the specific vibrational energy is different than the usual expression for the average specific vibrational energy of a Maxwell-Boltzmann distribution of harmonic oscillators, given by

$$\epsilon_{vib}(T_{vib}) = \frac{k_B T^0_{vib}}{M} \frac{1}{e^{T^0_{vib}/T_{vib}} - 1}, \tag{35}$$

where T^0_{vib} is the characteristic vibrational temperature for the particular molecule ($T^0_{vib} \approx 3395K$ for N_2). It is instructive to compare the vibrational temperature obtained by use of Equation 34 with the vibrational temperature as it appears in Equation 35. If T_{vib} in Equations 34 and 35 is labelled T_{vib1} and T_{vib2}, respectively, then by conservation of energy the two vibrational temperatures can be related, as shown in Figure 20. It is observed that the vibrational temperatures used in

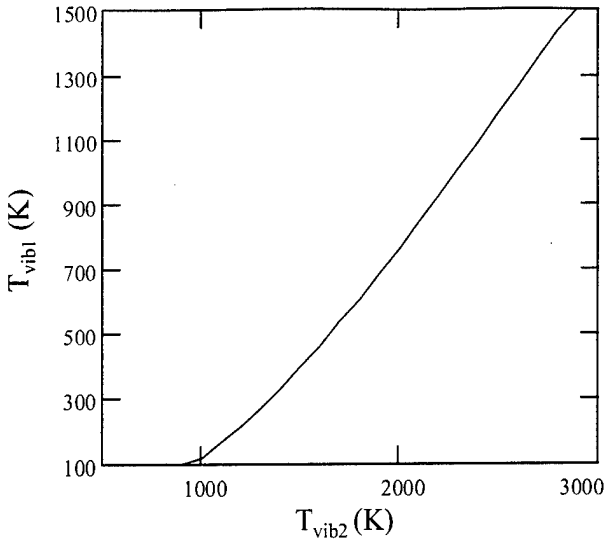

Figure 20. Comparison of T_{vib} given by Equation 34 (T_{vib1}) with T_{vib} given by Equation 35 (T_{vib2}).

the simplified expression for the specific vibrational energy are much less than the vibrational temperatures used in the usual definition of the same. For example, a vibrational temperature typically encountered in a glow discharge in N_2 is $2000K$, which is approximately equivalent to $800K$ in this simplified analysis. The use of Equation 34 allows the ratio of specific heats (γ) to be represented conveniently as $9/7$. This essentially gives two full degrees of freedom to the vibrational mode, with each receiving $1/2\,k_B T$ of thermal energy, consistent with classical thermodynamics. In this case, the shock adiabatic (Equation 28) can be written as

$$\frac{7}{2}P_1V_1 + \epsilon_{vib}(T_{vib_1}) - \frac{7}{2}PV - \epsilon_{vib}(\frac{PVM}{k_B}) + \frac{1}{2}(V_1 + V)(P - P_1) = 0 \qquad (36)$$

where T_{vib_1} denotes the ambient vibrational temperature in front of the shock and $\frac{PVM}{k_B}$ represents the equilibrium temperature behind the shock, which is a function of pressure and specific volume. If the vibrational temperature in front of the shock

is in equilibrium with the gas temperature in front of the shock, then

$$T_{vib_1} = T_{gas_1} = \frac{P_1 V_1 M}{k_B} \tag{37}$$

and Equation 36 can be rewritten as

$$\frac{9}{2} P_1 V_1 - \frac{9}{2} PV + \frac{1}{2}(V_1 + V)(P - P_1) = 0 \tag{38}$$

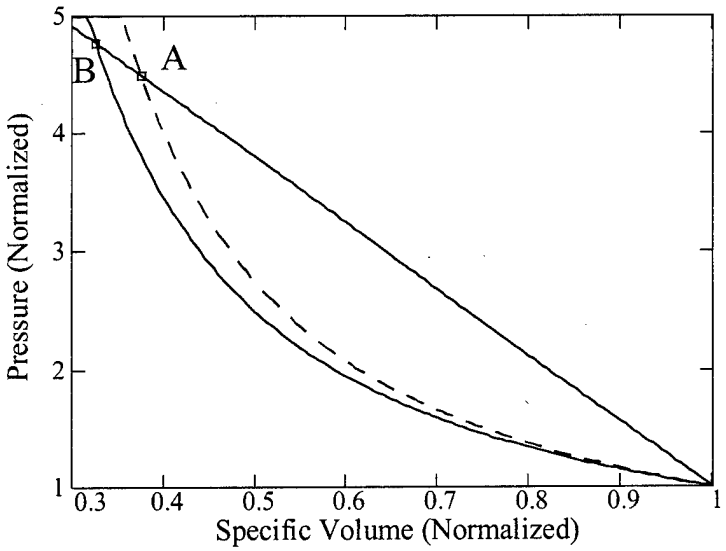

Figure 21. Shock adiabatics for gases with γ=7/5 (dashed) and γ=9/7 (solid) and a mass flux line for a shock propagating with a velocity of 706 m/sec.

The solution to Equation 38 is shown in Figure 21 (solid), along with the previous solution to Equation 30 (dotted). A shock with a propagation speed of 706 m/sec is also shown. The time scale for the fluid to cross the shock front is much smaller than the time scale for vibrational energy relaxation, thus the vibrational energy can be considered to be 'frozen' on this time scale, with the gas having a γ of 7/5. As a result, immediately after crossing the shock front, the flow parameters are those given by point 'A'. The initial jump to 'A' can be considered instantaneous, although in reality it takes a few (4-5) collisions before the conditions at 'A' are

realized. As equilibrium (point 'B') is approached, energy is transferred from the translational and rotational modes into the vibrational modes. Note that as equilibrium is approached, both the pressure and density of the fluid element increase. The conditions at 'B' are the same as those determined from a more complex algorithm which takes into account the transfer of energy into the vibrational manifold (see, for example, [5:508]).

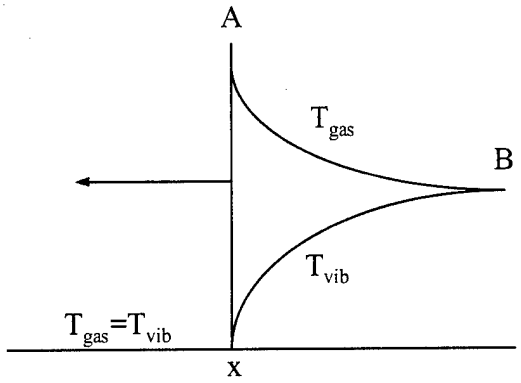

Figure 22. Temperature distribution in a shock propagating through an equilibrium gas. Point 'A' is just behind the shock front, while point 'B' is in the equilibrium region.

An alternate view of the equilibrium process is depicted in Figure 22. As a fluid element crosses the shock, the gas temperature rises sharply, while the vibrational temperature remains fixed at the upstream value. As the fluid element progresses further downstream, energy from the translational and rotational modes is gradually transferred to the vibrational mode, with the fluid reaching equilibrium at point 'B'.

2.4.1.2 Nonequilibrium Vibrational Relaxation. Suppose now that the shock is propagating into a region of gas in which the vibrational temperature is not the same as the gas temperature. This region is in a nonequilibrium state. It is natural to ask how this region could arise. One answer lies in examining the effects of a glow discharge plasma on the vibrational energy of the neutral gas. The electrons in

the plasma collisionally excite the vibrational states of the molecules in the discharge. Through anharmonic pumping effects, the temperature which is characteristic of the vibrational energy can be many times greater than the gas temperature [49:147]. In this case, T_{vib_1} does not equal the local gas temperature, but can be many times greater than it. Assuming full equilibrium is eventually achieved in the downstream region, Equation 36 still remains valid and the adiabatic can be drawn for any initial vibrational temperature T_{vib_1}.

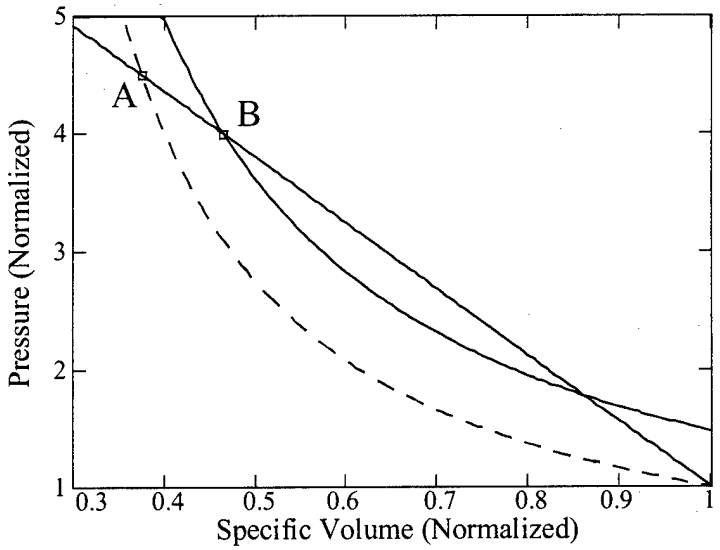

Figure 23. Shock adiabatics for a gas with γ=7/5 (dashed) and for a nonequilibrium gas with $\gamma = 9/7$ (solid). The ambient translational and vibrational temperatures are $300K$ and $800K$, respectively. The mass flux line corresponds to a shock propagating with a velocity of 706 m/sec.

As an example, consider the case in which $T_{vib_1} = 800K$, and $T_{gas_1} = 300K$, as in Figure 23. A shock propagating at a velocity of 706 m/sec is also shown. Point 'A' is the intersection of the $\gamma = 7/5$ adiabatic (dashed) with the constant mass flux line, which reflects equilibration of the translational and rotational modes just behind the shock front, with the vibrational modes frozen. Point 'B' is the intersection of the equilibrium adiabatic (solid) with the constant mass flux line. Note that in this nonequilibrium case, the equilibrium adiabatic does not pass through the initial

point (1,1). A fluid element in front of the shock travels toward the shock at 706 m/sec (in the shock front frame). Point 'A' is reached instantaneously after crossing the shock front. Now, instead of the vibrational mode being a sink for translational and rotational energy, it becomes a source. That is, as equilibrium is approached (point 'B'), the energy present in the vibrational mode is transferred to the other modes until the vibrational temperature equals the gas temperature. Note in this case both the pressure and density decrease as equilibrium is approached.

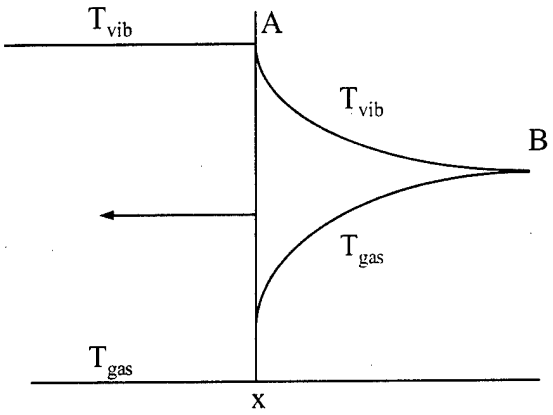

Figure 24. Temperature distribution in a shock propagating through an equilibrium gas. Point 'A' is just behind the shock front, while point 'B' is in the equilibrium region.

A complementary view of the equilibration for the nonequilibrium state is shown in Figure 24. Here, a shock propagates into a gas which is initially in a nonequilibrium state. As a fluid element crosses the shock, the gas temperature rises sharply, while the vibrational temperature remains constant. As the fluid element flows into the downstream region, energy from the vibrational mode is gradually transferred to the translational and rotational modes, with the fluid reaching equilibrium at point 'B'.

In the case of nonequilibrium energy relaxation, there is a minimum value for the slope of a line drawn from the initial point that can intersect the equilibrium adiabatic. This limiting line is tangent to the equilibrium adiabatic, with the point

of tangency called the Chapman-Jouguet point. Since the slope of a constant mass flux line is related to the shock velocity, the presence of a minimum mass flux results in a minimum shock velocity. According to the theory outlined by Osipov, et al. [93], which is based on the work of Zel'Dovich [123] and Landau [79], a shock wave which enters a nonequilibrium region at a velocity less than the minimum shock velocity the will accelerate until the minimum velocity is achieved. As an example, consider

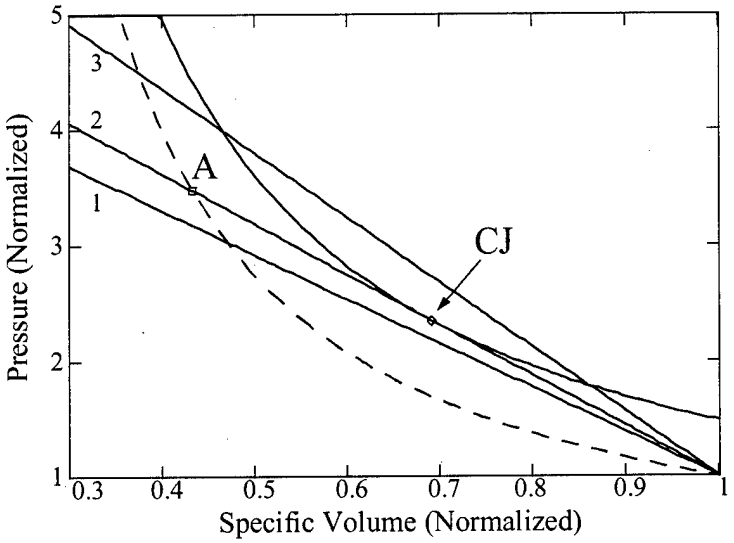

Figure 25. Shock adiabatic for a gas with γ=7/5 (dashed) and for a nonequilibrium gas with $\gamma = 9/7$ (solid) where $T_{gas_1} = 300K$ and $T_{vib_1} = 800K$. Point 'CJ' is the Chapman-Jouguet point. The mass flux lines correspond to shock velocities of 585 m/sec (curve 1), 624 m/sec (curve 2) and 706 m/sec (curve 3).

the nonequilibrium case in which the values of the vibrational and translational temperatures are $800K$ and $300K$, respectively. The corresponding adiabatics, shown in Figure 25, are identical to those discussed in Figure 23. A minimum constant mass flux line (curve 2) is tangent to the equilibrium adiabatic at the Chapman-Jouguet point ('CJ') and corresponds to a shock velocity of 624 m/sec. According to theory, this is the minimum allowable steady-state velocity in the nonequilibrium region. According to an interpretation of this theory by Bystrov, et al. [27], no acceleration (or deceleration) is expected for a shock which enters the equilibrium region at a

speed which is greater than the minimum shock speed. For example, Figure 25 also shows a shock with a velocity of 706 m/sec (curve 3). Since this shock enters the nonequilibrium region at a velocity greater than the minimum shock velocity, no change in the shock speed is expected according to Bystrov. However, consider the shock which propagates into the nonequilibrium region with an initial velocity of 585 m/sec (curve 1). Since the initial shock speed is less than the minimum shock speed, the shock is expected to accelerate to the new minimum velocity (624 m/sec). When the steady-state has been reached (that is, when the shock has reached the new minimum shock velocity) a fluid element crossing the shock will instantaneously move from the initial point to the point 'A', then relax down the constant mass flux line to the Chapman- Jouguet point ('CJ') at some finite rate, which depends on the nonequilibrium vibrational relaxation kinetics.

2.4.2 Nonequilibrium Vibrational Relaxation Time. In the previous section, it was shown that variations in the flow parameters will occur as a fluid element passes from the shock front region (point 'A') towards the equilibrium region (point 'B'). For a gas initially in equilibrium, the characteristic time associated with these variations is usually long compared with the time it takes a fluid element to cross the shock layer. In this case, the energy transfer does not effect the parameters in the shock front region. However, for a gas initially in a nonequilibrium state, the characteristic time associated with these variations may be several orders of magnitude shorter than that achieved under equilibrium conditions. In this case, the energy transfer may be sufficiently rapid to cause significant variations in the flow parameters near the shock front, as well as cause significant changes in the shock propagation velocity on short time scales. The calculation of the vibrational relaxation time under nonequilibrium conditions is the focus of this section.

A discussion of nonequilibrium vibrational relaxation times must begin with an introduction to the vibrational distribution function (VDF). The VDF defines the number density of molecules in each possible vibrational state in a unit volume

of gas. The calculation of the VDF is important for two reasons. First, the VDF determines the amount of energy contained within the vibrational manifold, and thus partly determines how much energy can be released into the post-shock region of the flow. Secondly, the VDF determines the effective vibrational energy relaxation time, τ_{eff}. Both of these will be addressed in greater detail shortly. The VDF can be determined by solving a set of master equations which describe the relevant kinetic vibrational processes. The master equation can be written as [49:142]

$$\begin{aligned}\frac{dN_v}{dt} &= P_{v-1,v}N_{v-1}N_{tot} + P_{v+1,v}N_{v+1}N_{tot} \\ &\quad -P_{v,v+1}N_vN_{tot} - P_{v,v-1}N_vN_{tot} \\ &\quad +\sum_m \left[Q_{v+1,v}^{m,m+1}N_{v+1}N_m + Q_{v-1,v}^{m,m-1}N_{v-1}N_m \right. \\ &\quad \left. - Q_{v,v+1}^{m,m-1}N_vN_m - Q_{v,v-1}^{m,m+1}N_vN_m\right] \\ &\quad -R\ N_0\ \delta_{v,0} + R\ N_0\ \delta_{v,1}, \end{aligned} \tag{39}$$

where only single quantum transitions have been considered. In this equation, N_v is the number density of molecules in vibrational state v, while the terms on the right hand side describe the time rate of change of N_v due to various kinetic processes. The vibration-translation (VT) collision process, denoted $P_{v,m}$, is the rate at which a molecule in the vibrational state v will transition to the state m in a binary collision with another molecule. The vibration-vibration (VV) collision process, represented by $Q_{v,v-1}^{m,m+1}$, is the rate at which a molecule in vibrational state v will transition to the state $v-1$ in a binary collision, with the collision partner simultaneously promoted from the state m to $m+1$. A pump (R), restricted to excitation of molecules from the ground state ($v=0$) to the first excited state ($v=1$) by the Kronecker delta function (δ), is also modeled in Equation 39. This pump is representative of the electron impact excitation process present in a weakly ionized molecular plasma.

The VT transition rates, P (having units of cm^3/sec as written in Equation 39), can be calculated for an anharmonic oscillator based on Keck and Carrier's semi-

empirical modification [72] to the Schwartz-Slawsky-Herzfeld (SSH) theory [103]. The VV transition rates, Q (also having units of cm^3/sec as written in Equation 39) can be calculated based on the formalism of Bray [24]. These rates are functions of both the vibrational quantum number(s) and the gas temperature, but are independent of the density. The transition rates are shown in Figure 26 for $P_{v,v-1}$ (solid)

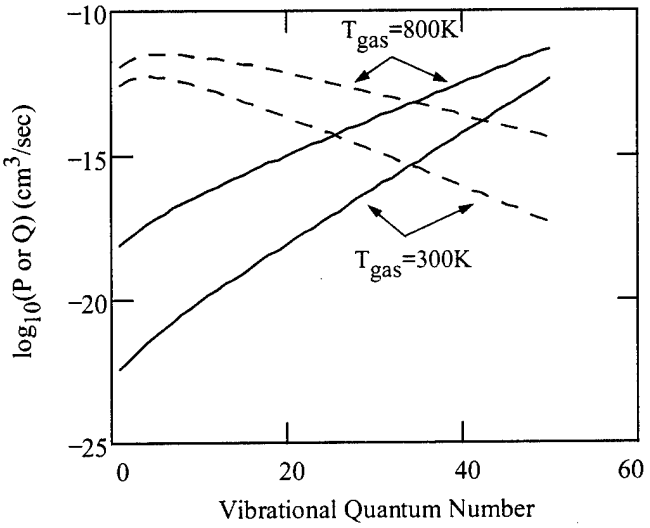

Figure 26. Dependence of the rates $P_{v,v-1}$ (solid) and $Q^{0,1}_{v,v-1}$ (dashed) (in units of cm^3/sec) on the vibrational quantum number for N_2.

and $Q^{0,1}_{v,v-1}$ (dashed) in N_2 at two different gas temperatures. The VV process dominates at low quantum numbers, while the VT process dominates at higher quantum numbers. Both VV and VT rates increase with gas temperature.

Once the transition rates are known, Equation 39 can be applied to each v level and the resulting system of coupled equations solved numerically. Calculated steady-state vibrational distribution functions for an anharmonic oscillator (N_2) under typical nonequilibrium conditions are shown in Figure 27 for three gas temperatures. These calculations were performed using a vibrational kinetics code obtained from Wright Laboratory, Wright-Patterson AFB, OH [35], which was modified and validated for the present research. In Figure 27, each of the distributions has the same characteristic vibrational temperature, T^{10}_{vib}, of 1700K, which is defined based

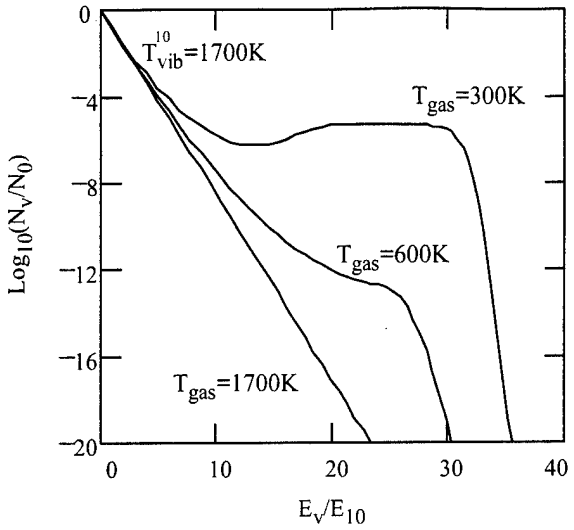

Figure 27. Distribution of N_2 molecules in vibrational states under typical nonequilibrium conditions. The energy axis has been normalized by E_{10}.

on the relative populations of the ground and first excited state:

$$T^{10}_{vib} = \frac{E_{10}}{k_B \ln(N_0/N_1)}, \tag{40}$$

where E_{10} is the energy difference of the first excited state and the ground state. An equilibrium (Maxwell-Boltzmann) distribution is represented by a straight line on this semi-log plot, as shown by the VDF for the case in which $T_{gas} = 1700K$. The more a VDF departs from this equilibrium distribution, the greater the nonequilibrium between the vibrational mode and the translational/rotational modes. The general shape of the distribution functions can be explained on the basis of the properties of an anharmonic oscillator. In such a molecule, the preferential upward pumping of vibrational quanta through vibration-vibration (VV) collisions competes with the deactivation of vibrational states by vibration-translation (VT) collisions. The relative magnitudes of these two effects are different in different parts of the

distribution, resulting in significant departure of the VDF from the equilibrium form under some circumstances [49:147]. [1]

In order to heat the gas quickly, the vibrational energy relaxation time must be short. A simple relationship between vibrational energy relaxation times and VT probabilities has been determined for the case of a harmonic oscillator described by a Boltzmann VDF [49:83]. Unfortunately, neither of these assumptions is valid for the case in which a shock propagates through a gas of anharmonic oscillators described by a nonequilibrium VDF. However, an effective relaxation time, τ_{eff}, can be calculated from the approximate relation [49:56]

$$\frac{d\epsilon_{avg}}{dt} \approx \frac{\epsilon_{avg}}{\tau_{\text{eff}}}, \tag{41}$$

where ϵ_{avg} is the average energy, calculated from the expression

$$\epsilon_{avg} = \frac{\sum_{v=0}^{v_{max}} N_v \epsilon_v}{\sum_{v=0}^{v_{max}} N_v}, \tag{42}$$

where N_v is the VDF which gives the number density of molecules in vibrational state v and ϵ_v is the energy of the vth level. The left hand side of Equation 41 can be written as

$$\frac{d\epsilon_{avg}}{dt} = \frac{\sum_{v=0}^{v_{max}} N_v \, N_{tot} \left[(\epsilon_{v+1} - \epsilon_v) P_{v,v+1} - (\epsilon_v - \epsilon_{v-1}) P_{v,v-1}\right]}{\sum_{v=0}^{v_{max}} N_v}, \tag{43}$$

where both $P_{v,v+1}$ for $v = v_{max}$ and $P_{v,v-1}$ for $v = 0$ are zero. Since both ϵ_{avg} and $d\epsilon_{avg}/dt$ are determined by the VDF, τ_{eff} can be calculated once the VDF is known.

[1] The ripples in the numerical VDFs are due to the graphic conversion utility program used and were not present in the raw numerical data.

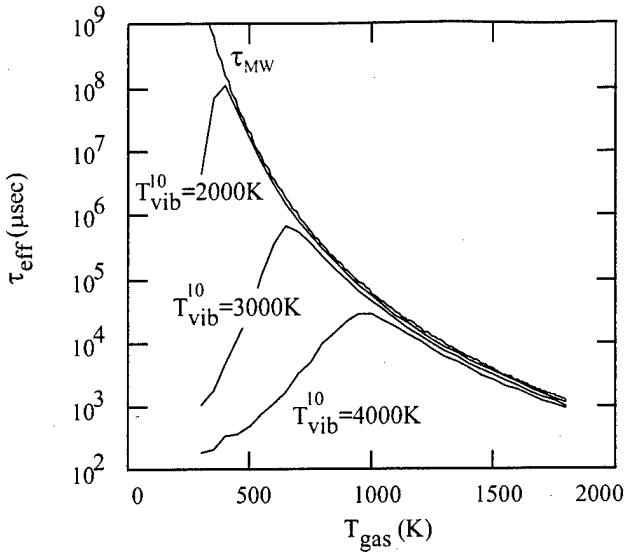

Figure 28. Effective relaxation times in N_2 in nonequilibrium conditions at various vibrational temperatures (calculated at a pressure of 1 atm). The standard Millikan/White relaxation times are also shown (τ_{MW}).

Representing the vibrational distribution function in an approximate analytic form, τ_{eff} has been computed over a range of vibrational and gas kinetic temperatures for N_2 at a pressure of 1 atmosphere. The results are shown in Figure 28. Measured equilibrium vibrational relaxation times given by Millikan and White [84], at a pressure of 1 atmosphere, are shown in this figure as well. It is observed that under highly nonequilibrium conditions, the effective relaxation times are very short, being on the order of $10^2 - 10^3 \mu$sec. The nonequilibrium relaxation times can be many orders of magnitude shorter than the equilibrium relaxation times. However, the difference is especially noticeable at temperatures less than the temperature at which τ_{eff} peaks. The nonequilibrium times converge to the Millikan-White values at the higher gas temperatures, once the peak in τ_{eff} has been reached.

It is important to recognize that the relaxation times shown in Figure 28 will scale inversely with both gas density and VT rates (Equation 43). Thus a relaxation time of $10^2 \mu$sec (0.1 msec) at a pressure of 760 torr (1 atm) will increase to approximately 2.5 msec at 30 torr, a typical pressure at which weakly ionized plasmas are

generated in the laboratory. Any impurity in the N_2 gas will decrease the effective relaxation time, since the VT rates of the associated impurities are usually much greater than those of $N_2 - N_2$.

Two assumptions were made in order to approximate the nonequilibrium VDF used in the previous calculation of τ_{eff}. First, the VDF is assumed to follow the form given by Bailey [8], in which the approximate steady-state nonequilibrium VDF for a particular gas is determined by the vibrational and gas temperatures. Secondly, as these temperatures evolve in time, the VDF is assumed to evolve through a series of steady-state distributions. Thus, at any moment in time the VDF is represented by a pseudo-steady-state form. This essentially assumes that the time constant associated with VV collisions is much smaller than the characteristic time of any other process in the system.

As an example of the influence of vibrational relaxation under nonequilibrium conditions, consider the work of Rukhadze, et al. [101] who examined the effect of the shortened relaxation times on shock dynamics. In his example, illustrated in

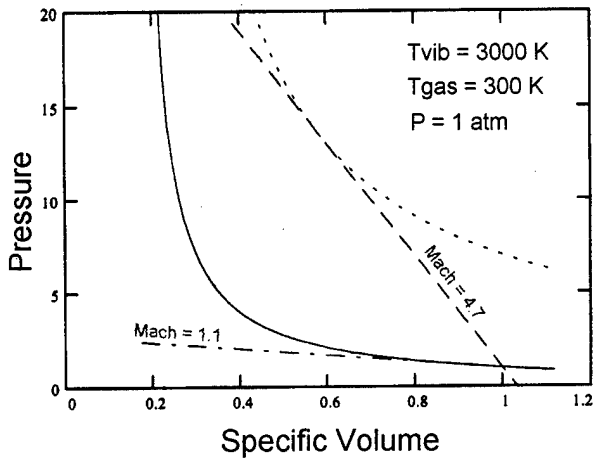

Figure 29. Shock adiabatics corresponding to Rukhadze's nonequilibrium example in N_2 [Ref: [101]]. The shock accelerates from Mach 1.1 to Mach 4.7 in approximately 45 msec.

Figure 29 with the use of shock adiabatics. Rukhadze used N_2 at a gas temperature of $300K$ and a vibrational temperature of $3000K$ to provide a nonequilibrium region into which a shock propagated. The initial shock velocity was Mach 1.1 (relative to the speed of sound at $300K$ with $\gamma = 7/5$). Under these conditions, the shock is propagating well below the Chapman-Jouguet minimum, where the steady-state propagation velocity is Mach 4.7. As the vibrational energy behind the shock front relaxes, energy is transferred from the internal mode to the translational and rotational modes. During this energy transfer, the flow parameters behind the shock are altered, resulting in a pressure increase as the shock accelerates in order to reach a steady-state at the Chapman-Jouguet operating point. The energy transfer is rapid at first, on the order of msec under the given initial conditions (Figure 28). However, as the gas temperature rises, τ_{eff} increases, resulting in a slower energy transfer time. This behavior continues until the gas temperature reaches approximately $700K$, corresponding to the peak in the τ_{eff} curve. Once this peak is reached, any further increase in gas temperature results in a decrease in the relaxation time. According to the numerical calculation of Rukhadze, the accelerated relaxation of the vibrational energy in this temperature regime results in the shock speed quickly increasing to the Chapman-Jouguet velocity.

In the case just discussed, the time required to reach equilibrium in the post-shock region was approximately 45 msec, which is of the order of the peak τ_{eff} for a characteristic vibrational temperature of $3000K$. Rukhadze reports that with the vibrational temperature increased to $4000K$ and all other parameters held constant, the calculated equilibration time is reduced to 20 μsec. This time is quite short and is comparable to time scales on which variations in the density and pressure at the shock front have been observed ([75] and [89], for example). If the energy relaxation time is short enough and sufficient energy can be coupled into the gas flow, interesting aerodynamic effects can result. For example, consider an aerodynamic vehicle with a detached shock formed on the leading edge. If a sufficient amount of energy can be

coupled into the translational mode in the region between the shock front and the vehicle surface, it is possible to increase the shock standoff distance. This increase in shock standoff as thermal energy is added to the flow is not normally encountered in aerodynamic situations, where the shock standoff decreases as thermal energy is transferred from the flow to other degrees of freedom [5:515]. The increase in shock standoff distance under nonequilibrium conditions may also lead to a reduction in the heat flux to the vehicle's surface, as Serov, et al. [105] observed for objects passing through a plasma region in ballistic experiments.

In this section is has been shown that nonequilibrium VDFs can lead to effective vibrational relaxation times which can be many orders of magnitude shorter than the relaxation times encountered under equilibrium conditions. These relaxation times scale inversely with both gas density and vibration-translation (VT) rates. Since the gas density and temperature behind a shock are greater than the density and temperature in front of the shock, the vibrational relaxation times behind a shock are less than the relaxation times in front of the shock. When the release is rapid and the energy added substantial, nonequilibrium relaxation can lead to interesting and surprising results. The investigation of these gas dynamic effects is the focus of Chapter IV.

2.5 *Thermal Inhomogeneities*

Thermal inhomogeneities can lead to variations in the flow parameters and shock speed. These inhomogeneities may originate from plasma generation, maintenance or decay. It is only by understanding those effects which can be attributable to thermal inhomogeneities that progress can be made in understanding those effects which cannot. The purpose of the present section is to lay the theoretical framework for consideration of thermal effects.

A sharp interface in a gas at two temperatures offers the simplest example of the effects of a thermal inhomogeneity on shock characteristics. The interface separates gas 1 at a temperature T_1 from gas 2 at a temperature T_2, with the pressure across the interface assumed to be a constant. The ratio of the heat capacity at constant pressure (C_p) to the heat capacity at constant volume (C_v) (also known as the adiabatic exponent) will be denoted as γ_1 for gas 1 and γ_2 for gas 2. A shock will be propagated through this thermal interface and the resulting modifications to the shock characteristics will be examined.

An analytic solution to the problem just posed has been claimed by a number of researchers ([2], [41], [115], [118]), although the solutions of [41] and [115] appear to be in error, sometimes resulting in imaginary values for the shock velocity. A correct solution describing the influence of a thermal discontinuity on the shock wave Mach number [2] is

$$\frac{2}{\gamma_1+1}M_1\left(1-\frac{1}{M_1^2}\right)+\frac{2}{\gamma_1-1}\left[\frac{[2\gamma_1 M_1^2-(\gamma_1-1)][(\gamma_1-1)M_1^2+2]}{(\gamma_1+1)^2M_1^2}\right]^{1/2}$$
$$\times\left[1-\left\{\frac{\frac{2\gamma_2}{\gamma_2+1}M_2^2-\frac{\gamma_2-1}{\gamma_2+1}}{\frac{2\gamma_1}{\gamma_1+1}M_1^2-\frac{\gamma_1-1}{\gamma_1+1}}\right\}^{\frac{\gamma_1-1}{2\gamma_1}}\right]=\frac{2}{\gamma_2+1}\sqrt{\frac{T_2}{T_1}}M_2\left(1-\frac{1}{M_2^2}\right). \qquad (44)$$

Once the Mach number of the shock in the heated region is known, the density and pressure jumps at the shock front are determined by application of the Rankine-Hugoniot relations. Therefore, given the gases (γ_1, γ_2), temperatures (T_1, T_2) and the

initial shock wave velocity (M_1), Equation 44 predicts the new shock wave velocity in the heated region (region 2), from which the other shock characteristics can be determined.

Wright [118] presents two different forms of Equation 44, one of which is applicable for the case in which $T_2 > T_1$ and the other for the case in which $T_2 < T_1$. [As an aside, it appears that Wright was interested in the effect of an interface that separated two different gases, rather than an interface that separated the same gas at two different temperatures. However, the analysis is the same in either case.] The former case leads to the formation of a reflected rarefaction wave, while the latter case leads to the formation of a reflected shock [118:78]. Equation 44 is general in that gas 1 and gas 2 may be different, however assuming the two gases to be the same makes the analysis consistent with the experimental conditions, where only one gas type is used.

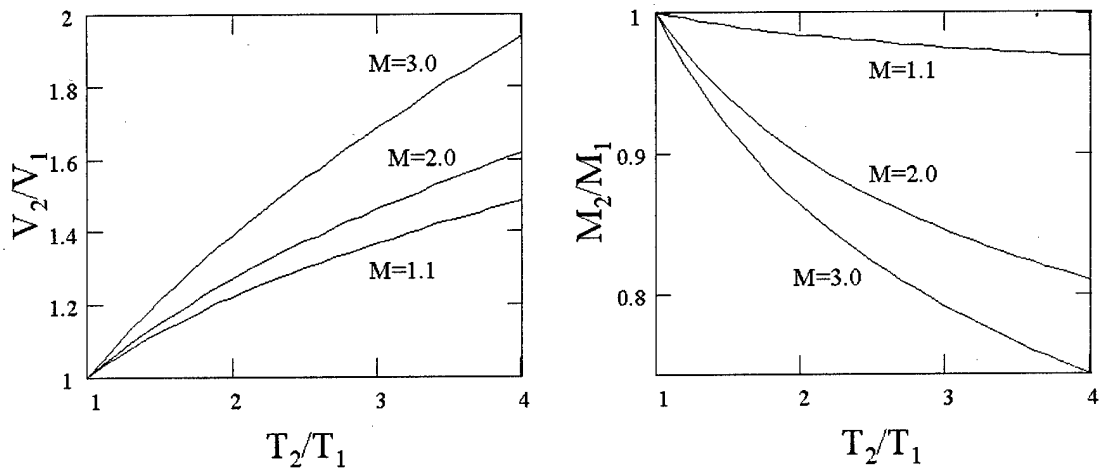

Figure 30. Variation in shock velocity ratio (left) and Mach number ratio (right) with T_2/T_1 for a shock incident on an infinite planar thermal interface.

Treating the temperature ratio at the interface as the independent variable, solutions to Equation 44 (specialized for Argon) at three different initial Mach numbers are shown in Figure 30. On the right is plotted the ratio of the Mach number in

the heated region (M_2) to the initial Mach number (M_1) while on the left is plotted the ratio of the velocity in the heated region (V_2) to the initial velocity (V_1). For the limiting case in which $T_2 = T_1$, the interface is obviously fictitious and both the Mach number and velocity of the shock remain unchanged, as required. For the case in which $T_2 > T_1$, the new Mach number will always be less than the initial Mach number, although the new velocity will always be greater than the initial velocity. The magnitude of these differences are greater for both higher initial shock velocities and Mach numbers.

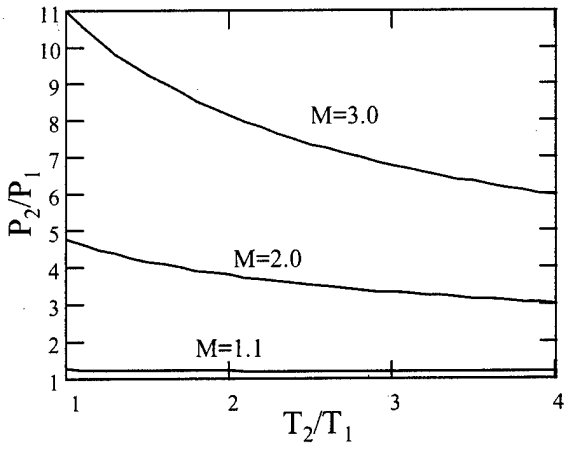

Figure 31. Variation in pressure ratio at the shock front (P_2/P_1) with T_2/T_1 for a shock incident on an infinite planar thermal interface.

The corresponding pressure ratio at the shock front is shown in Figure 31. P_2 is the pressure just behind the shock front while P_1 is the ambient pressure in front of the shock. As the shock enters a heated region, the velocity increases while the Mach number of the shock decreases leading to a decrease in the pressure ratio at the shock front, in accordance with the Rankine-Hugoniot relations. Although not shown, a decrease in the Mach number also leads to a decrease in the density jump at the shock front, also in agreement with the Rankine-Hugoniot relations.

In this section, the influence of a simple thermal inhomogeneity on shock parameters has been examined. The shock velocity increases as the shock propagates

into a gas at a higher temperature, although the Mach number of the shock decreases. The decrease in the shock Mach number leads to decreases in both the pressure and density jump at the shock front as well. Experimentally, researchers are divided as to whether thermal effects play a role in the observed plasma/shock anomalies. It is difficult to determine which of the cited papers are accurate in their assessment of thermal effects, due to the lack of both experimental and computational details in the vast majority of cases. It seems clear that an examination and assessment of the role of thermal inhomogeneities on shock propagation is required. Such will be the focus of Chapter V.

III. Plasma Effects

3.1 Introduction

It has been suggested by some researchers that the phenomena which have been observed in plasma/shock interaction experiments are linked to the presence of charged particles in the flow ([11], [12], [13], [51], [75], [85], for example). These phenomena have been observed in weakly ionized plasma, with fractional ionizations, defined as $n_i/(n_n+n_i)$ (with n_i being the electron number density and n_n the neutral number density), as low as 10^{-6}. As well as being weakly ionized, the plasma is typically in a nonequilibrium state. That is, the electron temperature is of the order of a few electron volts (with 1 eV=11604 K) while the heavy particle temperature is typically a few hundred K. Such a nonequilibrium state can give rise to new shock structures in the flow ([6], [65], [85]) and is the reported cause of at least some of the experimental anomalies. The influence of a weakly ionized nonequilibrium plasma on the shock structure and characteristics will be examined in this section.

The effect of a plasma on the shock structure will be examined using a two fluid plasma approximation, in which the charged particles (electrons and ions) are combined as one component and the neutrals as the other. The use of a two component system to describe the plasma is based on the premise that the ions and electrons are closely linked to each other. This is reasonable since the electrons' light mass allows them to react very quickly to changes in the electric field caused by changes in the ion density and velocity.

Plasma/shock interactions will be examined using two methods. The steady-state approach used by Avramenko, et al. [6] will be used first, followed by an unsteady approach. The assumption of a steady-state allows the fluid equations to be transformed from partial differential equations to ordinary differential equations. The density and velocity distribution of the neutral component will be specified, while the density and velocity of the charged component will be determined by the

solution of the conservation of mass and momentum equations. In this simplified analysis, no conservation of energy equation will be used, either for the neutrals or the charged component. This implies that the temperature of each component remains constant. It will be further assumed that the neutrals and ions are in equilibrium with each other, thus the heavy particle temperature will be treated as a parameter. The electron temperature will also be assumed constant, although this temperature can be different from the heavy particle temperature in order to allow a state of nonequilibrium to exist in the plasma. Allowing the electrons and ions to have different temperatures does not conflict with treating them as a single component fluid. That is, the electrons and ions are assumed to have the same mean flow velocity, but are allowed to have different random thermal velocities. Whereas the previous treatments of the ion momentum equation, by both Ingard [64] and Avramenko [6], neglected the nonlinear term, the present analysis will retain it. This will allow the consideration of stronger shocks than that previously examined, without being limited to small amplitude waves.

Following the steady-state analysis, a time-dependent analysis will be used to examine plasma effects on the shock structure. Unlike the previous approach, in which the neutral component motion was prescribed, no assumptions will be made with regard to the structure of the neutral component. Rather, the density, velocity and temperature of both the neutral and charged component will be determined by solution of the Euler equations for a two fluid plasma.

3.2 Steady-State Analysis

3.2.1 Model Equations. The model equations for a two-fluid plasma in the steady-state approximation have been derived previously (Chapter II), with the result (repeated here) given as

$$-V_{shock}\frac{d\rho_i}{d\xi} + \frac{d}{d\xi}(\rho_i V_i) = 0 \qquad (45)$$

$$\frac{d}{d\xi}\left[\frac{\hat{V}_i^2}{2} - V_{ia}^2 \ln\left(\frac{\hat{V}_i}{V_{shock}}\right)\right] - \nu_{in}(\hat{V}_i - \hat{V}_n) = 0 \quad (46)$$

where $\hat{V}_i$ and $\hat{V}_n$ are the ion and neutral flow velocities in the shock front frame and ν_{in} is the ion-neutral momentum transfer collision cross section, defined in Equation 11. An analytical integration of Equation 45 yields Equation 21, which is repeated here:

$$\rho_i(\xi) = \rho_{i0}\left(1 - \frac{V_i(\xi)}{V_{shock}}\right)^{-1}, \quad (47)$$

where ρ_{i0} is the ion mass density far upstream of the shock front. Previously, the nonlinear term in Equation 46 (first term in the brackets on the left hand side) was neglected ([6], [64]). In the present analysis it will be retained.

In general, the neutral component would be described by equations analogous to Equations 45 and 46 (lacking, of course, the electric field term). However, in the simplified case considered here, the motion of this component will be assumed to follow a known functional form. The neutral velocity and density profiles will be given as

$$\hat{V}_n(\xi) = V_{shock} - (V_{shock} - \hat{V}_1)\left(\frac{1}{\exp(\xi/\tilde{\xi}) + 1}\right) \quad (48)$$

$$\rho_n(\xi) = (\rho_{n1} - \rho_{n0})\left(\frac{1}{\exp(\xi/\tilde{\xi}) + 1}\right) + \rho_{n0} \quad (49)$$

where the velocity has been defined in the shock front frame. The characteristic distance $\tilde{\xi}$ is used to control the width of the neutral shock. The subscripts 0 and 1 denote regions in front of and behind the shock front, respectively. Thus, ρ_{n0} and ρ_{n1} are the neutral mass densities in the ambient and perturbed regions of the flow, respectively. The use of Fermi-type functions, instead of the Heaviside step functions used by Avramenko, et al. [6], are advantageous computationally, in that the velocity and density profiles vary smoothly rather than discontinuously. In addition, the use of a continuous function of the Fermi-type permits an assessment of global charge

conservation, which was not made with the discontinuous Heaviside functions. This point will be addressed in greater detail shortly.

Equation 46 can be solved numerically for the ion flow velocity in the shock front frame, the solution transformed into the laboratory frame by use of Equation 15, and the result then used in Equation 47 to determine the ion mass density. A fourth order Runga-Kutta integrator was used in the numerical calculations.

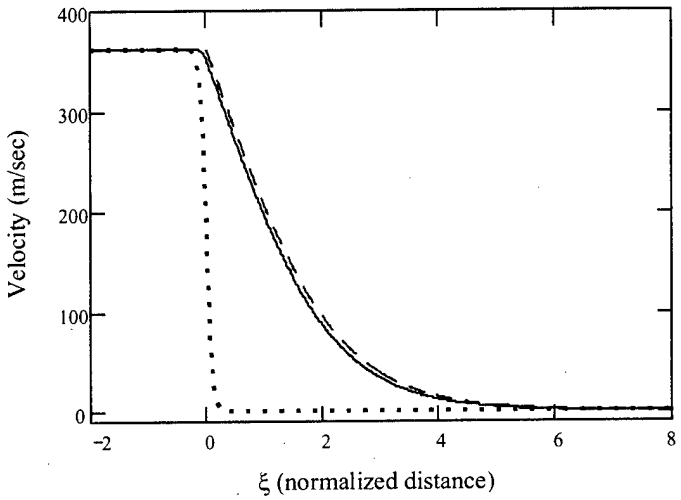

Figure 32. Velocity of the charged component precursor from numerical solution to equation 14 (solid) in front of a neutral shock (dotted). The calculation was performed for a Mach 2 shock in Argon. The distance has been normalized by Avramenko's estimate of the precursor length, ξ_0, which evaluates to 0.23 mm under the present conditions. Avramenko's analytic solution for the charged component precursor (dashed) is shown for comparison.

3.2.2 Steady-State Results. The calculated velocity profile of the charged component (solid) and of the neutral shock (dotted) are shown in Figure 32 in the laboratory frame for the case of a Mach 2 shock propagating through an Argon discharge. In this calculation, the electron temperature was taken to be 2 eV, the neutral gas temperature was $300K$, the pressure was 30 torr, the ion-neutral momentum transfer cross-section was 1×10^{-19} m^2 and the fractional ionization was 10^{-6},

which are values typical of a glow discharge in Argon. The spatial distances have been normalized by Avramenko's analytic estimate of the precursor width, ξ_0, which is (to within a constant of the order of unity) equal to $T_e/T_n\,\lambda_{in}$, where λ_{in} is the ion-neutral mean free path. Under the given conditions, ξ_0 evaluates to approximately 0.23 mm. The velocity in front of the neutral shock is zero until near the shock front, then increases rapidly to a value of 363 m/sec, consistent with the Rankine-Hugoniot relation for a Mach 2 shock in Argon. The characteristic distance of the neutral shock used in these calculations ($\tilde{\xi}$) was 0.05, resulting in a neutral shock width of approximately 14 neutral-neutral mean free paths, which is of the order of previous estimates for the neutral shock width [114:421]. Ahead of the neutral shock there is a broad region in which the ions are perturbed from their ambient value. Avramenko calls this the ion-acoustic shock wave, since the structure is similar to a diffuse shock front [6:463]. The ion-acoustic shock calculated from a numerical solution to equation 46 is shown as a solid line, while Avramenko's analytic estimate (Equation 25) is shown as the dashed line. The ion-acoustic shock (or charged component precursor) extends in front of the neutral shock a distance of approximately $4\,\xi_0$, or nearly 1 mm, which is approximately 100 neutral-neutral mean free paths.

The density profiles of the neutral shock and of the precursor are shown in Figure 33. The distance has been normalized by ξ_0, while the densities have been normalized by the respective upstream ambient values. The density of the precursor determined from the numerical solution of Equation 46, with use of Equation 47, is shown as the solid line. The analytic estimate is shown as the dashed line. The agreement is quite good. Downstream of the shock front, the normalized density of both the neutrals and the charged component is 2.286, which is consistent with the Rankine-Hugoniot relation for a Mach 2 shock in Argon.

Although the charged component precursor appears quite dramatically in Figure 33, it is important to realize that it has been normalized by the upstream ambient ion number density. Since the fractional ionization in the plasma considered here is

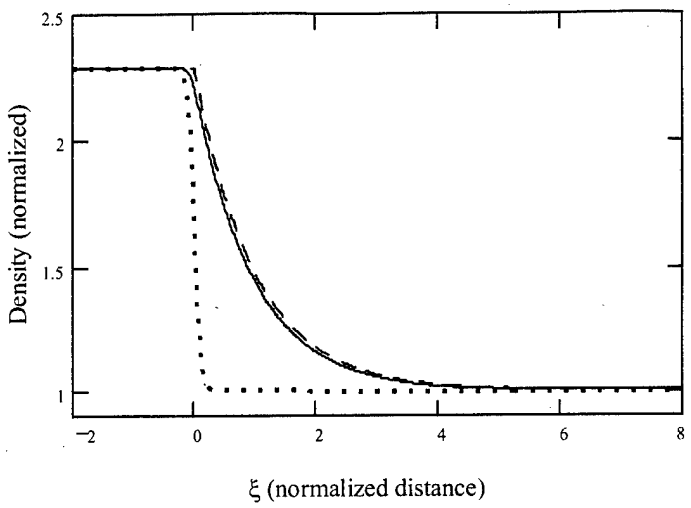

Figure 33. Density of the charged component precursor determined numerically (solid) in front of a neutral shock (dotted). The calculation was performed for a Mach 2 shock in Argon. The distance has been normalized by ξ_0, while the densities have been normalized by the respective ambient values. Avramenko's analytic solution for the charged component precursor (dashed) is shown for comparison.

very small (10^{-6}), the relative contribution of the precursor to the total mass density is small. Thus the total mass density (sum of the neutral and charged component profiles) is essentially given by the neutral profile of Figure 33.

The electric field in the shock front region can be determined by use of the electron momentum equation. Neglecting the electron inertia terms and requiring a balance between the terms representing the electron pressure gradient, electric field and electron-neutral collisions, the electric field can be approximately determined. Performing the given operations, the electric field can be written as

$$E_x(x) = \frac{1}{q}\left[\frac{8}{3}\sqrt{2}\left(\frac{M_e k_B T_e}{\pi}\right) V_{shock}\, n_{n0}\, \sigma_{en}\left(1 - \frac{V_i(x)}{V_n(x)}\right) - V_i(x) k_B T_e \frac{d}{dx}\left(\frac{1}{V_i(x)}\right)\right] \quad [\mathrm{V/m}] \tag{50}$$

where n_{n0} is the upstream ambient neutral number density and q is the elementary unit of charge. In deriving Equation 50, use has been made of the quasi-neutrality property of the plasma. The first term on the right hand side of this equation represents the contribution of the electron-neutral collisions to the electric field, while the second term represents the contribution of the electron pressure gradient to the electric field. It will be shown that the first term is minor in comparison to the second.

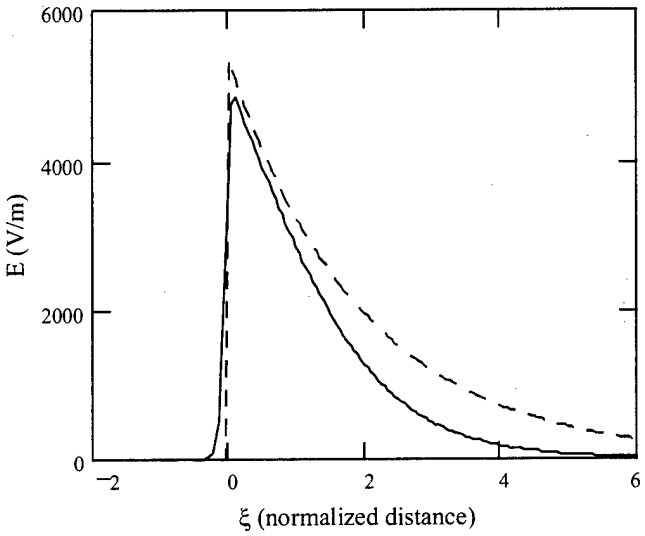

Figure 34. Electric field in the shock front region determined numerically (solid) and analytically (dashed) (from [65]) for a Mach 2 shock in Argon. The distance has been normalized by ξ_0.

Applying Equation 50 to the present case of a Mach 2 shock in Argon results in the electric field shown in Figure 34 (solid). Ingard and Schulz's [65] analytic estimate (Equation 4) for the same conditions (dashed) is shown for comparison. Although the analytic estimate was derived assuming small-amplitude waves, the agreement with the numerical result is, perhaps, better than expected under these shock (large-amplitude waves) conditions.

It was mentioned previously that the total electric field is comprised of two parts: a collision term and a pressure gradient term. The contribution of the former

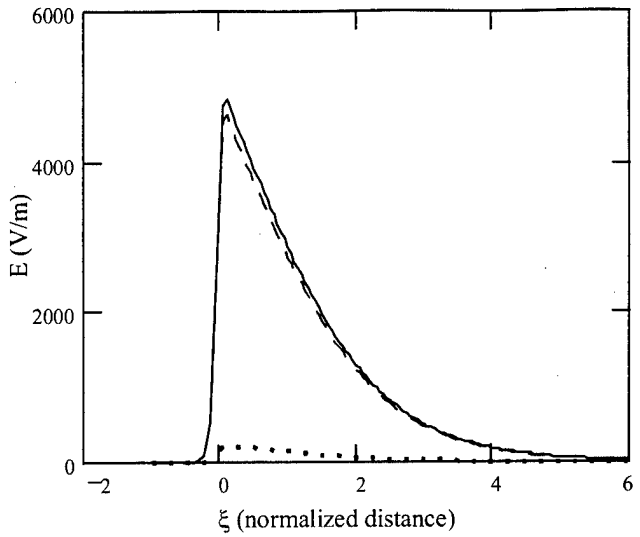

Figure 35. Contributions of the collision (dotted) and pressure gradient (dashed) term to the total electric field (solid) in the shock front region for a Mach 2 shock in Argon. The distance has been normalized by ξ_0.

is much smaller than the contribution of the latter, as shown in Figure 35. Here, the contribution from the collision term is shown as the dotted line, while the contribution from the pressure gradient term is shown as the dashed line. The total electric field is shown as the solid line.

The peak electric field ($\approx$ 50 V/cm) is of the same order of magnitude as the axial electric field typically found in a glow discharge in Argon at 30 torr (see Figure 104 in Appendix D). However, the field in the present case is localized to only a small region around the shock front, thus the potential voltage drop experienced by an electron is small, being approximately 1.7 Volts in the present case. By comparison, the electron thermal energy is 2.0 eV. The potential increase is small compared to the ionization energy of Argon (15.68 eV) and is unable to significantly increase ionization at the shock front.

Although both the electric fields rise sharply near ξ=0, the numerically determined field has a finite positive slope in this region, while the analytically determined field rises infinitely fast. The presence of a region in which the spatial derivative of

the electric field is positive is necessary to ensure global charge conservation. In order to see this more clearly, consider Gauss's law describing the relationship between charge density and electric field:

$$\vec{\nabla} \cdot \vec{E} = \frac{q}{\epsilon_0}(n_i - n_e) \tag{51}$$

If the ions outnumber the electrons, then the spatial derivative of the electric field will be positive, while if the electrons outnumber the ions the reverse will be true. Thus, if some region exists in which the electron number density is greater than the ion number density, there must also be a region in which the ion number density is greater than the electron number density in order to ensure global charge conservation.

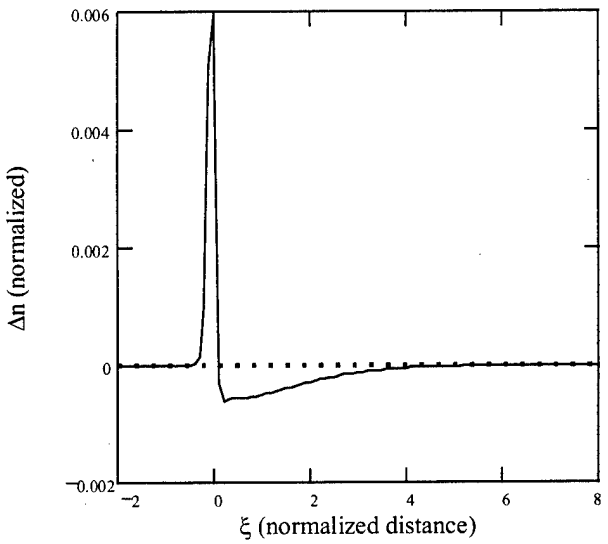

Figure 36. Net charge density in the shock front region for a Mach 2 shock in Argon. The distance has been normalized by ξ_0, while Δn has been normalized by the upstream ambient electron number density.

The difference in the ion and electron number densities, Δn (defined as $\Delta n = n_i - n_e$), can be determined through the use of Equation 51 once the electric field is known. This difference is shown in Figure 36 for a Mach 2 shock in Argon. The distance has been normalized by ξ_0, while the number density has been normalized

by n_{e0}, the electron number density in the upstream ambient gas. The large spike near ξ=0 indicates an abundance of ions near the neutral shock front, while an abundance of electrons is present throughout the precursor region in front of the neutral shock. The integrated areas of each region are approximately equal, with a relative difference of less than 0.06%, resulting in global charge conservation as required.

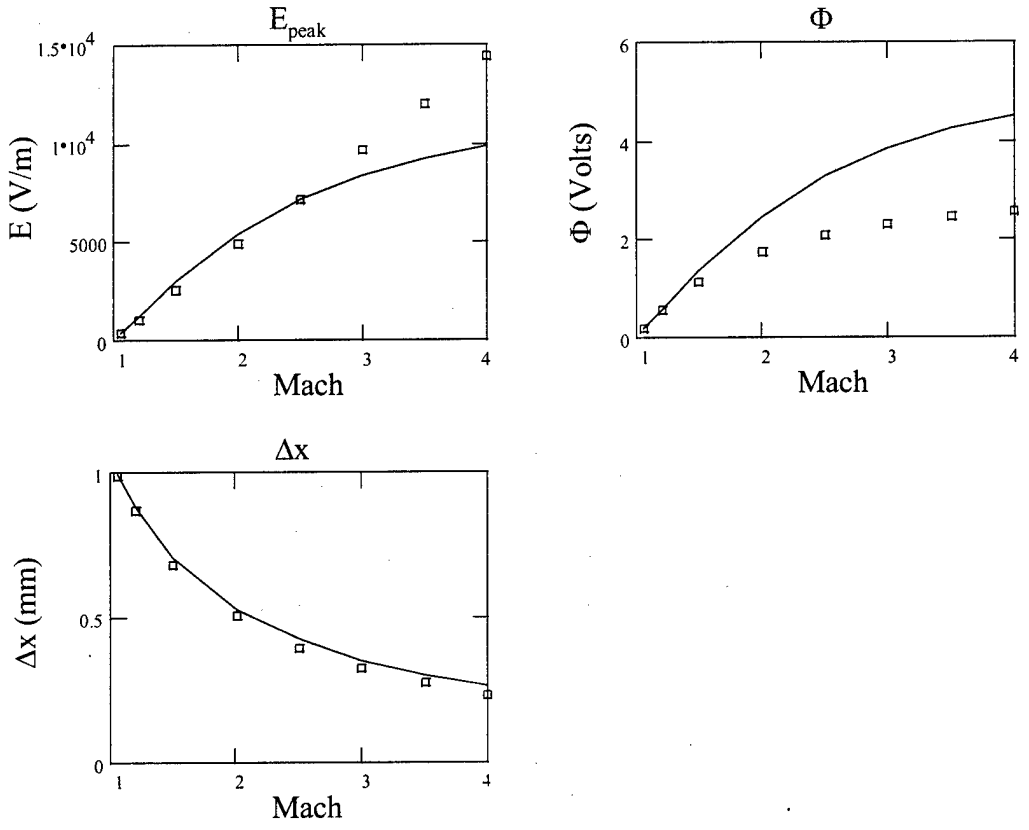

Figure 37. Numerically determined (boxes) peak electric field (E_{peak}), potential drop (Φ) and shock precursor width (Δx) compared with analytic estimates at the same conditions (solid curves).

A comparison of the numerically determined values (boxes) of the peak electric field (E_{peak}), potential drop (Φ) and width of the precursor region (Δx) with analytic

estimates (solid curves) of the same parameters are shown in Figure 37 for a range of Mach numbers. To generate these curves, a shock (of varying speed) was assumed to travel through a plasma characterized by parameters typical of a glow discharge in Argon (P=30 torr, T_e=2 eV, T_n=300K, $\alpha = 10^{-6}$). The analytic estimates for the peak electric field and potential are based on Ingard's result (Equation 4), while the estimate for the precursor width is based on Avramenko's work [6]. The width of the precursor is defined as the distance in front of the neutral shock at which the ion density reaches a value equal to 1/10 of the total rise above the ambient density. The numerically determined precursor width agrees well with the analytic estimates throughout the Mach number range considered ($1.06 \leq M \leq 4$). The peak electric field from the calculation agrees well with the analytic estimate up to Mach 2.5, while the calculated potential agrees with the analytic estimate only up to approximately Mach 1.5. The disagreement in the electric field and potential is not surprising, since the analytic estimate is based on linearized fluid equations, which assume small amplitude waves. As the Mach number increases, the amplitude of the shock becomes increasing larger, leading to greater differences between the numeric and analytic values. The analytic estimate for the precursor width does not appear to suffer from this affliction, in spite of having been derived in a linearized analysis.

3.3 Time-Dependent Analysis

In the steady-state analysis, the equations describing the conservation of mass and momentum were transformed into the shock front frame and subsequently solved. A precursor of charged particles was found to be present in front of the neutral shock, in which the electron and ion number densities were nearly equal. The small difference in charge density produced an electric field, which resulted in a potential drop of a few volts under conditions typical of a glow discharge in an Argon plasma. In this analysis, several assumptions were made which, while simplifying the problem, removed some of the relevant physical processes from the system. These assumptions included treating the shock velocity and heavy particle temperature as constants, as well as assuming the density and velocity profiles of the neutral component to be of a specified form. These assumptions effectively prevent the charged particles from influencing the flow of the neutral component. In this section, the simplifying assumptions mentioned previously will be removed and the resulting shock structure of both the neutral and charged component will be examined and compared to previous results. The electron temperature will, however, still be assumed to be a constant. Furthermore, no ionization sources or losses will be treated (i.e., no additional ionization and no recombination, attachment, etc.).

3.3.1 Model Equations. In one spatial dimension, the conservation equations for the two component plasma written in the Toth formalism [112] become

$$\frac{\partial \vec{U}}{\partial t} + \frac{\partial \vec{E}}{\partial x} = \vec{S}_1 + \vec{S}_2 + \vec{S}_3, \tag{52}$$

where the right hand side is comprised of sources from the Euler equation ($\vec{S}_1$), from coupling between the separate species ($\vec{S}_2$) and from the self-induced electric field

($\vec{S}_3$). The vector of conserved variables ($\vec{U}$) is defined as

$$\vec{U} = \begin{bmatrix} \rho_n \\ \rho_n V_n \\ \rho_n \left(\frac{1}{2} V_n^2 + \frac{1}{\gamma - 1} \frac{k_B T_n}{M} \right) \\ \rho_i \\ \rho_i V_i \\ \rho_i \left(\frac{1}{2} V_i^2 + \frac{1}{\gamma - 1} \frac{k_B T_i}{M} \right) \end{bmatrix}, \tag{53}$$

while the flux vector ($\vec{E}$) is defined as

$$\vec{E} = \begin{bmatrix} \rho_n V_n \\ \rho_n V_n^2 \\ \rho_n V_n \left(\frac{1}{2} V_n^2 + \frac{1}{\gamma - 1} \frac{k_B T_n}{M} \right) \\ \rho_i V_i \\ \rho_i V_i^2 \\ \rho_i V_i \left(\frac{1}{2} V_i^2 + \frac{1}{\gamma - 1} \frac{k_B T_i}{M} \right) \end{bmatrix}. \tag{54}$$

The sources from the Euler equations ($\vec{S}_1$) can be written as

$$\vec{S}_1 = -\frac{\partial}{\partial x} \begin{bmatrix} 0 \\ P_n \\ P_n V_n \\ 0 \\ P_i \\ P_i V_i \end{bmatrix}, \tag{55}$$

with P_n and P_i being the neutral and ion pressure, respectively. The sources describing momentum and energy coupling between species can be written as

$$\vec{S}_2 = \begin{bmatrix} 0 \\ P_{in} + P_{en} \\ Q_{in} + Q_{en} \\ 0 \\ -P_{in} \\ -Q_{in} - Q_{ie} \end{bmatrix}, \tag{56}$$

where P_{in} and P_{en} is the momentum gained by the neutrals through collisions with ions and electrons, respectively, while the energy gained by the neutrals through collisions with ions and electrons is denoted by Q_{in} and Q_{en}. The energy lost by the ions in collisions with electrons is denoted as Q_{ie}. According to Jaffrin [68], these terms are defined as

$$P_{in} = \frac{4\sqrt{2}}{3}\frac{\rho_n}{M_n}\frac{\rho_i}{M_i}\left[\frac{M_i}{\pi}k_B(T_n + T_i)\right]^{1/2}\sigma_{in}(V_i - V_n) \tag{57}$$

$$P_{en} = \frac{8\sqrt{2}}{3}\frac{\rho_n}{M_n}\frac{\rho_i}{M_i}\left[\frac{M_e k_B T_e}{\pi}\right]^{1/2}\sigma_{en}(V_i - V_n) \tag{58}$$

$$\begin{aligned} Q_{in} &= 2\sqrt{2}\frac{\rho_n}{M_n}\frac{\rho_i}{M_i}\sigma_{in}\left[\frac{k_B(T_n + T_i)}{M_i\pi}\right]^{1/2} \\ &\quad \times\left[k_B(T_i - T_n) + \frac{1}{3}M_i(V_i - V_n)(V_i + V_n)\right] \end{aligned} \tag{59}$$

$$\begin{aligned} Q_{en} &= 8\sqrt{2}\frac{\rho_n}{M_n}\frac{\rho_i}{M_i}\frac{\sigma_{en}}{M_i}\left[\frac{M_e k_B T_e}{\pi}\right]^{1/2} \\ &\quad \times\left[k_B(T_e - T_n) + \frac{1}{3}(V_i - V_n)(M_n V_n + M_e V_i)\right] \end{aligned} \tag{60}$$

$$Q_{ie} = 8\sqrt{2}\left(\frac{\rho_i}{M_i}\right)^2 \frac{\sigma_{ei}}{M_i}\left[\frac{M_e k_B T_e}{\pi}\right]^{1/2} \times \left[k_B(T_e - T_i) + \frac{1}{3}(V_i - V_n)(M_i V_i + M_e V_i)\right] \quad (61)$$

where the cross-sections of the various processes are denoted by σ. In these expressions, the plasma has been assumed to be quasi-neutral ($n_e \approx n_i$) and the electron and ion velocities have been assumed to be equal, consistent with the two fluid plasma approximation. In all the time-dependent calculations performed, electron-ion and electron-neutral collisions were neglected (the σ_{ei} and σ_{en} cross-sections were set to zero).

The source vector due to the electric field is defined as

$$\vec{S}_3 = -\frac{k_B T_e}{M_i}\frac{\partial \rho_i}{\partial x} \times \begin{bmatrix} 0 \\ 0 \\ 0 \\ 0 \\ 1 \\ V_i \end{bmatrix}, \quad (62)$$

where the electric field has been approximated as (see Equation 7)

$$E = -\frac{k_B T_e}{\rho_i q}\nabla \rho_i. \quad (63)$$

This equation, derived from the electron momentum equation, neglects the electron-neutral collision term, which has already been shown to be small (see Figure 35).

The system of coupled partial differential equations represented by Equation 52 were solved in finite difference form using a second-order accurate MacCormack

algorithm[2] with the flux corrected transport (FCT) scheme reported by Toth, et al. [112]. The FCT method was used to rid the solution of the numerical oscillations that would otherwise occur in second-order accurate algorithms, especially near shocks. The MacCormack/FCT method offers stability and sharp resolution for a relatively small effort in coding [112]. Further details regarding the computational scheme can be found in Appendix C.

3.3.2 Code Validation. The Riemann problem provides a standard test for a practical computational fluid dynamics code. Consider a tube with an impenetrable diaphragm at some longitudinal station, as shown in Figure 38. The diaphragm separates the left and right sides of the tube. The left side of the tube is filled with a gas at some pressure (P_4) and temperature (T_4) and the right side of the tube contains gas at another pressure (P_1) and temperature (T_1). If the diaphragm were to be ruptured, the gas would flow from the high pressure side to the low pressure side. The Riemann problem consists of finding the velocity, pressure, density and temperature of the gas at any position (x) down the length of the tube for any time (t). Assuming the flow to be one-dimensional and neglecting thermal conductivity and viscosity, the problem has an analytical solution, making it ideal for testing a fluid dynamics code in an environment in which shocks are present. The development of the analytic solution is covered quite well in a number of sources ([40], [61], [18], [79] for example) and will not be repeated here.

The Riemann problem was solved numerically for a shock tube with a length of 100 cm. The diaphragm was located at 40 cm with respect to the high pressure end of the tube. The working gas was Argon with an initial pressure ratio (P_4/P_1) and temperature ratio (T_4/T_1) of 10.0 and 1.25, respectively. These values of temperature and pressure ratios were chosen to allow comparison of the numerical solution using

[2] Although the algorithm is reported to be second-order accurate, this accuracy was only achieved in the present research in the solution of linear problems. For nonlinear problems, the formal accuracy was of first order. Even so, however, the algorithm provided results well within the error bounds of experimental measurements.

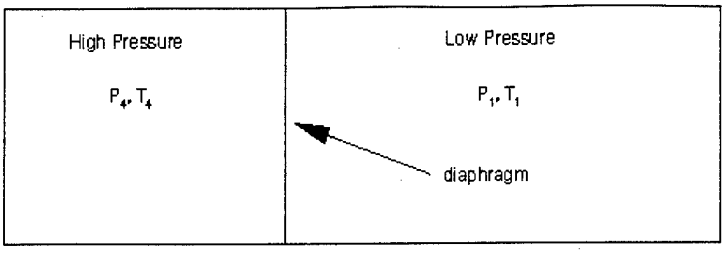

Figure 38. Initial conditions in a typical shock tube.

the MacCormack/FCT scheme to numerical solutions from other algorithms (see [61], for example). The fractional ionization, α, was 10^{-6}. In this validation test, T_e and σ_{in} were set to zero, essentially turning off both the electric field and ion-neutral collisions. As a result, the numerical solution for both the neutrals and ions, which should be the same, could be compared to the exact solution. The one-dimensional calculation was performed on a grid with 401 nodes in the x direction. A comparison between the analytic solution to the Riemann problem (symbols) and the numerical solutions to the Euler equations (solid curve) along the shock tube centerline is shown in Figure 39. In this figure, the ion solution (solid) is shown overlapping the neutral solution (dotted) at each location, as expected under the given conditions. The values of pressure, temperature and density have been normalized to the respective upstream ambient value.

The primary features of a Riemann solution are also shown in this figure. The shock front is a localized region with very large gradients in all of the flow parameters. The contact surface is also a localized region with a large density gradient, across which, however, the pressure and velocity are continuous. The contact surface separates gas that was initially on the left side of the diaphragm from gas that was initially on the right side of the diaphragm. The contact surface acts as a piston, pushing the gas in front of it to the right. The expansion fan represents the propagation of signals into the high pressure side of the shock tube. The agreement between the calculated solution and the exact solution is good, with relative errors in the

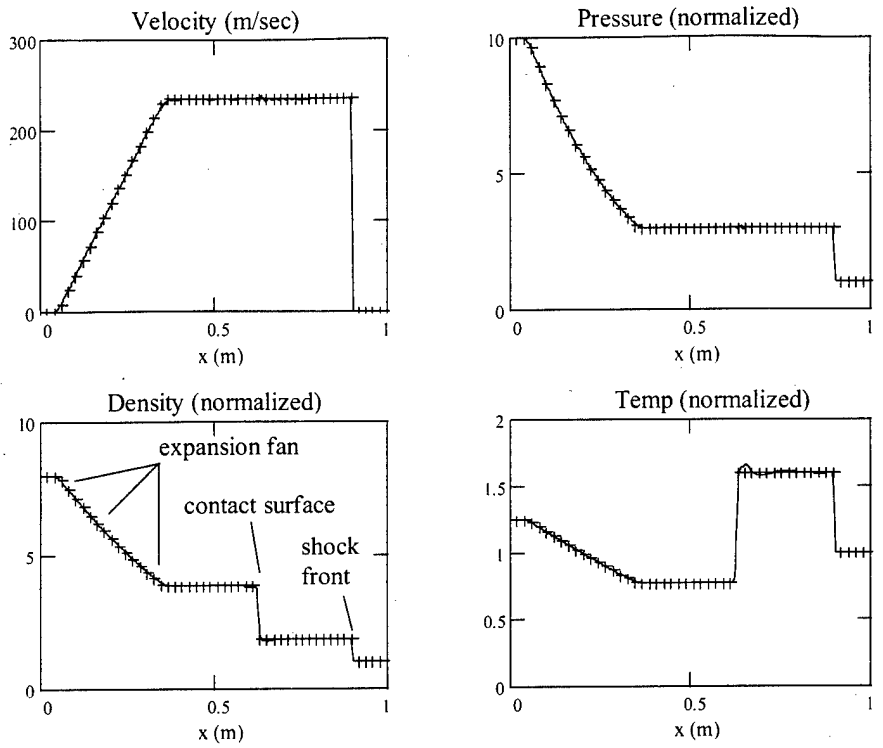

Figure 39. Analytic (+) and numeric solutions to the Riemann problem in Argon with neutral-charged particle coupling turned off and $T_e = 0K$. The ion solution (solid) is shown overlapping the neutral solution (dotted).

pressure of less than 1% throughout the domain except at the leading and trailing edges of the expansion fan, near the contact surface and near the shock front. The relative errors in these regions are typically less than 5%, with the relative error at one or two nodes very near the shock front being much higher ($\approx 50\%$). However, the higher relative errors at this latter location can be attributed to the MacCormack/FCT method, which typically captures the shock front in 3 computational nodes, essentially smearing the front, whereas the exact solution is discontinuous at this point. In general, the relative error throughout the physical domain can be reduced by increasing the number of grid nodes in the computational domain, accompanied (of course) by an increase in the computational requirements (memory, CPU time). Increasing the number of nodes does not prevent the MacCormack/FCT

method from smearing the shock front region, however, thus the high relative error in one or two bins near the shock front will remain high. [3]

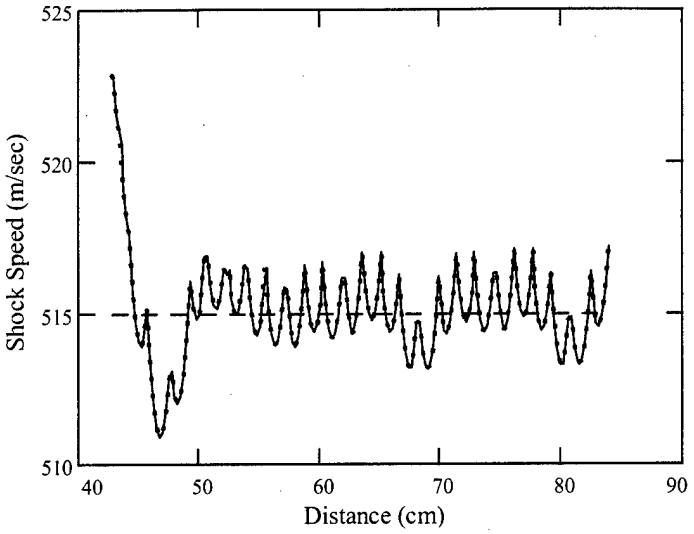

Figure 40. Analytic (dashed) and numerically determined neutral (dotted) and ion (solid) shock speed (Argon with $P_4/P_1 = 10.0$, $T_4/T_1 = 1.25$). In this validation, neutral-charged particle coupling was turned off and $T_e = 0K$

The numerically determined shock velocity can also be compared to the analytic value. This is useful because unlike flow velocity, density, temperature or pressure, the numerical value of the shock velocity is not a direct output of the solution to the fluid equations. Rather, it is determined by observation of the temporal evolution of the shock front position. The general procedure is to track the spatial position of the shock front (x_{shock}) in time (t), then determine the shock speed from $V_{shock} = dx_{shock}/dt$. Further details regarding the numerical determination of the shock speed are given in Appendix B. Figure 40 shows the analytically determined shock speed (dashed line) compared to both the numerically determined neutral (dotted) and ion (solid) shock speed. The neutral and ion shock speeds are the same under the given conditions. The diaphragm is located at 40 cm, so that at time

[3]The barely discernable ripples in the numerical solution in the expansion fan are due to the graphic conversion utility program used and were not present in the raw numerical data.

$t = 0$, the shock speed is zero there. The analytic shock speed (under the present conditions) is Mach 1.597, which is approximately equivalent to 515 m/sec when the ambient gas temperature is $300K$. The small oscillations in the shock speed have an amplitude of less than 1 m/sec and are caused (primarily) by the uncertainty with which the position of the shock front is known at any instant in time. That is, the shock front position at any time is known numerically only to within the spatial resolution of the solution, which is the interval between adjacent nodes.

Another test of the two-component plasma code is to check its ability to produce an ion-acoustic wave which travels at the ion-acoustic velocity. As stated previously, an ion-acoustic wave is a small-amplitude propagation in which the electrons and ions are in phase with each other and move at the same flow velocity, while the neutrals move separately. According to Jones, et al. [70:78], the ion-acoustic wave in a plasma is "analogous to the ordinary sound wave in air. The ions of the plasma provide most of the inertia of the wave, while the electrons provide most of the thermal pressure to drive the wave." If ion-neutral collisions are neglected, a small-amplitude ion-acoustic wave propagates at the ion-acoustic velocity, just as a small-amplitude sound wave in air propagates at the acoustic velocity (the speed of sound). In a plasma, the ion-acoustic speed is given by Equation 16. Note that if the electron temperature were zero, then the ion-acoustic velocity would be equivalent to the neutral gas speed of sound. For non-zero electron temperatures, the ion-acoustic velocity is always greater than the neutral sound speed. In one-dimension, γ_e is equal to unity [70:78].

In order to computationally generate an ion-acoustic wave, a Riemann problem was used in which the initial conditions were such that a small amplitude wave was produced in Argon. In this case, the temperatures on each side of the diaphragm were equal, while the initial pressure ratio was 1.001. The ion-neutral collision terms in Equation 52 were turned off, allowing the ions to flow independent of the neutrals. Analytically, these conditions produce a neutral wave with a Mach number

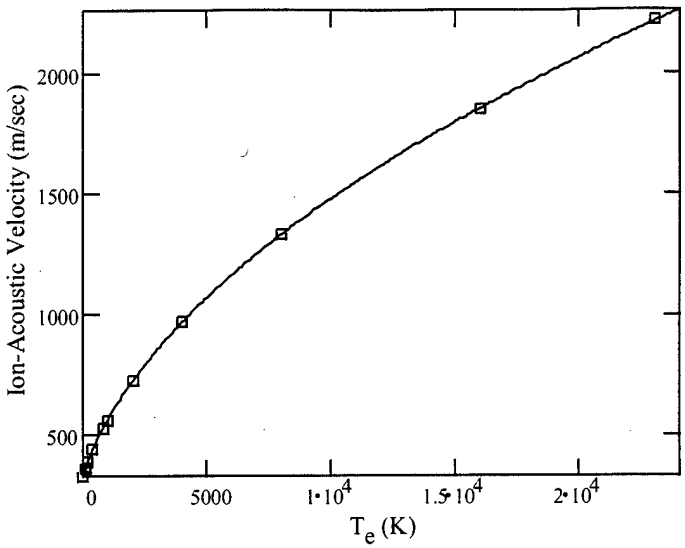

Figure 41. Variation of the ion-acoustic velocity with electron temperature determined numerically (boxes) and analytically (solid curve) for a small-amplitude wave in Argon at $300K$. The wave was generated within a shock tube with a pressure ratio (P_4/P_1) of 1.001 and a temperature ratio (T_4/T_1) of 1.000.

of 1.0002, which is very nearly the speed of sound and which travels at this speed independent of T_e. Thus two waves modes are present in the simulation: an acoustic mode (neutrals) and an ion-acoustic mode (ions). The electron temperature was varied from $0K$ to $23,000K$ (2 eV), which encompasses the range of T_e observed in a typical glow discharge in Argon. The variation of the ion-acoustic wave velocity with T_e is shown in Figure 41 as determined numerically (boxes) and analytically (solid curve). The agreement is seen to be quite good over the entire T_e range considered, with relative errors between the two of the order of 0.2% or less.

The present two-component plasma code has been shown to both solve the Riemann shock problem correctly and to produce an ion-acoustic wave of the proper velocity over a wide range of electron temperatures. With confidence in the code established, it will be used to examine neutral shock/plasma interactions within the two-fluid plasma approximation.

3.3.3 Time-Dependent Results. The numerical code was exercised under conditions representative of both weakly ionized and strongly ionized plasmas. Results from the former case, in which the fractional ionization (α) is of the order of 10^{-6}, will be discussed first. Results from the latter case, in which the fractional ionization was allowed to be as high as 10^{-1}, will then be presented.

3.3.3.1 Weakly Ionized Plasma. A simulation of a Riemann problem for weakly ionized ($\alpha = 10^{-6}$) Argon at 30 torr was used to generate a shock. The initial pressure and temperature ratios within the shock tube were 22.2 and 2.0, respectively. These parameters result in a shock front velocity equivalent to Mach 2.001, similar to the shock used in the steady-state analysis. The electron temperature in the simulation was 2 eV, while the ion-neutral momentum transfer cross-section, σ_{in}, was 4×10^{-21} m^2, resulting in the value of ξ_o (the characteristic distance for ion-acoustic wave damping) evaluating to 5.75 mm. The value of σ_{in} used in this simulation is 25 times smaller than the value used in the steady-state analysis. Higher values of σ_{in} resulted in numerical oscillations in the solution due to small differences between V_i and V_n and T_i and T_n. Since the solution will be plotted along the nondimensional coordinate ξ, obtained by normalizing x by ξ_o (which is inversely proportional to σ_{in}), the difference in the cross-sections is believed to be minor. This assessment is based on comparison of the numerical solution from numerous calculations with the approximate analytic solution of Avramenko (discussed previously) for σ_{in} values equal to a fraction of the limiting value.

The velocity of the neutral (dotted) and charged component (solid) from the time-dependent simulation are shown in Figure 42. Avramenko's analytic solution calculated under the same conditions (Equation 22) is shown for comparison (dashed). The agreement is fairly good. In front of the precursor, the velocity of both components is zero, while downstream of the shock front the velocity is approximately equal to the value predicted from the Rankine-Hugoniot relation for a Mach 2 shock in Argon (363 m/sec). The width of the neutral shock is larger in this

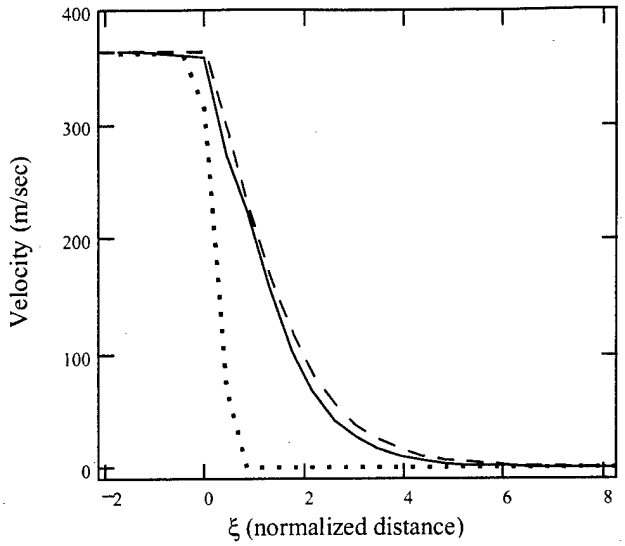

Figure 42. Velocity of the charged component precursor (solid) and neutral component (dotted) from numerical solution of equation 52. The analytic solution (dashed) given by [6] is shown for comparison. The calculation was performed for a Mach 2 shock in Argon. The distance has been normalized by ξ_0, which evaluates to 5.75 mm under the present conditions.

simulation than in the steady-state analysis, being approximately 7.5 mm in width. This translates, however, into capturing the shock front in approximately 3 bins in the present computational grid, which is quite good for a numerical simulation. Reducing the spatial width of each cell should decrease the neutral shock width as well, although doing so would obviously increase the computational cost of the simulation.

The normalized densities of the neutral component (dotted) and of the charged component (solid) are shown in Figure 43. The normalized density corresponding to Avramenko's analytic solution (Equation 25) is also shown (dashed). The agreement between the solutions is quite good. In this figure, the densities of the neutral and charged component have been normalized by their respective upstream ambient values. Thus, far upstream of the shock front the value of each is unity, while downstream of the shock front the value is consistent with the Rankine-Hugoniot prediction for a Mach 2 shock in Argon (ρ_1/ρ_0=2.286).

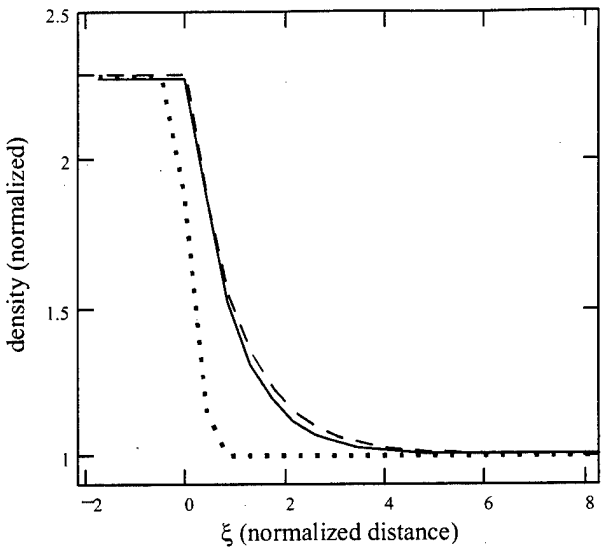

Figure 43. Density of the charged component precursor (solid) and neutral component (dotted) from numerical solution of equation 52. The calculation was performed for a Mach 2 shock in Argon. The analytic solution (dashed) given by [6] is shown for comparison. The distance has been normalized by ξ_0, which evaluates to 5.75 mm under the present conditions.

Once the charged component density has been determined, the electric field at each spatial location can be calculated by use of Equation 63. The result is shown in Figure 44 for the present simulation (solid) as well as for the analytic solution of Ingard (dashed) (Equation 4) under the same conditions. The agreement is generally quite good, except near the peak and along the neutral shock front region. Some of these differences are likely due to the central difference form used to represent the gradient in Equation 63, which would tend to smooth out sharp features in the ion density, as well as due to the finite grid size in the computational simulation. With that said, the presence of a region in which the spatial gradient of the electric field is positive is essential in order to globally conserve charge, as has been shown previously. The present numerical solution has such a region, while the analytic solution does not.

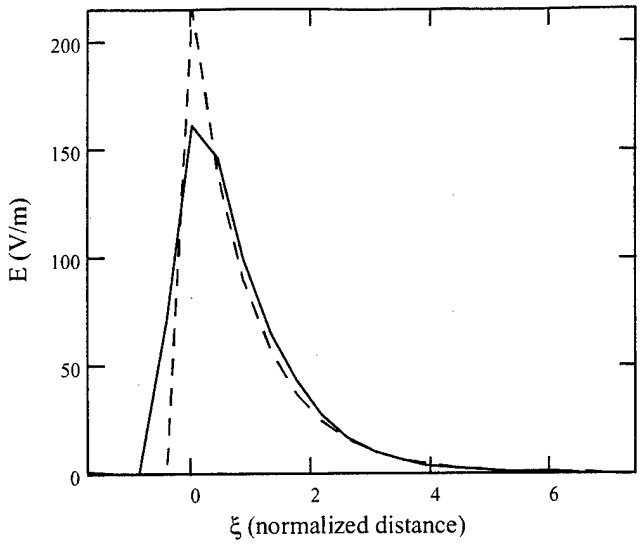

Figure 44. Electric field in the shock front region determined numerically (solid) and analytically (dashed) (from [65]) for a Mach 2 shock in Argon. The distance has been normalized by ξ_0.

3.3.3.2 Strongly Ionized Plasma. Although the plasma present in the plasma/shock experiments conducted in glow discharges can be characterized as weakly ionized ($\alpha \approx 10^{-6}$), it is interesting to examine the effect of higher degrees of fractional ionization on shock propagation. To that end, the fractional ionization was varied from 10^{-6} to 10^{-1}, with the latter limit corresponding to a highly ionized plasma. In all cases, the other parameters defining the plasma Riemann problem were fixed: the initial pressure and temperature ratio were 10.0 and 1.25, respectively, the initial gas and electron temperature were $300K$ and 2 eV, respectively, and the ion-neutral momentum transfer cross-section was 4×10^{-21} m^2. These parameters define a shock velocity of 515 m/sec (Mach 1.597 at $300K$) in weakly ionized Argon. As the degree of fractional ionization is increased, three interesting effects are evident: 1) the shock front region appears to diffuse, or spread out 2) the density jump across the shock front decreases and 3) the shock front velocity increases. All of these effects have been reported in the literature, although the ambient plasma in these cases is weakly ionized.

The variation in the total density with distance near the shock front region is shown in Figure 45 for various degrees of fractional ionization. The total density has been normalized by the total upstream ambient density, which is the same regardless of the degree of fractional ionization. For the case of very weak ionization (10^{-6}),

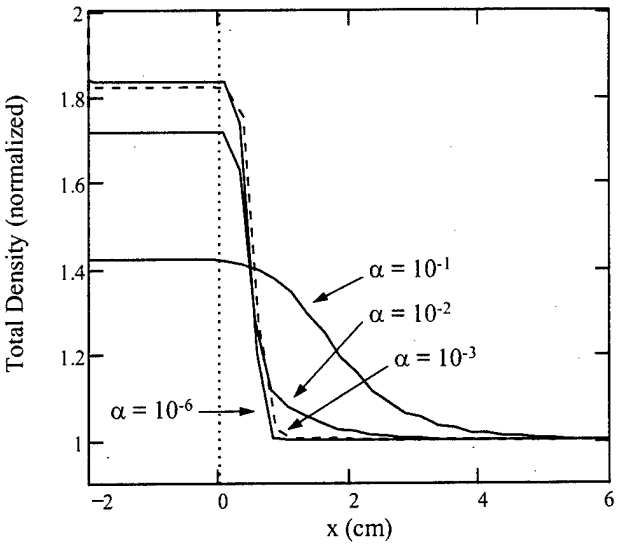

Figure 45. Variation in the total density with distance in the shock front region for various degrees of fractional ionization (α). The density has been normalized to the upstream ambient total density. The calculations are for Argon at 30 torr with $T_{gas} = 300K$ and $T_e = 2$ eV.

the density jump at the shock front corresponds to that expected by application of the Rankine-Hugoniot relations to a Mach 1.597 shock in Argon (1.84). The width of the shock front in this case is 3 spatial bins along the numerical grid, which corresponds to approximately 0.75 cm in the present case. Since capturing the shock front region in approximately 3 spatial bins appears to be typical of the present numerical integration algorithm (even for a completely neutral gas), this width (0.75 cm) is considered a nominal shock front width. As the fractional ionization is increased, the density behind the shock front decreases and the width of the shock increases. At the highest fractional ionization considered (10^{-1}), the density jump at the shock front is approximately 1/2 of the nominal value while the total width of the shock front

is approximately 5 cm (20 spatial bins), which is more than 4 cm greater than the nominal shock front width. A fractional ionization threshold, α_{crit}, of approximately 10^{-3} is apparent in Figure 45. Shocks propagating through plasma with $\alpha < \alpha_{crit}$ are essentially unaltered from shocks propagating through a neutral gas, as far as the neutral component is concerned.

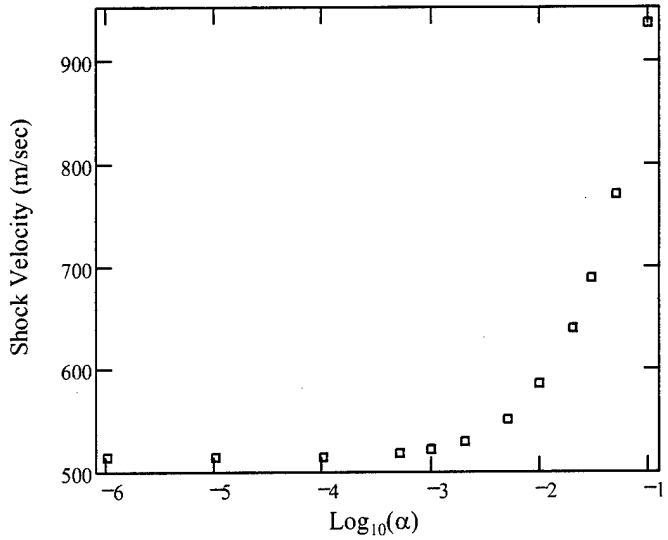

Figure 46. Variation in the neutral shock velocity with fractional ionization (α). The calculations are for Argon at 30 torr with $T_{gas} = 300K$ and $T_e = 2$ eV.

The variation of the velocity of the neutral shock front with fractional ionization is shown in Figure 46. For weak ionization ($\alpha < \alpha_{crit}$) the shock front velocity is unaltered from the nominal shock velocity in the present case (515 m/sec). However, for fractional ionizations greater than α_{crit}, the neutral shock velocity rapidly increases. At the highest α considered (10^{-1}), the shock velocity is nearly twice the nominal value.

Each of the previous effects can be understood by examining the coupling terms between the neutral and charged components in the momentum and energy equations. These terms (P_{in}, defined by Equation 57 and Q_{in}, defined by Equation 59) can be shown to be proportional to the fractional ionization, α. Previously, it

was shown that V_i is greater than V_n in the shock front region under nonequilibrium conditions ($T_e > T_n$), due to the presence of the ion-acoustic waves. This is true even for low fractional ionizations. Likewise, T_i is greater than T_n, for sufficiently high T_e, throughout the shock front region due to the presence of the electric field (which is proportional to T_e). Therefore, P_{in} and Q_{in} act as source terms for the neutral fluid, which transfer momentum and energy, respectively, from the ion-acoustic wave to the neutral shock. When the fractional ionization is sufficiently high, these source terms in the neutral equations are comparable to the source terms arising from Euler's equations ($\vec{S}_1$, given by equation 55), resulting in the charged component altering the neutral shock from its nominal values. As energy is added to the neutral gas in the shock front region, the shock essentially flows into a heated region, resulting in a shock velocity increase, as shown in Figure 30 in Chapter II. Note from this same figure, however, that although the shock velocity increases as it enters a heated region, the shock Mach number decreases, resulting in a lower density jump at the shock front, in accordance with the Rankine-Hugoniot relations.

3.4 Conclusion

A steady-state analysis of the fluid equations for a two fluid plasma has been performed. This analysis essentially confirms the analytic solutions obtained previously by Avramenko, et al. [6], in which a precursor of charged particles is predicted in front of the neutral shock front. This precursor has a width of the order of $T_e/T_n\ \lambda_{in}$, which means that a state of nonequilibrium must exist for the precursor to be present. Slight deviations from charge neutrality exist in this region, in which the ions slightly outnumber the electrons near the neutral shock front and in which the electrons slightly outnumber the ions in front of the neutral shock. The small deviations from charge neutrality create a space charge associated with an electric potential. This potential, of the order of the electron temperature, is small relative to the ionization potential of the Argon gas.

The time-dependent analysis has removed many of the simplifying assumptions present in the steady-state analysis. These assumptions include treating the heavy particle temperature as a constant throughout the shock region, as well as treating the shock velocity as a constant. In addition, the steady-state analysis assumed a fixed form for the neutral velocity and density profiles, effectively preventing the charged component from influencing the neutral flow. In the time-dependent analysis, these assumptions have been removed, with the solution of the Euler equations describing a two component plasma determining the densities, velocities and temperatures of each component, as well as the shock front velocity. A precursor of charged particles was again found leading the neutral shock. The numerically determined precursor was found to be in close agreement with previous analytic results for the density and velocity profiles. An electric field was again found in the precursor region, with the values of this field also in close agreement with previous analytic results. The resulting potential drop from the field remains minor compared with the ionization energy of Argon. Under plasma conditions typically encountered in glow discharges, the charged particles are observed to have practically no influence on the density, velocity and temperature of the neutral component in the parameter space investigated. The neutral shock velocity also remained unaffected by the plasma component under these conditions.

In order for ion-acoustic wave damping to effect the neutral flow, two requirements must be met: 1) the energy density in the ion-acoustic wave must amount to an appreciable fraction of the energy density in the ambient neutral gas and 2) the time scale on which energy is transferred from the ion-acoustic wave to the neutral gas must be less than the transit time associated with a neutral particle crossing the charged particle precursor in front of the neutral shock. Analytic estimates of both of these requirements can be made. An estimate of the minimum value of fractional ionization required to achieve the energy density requirement will first

be derived, followed by a comparison of the ion-neutral energy transfer time to the neutral particle transit time under typical glow discharge conditions.

The energy density of the ions and neutrals can be defined as

$$E_{i,n} = \left(\frac{1}{\gamma - 1} \frac{k_B T_{i,n}}{M_{i,n}} + \frac{1}{2} V_{i,n} \right) \rho_{i,n}. \tag{64}$$

Requiring the ion energy density to be one-tenth of the neutral energy density in front of the neutral shock, and assuming that the ion flow velocity is of the same order as the ion thermal velocity in this same region, leads to the following relationship:

$$\frac{E_i}{E_n} = 2 \frac{T_i}{T_n} \alpha, \tag{65}$$

where α is the fractional ionization. The upper limit of the ratio T_i/T_n can be bounded by the ratio of the temperatures on either side of the shock front (as given by the Rankine-Hugoniot relations), but is of the order of or less than 10 for Mach numbers less than 6 (with $\gamma = 5/3$). Assuming the ratio is 10 (which leads to the lowest estimate for α), the following requirement for α is established:

$$\alpha \geq 5 \times 10^{-3}. \tag{66}$$

Under conditions typically encountered in a glow discharge, the fractional ionization is approximately three orders of magnitude less than this minimum required amount.

An estimate for the ratio of the ion-neutral energy transfer time to the neutral particle precursor transit time can be made by first estimating the width of the precursor (Δ) to be approximately equal to $2\ T_e/T_i \lambda_{in}$ (see Figures 42 and 43). A neutral particle will cross this distance at a speed approximately equal to the shock speed, resulting in a precursor transit time ($\tau_{transit}$) equal to Δ / V_{shock}. Given that the mean time between ion-neutral collisions (τ_{in}) is equal to $1/N_n \sigma_{in} V_{rel}$, the following

ratio can be derived:

$$\frac{\tau_{in}}{\tau_{transit}} = M_{shock}\frac{\sqrt{\gamma\pi}}{8}\frac{T_n}{T_e}. \tag{67}$$

Under conditions typically encountered in plasma/shock experiments conducted in a glow discharge ($M_{shock} \leq 6$, $T_n \approx 400K$, $T_e \approx 12,000K$), this ratio is much less than one, indicating that the ions can efficiently transfer their energy to the neutral flow in the required time. Thus, under these conditions, if the fractional ionization is sufficiently high ($\alpha \geq 5 \times 10^{-3}$), ion-acoustic wave damping can be expected to alter the neutral flow. If the fractional ionization is below the threshold amount, then ion-acoustic wave damping is expected to have an insignificant effect on the neutral flow, consistent with the numerical results obtained for a weakly ionized plasma.

Interestingly, variations in the flow parameters of the neutral component were observed numerically for fractional ionizations greater than approximately 10^{-3}. In these cases, both the neutral shock velocity and neutral shock width were greater than in the low fractional ionization cases. Additionally, the density behind the shock wave front was reduced from the nominal values. Each of these effects is consistent with experimental observations of plasma/shock interactions, although the plasma in these cases is generally weakly ionized. It must be emphasized, therefore, that the degree of ionization required to achieve these results is three orders of magnitude (or more) greater than that normally encountered in a glow discharge plasma.

There has been, however, some experimental evidence that additional ionization is present in the shock front region ([50], [32], [33]). If these measurements are accurate, then it may be possible for the fractional ionization in the shock front region to be significantly greater than that normally present in the quiescent plasma in front of the shock. In such a case, energy transfer from the ion-acoustic wave to the neutral shock may become a relevant process, resulting in a perturbation of the neutral flow. In addition, if some kinetic based plasma process is at work in the shock front region, it is possible for the fractional ionization in this region to be altered. A kinetic based effect may not be predicted by a solution method which uses

the fluid equations as a basis. Such is the case, for example, in the phenomena of Landau waves in plasma physics, which describes the collisionless damping of waves [36:51]. This process, in which energy is transferred between the particles and the wave, is a kinetic based effect and is not predicted when the plasma is modeled by fluid equations. However, a similar process has yet to be proposed in the study of plasma/shock interactions in weakly ionized gas.

IV. Vibrational Energy Relaxation Effects

4.1 Introduction

Post-shock energy addition has been proposed as a likely candidate to explain the increase in shock velocity that has been observed in plasma/shock interaction experiments ([9], [42], [26], [116], [75], [74], [27], [89], [33], [105], for example). The proposed energy addition processes have included electron-ion recombination, atomic association, electronic de-excitation and vibrational relaxation. The present chapter is focussed on the study of post-shock energy addition in the form of nonequilibrium vibrational energy relaxation. In the experiments involving molecular gases, the nonequilibrium store of vibrational energy is created by the plasma, through electron impact excitation of vibrational states. It has been shown previously (Chapter II) that the release of this energy occurs preferentially in the post-shock region, where the effective relaxation times are lower due to the higher vibrational-translation (VT) rates and gas density in this region.

In order for vibrational energy relaxation to significantly affect the shock parameters, two requirements must be met: 1) the amount of energy added to the flow must be significant (compared to the thermal energy already present in the flow) and 2) this energy must be added quickly (on the time scale of the transit time for the shock to propagate some characteristic length). In this chapter, two aspects of nonequilibrium vibrational energy relaxation will be addressed. In the first, the influence of the release of vibrational energy into the post-shock flow on shock speed will be considered for a design gas which meets both of the criteria given above. In the second, an actual gas will be used to determine, under realistic conditions, how much energy can be stored in the vibrational manifold in nonequilibrium, how much of this energy can be released into the flow and how fast this release of energy can occur. Finally, some assessments will be made regarding vibrational energy relaxation as a viable mechanism in explaining experimental observations.

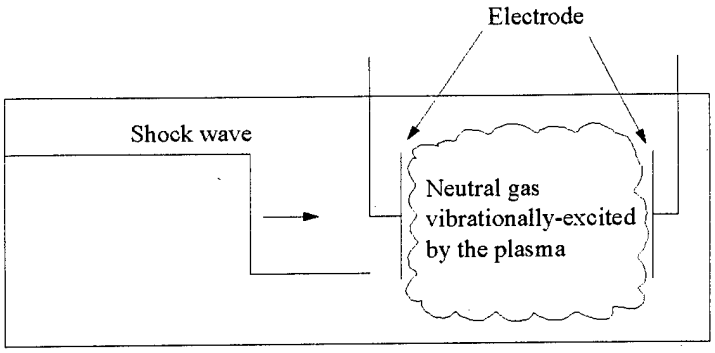

Figure 47. General experimental arrangement in which a shock interacts with a gas which has been vibrationally excited by the plasma.

The general experimental arrangement, as reported in the literature, is shown in Figure 47. A steady-state glow discharge of limited spatial extent vibrationally excites the gas, resulting in a nonequilibrium state in which the vibrational temperature (T_{vib}) is greater than the gas temperature (T_{gas}). The low fractional ionization of these plasmas means that the gas is composed almost entirely of neutral molecules. A shock propagates into the vibrationally excited gas, which results in the (reported) release of the vibrational energy into the region behind the shock front.

4.2.1 Model Equations. The equations used to describe the motion of the gas are the Euler equations, which are

$$\frac{\partial}{\partial t}\rho + \frac{\partial}{\partial x}(\rho v) = 0 \tag{68}$$

$$\frac{\partial}{\partial t}(\rho v) + \frac{\partial}{\partial x}(\rho v^2 + P) = 0 \tag{69}$$

$$\frac{\partial}{\partial t}(\rho \epsilon) + \frac{\partial}{\partial x}\left[(\rho \epsilon + P)v\right] = \frac{\rho(\epsilon_{vib} - \epsilon_{vib}^{eq})}{\tau} \tag{70}$$

$$\frac{\partial}{\partial t}(\rho \epsilon_{vib}) + \frac{\partial}{\partial x}(\rho \epsilon_{vib} v) = -\frac{\rho(\epsilon_{vib} - \epsilon_{vib}^{eq})}{\tau} \tag{71}$$

where ρ is the mass density, v is the flow velocity, P is the gas pressure and τ is the characteristic time over which the vibrational energy changes. These equations

describe the conservation of mass (Equation 68), momentum (Equation 69) and energy (Equations 70 and 71) for an inviscid fluid. The conservation of energy is represented by two equations, with Equation 70 describing the conservation of energy in the forms of kinetic flow, thermal translation and thermal rotation and Equation 71 describing the conservation of vibrational energy. In Equation 70, ϵ describes the specific energy in the translational, rotational and directed flow modes and is defined as

$$\epsilon = \frac{5k_BT}{2M} + \frac{v^2}{2} \tag{72}$$

Note that the translational and rotational thermal modes have been combined, which assumes that these two modes always remain in equilibrium with each other. The specific vibrational energy (ϵ_{vib}) is modeled as

$$\epsilon_{vib} = \frac{k_BT_{vib}}{M}, \tag{73}$$

consistent with the definition of the specific vibrational energy introduced previously in Chapter II. The equilibrium specific vibrational energy (ϵ_{vib}^{eq}) is defined by the use of Equation 73 with $T_{vib} = T_{gas}$. Although the vibrational energy defined in this manner is different from the definition commonly used ([5:488], for example), the intent of the present section is to use these equations to examine the effects of nonequilibrium vibrational relaxation on shock propagation, without being limited by the capabilities or limitations of a physical gas. To that end, both the amount of energy stored in the vibrational manifold (T_{vib}) and the time constant associated with the release of this energy (τ) were chosen to cause an appreciable effect in the shock flow.

Equations 68 through 71 are four equations with five unknowns. An equation of state ($P = \rho k_BT/M$) is used to close the set, with the remaining primitive variables being the gas temperature (T), flow velocity (v), density (ρ) and specific vibrational energy (ϵ_{vib}). These equations were solved numerically using a MacCor-

mack predictor-corrector scheme with explicit time integration. A flux corrected transport (FCT) scheme was used in order to prevent oscillations in regions of large gradients. The actual MacCormack/FCT method used was that given by Fletcher [44:151–166]. Further details regarding this algorithm are given in Appendix B (see the discussion of the x sweep operator).

4.2.2 Code Validation. The code was validated by comparing the numerical and analytical solutions to the Riemann (shock tube) problem for a gas with the same molecular weight as N_2. The pressure and temperature ratios defining the Riemann problem were 10.0 and 1.25, respectively, resulting in a shock with a nominal propagation speed of 571 m/sec. The gas on both sides of the diaphragm was initially in an equilibrium state, with the temperature on the low pressure side equal to $300K$. The shock tube was 200 cm long with the diaphragm located at 80 cm from the high pressure end of the tube. The vibrational relaxation time constant (τ) used in this validation was very short, being equal to 20 times the Δt used in the integration. This value of τ was large enough to allow the temporal and spatial resolution of the relaxation process, while at the same time being small enough to allow a comparison to the exact solution with $\gamma = 9/7$, which assumes instantaneous vibrational relaxation. A comparison of the numerical solution (solid) to the exact solution (dotted) is shown in Figure 48. The density, temperature and pressure have been normalized by their respective upstream ambient values. The agreement between the solutions is quite good. The small spike in the gas temperature at the shock front is physical and is discussed below.

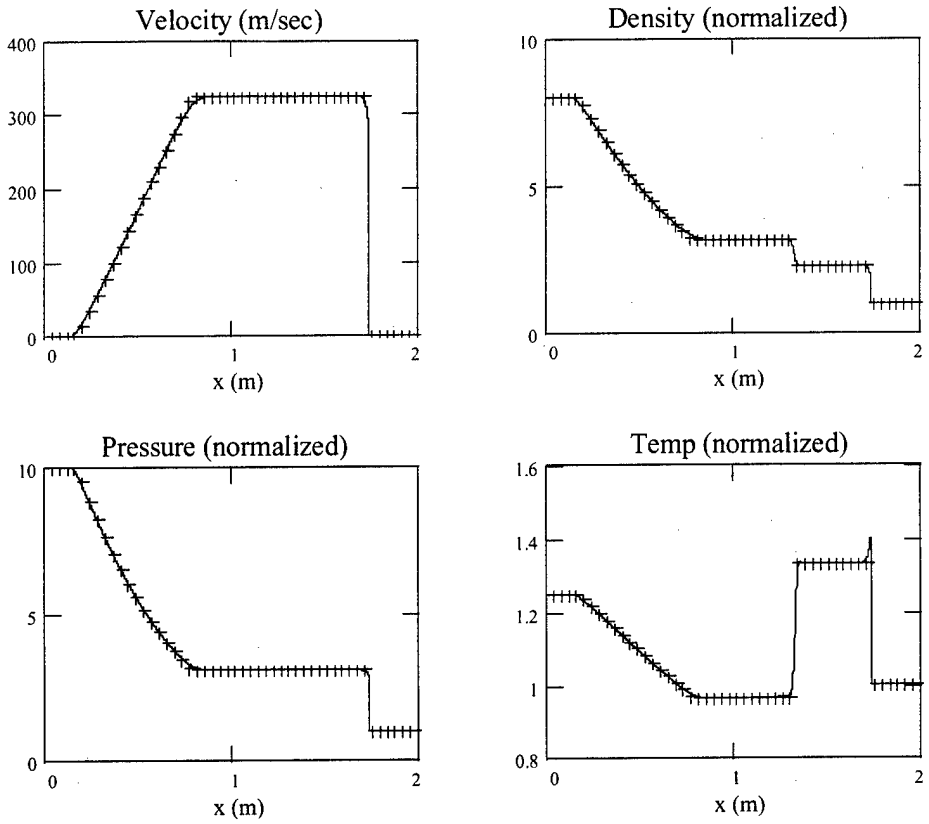

Figure 48. Exact solution with $\gamma = 9/7$ (+'s) and numerical solution (solid) of Euler's equations for a gas with a finite vibrational relaxation time. The shock propagates through gas which is initially in an equilibrium state ($T_{\text{gas}} = T_{\text{vib}}$). The spike in the temperature at the shock front is physical.

A close-up of the vibrational and gas temperature profiles in the shock front region is shown in Figure 49. The gas temperature (solid) initially rises rapidly at

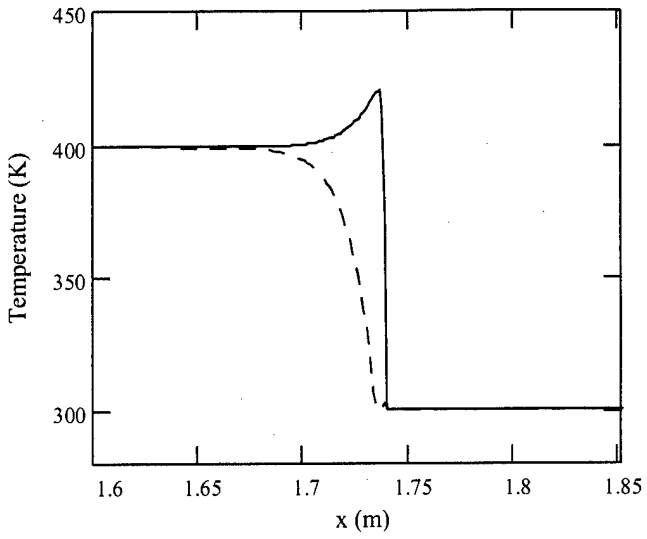

Figure 49. Gas temperature (solid) and vibrational temperature (dashed) in the shock front region for a shock propagating through gas in an equilibrium state.

the shock front to a value of 420K, then decreases gradually in the post-shock region to a temperature of $400K$ as energy is taken from the flow and transferred into the vibrational modes. These post-shock temperatures are precisely those values predicted based on the Rankine-Hugoniot relations for a gas with a γ of 7/5 and 9/7, respectively, at a shock velocity of 571 m/sec. Due to the finite vibrational relaxation time, the vibrational temperature (dashed) rises gradually in the post-shock region until the vibrational and translational/rotational modes achieve equilibrium. The peak in the gas temperature corresponds precisely to the analytically predicted temperature just behind the shock front for a gas with a γ of 7/5 (i.e., a gas with no vibrational modes). The equilibrium temperature corresponds precisely to the analytically predicted temperature in the post-shock region for a gas with a γ of 9/7 (i.e., full equilibration between translation, rotation and vibration). Longer vibrational relaxation times result in a spike with a wider spatial width and vice-versa.

As mentioned previously, the value of the relaxation time constant (τ) used in this calculation was equal to 20 times the value of the time step used in the integration of the fluid equations (Δt). Therefore, the vibrational relaxation length shown in Figure 49 is not independent of the grid resolution. However, the peak gas temperature and the final equilibrium temperature are independent of the grid resolution.

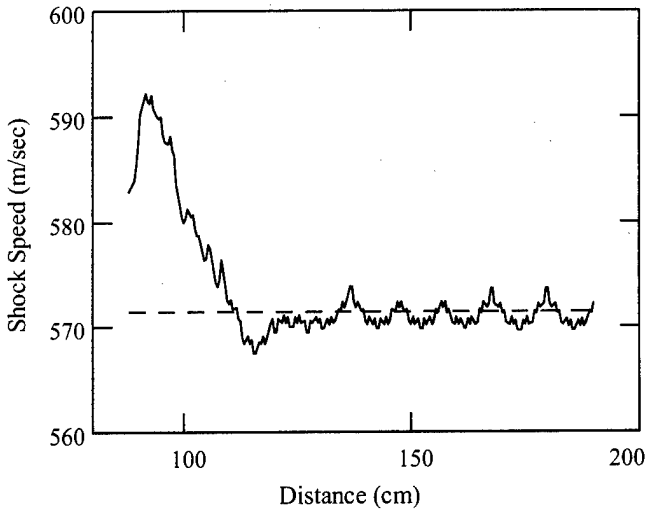

Figure 50. Numerically (solid) and analytically (dashed) determined shock velocity for the Riemann problem in which the shock propagates through gas with a finite vibrational relaxation time. The gas is initially is an equilibrium state.

As previously mentioned (Chapter III), the shock speed is another indicator of the quality of the numerical solution, although it is not one of the variables directly obtained in the integration of the fluid equations. The shock speed can be determined by tracking the spatial position of the shock front (x_{shock}) in time (t), then calculating the derivative of the trajectory from $V_{shock} = dx_{shock}/dt$. Further details regarding the numerical determination of the shock speed are given in Appendix B. A comparison between the shock speed determined analytically (dotted) and numerically (solid) is shown in Figure 50. Here, the shock speed determined numerically is within approximately 0.5% of the analytic value (571 m/sec). The

small oscillations in the shock speed have an amplitude of less than 2 m/sec and are caused (primarily) by the uncertainty with which the position of the shock front is known at any instant in time. That is, the shock front position at any time is known numerically only to within the spatial resolution of the solution, which is the interval between adjacent nodes.

In this validation, the shock propagated into gas that was initially in an equilibrium state. Both the flow parameters in the shock front region and the shock velocity were found to be in good agreement with analytic values. In the next section, a shock will be propagated into gas that is initially in a nonequilibrium state. This is representative of the nonequilibrium conditions that may be present in a neutral gas due to the presence of a weakly ionized plasma.

4.2.3 Numerical Results. In this section, the experimental arrangement depicted in Figure 47 will be modeled as shown in Figure 51. Here, a shock tube is used to generate a shock, which then propagates into a gas with a nonequilibrium store of vibrational energy. The low pressure side of the shock tube is divided into

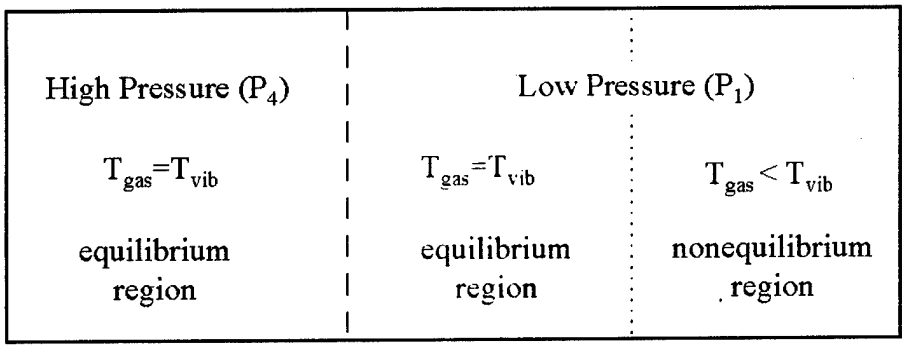

Figure 51. Shock tube used to model the nonequilibrium vibrational relaxation effects. The pressure is continuous throughout the low pressure side of the shock tube.

two regions: an equilibrium region and a nonequilibrium region. The equilibrium region is characterized by $T_{vib} = T_{gas}$ and represents the region through which a shock would propagate in the absence of a plasma, as depicted by the left half of

Figure 47. The nonequilibrium region is characterized by $T_{vib} > T_{gas}$ and represents the plasma region into which the nominal shock propagates, as depicted by the right half of Figure 47. As the shock front passes into the nonequilibrium section, the excess vibrational energy is released into the post-shock region. As this energy is transferred to the other modes, it heats the gas. It will be shown that this release of energy will accelerate the shock wave to a higher velocity.

The shock tube used in this nonequilibrium example is the same as that used in the code validation (200 cm long with a diaphragm located at 80 cm). An equilibrium region (characterized by equal gas and vibrational temperatures of $300K$) will extend 20 cm to the right of the diaphragm, with an abrupt transition to a nonequilibrium region (characterized by a vibrational temperature of $600K$ and a gas temperature of $300K$) at 100 cm. The vibrational energy corresponding to a vibrational temperature of $600K$, as used in Equation 73, is equivalent to the vibrational energy corresponding to a vibrational temperature of approximately $1700K$, as used in the usual definition of specific vibrational energy (Equation 35). Since a vibrational temperature of $1700K$ is considered typical of that encountered in a glow discharge in N_2, the present use of a vibrational temperature of $600K$ is understandable. When the diaphragm bursts, the shock forms and propagates at a velocity of 571 m/sec in the equilibrium gas, as in the validation case previously discussed. The minimum steady-state shock velocity (V_{CJ}), defined by the Chapman-Jouguet point (Chapter II), under these conditions is 550 m/sec. Since the shock velocity will enter the nonequilibrium region with a velocity greater than V_{CJ}, no acceleration is expected according to the common interpretation of the theory [27].

The numerical solution obtained under the given nonequilibrium conditions is shown in Figure 52. The shock structure observed in this nonequilibrium case is quite different from that observed in the equilibrium case. In the equilibrium case, the density and pressure in a fluid element increased as the fluid element was transported from the point just behind the shock front to the post-shock equilibrium

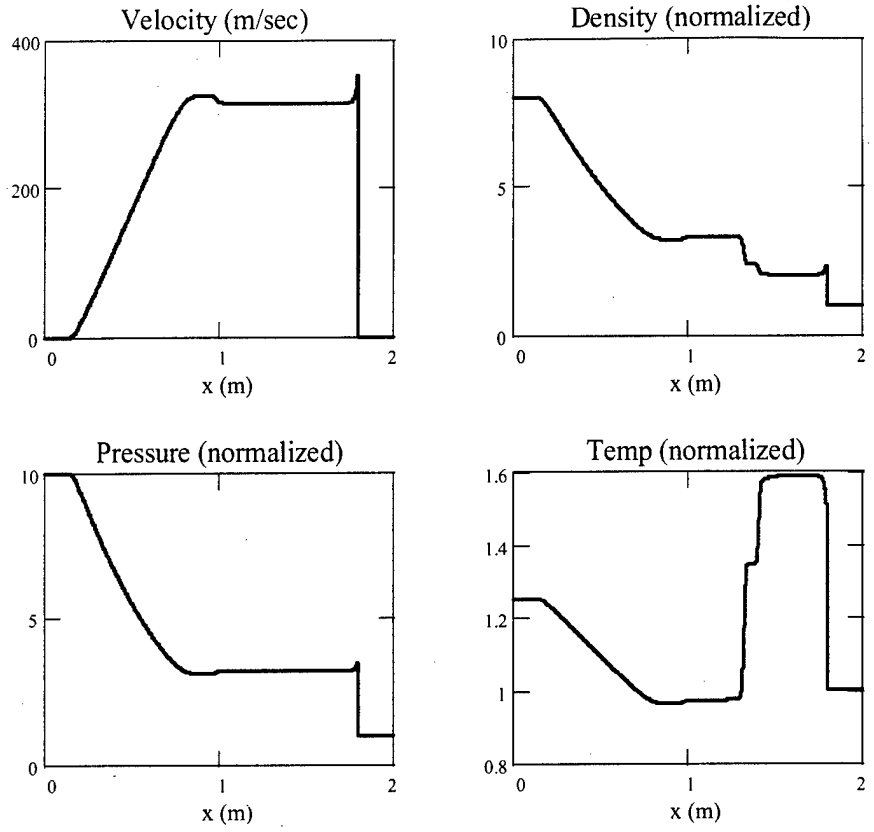

Figure 52. Numerical solution of Euler's equations for a gas with a finite vibrational relaxation time. The shock propagates through gas which is initially in a nonequilibrium state ($T_{\text{gas}} = 600K, T_{\text{vib}} = 300K$).

region (Figure 48). In the nonequilibrium case, the density and pressure in a fluid element decrease as the fluid element is transported from the point just behind the shock front to the post-shock equilibrium region. In addition, in the equilibrium case the gas temperature rises sharply across the shock front, then decreases as equilibrium is approached. In the nonequilibrium case, the gas temperature rises sharply across the shock front, then continues to rise as equilibrium is approached.

The vibrational and gas temperature profiles in the shock front region are shown in Figure 53. Here the gas temperature (solid) rises sharply across the shock

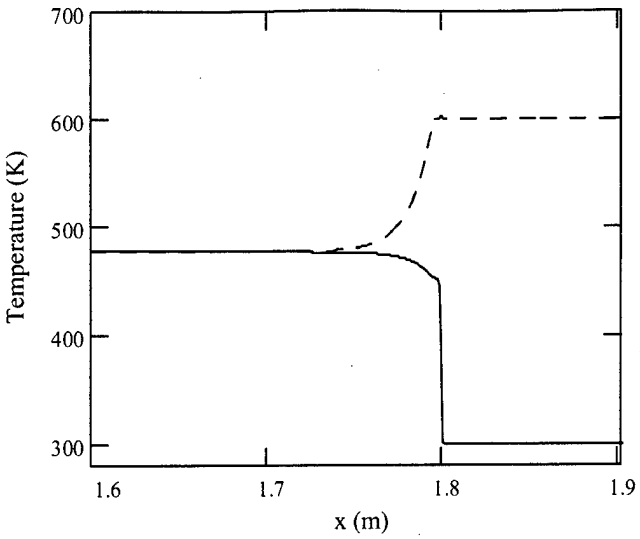

Figure 53. Gas temperature (solid) and vibrational temperature (dashed) in the shock front region for a shock propagating through gas in a nonequilibrium state.

front to a value of approximately $450K$, then rises more gradually until equilibrium is achieved at a temperature of approximately $480K$. The vibrational temperature (dashed), on the other hand, decreases gradually until equilibrium is reached. In this case, energy is transferred from the vibrational modes into the translational and rotational thermal modes. This energy transfer heats the gas and increases the pressure in the equilibrium region above the equilibrium value obtained in the previous case. The increased pressure, in turn, causes the shock front to accelerate to a higher velocity.

The variation in the numerically determined shock velocity with distance is shown in Figure 54 (solid). The shock accelerates rapidly upon entering the nonequilibrium region, even though the initial shock velocity (571 m/sec) is greater than V_{CJ}, the minimum steady-state velocity (550 m/sec). This is an apparent contradiction to the commonly reported understanding of nonequilibrium shock theory. The dashed line shown in Figure 54 is an analytic prediction of the new steady-state shock speed in the nonequilibrium region. The numerically determined shock speed

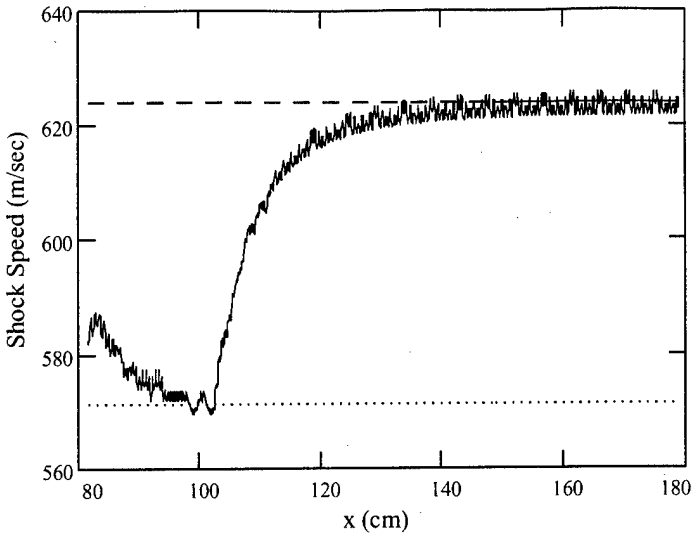

Figure 54. Numerically determined shock velocity (solid) for the Riemann problem in which the shock propagates through gas initially in both equilibrium and nonequilibrium states. The shock velocities under equilibrium (dotted) and nonequilibrium (dashed) conditions are analytically determined. The velocity according to the Chapman-Jouguet regime is 550 m/sec. The nonequilibrium region starts at 100 cm.

is observed to converge to within 0.2% of the analytic value. The derivation of the analytic prediction of the shock speed in the nonequilibrium region of the shock tube is the subject of the next section. The time (distance) required to achieve the new steady-state shock velocity depends on the characteristic vibrational relaxation time (distance). If this time is short, then the energy is transferred quickly between the various modes and the shock speeds up quickly. If this time is long, then the transfer of energy takes place slowly. Independent of relaxation time, however, the eventual steady-state shock speed converges to the same value.

4.2.4 Analytic Determination of Shock Speed. According to the theory of shock propagation in nonequilibrium gases as discussed by Osipov, et al. [93], which is based on the work of Landau [79] and Zel'Dovich [123], a shock propagating into a medium at a velocity less than the minimum steady-state shock velocity, V_{CJ}

(defined by the Chapman-Jouguet point as discussed in Chapter II), will accelerate until its velocity matches the minimum velocity; i.e., the shock will accelerate until the downstream equilibrium flow conditions match those at the Chapman-Jouguet point. Osipov's theory does not predict acceleration beyond V_{CJ}. A shock entering a nonequilibrium region with a velocity equal to or greater than V_{CJ} is also unaccelerated according to Bystrov, et al. [27]. It was observed that the computational results from the present work did not support these claims in all cases. Computationally, shocks with initial velocities below some value, V_{crit} (where $V_{crit} < V_{CJ}$), accelerated to a steady-state velocity equal to V_{CJ}, in accordance with previous theory. However, shocks with initial velocities greater than V_{crit} were observed to accelerate to steady-state velocities greater than V_{CJ}, in apparent contradiction with the theory. In addition, shock acceleration occurred even when the initial shock velocity was greater than V_{CJ}, also in apparent contradiction with theory. It will be shown in this section that the present numerical results are correct and that the previous understanding of the theory describing shock propagation in nonequilibrium gases has been either incomplete or incorrect.

The foundation for the analytic determination of the steady-state shock velocity in the nonequilibrium region rests on Emanuel's development of the solution to the Riemann problem [40:181-183]. Here, his notation is adopted and his development refined to apply to nonequilibrium conditions. Emanuel's development of the Riemann solution is followed precisely up to the point just beyond his equation (10.2), with the chief result being

$$\frac{P_5}{P_4} = \left[1 - \left(\frac{\gamma_4 - 1}{2}\right)\frac{U_5}{C_4}\right]^{\frac{2\gamma_4}{\gamma_4 - 1}}. \tag{74}$$

where C is the speed of sound, U is the flow velocity in the laboratory frame and the subscripts 4 and 5 refer to the region of undisturbed high pressure gas and the region between the contact surface and expansion fan, respectively. This equation

assumes that the flow between these two regions is isentropic, which is the case in nonequilibrium relaxation as well, since the nonequilibrium gas will always be to the right (upstream) of the original contact surface (Figure 51). The pressure and velocity are continuous across the contact surface, thus $P_5 = P_2$ and $V_5 = V_2$. Using this in Equation 74 and writing P_2/P_4 as $(P_2/P_1)/(P_4/P_1)$ results in

$$\frac{P_2}{P_1} = \frac{P_4}{P_1}\left[1 - \left(\frac{\gamma_4 - 1}{2}\right)\frac{U_2}{C_4}\right]^{\frac{2\gamma_4}{\gamma_4 - 1}}, \tag{75}$$

where the subscript 1 denotes the undisturbed region in front of the shock and the subscript 2 denotes the region between the shock front and the contact surface. Equation 75 is the starting point for the extension of the analytic solution to the nonequilibrium cases. It is important to understand that no assumptions have been made regarding the equilibrium (or nonequilibrium) state of the gas in deriving Equation 75.

In the usual Riemann problem, the known parameters are the pressures on either side of the shock tube diaphragm (P_4 and P_1), the speeds of sound on either side of the diaphragm (C_4 and C_1) and the gas types on either sides of the diaphragm (γ_4 and γ_1). Thus, the unknown variables in Equation 75 are the pressure ratio at the shock front (P_2/P_1) and the flow velocity of the gas just behind the shock front (U_2). The usual approach to the problem then uses the Rankine-Hugoniot relations (which describe the relationship between shock Mach number and either pressure, density or flow velocity ratios at the shock front) to write Equation 75 as a transcendental equation with one unknown parameter. The solution is then determined by finding the root to Equation 75. Once this value is known, the shock velocity, pressure ratio at the shock front (P_2/P_1) and the flow velocity behind the shock (U_2) are all determined. In this approach to the problem, a gas in initial equilibrium has been assumed. Where was this assumption made? It was made implicitly in the use of the Rankine-Hugoniot relations, which were derived for a gas in initial equilibrium.

The shock adiabatics (discussed in Chapter II) could have been used (instead of the Rankine-Hugoniot relations) to find the root of Equation 75. In this case, the shock adiabatic corresponding to the final state of the gas (Equation 36) is used in conjunction with a line of constant mass flux, which defines a shock velocity. The intersection of these two curves then determines both the pressure ratio (P_2/P_1) and the flow velocity in the equilibrium region behind the shock front (U_2) (see Figure 21). In this figure, the equilibrium region is defined as the point B. The pressure ratio at this point (P_2/P_1) can be read directly off the curve, while the flow velocity at this point can be determined from the principle of conservation of mass flux (in the shock front frame) by

$$U_B = V_1 \sqrt{\frac{P_B - P_1}{V_1 - V_B}} \left(1 - \frac{V_B}{V_1}\right), \tag{76}$$

where U_B is flow velocity at the equilibrium point in the laboratory frame, V is the specific volume and P is the pressure. In the present notation, Equation 75 can be written as

$$\frac{P_B}{P_1} = \frac{P_4}{P_1} \left[1 - \left(\frac{\gamma_4 - 1}{2}\right) \frac{U_B}{C_4}\right]^{\frac{2\gamma_4}{\gamma_4 - 1}}, \tag{77}$$

where the subscript B has replaced the subscript 2 in denoting the equilibrium region behind the shock front, consistent with the notation previously adopted. Thus, numerically, the problem becomes one of just finding a constant mass flux line with the correct slope (shock velocity) such that the flow parameters at point B satisfy Equation 77.

The same thing can be done for the case in which the gas is initially in a nonequilibrium state, except that the shock adiabatic is given by Equation 36 with $T_{vib_1} \neq T_{gas_1}$. Equation 75 remains valid, with the unknown parameters still being P_2/P_1 and U_2. Both of these unknowns can be found by finding the intersection (point B) of the constant mass flux line (Equation 76) with the equilibrium state adiabatic (Equation 36) such that the flow parameters at point B satisfy Equation

77. Thus, a simultaneous solution of three equations is required. This is exactly what was done in the equilibrium case, with $T_{vib_1} = T_{gas_1}$ in Equation 36.

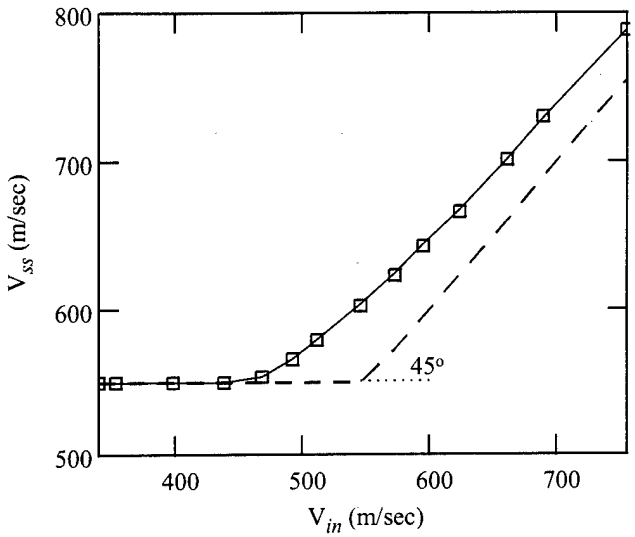

Figure 55. Variation of the steady-state shock velocity (V_{ss}) in the nonequilibrium region with the entrance shock velocity (V_{in}). The conditions in the nonequilibrium region remain fixed ($T_{vib} = 600K$, $T_{gas} = 300K$, $P =$ 760 torr). Shown are the shock velocity determined by the fluid code (boxes), by the nonequilibrium extension to the Landau/Zel'Dovich theory (solid) and by the old theory (dashed). The shock velocity corresponding to the Chapman-Jouguet condition is 550 m/sec.

Comparisons of the shock speeds determined by the different methods are shown in Figure 55. The numerically determined steady-state shock speed in the nonequilibrium region (boxes) agrees very well with the results from the present analytical method (solid curve), with relative errors between the two less than 0.2% under the present conditions. The commonly understood application of the classical theory is also shown (dashed). The shock velocity as the shock enters the nonequilibrium region (V_{in}) is plotted along the ordinate, while the steady-state shock velocity in the nonequilibrium region (V_{ss}) is plotted along the abscissa. In all cases, the nonequilibrium region was characterized by a vibrational temperature of $600K$, a gas temperature of $300K$ and a pressure of 760 torr. This defined a

minimum steady-state velocity (V_{CJ}) of 550 m/sec, corresponding to the Chapman-Jouguet point. The classical theory predicts that for cases in which $V_{in} \leq V_{CJ}$, the steady-state velocity should be equal to V_{CJ}. For cases in which $V_{in} > V_{CJ}$, the steady-state velocity should equal V_{in}. The present theory predicts a steady-state shock velocity equal to V_{CJ} only for shocks entering the nonequilibrium region with a velocity less than a certain critical shock velocity, V_{crit}, where $V_{crit} < V_{CJ}$.

The value of V_{crit} can be determined by using Equations 76 and 77. The minimum steady-state shock velocity that allows a fluid element to reach the equilibrium region is given by V_{CJ}. Taking the point B to be equal to the point CJ (see Figure 25), these equations become

$$U_{CJ} = V_1 \sqrt{\frac{P_{CJ} - P_1}{V - V_{CJ}}} \left(1 - \frac{V_{CJ}}{V_1}\right), \tag{78}$$

where U_{CJ} is flow velocity at the Chapman-Jouguet point in the laboratory frame, V is the specific volume and P is the pressure and

$$\frac{P_4}{P_1} = \frac{P_{CJ}}{P_1} \left[1 - \left(\frac{\gamma_4 - 1}{2}\right) \frac{U_{CJ}}{C_4}\right]^{-\frac{2\gamma_4}{\gamma_4 - 1}} \tag{79}$$

where the last equation has been rewritten by solving for P_4/P_1. Since the known nonequilibrium initial conditions (V_1, P_1, T_{vib_1}) define the Chapman-Jouguet point (P_{CJ}, V_{CJ}), the initial pressure ratio (P_4/P_1) is determined. The shock velocity corresponding to this pressure ratio defines V_0, which is an entrance velocity threshold. A shock entering the nonequilibrium region below this threshold will accelerate until the steady-state velocity is equal to the Chapman-Jouguet velocity (V_{CJ}). A shock entering the nonequilibrium region with a velocity in excess of V_{crit} will have a steady-state velocity greater than V_{CJ}. For the parameters corresponding to Figure 55, V_{crit} (determined by Equations 78 and 79) corresponds to 445 m/sec, which is in excellent agreement with the numerical results shown in this figure.

It has been reported by Bystrov, et al. [27] that the velocity of a shock in a plasma depends on the velocity of the shock as it enters the plasma, the properties of the plasma ahead of the shock front and the processes which occur behind the shock front. Bystrov suggests that the post-shock release of nonequilibrium vibrational energy cannot explain the observed shock variations in his experiment, based on his belief that the steady-state shock velocity in such cases is determined by the Chapman-Jouguet velocity. The results obtained in the present investigation suggest that this belief is incorrect. As Figure 55 clearly shows, the final steady-state shock velocity depends on the velocity of the shock as it enters the nonequilibrium region. In addition, this velocity depends on T_{vib_1}, which varies with differing plasma conditions in front of the shock. Finally, although full vibrational/translational equilibration was assumed in the present calculations, such need not be the case. For cases in which only part of the nonequilibrium vibrational energy is released, the shock velocity in the nonequilibrium (plasma) region will be less than that obtained assuming full equilibration (i.e., the shock velocity depends on the processes which occur behind the shock front). Therefore, the shock velocity behavior resulting from nonequilibrium vibrational relaxation is consistent with all of the qualitative observations reported by Bystrov.

4.3 Analysis of Vibrational Kinetics

In the previous section it was shown that it is possible, in principle, for nonequilibrium vibrational energy relaxation to increase the shock speed. In practice, however, two conditions must be satisfied in order for this to occur. First, an appreciable amount of energy must be extracted from the vibrational mode in the post-shock region. Second, this energy must be extracted quickly. In the calculations of the previous section, both of these requirements were met. However, both the amount of vibrational energy available for extraction and the time constant (τ) at which this energy was released were chosen without regard as to the physical properties (or limitations) of an actual molecular gas. Rather, the intent of the previous calculations was to examine the influence of vibrational energy relaxation given a gas which met both requirements. In the present section, the ability of an actual gas to met the stated conditions will be examined.

Pure molecular nitrogen will be used as the test gas in this analysis of the vibrational kinetics. This choice was made based on the availability of experimental data taken in pure N_2 gas. In addition, since N_2 comprises nearly 80% of air, the substance through which all aerodynamic vehicles must fly, it seems reasonable to use this gas as a starting point. In reality, of course, air is not made of pure molecular nitrogen, but has many other constituents which can change the kinetic rates upon which the present study is based. However, it will be assumed that air can be simulated by pure molecular nitrogen well enough to permit order of magnitude calculations of the relevant parameters.

4.3.1 How Much Energy Can Be Released? The maximum amount of nonequilibrium vibrational energy which can be added to the flow in the post-shock region depends on two things. These are the amount of energy initially contained in the vibrational manifold for the gas in front of the shock and the amount of energy contained in the vibrational manifold for the gas at equilibrium in the post-shock

region. The difference between these two is the energy added to the flow. In order for vibrational energy relaxation to lead to significant variations in the flow field, the amount of energy added to the flow behind the shock front must comprise an appreciable fraction of the thermal energy already present in the flow in the post-shock region (estimated to be approximately 10% or more).

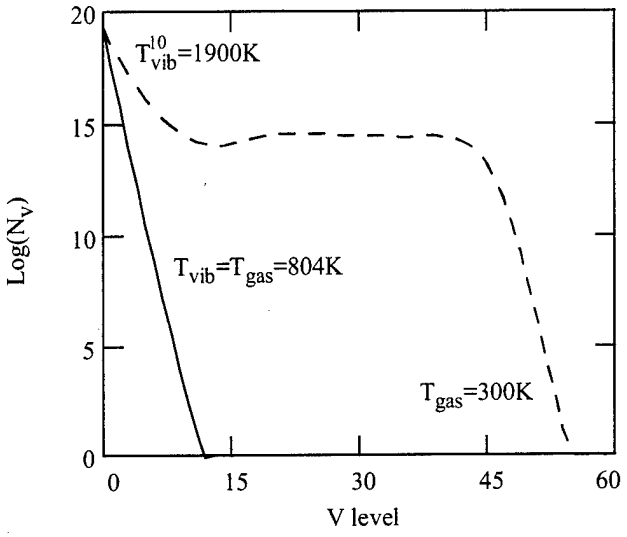

Figure 56. Nonequilibrium (dashed) and equilibrium (solid) vibrational distribution functions in N_2. The nonequilibrium distribution is representative of that obtained in a glow discharge plasma, while the equilibrium distribution is representative of that obtained in the equilibrium region downstream of a Mach 3 shock. The amount of energy added to the flow per molecule is approximately equal to the difference between the average energies of these two distributions.

As an example, consider the two vibrational distribution functions (VDFs) shown in Figure 56. Here, a nonequilibrium VDF (dashed), representative of conditions within a weakly ionized N_2 plasma region, can be compared to an equilibrium VDF (solid), representative of conditions in the equilibrium region behind a shock front. The average specific vibration energy corresponding to the nonequilibrium VDF is approximately equivalent to the specific vibrational energy given by the Equation 73 with a vibrational temperature of $600K$. The nonequilibrium VDF

shown here was calculated by solving the coupled set of rate equations for each vibrational level of N_2 until a steady-state solution was obtained. The calculations were performed using the same vibrational kinetics code discussed in Chapter II [35]. The electron impact excitation of ground state molecules normally present in a weakly ionized plasma was simulated in the rate equations by an excitation rate, $R\,N_0$ (Equation 39), which serves as a pump. This pump promoted ground vibrational state molecules (v=0) to the first excited state (v=1) at a constant frequency (v is the vibrational quantum number). The nonequilibrium VDF in Figure 56 is characterized by a vibrational temperature, T_{vib}^{10}, of $1900K$, where T_{vib}^{10} is based on the relative populations of the v=0 and v=1 state. The calculation assumed gas at a pressure of 760 torr (1 atm) and a gas temperature of $300K$. The equilibrium VDF is a Maxwell-Boltzmann distribution with a characteristic temperature of $804K$, which, by the Rankine-Hugoniot relations, is the gas temperature just behind the shock for a Mach 3 shock in N_2. The maximum amount of energy per molecule which can be extracted from the nonequilibrium VDF and added to the flow is the difference between the average energies of these two distributions. Shocks with higher (lower) Mach numbers will produce higher (lower) post-shock gas temperatures, resulting in equilibrium distributions with a higher (lower) average energy than the one shown in Figure 56. This leads to less (more) vibrational energy added to the flow for a given nonequilibrium VDF. Likewise, higher (lower) pumping rates lead to nonequilibrium VDFs with higher (lower) average energies, which allow more (less) energy to be added to the flow for a given shock velocity.

The maximum amount of energy available for extraction per molecule can be estimated by subtracting the average vibrational energy at equilibrium (approximating the equilibrium gas temperature in the post-shock region as the gas temperature just behind the shock front) from the average steady-state nonequilibrium vibrational energy:

$$\Delta\epsilon = \epsilon_1^{noneq} - \epsilon_2^{eq}, \tag{80}$$

where ϵ^{noneq} is the average energy of the steady-state nonequilibrium vibrational distribution and ϵ^{eq} is the average energy of the equilibrium vibrational distribution. The subscripts 1 and 2 refer to the regions in front of and behind the shock front, respectively. The energy difference calculated from Equation 80 can be normalized by the specific energy initially present in the translational and rotational modes at the post-shock gas temperature (T_2):

$$\epsilon^{thermal} = \frac{1}{\gamma - 1} \frac{k_B T_2}{M}. \tag{81}$$

As stated previously, significant alterations to the flow field are estimated to occur when the amount of energy added to the flow is approximately 10% (or more) of the thermal energy already present in the flow.

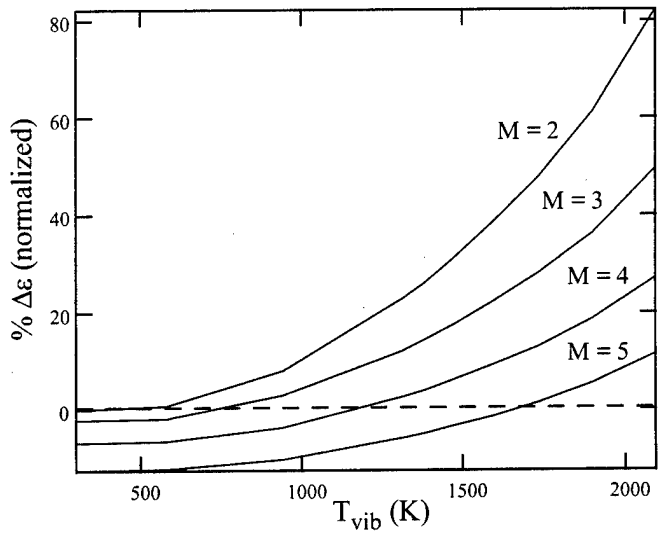

Figure 57. Maximum amount of vibrational energy (estimated) available for release into the post-shock region at four Mach numbers (shown as a % of the thermal energy initially present in the post-shock region). Energy flows from the vibrational modes to translation/rotation for positive values, and from translation/rotation to vibration for negative values.

An estimate of the maximum amount of nonequilibrium vibrational energy available for release into the flow behind a shock has been determined over a range

of conditions which are realistically achievable in a glow discharge plasma (Figure 57). Here, steady-state nonequilibrium VDFs characterized by vibrational temperatures (T_{vib}^{10}) from $300K$ to $2000K$ were calculated in N_2 at a pressure of 1 atm and a gas temperature of $300K$. Positive values indicate that in order to reach equilibrium behind the shock front, energy will flow from the vibrational modes into the translation/rotation modes. Negative values indicate that the reverse is true. As the shock Mach number rises, so does the post-shock equilibrium gas temperature. Thus, what was a vibrational energy source at one Mach number can become a vibrational energy sink at a higher Mach number, all else being equal.

The vibrational energy represented in Figure 57 is the maximum amount of energy available for release at a given T_{vib}^{10} and shock speed. How much of this energy is released depends on the time scale of interest. If the time scale of interest is very long, nearly all of the energy can be released, while if the time scale is short, very little may be released. How much vibrational energy can be released on a given time scale is the subject of the next section.

4.3.2 How Fast Can the Energy Be Released? In shock/plasma experiments conducted to date with molecular gases, the experimental shock tubes are of the order of 1 meter in length. Therefore, for the present analysis, the time scale of interest will be the time it takes a shock of a given velocity to travel a length of 1 meter. How much vibrational energy can be released into the flow during this time depends on the kinetic rates of the vibration-vibration (VV) and vibration-translation (VT) energy exchange processes. The temporal release of nonequilibrium vibrational energy, properly accounting for the VV and VT energy exchange mechanisms, was investigated with the use of the same vibrational kinetics code used previously to calculate the steady-state nonequilibrium VDFs.

A steady-state nonequilibrium vibrational distribution function with realistic parameters was used to represent the vibrational state of the gas in front of the shock

($T_{vib}^{10} = 1900K$, $T_{gas} = 300K$, pressure = 1 atm). The passage of the fluid element across the shock front was simulated by the increase in density and gas temperature consistent with the Mach number of the shock. The increase in density and gas temperature behind the shock lead to an increase in the VT rates, which results in the release of vibrational energy into the flow. The amount of this energy release was tracked throughout the time-dependent calculation, with the result shown in Figure 58 for a Mach 4 shock in N_2. In this case, the maximum amount of vibrational

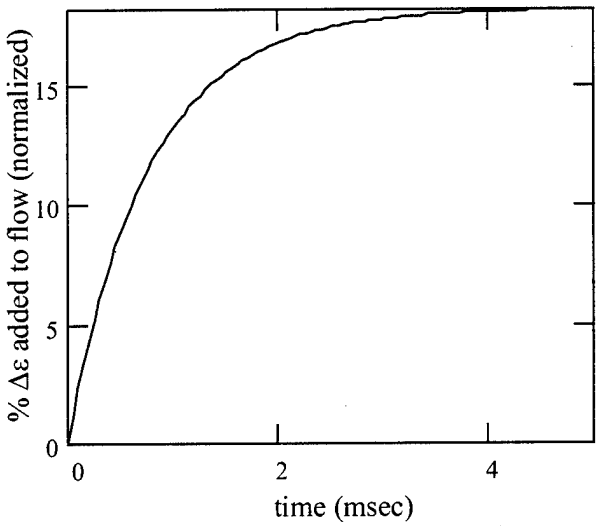

Figure 58. Amount of vibrational energy added to the flow (shown as a % of the thermal energy initially present in the post-shock region) for a Mach 4 shock in N_2. The initial nonequilibrium vibrational distribution ($T_{vib}^{10} = 1900K$) was calculated for a gas at a temperature of $300K$ and a pressure of 1 atm.

energy which can be released into the flow is approximately 18% of the thermal energy initially present in the post-shock region (see Figure 57). A Mach 4 shock (traveling in $300K$ gas) can travel 1 meter in a time of 0.71 msec. In this time, an amount of vibrational energy equal to approximately 10% of the thermal energy initially present in the post-shock region can be released. This is the amount of energy estimated to begin to cause interesting effects in the flow. It is seen from

Figure 58 that, under the present conditions, the maximum amount of energy will be released into the flow in approximately 4 msec.

For a given nonequilibrium vibrational distribution, there appears to be an optimum shock speed which defines the conditions under which the most vibrational energy can be extracted and released into the flow behind a shock. A shock with a low Mach number will take the longest time to traverse a given distance, therefore providing more time during which energy will be extracted from the vibrational manifold. However, the low Mach number also produces low gas temperature and density jumps across the shock front, resulting in a long vibrational relaxation time constant (τ_{eff}), since τ_{eff} is inversely proportional to both density and VT rates (VT rates increase with increasing gas temperature, as shown in Figure 26). Therefore, although more time is available during which energy release can occur, the amount of energy released on the time scale of interest is small. On the other hand, shocks with high Mach numbers will have high density and temperature jumps, resulting in shorter τ_{eff}s and a quicker energy release. However, the higher shock speed means that there will be less time during which the vibrational energy can be extracted. In addition, the higher post-shock temperatures from the fast shocks result in higher initial post-shock thermal energies. Thus, although the vibrational energy can be extracted quickly, its relative contribution to the total thermal energy in the flow may be minor.

4.4 Conclusion

The release of excess vibrational energy in the post-shock region results in increases in the shock speed. Assuming that full equilibration among the various thermal modes (translation, rotation, vibration) is achieved in the post-shock region, an analytic expression has been derived, from which the shock speed in the nonequilibrium region can be determined for a Riemann shock problem. This analytic solution agrees well with results from a numerical solution to Euler's equations,

many of the plasma/shock experiments reported in the literature were conducted in air, this may have been the case. However, while the increased VT rates would reduce the vibrational energy transfer time, they would also reduce the amount of energy contained within the vibrational manifold. So although the vibrational energy could be transferred quicker, there would be less energy to transfer.

To further study the quantitative effects of nonequilibrium vibrational energy transfer, a more detailed fluid approach would be required. In this refined study, each vibrational level should be treated as a separate gas. Taking into account the VV and VT energy exchange processes in this manner would eliminate the need for an effective relaxation time constant (τ), as used in the present analysis. Thus, the variations in flow parameters and shock speed could be more accurately tracked, leading to a more refined assessment of the role of nonequilibrium vibrational relaxation.

Although the focus of this chapter was on post-shock energy addition in the form of nonequilibrium vibrational relaxation, one cannot ignore the fact that the shock phenomena which have been observed in molecular gases have been observed in atomic gases as well ([33], [12] and [41], for example). Since such gases obviously lack vibrational degrees of freedom, some other mechanism must be at work. Although it is true that a weakly ionized plasma in an atomic gas may have processes such as de-excitation of electronic states and recombination ongoing, the low number density of the relevant species argues against these mechanisms being sufficiently strong to account for the observed variations in shock velocity and shock structure.

V. *Thermal Effects*

5.1 Introduction

Anomalous behavior has been observed as a shock propagates through a plasma. This behavior has not been observed when the shock propagates through a homogeneous neutral gas at a fixed temperature. In the shock experiments conducted in a plasma, it is difficult to completely avoid heating of the neutral gas. That is, experimentally it is difficult to create a plasma that does not heat the neutral gas. Alternatively, one could try to heat the gas without creating a plasma (by the use of a hot Ni-Cr wire placed down the tube centerline, for example). However, such attempts may have difficulty in obtaining the same peak temperatures and/or a similar radial temperature profile as observed when the heating is due to the plasma. Another complication possibly introduced by this method is the presence of the associated heating apparatus in the shock tube, which may affect the gas flow and complicate measurements of density, pressure, etc. In an attempt to isolate plasma effects from thermal heating effects, pulsed discharges have been used. These devices produce a plasma over a short temporal duration, with the premise being that the neutral gas temperature doesn't change much during this time. However, difficulties arise in the analysis of such pulsed devices due to the transient nature of the plasma. A steady-state glow discharge is a much simpler system to analyze due to the absence of significant variations in the plasma parameters.

Shock characterization and modification are conveniently classified according to the method of initiating the shock. There are two common methods used to generate a shock. The first uses a classical shock tube arrangement in which a breakable diaphragm separates high and low pressure gas. When the diaphragm is ruptured, the gas flows from high to low pressure, producing a shock in the process. The experimental apparatus which produces a shock in this manner is commonly called a shock tube, while the theoretical analysis of this problem is commonly

called the Riemann (or shock tube) problem [61]. The second method uses a burst of energy to locally heat the gas in a small region of a tube. This heating leads to a local increase in the pressure, which causes the gas to flow to regions of lower pressure. The burst of energy is typically due to the discharge of an electrical capacitor. This method of impulsively generating a shock is called a spark-initiated shock. A typical

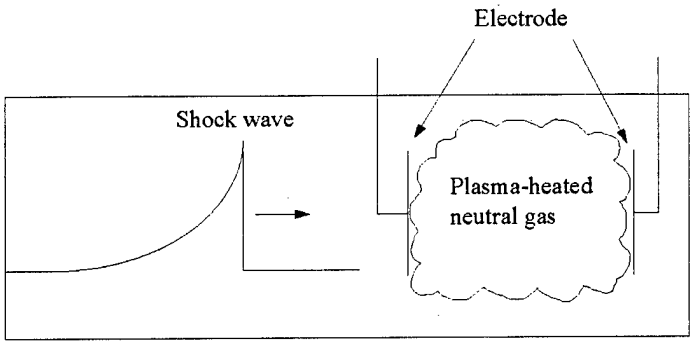

Figure 59. Typical experimental arrangement in which a shock propagates into a plasma-heated gas.

experimental arrangement is shown in Figure 59, in which a shock (produced by a spark discharge, as shown in this example) propagates into a plasma. A steady-state glow discharge of limited spatial extent heats the neutral gas. In general, the temperature of the gas throughout the heated region (and in the absence of a shock) will be a function of position and time (i.e., $T = T(r, \theta, z, t)$, in cylindrical coordinates). In the present analysis, symmetry in the $\hat{\theta}$ direction and steady-state conditions will be assumed, thus $T = T(r, z)$. A shock is produced and propagates for some distance in ambient gas before it enters the region containing the hot gas. Any modifications to the shock due to the presence of thermal inhomogeneities are termed thermal effects. Although the plasma is comprised of ions, electrons and neutral gas particles, the relative fraction of the charged specie are very small. Typical ionization fractions in a glow discharge plasma are in the range $10^{-6} - 10^{-8}$ [98:3] (i.e., approximately one electron/ion pair for every ten million neutral gas particles).

The minority of electrons and ions in the flow was the basis for the conclusion in Chapter III that charged particles have an insignificant effect on the shock.

In this chapter shock modification due to thermal inhomogeneities will be examined using a two-dimensional computational fluid dynamics code written for this purpose. This code simulates both the Riemann problem and the spark-initiated shock problem, each of which has been used in shock propagation experiments involving a plasma. Code details are given in the next section and in Appendix B. Results will be presented which validate this code for both types of problems. The code will then be used to study thermal effects on shock propagation, beginning with a simple thermal discontinuity. A more general class of two-dimensional thermal inhomogeneities is then treated and related to glow discharge conditions. The assessment of thermal effects concludes with simulations of and comparisons to experiments conducted by both Western [46] and Russian ([115], [52]) researchers.

5.2 Model Equations

The model equations used in this analysis are the two-dimensional Euler equations. These four equations (conservation of mass, conservation of $\hat{x}$ momentum, conservation of $\hat{y}$ momentum and conservation of energy) are augmented by a fifth equation in the case of a spark-initiated shock. This last equation is used to describe the physical process of energy from the spark discharge coupling into the neutral gas. This equation governs the temporal and spatial release of energy into the flow, thereby producing a shock wave similar to that produced by a spark source. The form of this equation is very similar to that used to describe either the release of vibrational energy or the detonation of chemical energy in the flow. The latter analogy is adopted as the model describing the generation of a spark-initiated shock. Accordingly, the fifth equation expresses the principal of conservation of chemical energy. In the case of a Riemann (or shock tube) problem the use of a conservation of chemical energy equation is not required.

The equations used to model the flow can be written as [62:69]

$$\frac{\partial \vec{U}}{\partial t} + \frac{\partial \vec{E}}{\partial x} + \frac{\partial \vec{F}}{\partial y} = -\alpha \vec{H} + \beta \vec{Q} \tag{82}$$

where $\vec{U}$ is the vector of conserved quantities, $\vec{E}$ and $\vec{F}$ are flux vectors, $\vec{H}$ is a vector of sources due to axisymmetric geometry and $\vec{Q}$ is a vector of sources describing energy addition to the flow for a spark-initiated shock. Each of these vectors are defined below. The coefficient α is 1 for two-dimensional axisymmetric geometry and 0 for two-dimensional planar geometry, while the coefficient β is 1 for a spark-initiated shock problem and 0 for a Riemann problem. The vector of conserved variables ($\vec{U}$) is defined as

$$\vec{U} = \begin{bmatrix} \rho \\ \rho V_x \\ \rho V_y \\ \rho \left\{ \frac{1}{2} \left(V_x^2 + V_y^2 \right) + \frac{1}{\gamma - 1} \frac{k_B T}{M} \right\} \\ \rho \epsilon_{chem} \end{bmatrix} \tag{83}$$

where ρ is the mass density of the gas, V_x is the flow velocity in the $\hat{x}$ direction, V_y is the flow velocity in the $\hat{y}$ direction, γ is the usual ratio of specific heats, k_B is Boltzmann's constant, T is the gas temperature, M is the mass of the gas particle considered, and ϵ_{chem} is the specific chemical energy to be used in generating a shock in the spark-discharge case. Each of the variables in $\vec{U}$ is a function of x, y and t; i.e., $\rho = \rho(x, y, t)$, $V_x = V_x(x, y, t)$, etc. The flux vectors $\vec{E}$ and $\vec{F}$ are defined as

$$\vec{E} = \begin{bmatrix} \rho V_x \\ \rho \left(V_x^2 + \frac{k_B T}{M} \right) \\ \rho V_x V_y \\ \rho V_x \left\{ \frac{1}{2} \left(V_x^2 + V_y^2 \right) + \frac{\gamma}{\gamma - 1} \frac{k_B T}{M} \right\} \\ \rho \epsilon_{chem} V_x \end{bmatrix} \tag{84}$$

and

$$\vec{F} = \begin{bmatrix} \rho V_y \\ \rho V_x V_y \\ \rho \left(V_y^2 + \frac{k_B T}{M} \right) \\ \rho V_y \left\{ \frac{1}{2} \left(V_x^2 + V_y^2 \right) + \frac{\gamma}{\gamma - 1} \frac{k_B T}{M} \right\} \\ \rho \epsilon_{chem} V_y \end{bmatrix}, \tag{85}$$

the axisymmetric source vector $\vec{H}$ is defined as

$$\vec{H} = \frac{1}{y} \begin{bmatrix} \rho V_y \\ \rho V_x V_y \\ \rho V_y^2 \\ \rho V_y \left\{ \frac{1}{2} \left(V_x^2 + V_y^2 \right) + \frac{\gamma}{\gamma - 1} \frac{k_B T}{M} \right\} \\ \rho \epsilon_{chem} V_y \end{bmatrix} \tag{86}$$

while the vector of sources used for the spark-initiated shock problem is defined as

$$\vec{Q} = \begin{bmatrix} 0 \\ 0 \\ 0 \\ \frac{\rho \epsilon_{chem}}{\tau} \\ -\frac{\rho \epsilon_{chem}}{\tau} \end{bmatrix} \tag{87}$$

where τ governs the temporal release of the chemical energy. The first equation in 82 expresses conservation of mass, the second and third equations describe the conservation of momentum in the $\hat{x}$ and $\hat{y}$ directions, respectively. The fourth equation expresses the conservation of directed kinetic energy and thermal energy, where the former depends on the mass flow velocity and the latter depends on the number of degrees of freedom possessed by the gas particle under consideration and the gas temperature. As an example of the latter, consider an Argon atom ($\gamma = 5/3$) which possesses three degrees of freedom. With $\frac{1}{2} k_B T$ of energy per degree of freedom its

specific thermal energy is $\frac{3}{2}\frac{k_B T}{M}$, which is equivalent to $\frac{1}{\gamma-1}\frac{k_B T}{M}$. The fifth equation in 82 describes the conservation of chemical energy.

These equations were solved using an explicit MacCormack method [82] combined with a flux corrected transport [23] algorithm. Strang-type splitting [109] was used in order to extend the one-dimensional MacCormack algorithm to two-dimensions. The source terms represented by the right hand side of Equation 82 were handled by an implicit method suggested by Yee [120:36]. Further details regarding the numerical solution of Equation 82 are given in Appendix B.

The MacCormack scheme (with second-order accuracy) was chosen due to both its suitability for solving nonlinear Equations [62:192] and its relative programming ease. However, the use of a second-order accurate method by itself would lead to oscillations in the solution near shocks. The FCT method was adopted as a way to get rid of these numerical oscillations by preventing them before they are allowed to grow [61:127]. Of course, other methods could be used to accomplish the same goal (Godunov method, artificial viscosity, etc.), however the MacCormack/FCT method offers stability and sharp resolution for a relatively small effort in coding [112]. Higher-order Godunov schemes like the Roe method produce more accurate solutions than the MacCormack/FCT scheme, however they are more complicated to code and more expensive to run [44:173]. Additionally, the FCT method is more accurate than using artificial viscosity to damp out the oscillations [44:173].

5.3 Code Validation

5.3.1 Riemann Problem. The Riemann problem was solved numerically in two-dimensional planar geometry for a shock tube with a length of 50 cm and a half-width of 2.5 cm. The diaphragm was located at 20 cm with respect to the high pressure end of the tube. The working gas was Argon with an initial pressure ratio (P_4/P_1) and temperature ratio (T_4/T_1) of 10.0 and 1.25, respectively. The two-dimensional calculation was performed on a grid with 401 nodes in the x direction

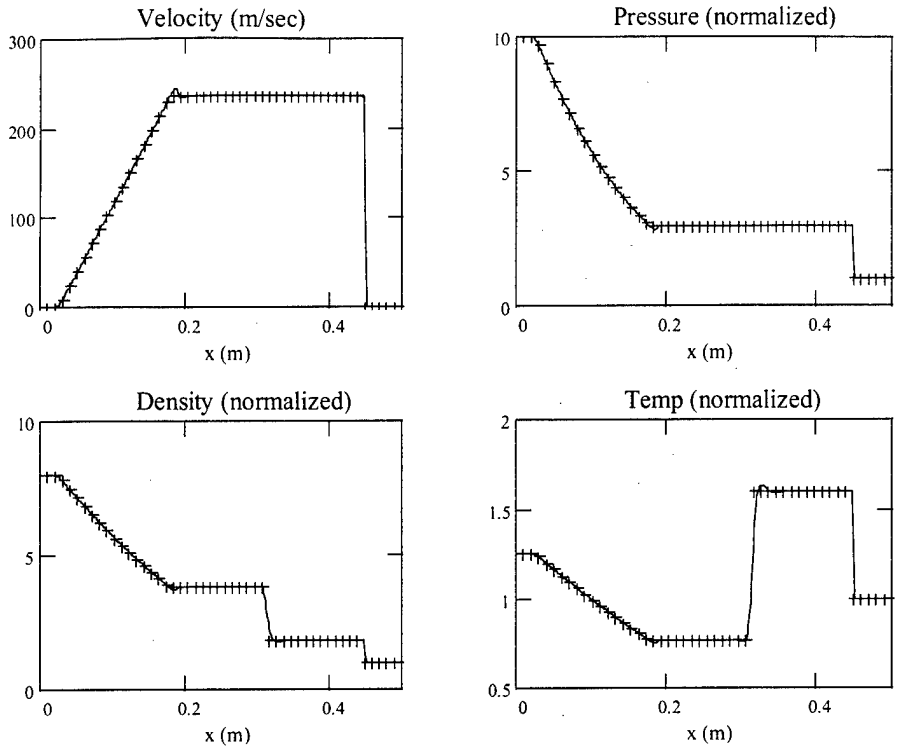

Figure 60. Analytic (+) and numerical (solid curve) solution to the Riemann problem (Argon with $P_4/P_1 = 10.0$, $T_4/T_1 = 1.25$).

(along the tube axis) and 23 nodes in the y direction (across the tube). A comparison between the analytic solution to the Riemann problem (symbols) and the numerical solution to the Euler equations (solid curve) along the shock tube centerline is shown in Figure 60. In this figure, the values of pressure, temperature and density have been normalized to the respective upstream ambient value. The agreement is quite good, with relative errors in the pressure being less than 1% throughout the flow field except at the leading and trailing edges of the expansion fan, near the contact surface and near the shock front. The relative errors in these regions are typically less than 5%, with the relative error at one or two nodes very near the shock front being much higher ($\approx 50\%$). As discussed previously in Chapters III and IV, the higher relative errors near the shock front can be attributed to the MacCormack/FCT method, which smears this region over approximately 3 spatial nodes. In general, the relative

error throughout the physical domain can be reduced by increasing the number of grid nodes in the computational domain, accompanied (of course) by an increase in the computational requirements (memory, CPU time). Increasing the number of nodes does not prevent the MacCormack/FCT method from smearing the shock front region, however, thus the high relative error in one or two bins near the shock front will remain high. [4]

The transverse symmetry of the solution is illustrated in Figure 61, where the full two-dimensional density (top) and pressure (bottom) solutions are shown. The primary features of a Riemann solution are also shown in this figure. In this figure, the tube centerline is along $y = 0$, while the tube wall is along the maximum y coordinate in the domain. The solution is observed to be independent of the transverse position, as it should be in this validation problem. The density and pressure in these plots have been normalized by their respective upstream values.

[4] Again, the barely discernable ripples in the numerical solution in the regions of the expansion fan and contact surface are due to the graphic conversion utility program used and were not present in the raw numerical data.

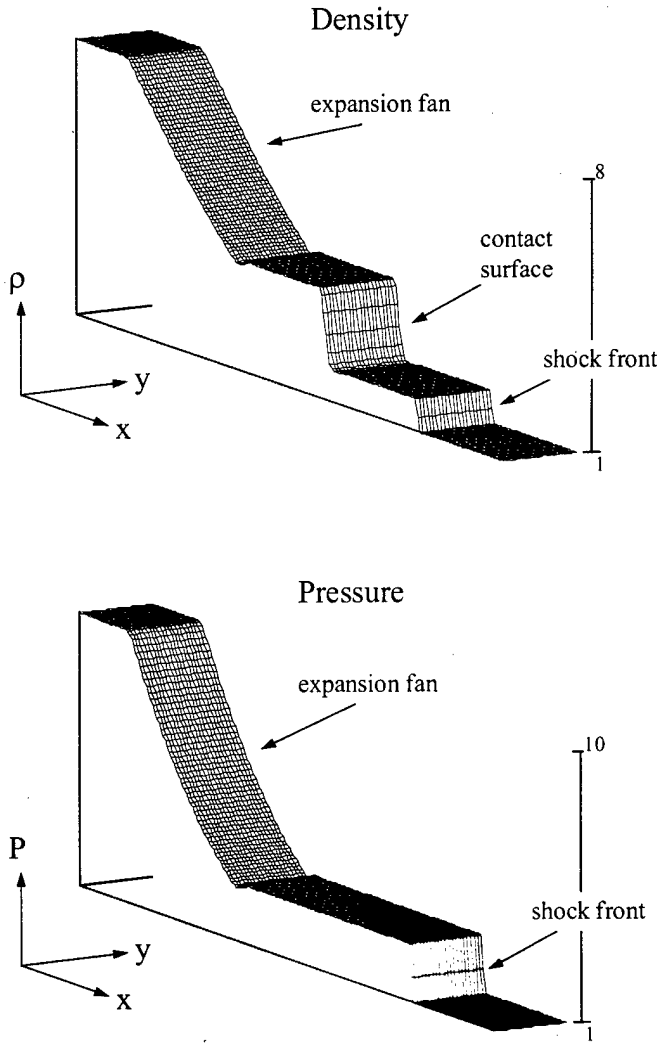

Figure 61. Density (top) and pressure (bottom) from the two-dimensional numerical solution to the Riemann problem (Argon with $P_4/P_1 = 10.0$, $T_4/T_1 = 1.25$). The density and pressure have been normalized to their respective ambient values.

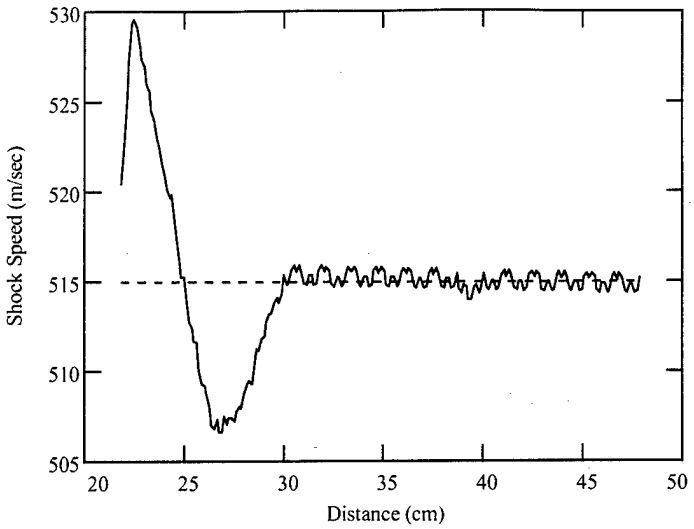

Figure 62. Analytic (dashed) and numerically determined (solid) shock speed along the centerline (Argon with $P_4/P_1 = 10.0$, $T_4/T_1 = 1.25$).

The numerically determined shock velocity can also be compared to the analytic value. This is useful because unlike flow velocity, density, temperature or pressure, the numerical value of the shock velocity is not a direct output of the solution to the fluid equations, as mentioned previously in Chapters III and IV. The shock speed can be determined by the temporal evolution of the shock front position, as described in Appendix B. Figure 62 shows the analytically determined shock speed (straight line) compared to the numerically determined shock speed. The diaphragm is located at 20 cm, so that at time t=0, the shock speed is zero. It is observed that the numerical shock velocity undergoes a transition period (lasting about 200 μsec under the present conditions) during which it speeds up, overshoots, undershoots, then converges to the proper analytic value. The analytic shock speed (under the present conditions) is Mach 1.597, which is approximately equivalent to 515 m/sec when the ambient gas temperature is 300 K. The small oscillations in the shock speed have an amplitude of less than 1 m/sec and are caused (primarily) by the uncertainty with which the position of the shock front is known at any instant in time. That is, the shock front position at any time is known numerically only to

within the spatial resolution of the solution, which is the interval between adjacent nodes.

5.3.2 Spark-Initiated Shock. In the Riemann problem, the existence of an analytic solution provides a useful tool to assess the quality of the numerical solution. In contrast, no analytic solution is known to exist in the case of a spark-initiated shock wave. However, since such initiation techniques have been widely used in the study of shock propagation in plasma, it is necessary to be able to suitably simulate the generation and propagation of a shock wave under such conditions. In this case, the lack of an analytic solution forces a comparison of the numerical solution to experimental observations in order to validate the code. Fortunately, observations of sufficient detail have been made [37] that allow a comparison to take place, at least qualitatively. Although the cited reference lacks many of the specifics necessary for a full quantitative comparison, the general nature and behavior of the reported observations are extremely valuable.

The spark-initiated shock is produced by discharging electrical energy across a spark gap. This energy deposition begins when a sufficiently high voltage breaks down the gas. The resulting plasma completes the electrical circuit and a current flows through the gas (plasma) across the spark gap, heating the gas in the process. As an example, consider an infinitesimal volume of gas. If a current flows through this test volume then the gas is heated, while the number density in the test volume initially remains constant. This results in a rise in the gas pressure within the test volume. Consider another test volume of gas through which no current flows and consequently does not get heated. Between the two test volumes a pressure gradient is created which makes the fluid flow in the direction of lower pressure. If the heating occurs quickly enough, then a pressure gradient is created with sufficient strength to generate a shock wave.

The experimentally measured density distributions of a shock pulse generated by a spark discharge at five instants in time (1.0, 1.7, 2.9, 5.6 and 9.8 μsec corresponding to curves 1, 2, 3, 4 and 5, respectively) are shown in Figure 63 (left), taken from [37]. Notable features of the pulse are the spreading of the shock envelope and the accompanying decrease in amplitude as time increases. The shock velocity is reported to be approximately 2000 m/sec at 'early times' (no specific time is mentioned), with the corresponding temperature in the central region to be approximately 40,000 K. In the experimental device of [37] a capacitor is used to store the electrical energy prior to its release. This capacitor (0.25 μf) is charged to a voltage of 10 KV, resulting in an energy release of 12.5 Joules. The results of a

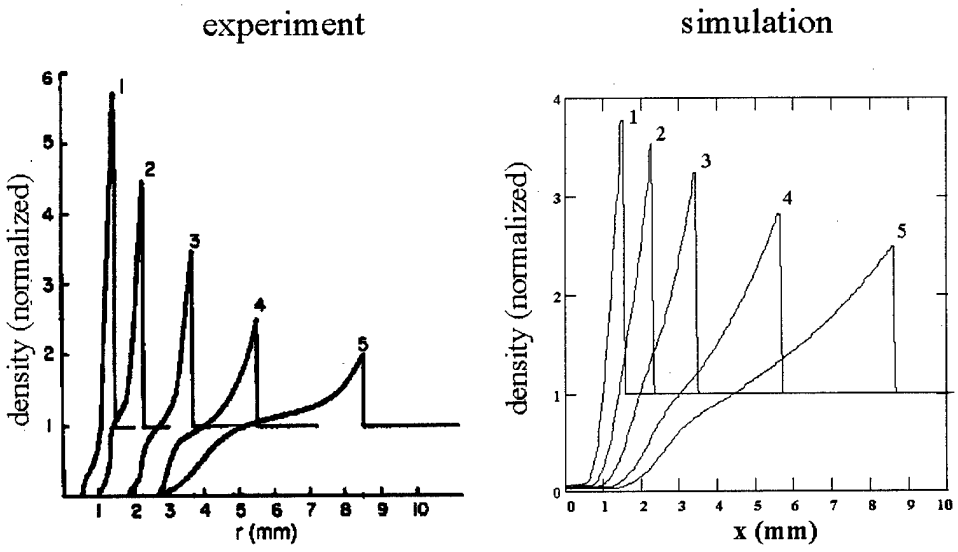

Figure 63. Spark-initiated shock density profile: experiment (left, from [37]) and simulation (right)

numerical calculation simulating a spark-initiated shock pulse are shown in Figure 63 (right). The calculation times for the simulation correspond to the times in the experiment. Although the numerical simulation does not reproduce the experimental density measurements exactly, the general behavior of the shock pulse is in fair agreement with measurements. The numerical simulation generates a shock pulse

whose amplitude decreases, and whose pulse width increases with time, consistent with experimental observations.

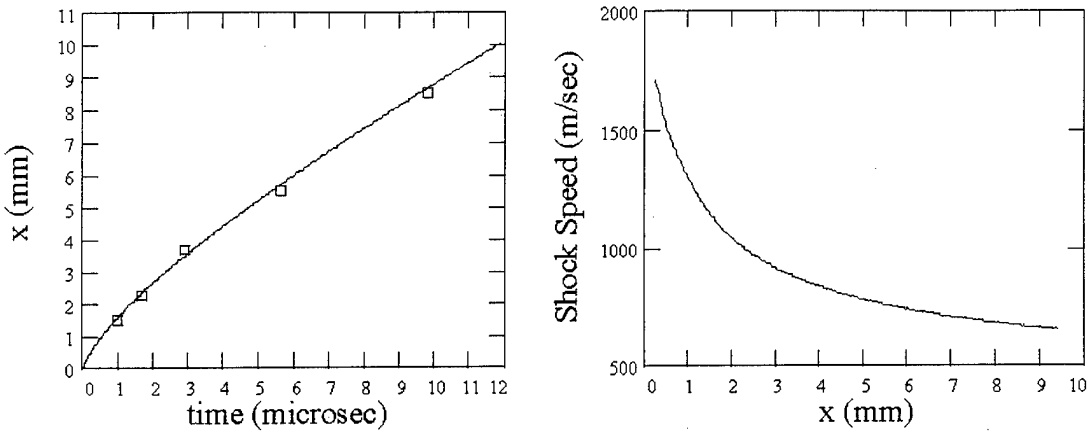

Figure 64. Variation of shock front position with time (left) from experiment (boxes) and from simulation (solid). Shock front speed (right) from simulation.

The position of the shock front as a function of time also closely replicates the observed data (Figure 64 (left)). The slope of this curve at any point in space (time) is the velocity of the shock at that same point in space (time). The simulated shock velocity is shown in Figure 64 (right) as a function of position. At a time of 0.15 μsec, the simulation predicts a shock velocity of 1700 m/sec and a temperature at the origin of 40,460 K, both in good agreement with reported values. The numerical simulation used an energy release of 3.92 Joules (assuming a tube radius of 10 cm), which is nearly a factor of three less than the energy released in the experiment. However, this difference might be explained by the difference in pressures between the simulation and experiment (30 torr in the simulation compared to an unknown pressure in the experiment) or by a different shock tube radius (which was not reported). Furthermore, some of the 12.5 Joules released in the experiment is lost due to radiation and does not heat the gas. Nevertheless, the favorable comparison

between the simulation and the experiment lead to the conclusion that the present numerical method used to generate and propagate a shock pulse is representative of spark-initiated shocks reported in the literature.

In addition to the validation tests discussed previously, in which the gas flow was primarily along the computational grid lines (both Riemann and spark-initiated spark problems), the code's ability to handle flows in general directions was tested. In these tests, a square computational grid comprised of 151 nodes in each direction (x, y) was used to simulate a physical domain of 10 cm by 10 cm. Both small-amplitude and large-amplitude pressure disturbances were generated at the center of the domain, simulating point explosions of various strengths. In the former case, acoustic disturbances were observed to propagate radially outward from the center in all directions at nearly equal velocities (within 3% of the acoustic velocity). Pressure contours for this simulation are shown in Figure 65. Here, the small-amplitude wave has propagated for a time of 1.188^{-4} sec in Argon at an ambient temperature of $300K$. Although the physical domain was represented on a Cartesian grid, the resulting pressure contours are nearly circular, indicating the pressure disturbances propagate at nearly equal velocities in all directions. If the pressure disturbance originating at the origin is large, shock waves will form. For this case, shock waves were also observed to propagate radially outward from the center in all directions, at (again) nearly equal velocities (a 3% spread in shock velocities was noted). In both cases, the slowest signal propagation speed occurred in angular directions that were at 45 degrees relative to the computational grid lines.

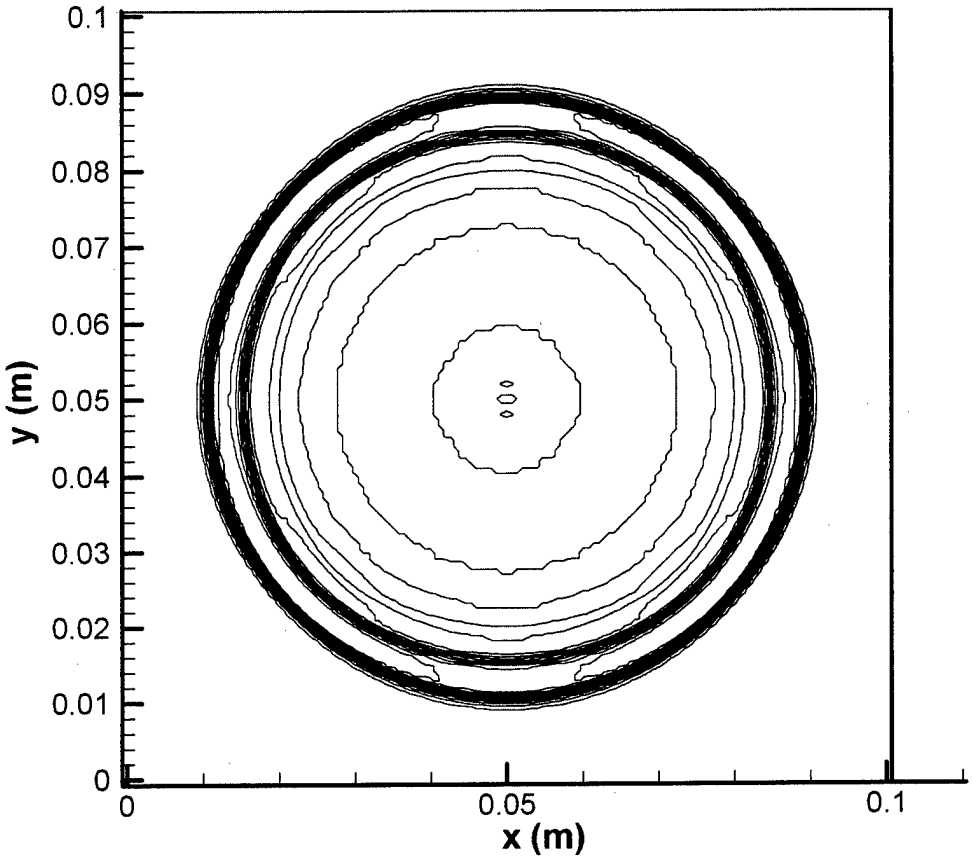

Figure 65. Pressure contours resulting from the propagation of a small-amplitude wave originating from the center of the domain ($x = 0.05$, $y = 0.05$). The velocity of the leading edge of the pressure disturbance in any direction is within 3% of the speed of sound.

5.4 Step Temperature Rise

A sharp discontinuity in the temperature offers the simplest example of the effects of a thermal inhomogeneity on shock characteristics. In this section, an infinite planar interface will be considered which separates gas 1 at a temperature T_1 from gas 2 at a temperature T_2. The ratio of the heat capacity at constant pressure (C_p) to the heat capacity at constant volume (C_v) (also known as the adiabatic exponent) will be denoted as γ_1 for gas 1 and γ_2 for gas 2. A shock will be propagated from gas 1 through the thermal discontinuity into gas 2, with the resulting modifications to the shock characteristics to be examined. Two cases will be considered. The first is for the case in which $T_2 > T_1$, while the second is for the case in which the inequality is reversed. The former case leads to transmitted shock and a reflected rarefaction wave, while the latter case leads to both a transmitted and reflected shock [118:78].

5.4.1 Riemann Problem.

5.4.1.1 Reflected Rarefaction Wave. A comparison of the calculated pressure and density profiles obtained for the case in which $T_1 = 300K$ and $T_2 = 600K$ (solid) and the exact Riemann solution in which $T_1 = T_2 = 300K$ (dashed) at the same instant in time is shown in Figures 66 and 67. The interface between T_2 and T_1 was initially located at x=35 cm. Although a heated region exists on the low pressure side of the shock tube, the pressure remains constant in this region (upstream of the shock front). This is representative of the steady-state condition in a glow discharge in which the pressure is maintained constant throughout the tube, although the heated gas in the plasma region may occupy only a small part of the tube. The relative positions of the two shock fronts indicate that the shock velocity in the heated case is higher than the nominal shock velocity.

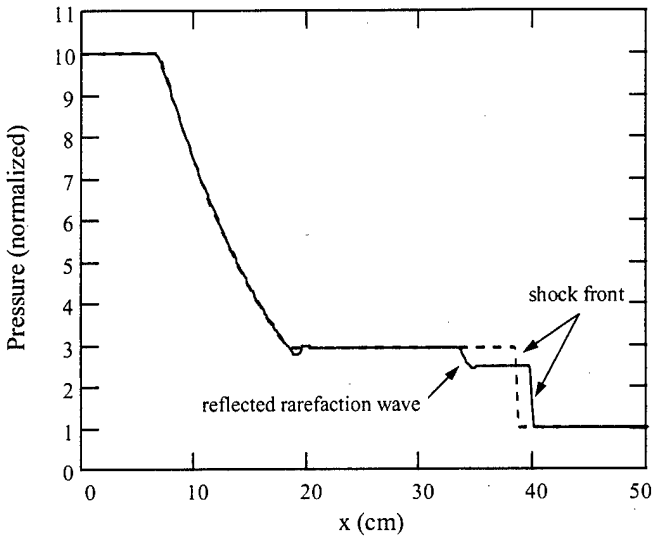

Figure 66. Pressure distribution for a Riemann shock propagating into gas with a step rise in temperature (solid) and exact solution for gas at room temperature (dashed). The heated region starts at $x = 35$ cm.

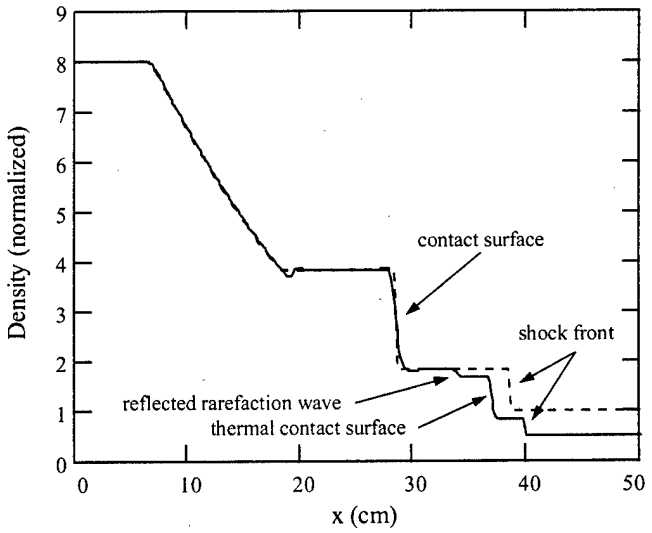

Figure 67. Density distribution for a Riemann shock propagating into gas with a step rise in temperature (solid) and exact solution for gas at room temperature (dashed). The heated region starts at $x = 35$ cm.

A comparison between the nominal Riemann solution and the solution in the present case reveals additional structure in the pressure and density profiles as the shock propagates into the heated gas. These structures are the reflected rarefaction wave and the thermal contact surface. The rarefaction wave has reflected off the thermal interface and is traveling to the left. The thermal contact surface separates gas that was initially on the left side of the thermal interface from the gas that was initially on the right side of the thermal interface, and travels to the right. This is analogous to the contact surface that forms in a Riemann shock, which separates gas initially on the left side of the diaphragm from the gas initially on the right side of the diaphragm. The thermal contact is not observed in the pressure plot, just as the contact surface is not present in the pressure plot. The thermal contact surface travels to the right, although at a lower velocity than the shock front velocity. Note that both the pressure and density jump at the shock front (P_2/P_1 and ρ_2/ρ_1, respectively) are lower in the heated gas than in the nominal case. This is due to the lower Mach number of the shock in the heated gas. The gas between the left end of the shock tube and the rarefaction wave hasn't felt the influence of the thermal discontinuity, so the numerical solution in this region agrees with the analytical solution (with a slight deviation near the location of the diaphragm, x=0.2).

The increase in the shock front velocity as the shock propagates into the heated region is shown in Figure 68. This figure also shows the analytic values of the shock velocity for both the nominal (dotted) and heated gas (dashed) case. The Mach number in the nominal case is 1.597 (515 m/sec), while in the heated case (solution to equation 44) the Mach number is 1.492 (675 m/sec). The numerically determined shock speed closely follows the analytical predictions.

The pressure ratio at the shock front (P_2/P_1), as determined by the code, is shown in Figure 69. The analytic values of the pressure ratio for both the nominal (2.94) and heated gas case (2.49) are also shown. The agreement between the

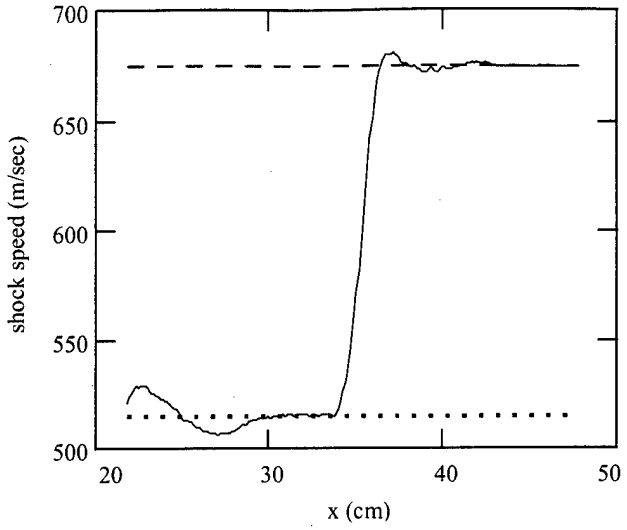

Figure 68. Variation in the shock velocity as a Riemann shock propagates through gas with a step rise in temperature (solid). The analytic shock velocities calculated for gas at $300K$ (dotted) and for a thermal jump to $600K$ (dashed) are also shown. The heated region begins at $x = 35$ cm.

numerical solution and the analytic predictions serve as another indication that the code is performing satisfactorily.

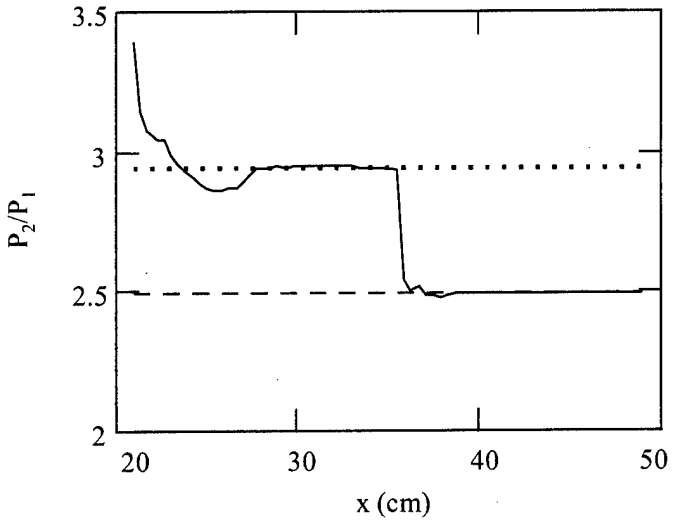

Figure 69. Variation in pressure ratio at the shock front (P_2/P_1) as a Riemann shock propagates through gas with a step rise in temperature (solid). The analytic P_2/P_1 ratios for gas at $300K$ (dotted) and for a thermal jump to $600K$ (dashed) are also shown. The heated region begins at $x = 35$ cm.

5.4.1.2 Reflected Shock Wave. A comparison between the solution obtained for the case in which $T_1 = 600K$ and $T_2 = 300K$ and the nominal Riemann solution at the same instant in time is shown in Figures 70 and 71. The thermal interface is located at $x = 35$ cm, as in the reflected rarefaction case. The relative positions of the shock fronts in the two cases indicate that the shock velocity in the cooled region is lower than the nominal shock velocity. This is shown explicitly in Figure 72. The analytic values of the shock velocity for both the nominal (515 m/sec) and cooled gas case (392 m/sec) are also shown. In contrast to the case in which $T_2 > T_1$ (leading to a reflected rarefaction), the case in which $T_2 < T_1$ leads to a reflected shock. This reflected shock travels to the left, while the original shock is transmitted through the thermal interface and travels to the right. The gas to the left of the reflected shock has not yet been influenced by the presence of the thermal interface, thus the numerical solution agrees with the analytic Riemann solution in this region. Note that the pressure and density jumps at the shock front are greater in the cool gas than in the nominal case. This is a direct result of the higher Mach number of the shock in the cool gas, even though the shock front velocity is lower in the cool gas as compared to the constant temperature case. The Mach number of the shock in the nominal case is 1.597, while in the cool gas the Mach number is 1.721 (solution to equation 1). The pressure ratio at the shock front (P_2/P_1), as determined by the code, is shown in Figure 73. This pressure ratio increases as soon as the shock front enters the cool gas region, due to the higher Mach number of the shock in this same region. The analytic values of the pressure ratio for both the nominal (2.94) and cooled gas case (3.45) are also shown in this figure.

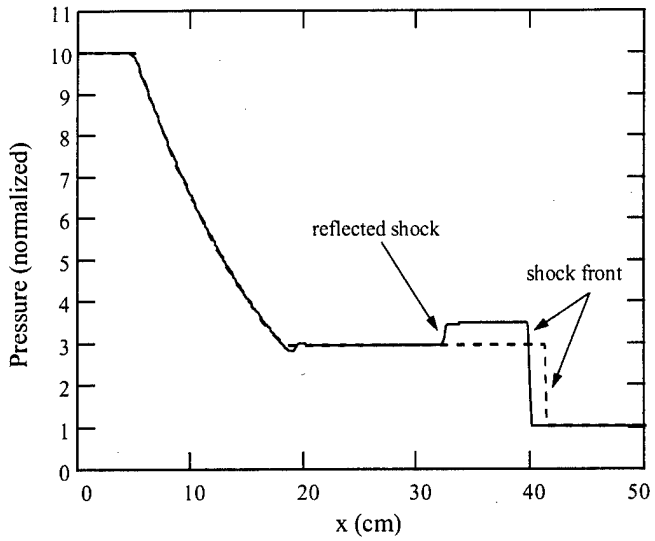

Figure 70. Pressure distribution for a Riemann shock propagating into gas with a step decrease in temperature (solid) and exact solution for gas at $600K$ (dashed). The cooled region starts at $x = 35$ cm.

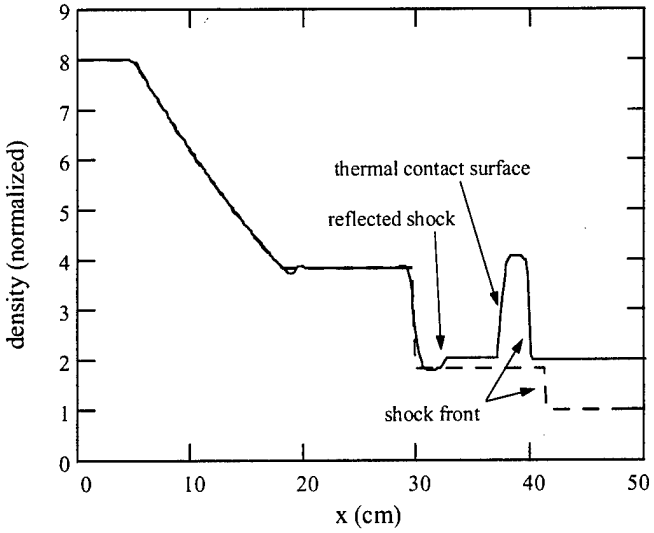

Figure 71. Density distribution for a Riemann shock propagating into gas with a step decrease in temperature (solid) and exact solution for gas at $600K$ (dashed). The cooled region starts at $x = 35$ cm.

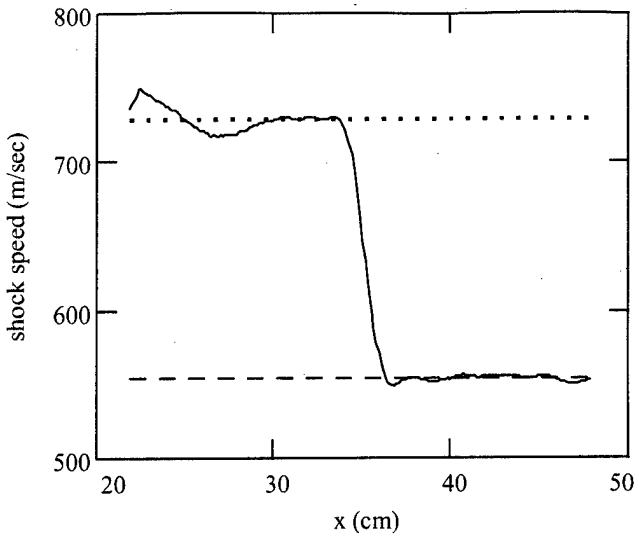

Figure 72. Variation in the shock velocity as a Riemann shock propagates through gas with a step decrease in temperature (solid). The analytic shock velocities calculated for gas at $600K$ (dotted) and for a thermal jump to $300K$ (dashed) are also shown. The heated region begins at $x = 35$ cm

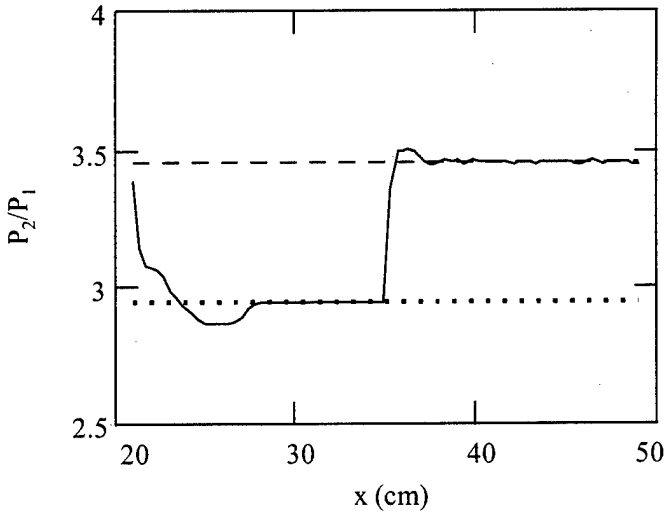

Figure 73. Variation in pressure ratio at the shock front (P_2/P_1) as a Riemann shock propagates through gas with a step decrease in temperature (solid). The analytic P_2/P_1 ratios for gas at $600K$ (dotted) and for a thermal jump to $300K$ (dashed) are also shown. The heated region begins at $x = 35$ cm.

5.4.2 Spark-Initiated Shock. In the previous section, the effect of a simple planar thermal interface on a Riemann shock wave was evaluated for two cases: $T_2 > T_1$ and $T_2 < T_1$. The former case led to an increase in the shock speed and the formation of a reflected rarefaction wave, while the latter case led to a decrease in the shock speed and the formation of a reflected shock wave. Here, attention is focused on a spark-initiated shock for the case in which $T_2 > T_1$, thus an increase in shock velocity and the formation of a reflected rarefaction wave are anticipated.

The structure resulting from a spark-initiated shock propagating into a heated region is shown in Figures 74 and 75. The shock was generated by simulation of a release of energy from a spark source located at the origin. The thermal interface was initially located at $x = 20$ cm with the temperature in the heated region (T_2) being $600K$ and the temperature in the ambient region (T_1) being $300K$. The shock pressure and density profiles obtained as the shock propagates through gas at a uniform temperature of $300K$, calculated for the same time, are also shown (dashed). The additional structure in the pressure and density profiles are analogous to that previously discussed in the Riemann example. The reflected rarefaction wave is clearly discernible, as is the thermal contact surface and transmitted shock front. The reflected rarefaction wave travels to the left, while the thermal contact surface and shock front travel to the right.

The computed variation of the shock front velocity with distance corresponding to the nominal and heated gas cases is depicted in Figure 76. Prior to the shock entering the heated region the computed shock velocities are identical. As the shock enters the heated region it accelerates to a new velocity. This new velocity is a solution to Equation 44, where the relevant entrance velocity (M_1) is the velocity of the shock just as it enters the heated region (approximately 520 m/sec in this example). This is an important distinction between the Riemann shock (which maintains a constant velocity in the absence of a thermal interface) and the spark-initiated shock (which continues to slow down as it propagates). Thus the velocity

of the spark-initiated shock initially decreases as it propagates away from the origin, speeds up as it enters the heated region, then continues to slow down as it propagates further down the tube.

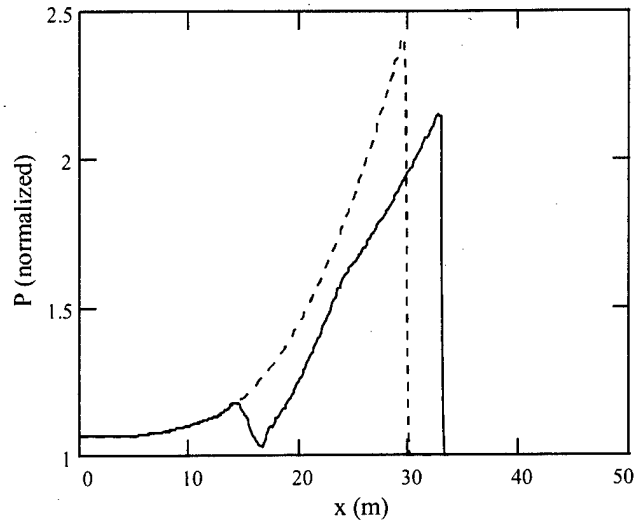

Figure 74. Pressure distribution for a spark-initiated shock propagating into gas with a step rise in temperature (solid) and into gas at room temperature (dashed). The heated region starts at $x = 20$ cm.

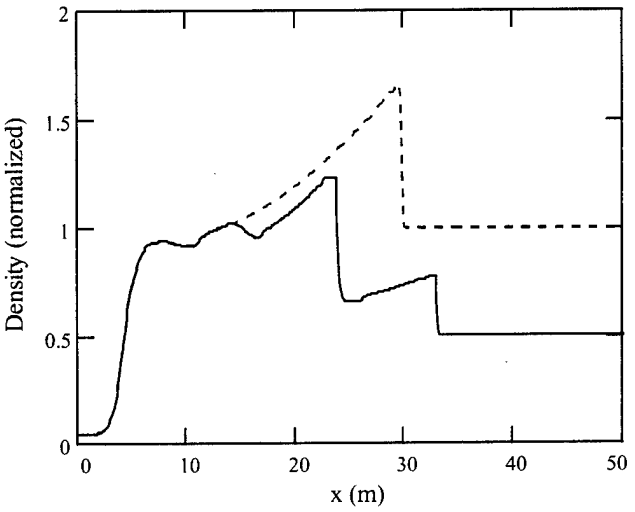

Figure 75. Density distribution for a spark-shock propagating into gas with a step rise in temperature (solid) and into gas at room temperature (dashed). The heated region starts at $x = 20$ cm.

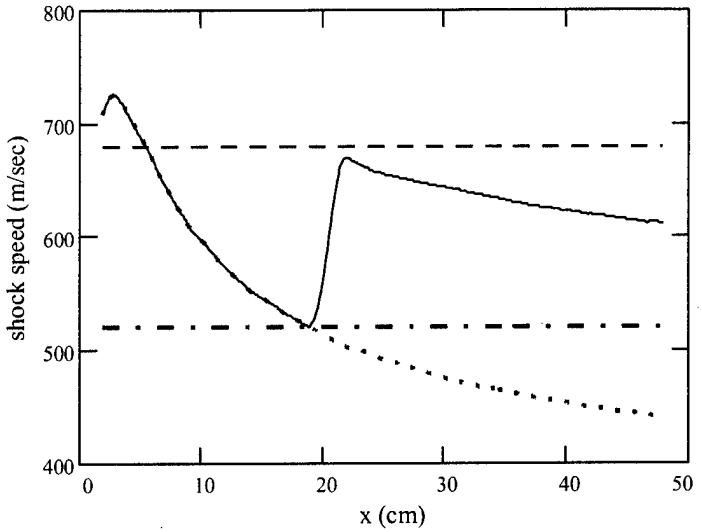

Figure 76. Variation in shock speed as a spark-initiated shock propagates through gas at $300K$ (dotted) and through a gas with a step increase in temperature (solid). The velocity of the shock as it enters the heated region (dot-dash) and the resulting solution of equation 44 (with $T_2 = 600K$) (dash) are also shown. The heated region begins at $x = 20$ cm

5.5 *Radial Temperature Profile*

In the previous section a step increase (or decrease) in temperature was considered in which the change occurred at the same longitudinal coordinate in the shock tube for every transverse location. In this section a transverse thermal profile will be introduced in which the gas temperature maximum will be along the centerline and decrease monotonically to the wall temperature. The temperature profile will be discontinuous in the direction parallel to the shock tube axis at the point x_0, as in the previous examples. A prototypical temperature profile will be used, in which

$$T(x,y) = \begin{cases} T_0, & \text{if } x < x_0 \\ T_0 + T_1 \, Cos\left(\frac{y}{Y}\frac{\pi}{2}\right), & \text{if } x \geq x_0 \end{cases} \tag{88}$$

where x is the axial coordinate, y is the transverse coordinate (in either axisymmetric or planar geometry), Y is either the shock tube radius (in axisymmetric geometry) or the half-width (planar geometry) and T_0 is the ambient temperature. Since the temperature in the heated region will always be greater than or equal to the ambient temperature, reflected rarefaction waves will form, as opposed to the formation of reflected shocks when the inequality is reversed. Propagation characteristics and shock structure for both Riemann and spark-initiated shocks will be addressed.

5.5.1 Riemann Problem. In this section, the assumed temperature profile as given by Equation 88 (with $T_0 = 300K$, $T_1 = 300K$ and $x_0 = 35$ cm) will be applied to a Riemann problem in planar geometry, and the resulting shock structure in the heated region will be examined. The imaginary diaphragm within the shock tube was located at $x = 20$ cm, with the tube having a length of 50 cm and a half-width of 2.5 cm. The initial pressure (P_4/P_1) and temperature (T_4/T_1) ratios were 10.0 and 1.25, respectively. Until the moment the shock front enters the heated region, the shock characteristics are given by the standard Riemann solution. Beyond this point, modifications to the shock structure become quickly evident. The variation

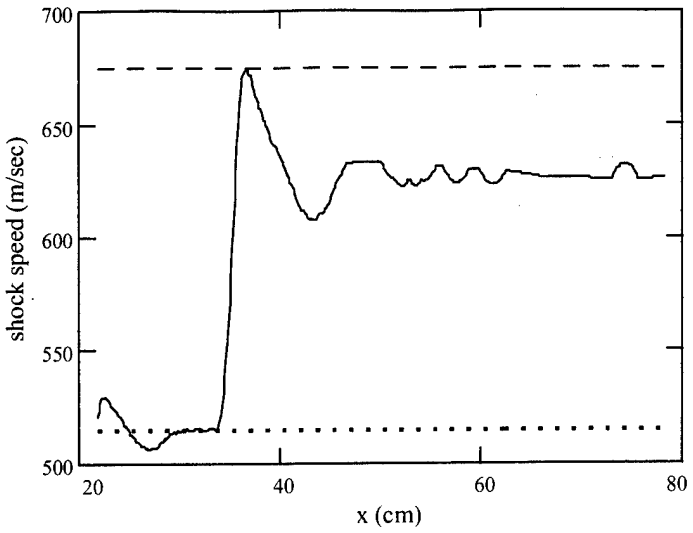

Figure 77. Variation in the centerline shock velocity as a Riemann shock propagates through a region with a radial thermal inhomogeneity (Equation 88) (solid). The analytic shock velocities calculated for gas at $300K$ (dotted) and a thermal jump to $600K$ (dashed) are also shown. The heated region begins at $x = 35$ cm.

in the shock front velocity along the centerline is shown in Figure 77 (curve 1). The analytic shock velocity obtained for the Riemann problem in the absence of a heated region, 515 m/sec (curve 2), and the solution to Equation 44 (with $T_1 = 300K$, $T_2 = 600K$, and $M_1 = 1.597$), 675 m/sec (curve 3), are also shown. After an initial transient, the shock velocity converges to the analytic value in the region where the gas temperature is $300K$, then rises steeply at the onset of the heated region, attaining the velocity corresponding to the peak temperature jump. The centerline shock velocity then slows down, during which time the shock velocity near the wall increases. The apparent ringing (or oscillation) in the shock velocity damps out at longer propagation distances, as the figure shows (note: the shock tube was lengthened to 70 cm for this calculation in order to allow the shock velocity reach a quasi-steady value).

The initially planar shock front begins to distort the moment the shock hits the heated region. The portion of the shock near the centerline of the tube travels

through gas with a higher temperature than the portion of the shock near the tube walls. As a result, the shock velocity near the centerline is initially higher than the shock velocity near the wall. The corresponding Mach number of the shock near the centerline is lower than the Mach number of the shock near the wall. As soon as the shock front is distorted, a pressure gradient in the transverse direction arises which attempts to lessen this distortion. This leads to a slowing down of the shock front along the centerline and a speeding up of the shock front along the wall.

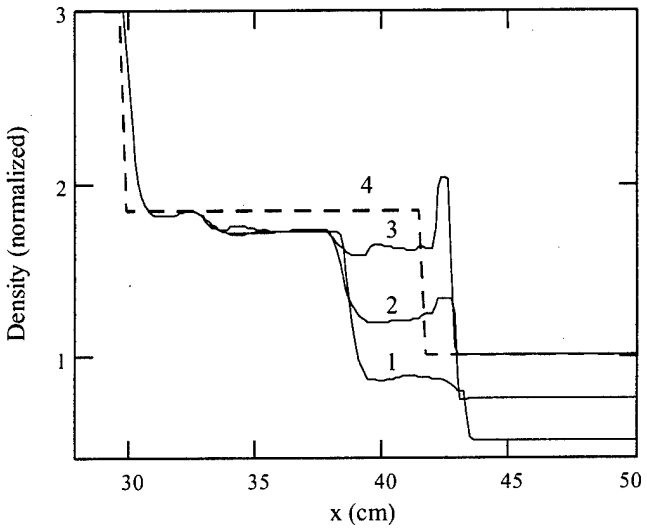

Figure 78. Density profiles near the shock front for a Riemann shock propagating into a region with a radial thermal inhomogeneity (equation 88) along the centerline (1), 3/4 of the distance to the wall (2) and along the wall (3). The analytic solution for gas at a uniform temperature of $300K$ at the same instant in time (4) is also shown (Argon with $P_4/P_1 = 10.0$, $T_4/T_1 = 1.25$).

Density profiles in the shock front region are shown in Figure 78 for three cuts down the shock tube: along the centerline (curve 1), 3/4 of the way to the wall (curve 2) and along the tube wall (curve 3). The analytic Riemann solution (curve 4) calculated for the same time as the other three curves (366 μsec), but in the absence of a heated region is also shown. A rarefaction wave can be seen at approximately $x = 34$ cm. This rarefaction wave has reflected off the thermal interface and is

traveling to the left. The shock fronts of each of the three curves are located ahead of the analytic solution, indicating that the shock velocity at each of these points is greater than the nominal shock velocity. Note that the shock fronts in the heated region (curves 1, 2 and 3) are not aligned with each other, indicating the shock front is no longer planar, but curved. The sudden rise in the calculated density profiles near $x = 30$ cm is due to the arrival of the contact surface, which is a characteristic feature of the Riemann solution.

The full two-dimensional planar solution for both density (top) and pressure (bottom) are shown in Figure 79 at a time of 420 μsec. In this figure, the centerline of the tube is to the left with the wall to the right. Both the density and pressure have been normalized to their respective ambient (unheated) values on the low pressure side of the diaphragm. Some features of the present solution are similar to the standard Riemann solution obtained previously (Figure 61), in which a heated region was not present. In addition, the present solution has similarities to the solution obtained when a step increase in temperature was present (Figures 66 and 67). At the shock front both the density and pressure jumps are lower on the centerline as compared to portions of the shock front closer to the wall. Both the normal contact surface and the thermal contact surface are clearly seen in the density field. The pressure is relatively constant in this region, except for the rarefaction wave which is clearly discernible. These observations are consistent with the one-dimensional results obtained previously. In front of the shock the pressure is constant, while the density varies transversely in an inverse cosine fashion, with the minimum density on the centerline (where the temperature is a maximum) and the maximum density at the wall (where the temperature is a minimum). In the shock front region, a local pressure maximum is observed at the wall, consistent with previous theoretical results of a shock propagating through a radial thermal inhomogeneity [115:473]. A local pressure minimum occurs near the centerline.

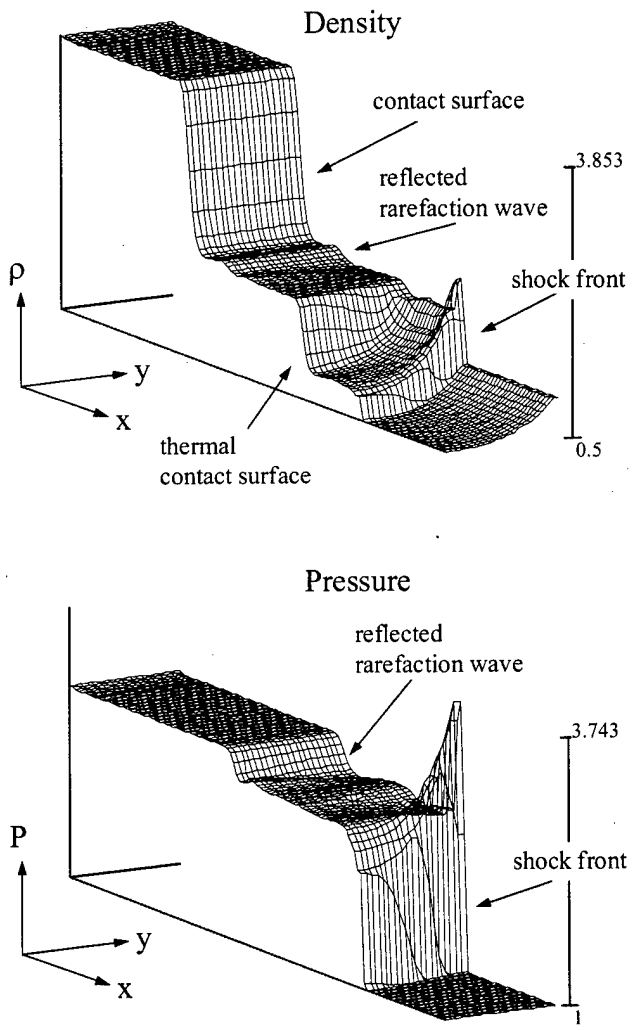

Figure 79. Density (top) and pressure (bottom) in a Riemann shock propagating into a region with a radial thermal inhomogeneity (equation 88). The expansion fan is not shown. (Argon with $P_4/P_1 = 10.0$, $T_4/T_1 = 1.25$).

The transverse variation of the peak pressure in the shock front region is understandable when one considers the transverse variation in the shock Mach number and the Rankine-Hugoniot relation governing the pressure jump at a shock front. The shock velocity at every transverse position along the shock front was nearly constant at the time these distributions were calculated. Therefore, the Mach number at every transverse location will be determined by the local gas temperature at that same point. Since the temperature along the centerline is a maximum, the shock Mach number along the centerline is a minimum. Conversely, the shock Mach number along the wall is a maximum since the temperature along the wall is a minimum. The Rankine-Hugoniot pressure relation then predicts that the pressure jump on the centerline must be a minimum and the pressure jump along the wall must be a maximum.

It was previously mentioned that the initially planar shock front distorts as the shock propagates into a region of gas with a radial thermal gradient. This distortion (or curvature) of the shock front does not continue unabated as the shock propagates, but reaches a quasi-stationary state in which the curvature appears to be relatively constant. This is consistent with previous numerical results [115:474]. The curvature of the shock front is most easily seen in plots of the pressure contours, as shown in Figure 80, corresponding to the pressure surface plot shown in Figure 79. The pressure peak in the shock front region observed in the surface plot is located in the upper right hand corner of Figure 80, indicated by the closeness of the contour curves.

Although the shock front shown in Figure 80 is clearly curved, it is less than one might imagine. As a comparison, Figure 81 shows pressure contours calculated under nearly identical conditions. In this figure the portion of the fluid dynamics code that integrates the Euler equations in the transverse direction (transverse coupling) was turned off. Without transverse coupling, the code is solving separate, uncoupled one-dimensional Riemann problems where each shock propagates into a region with

a temperature increase of differing magnitude (Equation 88). The amount of curvature in this case is much greater than the case in which the transverse coupling is allowed (the normal computational fluid dynamics mode). Additionally, the shock front curvature calculated with transverse coupling is relatively constant as the shock propagates, while the curvature calculated without transverse coupling will continue to increase as the shock propagates. In the normal computational mode, the transverse pressure gradient created by the shock curvature essentially acts as a source term in the Euler equations, seeking to equalize the pressure, density and velocity along the $\hat{y}$ direction in an effort to make the shock front planar.

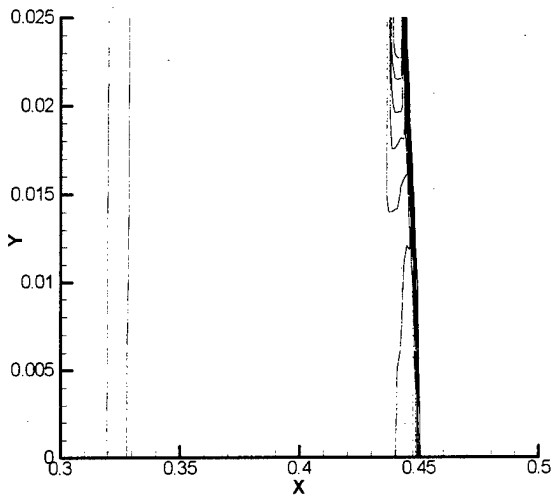

Figure 80. Pressure contours near the shock front for a Riemann shock propagating into a heated zone (equation 88) with transverse coupling.

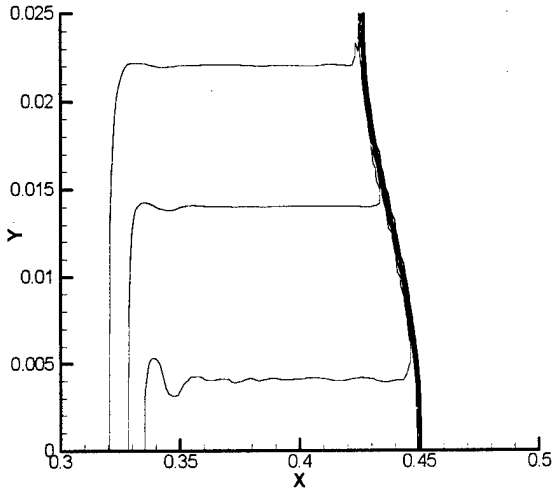

Figure 81. Pressure contours near the shock front for a Riemann shock propagating into a heated zone (equation 88) without transverse coupling.

5.5.2 Spark-Initiated Shock. In this section, the assumed temperature profile as given by Equation 88 (with $T_0 = 300K$, $T_1 = 300K$ and $x_0 = 20$ cm) will be applied to an impulsively generated shock and the resulting shock structure in the heated region will be examined. As in the examples considered previously, the shock tube used here has a length of 50 cm and a half-width of 2.5 cm.

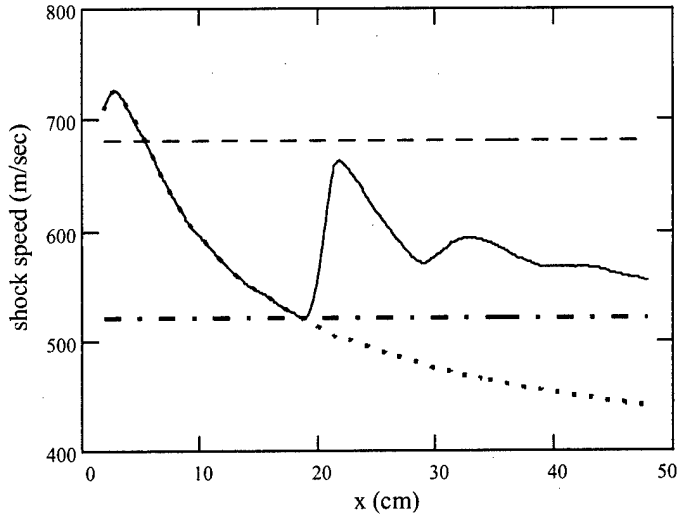

Figure 82. Variation in shock speed as a spark-initiated shock propagates through gas at room temperature (dotted) and through a region with a radial thermal inhomogeneity (equation 88) (solid). The velocity of the shock as it enters the heated region (dot-dashed) and the resulting solution of equation 44 (with $T_2 = 600K$) (dashed) are also shown.

The computed shock velocity along the tube centerline as the shock propagates through a gas with a radial temperature gradient (Equation 88) is shown in Figure 82 (curve 2). The variation of the shock velocity in the absence of a heated region is shown for comparison (curve 1). Before entering the heated region, the two shock velocities are the same, with the velocity just before entering the heated region approximately 520 m/sec (curve 3). Upon entering the heated region, the shock front quickly accelerates to a new velocity, but does not exceed 680 m/sec, the maximum predicted velocity (curve 4). This maximum velocity was calculated based on the solution to equation 44 (with $T_2 = 600K$ and $V_1 = 520$ m/sec). Note that the shock

velocity does not attain a constant value, as it did in the Riemann case presented previously, although the oscillation exhibited in the Riemann case is still present.

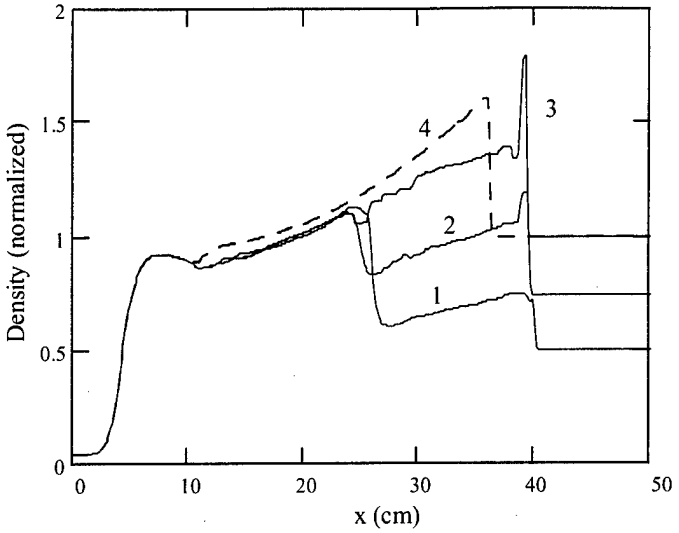

Figure 83. Density profiles as a spark-initiated shock propagates through a gas with a radial thermal inhomogeneity (equation 88) along the centerline (1), 3/4 of the distance to the wall (2) and along the wall (3). The solution for gas at a uniform temperature of $300K$ at the same instant in time (4) is also shown.

The longitudinal density profile corresponding to the present case is shown in Figure 83 for points along the centerline (1), 3/4 of the distance to the wall (2) and along the wall (3). The density profile computed at the same time for the case in which the shock propagates through room temperature gas (4) is shown for comparison. The shock fronts corresponding to the heated case have propagated further than the shock front corresponding to the room temperature case, indicating the higher shock velocity when the gas is hot. The shock front along the centerline is slightly displaced from the other shock fronts in the heated case, indicating a slight curvature in the shock front region. The reflected rarefaction wave is clearly visible, as is also the thermal contact surface.

The full density (top) and pressure (bottom) profiles are shown in Figure 84 for the case in which the gas is heated according to Equation 88. In front of the shock, the

pressure is constant while the density profile varies transversely in an inverse cosine-fashion, as in the Riemann example considered previously. The thermal contact surface is easily identifiable in the density plot, although it is much harder to pick out from the pressure plot. Since the shock was generated by a spark discharge, there is no contact surface as there was in the Riemann case. In the shock front region, the peak pressure occurs at the wall and a minimum pressure occurs on the centerline, consistent with the Riemann example considered previously.

The pressure maximum and minimum stem from the observation that the entire shock front region propagates through the radial thermal inhomogeneity at a constant velocity. The Mach number of the shock, however, is not constant since the speed of sound is temperature dependent. Since the pressure jump at the shock front (given by the Rankine-Hugoniot relation) increases with the shock Mach number (not shock speed), the pressure jump at the wall must be greater than the pressure jump on the centerline.

As a comparison to the case in which the shock propagates through gas with a thermal inhomogeneity, the density and pressure profiles for the case in which the shock travels through gas at a uniform temperature of $300K$ is shown in Figure 85. The solution in this figure was calculated for the same instant in time as the solution shown in Figure 84. Notice the lack of significant structure in this case, due to the lack of a thermal inhomogeneity in the ambient gas.

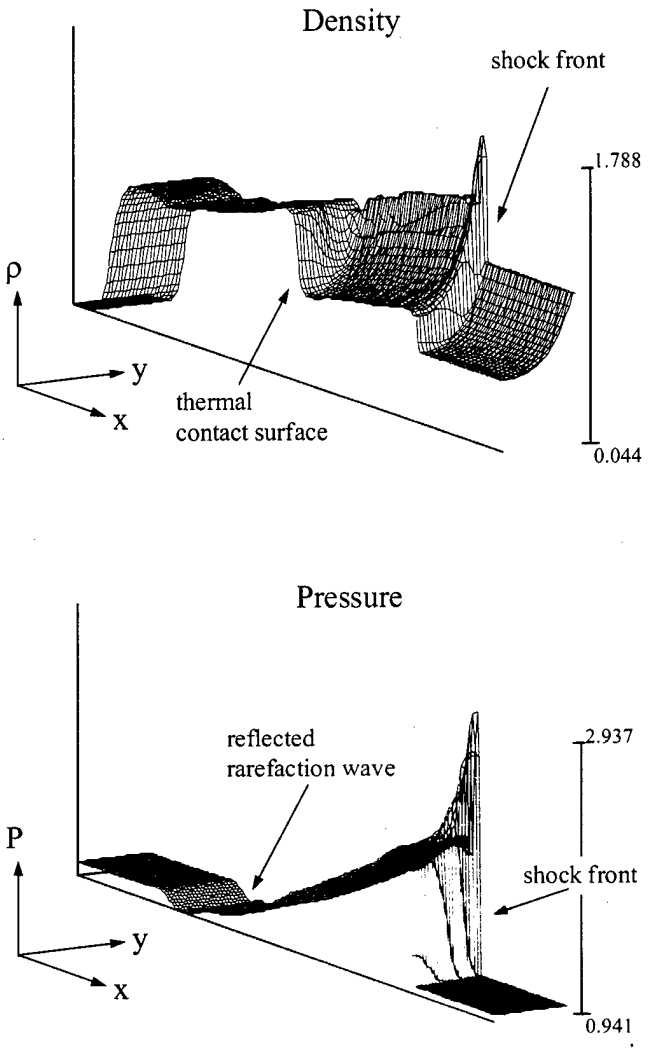

Figure 84. Density (top) and pressure (bottom) in a spark-initiated shock propagating through gas with a radial thermal inhomogeneity (equation 88).

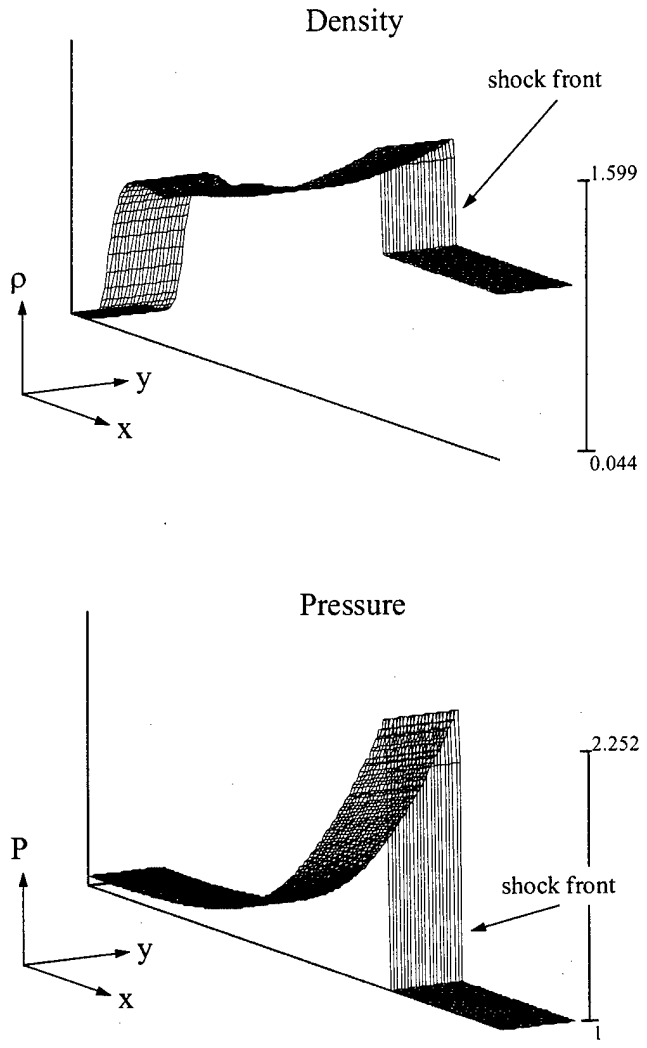

Figure 85. Density (top) and pressure (bottom) in a spark-initiated shock propagating through gas at $300K$.

5.6 Comparison to Experiment

5.6.1 Riemann Problem. Although there is quite a bit of literature reporting the use of Riemann-type shock tubes in investigating plasma/shock interactions ([27], [28], [41], [52], [54], [76], [77], [87], [89], [115]), there is very little literature providing sufficient experimental details to permit a numerical simulation and comparison with experiment. The lack of details lies primarily in either the absence of measured thermal profiles or the absence of enough information to allow the calculation of thermal profiles. Fortunately, both Voinovich [115] and Gridin [52] provide experimentally measured transverse temperature profiles. Enough details are given by Voinovich for a simulation and comparison of shock velocity, while Gridin [52] provides enough details to compare (qualitatively, at least) density profiles.

5.6.1.1 Shock Velocity. Voinovich, et al. [115] uses a Riemann-type shock tube to investigate the effect of a plasma on the propagation velocity of a shock in air. A shock with a velocity of Mach 2.13 (approximately 752 m/sec at $300K$) was generated and propagated into a plasma formed at one end of the shock tube by a gas discharge (operated at a pressure of approximately 20 torr). The shock velocity in the plasma under these conditions was found to be approximately 1100 m/sec ($\pm$ 4%). The radial temperature profile in the plasma was measured by various means, as shown in Figure 86. Curves 3 and 4 were determined by optical and thermocouple measurements, respectively. Curves 1 and 2 correspond to Equations 89 and 90, respectively, representing the lower and upper limits of the measurement error [115:472].

$$T_{gas}(r) = 500 + 580\ Cos\left(\frac{\pi r}{2R}\right) \tag{89}$$

$$T_{gas}(r) = 500 + 1136\ Cos^2\left(\frac{\pi r}{2R}\right) \tag{90}$$

A simulation of Voinovich's experiment was run using the two-dimensional fluid dynamics code in planar geometry on a grid with 963 nodes in the axial direction and

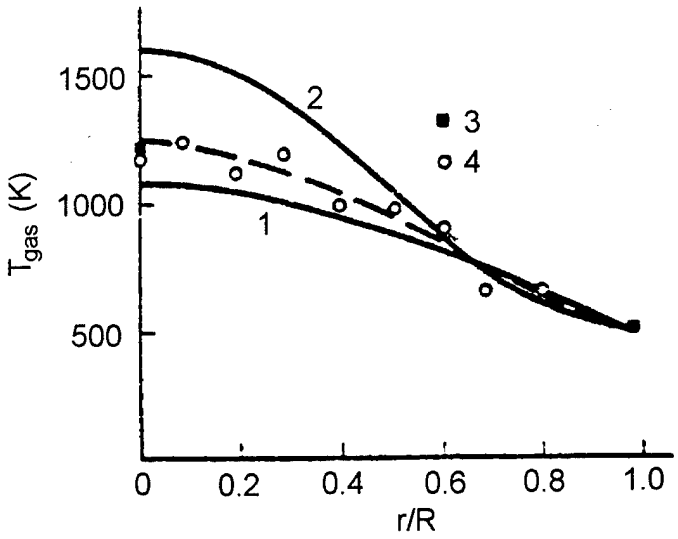

Figure 86. Radial distribution of gas temperature in a discharge in air [115]. The points are experimentally determined from optical measurements (3) and thermocouple measurements (4), while the curves correspond to equation 89 (1) and equation 90 (2).

23 nodes in the transverse direction. The initial pressure (P_4/P_1) and temperature (T_4/T_1) ratios in the shock tube were 20.0 and 2.45, respectively. The working gas in the experiment (air) was represented by pure molecular nitrogen in the simulation ($\gamma = 7/5$, molecular weight = 28). These parameters resulted in a shock velocity of 752 m/sec (Mach 2.13) in the ambient gas ($T = 300K$). The shock tube in the simulation was 120 cm long with a half-width of 2.5 cm, while the imaginary diaphragm was located at $x = 50$ cm. The gas temperature on the low pressure side of the diaphragm was initialized to $300K$, except for the region 60 cm $\leq x \leq$ 90 cm, which had a radial thermal profile given by the dashed curve fit to the temperature measurements of Figure 86.

The variation of shock velocity along the centerline with distance is shown in Figure 87 (solid). The measured shock velocity obtained under conditions corresponding to the experimental thermal profile of Figure 86 (dotted) and the analytic shock velocity obtained under ambient conditions, 752 m/sec (dashed) are also

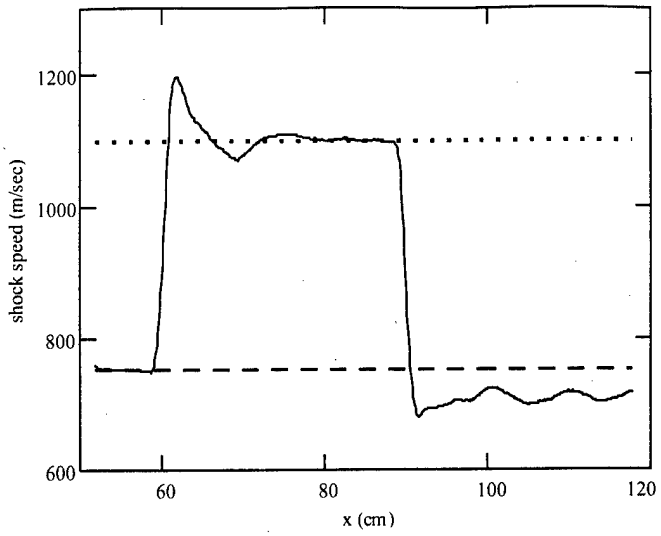

Figure 87. Variation in the shock velocity as a Riemann shock propagates through gas with a radial thermal inhomogeneity given by the dashed curve fit to data of Figure 86 (solid) compared to the experimentally measured shock velocity under the same conditions (dotted). The analytic shock velocity calculated for gas at $300K$ (dashed) is also shown.

shown. The shock velocity determined from the simulation increases rapidly as the shock initially enters the heated region, obtains a maximum velocity of nearly 1200 m/sec, then converges to a nearly constant velocity of 1100 m/sec, with small oscillations of less than 3 m/sec around this steady value. This compares extremely well with the experimental shock velocity of 1100 m/sec ($\pm$ 4%). As the shock leaves the heated region, the shock velocity rapidly decreases, reaches a minimum velocity of approximately 677 m/sec, then obtains a somewhat steady value of approximately 710 m/sec, with oscillations of $\pm$ 10 m/sec around this value. The peak value of the numerically determined shock speed (1197 m/sec) is within 1% of the shock speed determined analytically (Equation 44) for a thermal jump from $300K$ to $1250K$ (1210 m/sec), where the latter temperature corresponds to the peak temperature measured experimentally (Figure 86). The presence of an overshoot in the shock speed as the shock enters the heated region is consistent with the numerical results obtained previously for a Riemann shock propagating into a radial thermal

inhomogeneity (Figure 77). The velocity of the shock after leaving the heated region (708 m/sec) is within 6% of the incident shock velocity. This is very close to the experimental observation that the shock velocity after leaving the discharge region is within 4% of the incident velocity [115:469].

Simulations were also run for thermal profiles corresponding to curve 1 (resulting in a shock velocity of 1084 m/sec) and curve 2 (resulting in a shock velocity of 1162 m/sec) of Figure 86. These results are in good agreement with computed values reported by Voinovich of 1045 m/sec and 1120 m/sec, respectively, which were calculated using a different numerical method, but under similar conditions.

5.6.1.2 Density Profile. Gridin, et al. [52] used a transverse pulsed glow discharge in air, together with a Riemann-type shock tube to investigate shock/plasma interactions. The discharge was pulsed in order to minimize gas heating effects. The experimental arrangement is shown in Figure 88. The planar shock front, with a velocity of 1250 m/sec, is incident onto the plasma region from the left. The plasma was generated with the use of segmented cathodes (shown as the dots), while the anode (not shown) was a solid conductor. An optical interferometer was used in order to determine the temporal density variations during shock passage. The shock tube had a cross section of 10 cm x 10 cm.

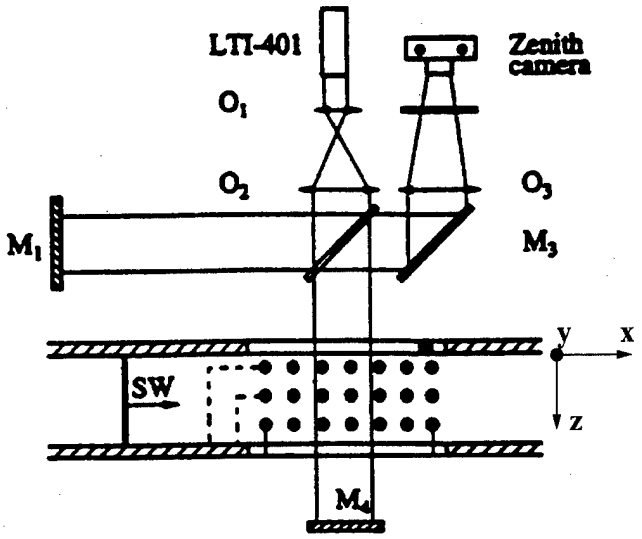

Figure 88. Schematic diagram of experimental setup used by Gridin [52]. LTI-401 is a He-Ne laser, segmented cathodes are shown as dots and optical mirrors and optical objectives are labeled as M and O, respectively. The shock wave (SW) is incident onto the plasma region with a velocity of 1250 m/sec.

The experimentally determined variation in the gas temperature is shown in Figure 89 for discharge run times of less than 1 msec. The thermal variation is with respect to the ambient temperature, which was taken to be $300K$. According to Gridin, the temperature varies from the ambient only near the cathode, in a localized region approximately 3 cm in the transverse direction. For discharge run times

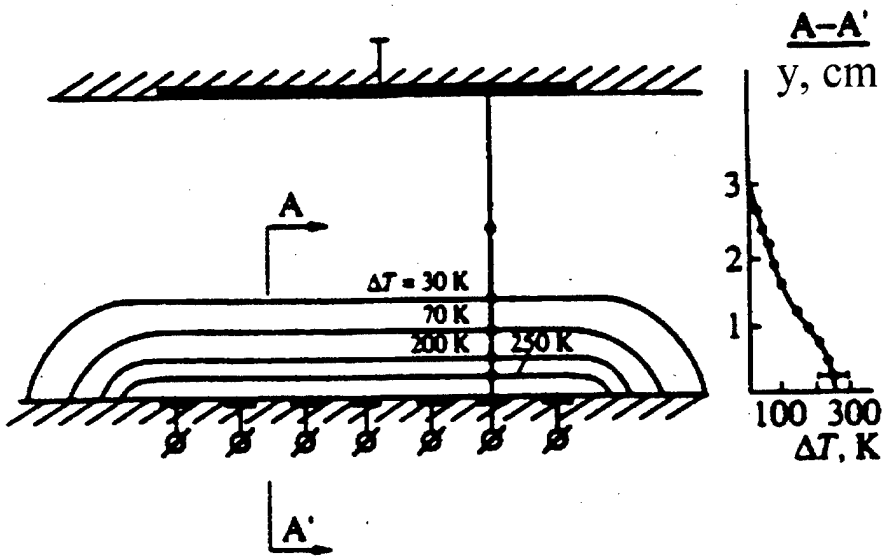

Figure 89. Experimentally determined temperature variation in the discharge region in air for discharge run times of less than 1 msec [52]. The segmented cathodes are located along the bottom while the solid anode is located at the top.

greater than 2 msec, the gas was rapidly heated to temperatures of approximately $2000K$ [52:455].

A simulation of the experiment was carried out using the two-dimensional code discussed previously. The simulated shock tube had a length of 240 cm and a full width of 10 cm. The diaphragm was located at 100 cm, with the heated region beginning at 120 cm and extending to the end of the shock tube. An initial pressure and temperature ratio (P_4/P_1 and T_4/T_1) of 100.0 and 5.0, respectively, was used in the simulation, resulting in a shock velocity of 1247 m/sec through the ambient gas. A transverse temperature distribution approximating that shown in Figure 89 was used in the heated portion of the shock tube (Equation 91). The pressure throughout the low pressure side of the shock tube was constant, consistent with experimental

observation [52:455].

$$T(x,y) = \begin{cases} 300K, & \text{for } (100 \text{ cm} < x < 120 \text{ cm}) \\ & \quad (0 \text{ cm} \leq y \leq 10 \text{ cm}) \\ 550K - 250K \frac{z}{3 \text{ cm}}, & \text{for } (120 \text{ cm} \leq x \leq 240 \text{ cm}) \\ & \quad (0 \text{ cm} \leq y \leq 3 \text{ cm}) \\ 300K, & \text{for } (120 \text{ cm} < x < 240 \text{ cm}) \\ & \quad (3 \text{ cm} < y \leq 10 \text{ cm}) \end{cases} \tag{91}$$

A simulated laser beam, with cross-sectional dimensions of 1 cm (x) x 2 cm (y), was used to sample the calculated density field in a manner similar to the interferometer. This sampling, consisting of averaging the density over the cross-sectional area of the laser beam, was calculated and recorded at each time step. The simulated laser was located at the point $x = 200$ cm, $y = 5$ cm, corresponding to a point half-way across the shock tube and 80 cm from the start of the heated region.

The result of the simulation is shown in Figure 90 (left) for the case in which the gas is heated according to Equation 91 (solid) and for the case in which the gas has a uniform temperature of $300K$ (dashed). Experimental results are shown in Figure 90 (right) for the case in which the shock propagates through a plasma (curve 2) and through gas at a uniform temperature (curve 1). Gridin's result from a two-dimensional calculation using a Total Variation Diminishing (TVD) scheme (curve 3) is also shown, as reported in [53]. The simulation from the present work is very similar to Gridin's calculated result. Both exhibit a localized density peak near the shock front, followed by a localized minimum, followed by a steady rise to the density value obtained in the absence of a either a heated region (simulation) or a plasma region (experiment). The results from both the present work and Gridin's simulation do not produce the qualitative features as measured experimentally.

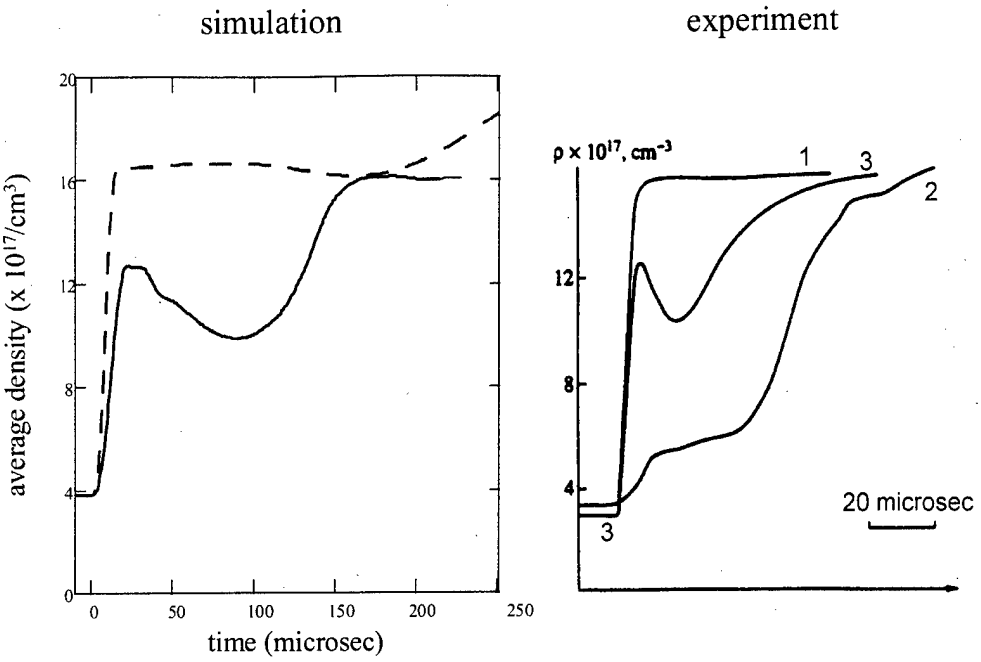

Figure 90. Density variations in a shock wave obtained from simulation (left) for gas at an ambient temperature of $300K$ (dotted) and for gas heated according to equation 91 (solid). Experimental density variations (right) were obtained for a shock in gas at a uniform temperature (1) and in a plasma (2) as reported by Gridin [52]. Gridin's numerical calculation taking into account thermal inhomogeneities (3) is also shown, as reported in [53].

A typical two-dimensional density field from the simulation is shown in Figure 91. The location of the thermal layer is clearly seen in front of the shock, confined to the region 0 cm $\leq y \leq$ 3 cm. The shock front region is curved slightly, due to the transverse thermal inhomogeneity. Behind the shock front are regions in which the density varies non-monotonically, eventually rising to the level consistent with the contact discontinuity.

It is interesting to compare the results from previous simulations (Figure 90 [solid, left] and [curve 3, right]) to experimental measurements as reported by Klimov, et al. [77] (who was, incidentally, a co-author with Gridin on [52] and [53]) as shown

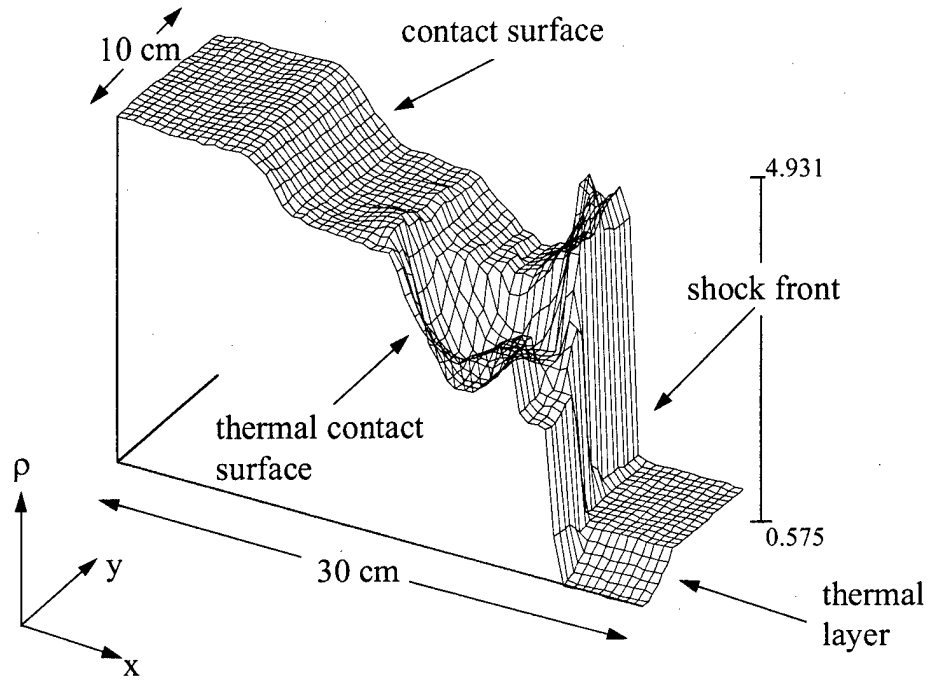

Figure 91. Calculated density corresponding to a shock passing through a thermal layer. The thermal layer is confined to the region 0 cm $\leq y \leq$ 3 cm.

in Figure 92. Here, the density variation is measured as a shock propagates through a plasma (1) and through gas in the absence of a plasma (2). The experimental conditions corresponding to Klimov's measurements are largely the same as those reported by Gridin. In both cases the incident shock velocity was 1250 m/sec, the shock tubes had the same cross-sectional area (10 cm x 10 cm) and both used a transverse pulsed glow discharge in air. Additionally, both used a Michelson interferometer to measure the density variations. The similarity between the previous simulations (taking into account only thermal inhomogeneities) and Klimov's measurement in plasma (1) is striking.

It should be noted that Klimov's measurements were made in air at a pressure of 2 torr and a current density of 100 mA/cm^2, while Gridin's measurements were made in air at a pressure of 12 torr and a current density of 30 mA/cm^2. In addition,

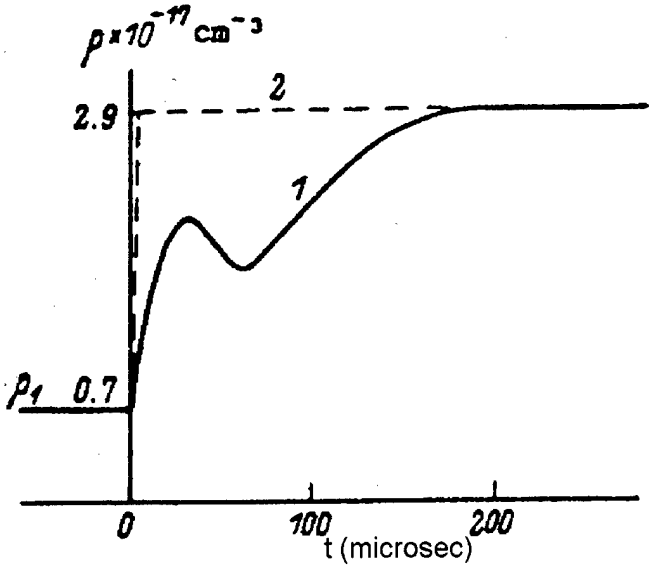

Figure 92. Density variation in a shock wave in air in the presence of a plasma (1) and in the absence of a plasma (2) (Ref: [77]).

the placement of the laser within the shock tube used by Klimov is not reported, thus the density may have been measured in a different location from Gridin's measurement.

5.6.2 Spark-Initiated Shock. A series of experiments conducted by Ganguly and Bletzinger [46] provides an opportunity to compare measurements to simulations. In these experiments, a spark-initiated shock was propagated into a glow discharge plasma. Simulations of these experiments were performed using a fluid dynamics code (Appendix B) with a radial temperature profile calculated using input parameters corresponding to the experimental conditions (Appendix D).

5.6.2.1 Experimental Setup. The experimental setup used by Ganguly and Bletzinger is shown in Figure 93 [46]. The cylindrical shock tube was constructed of 5 cm diameter glass. A glow discharge was ignited and sustained in the central portion of the tube, where the plasma is depicted as the cross-hatched region in the figure. The longitudinal extent of the plasma was approximately 12 cm while the radial extent of the luminous region of the plasma varied with discharge current. The electrodes were thin-walled cylinders, each two inches in length with a radius of 1/2 inch, with the cathode located closest to the spark gap. The shock was produced by an abrupt discharge of electrical energy across the spark gap. All distances and times were referenced to this longitudinal position and event, respectively. Two lasers beams, with their corresponding slits and detectors, were located along the shock tube at 30.2 and 42.2 cm. Both laser beams crossed the shock tube within the plasma region. Neutral gas (of the type under investigation) entered the shock tube through the gas inlet and was pumped out through the pump port. The velocity of the gas through the central portion of the shock tube was of the order of 1 m/sec. The experimentally measured data is of two types: shock arrival time and density variations. The arrival time of the shock at a given longitudinal station was determined by the time at which a laser beam (located at a fixed position) was disturbed by the passage of the shock front. The arrival time is referenced to the time at which the capacitor was discharged which produced the shock. Density variations were determined by use of a measurement technique called photo-acoustic deflection spectroscopy (PADS) [46]. This technique (described in greater detail in Appendix

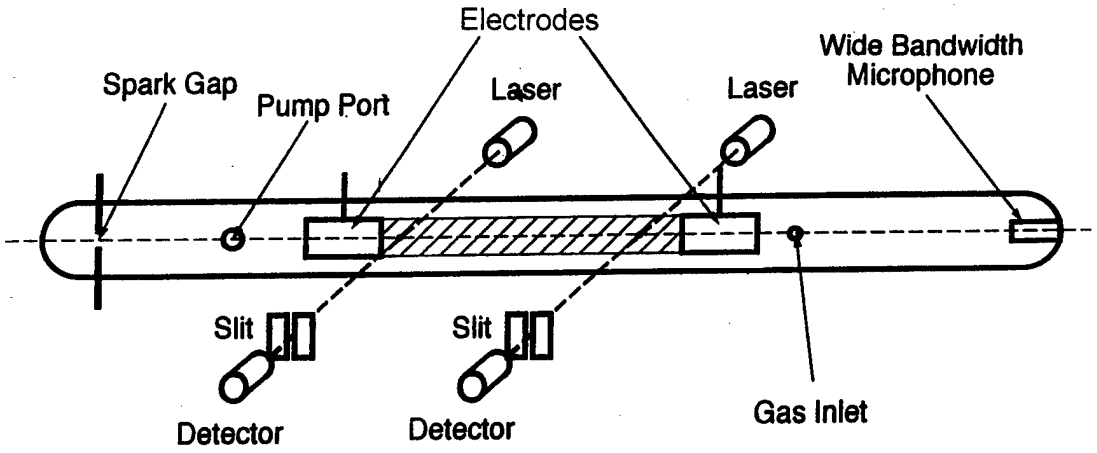

Figure 93. Spark-initiated shock experimental setup [46]

E) senses gradients in density which leads to a deflection of a laser beam that has been placed in the path of the oncoming shock. Through the use of slits and detectors, and with proper alignment of the equipment, this deflection can be measured. Under ideal conditions, the deflection of the laser beam will be proportional to the density gradient (in the direction transverse to the beam) integrated over the optical path length of the beam. The equations describing the physics of PADS [96] were applied to the numerically determined density fields at the simulated location of the laser beams within the fluid dynamics code. Although a plasma was present in the actual experiment, only a thermally heated region was used to represent the plasma in the simulations.

5.6.2.2 Calculated Radial Temperature Profiles. In quantifying the effect of a heated region on shock propagation, a temperature profile must be defined. It would be most convenient to input into the fluid dynamics code the actual experimentally determined temperature field. Given the absence of such data in the present experiment, the temperature field must be calculated using the parameters corresponding to the experimental conditions. This calculation was performed using

the method detailed in Appendix D, with input parameters provided by [46] and [20], corresponding to the experimental conditions. Typical results for Argon at a pressure of 30 torr are shown in Figure 94, with the discharge currents indicated. In these calculations, the wall temperature was assumed to be maintained at a value of $300K$. The calculated peak and average temperatures are shown in Figure 95 as a

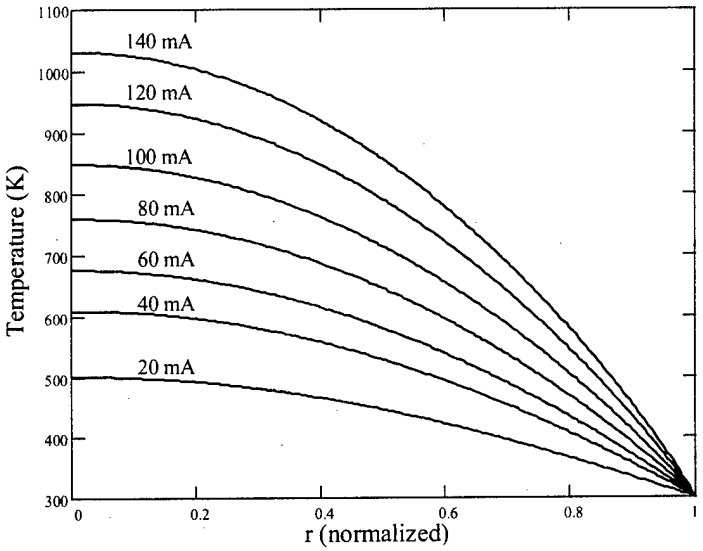

Figure 94. Calculated T(r) profiles in Argon (30 torr) at the indicated discharge currents [input parameters corresponding to data [46] and [20]].

function of the discharge current for Argon at a pressure of 30 torr ($T_{wall} = 300K$). The average temperature was defined as

$$T_{avg} = \frac{\int_0^R T(r)dr}{R}. \tag{92}$$

The use of an average temperature defined in this manner gave good results when one-dimensional fluid calculations where compared to the measured shock arrival time data.

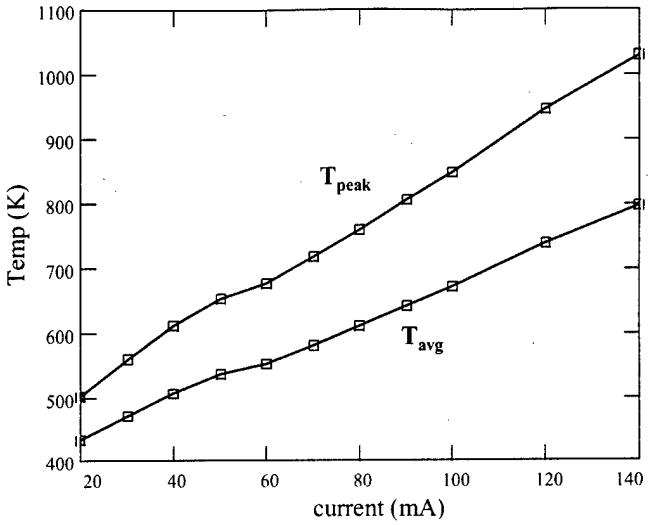

Figure 95. Calculated T_{peak} and T_{avg} in Argon (30 torr) at the indicated discharge currents [input parameters corresponding to data [46] and [20]].

The temperature throughout the shock tube was assumed to follow the relation

$$T(r,x) = \begin{cases} T_0, & \text{if } x < x_0 \\ T_{calc}(r), & \text{if } x \geq x_0 \end{cases} \tag{93}$$

where T_0 is the ambient temperature (assumed to be $300K$) and $T_{calc}(r)$ is the radial temperature profile calculated according to the method discussed in Appendix D. Using the experimental setup (Figure 93) as a guide, the point x_0 was set equal to 27.2 cm, which corresponds to the farthest edge of the electrode closest to the spark gap, which was approximately where the luminous plasma region began.

5.6.2.3 Shock Arrival Time: Simulation vs Data. Before the shock arrival times can be determined from a numerical simulation of the experiments, the amount of energy to be released in the simulation of the spark discharge must be determined. This energy is used to create the initial pressure pulse and subsequent shock wave. The value of energy to be used in the simulation was determined by requiring the arrival time of the shock front at 42.2 cm in the simulation (where

the gas was at a uniform temperature of $300K$ throughout the tube) to equal the experimentally determined arrival time of the shock front at the same location (in the absence of a plasma). Once this value of energy was established, it was used throughout all the simulations at the same pressure. Simulations at a different pressure require the calibration procedure to be repeated.

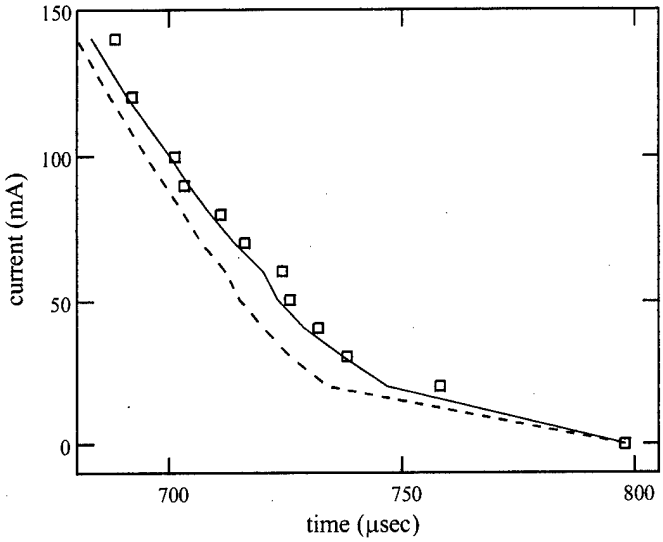

Figure 96. Shock arrival times at 42.2 cm in Argon at 30 torr [data (boxes) from [46], curves are simulations with $T_{wall} = 300K$ (solid) and $T_{wall} = 400K$ (dotted)].

A comparison of the experimentally measured and numerically predicted arrival times of the shock front in Argon (30 torr pressure) at 42.2 cm is shown in Figure 96. The experimental error in the measurements is $\pm 5\mu$sec [20]. The boxes represent the data while the solid curves have been calculated under conditions corresponding to the experiment. All required inputs to the thermal model used to calculate $T_{calc}(r)$ (used in Equation 93) were known except one: the shock tube wall temperature in the plasma region. In an effort to bound the theoretical prediction, this temperature was assumed to be in the range $300K$ to $400K$ and a series of calculations were carried out at each temperature. The curve corresponding to the longer arrival times (solid) was calculated assuming $T_{wall} = 300K$, while the curve corresponding

to the shorter arrival times (dotted) was calculated assuming $T_{wall} = 400K$. The general trend of the numerical calculations, based solely on the thermal effect, is in good agreement with the experiment results. This is particularly true for the case in which the assumed shock tube wall temperature is $300K$.

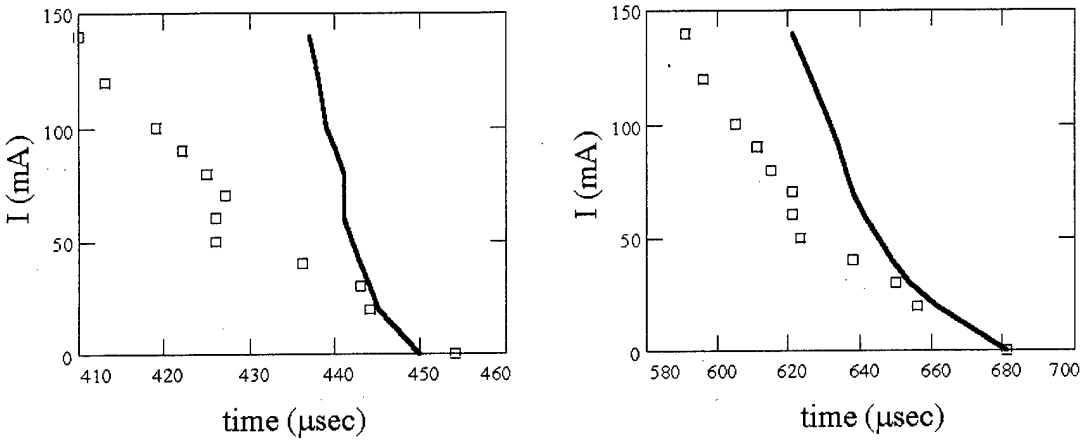

Figure 97. Shock arrival times at 30.2 cm (left) and 42.2 cm (right) in Argon at 10 torr [data (boxes) from [20], simulations (solid curves) with $T_{wall} = 300K$].

A similar comparison is made for the shock arrival times in Argon (10 torr pressure) at both 30.2 and 42.2 cm (Figure 97). It is observed that the experimental shock arrival times are earlier (up to tens of μsec) than the arrival times determined from the simulation. The general trend of the calculated arrival times is in agreement with the data, however, in that the shock arrival times decrease with increasing current. This is easily explained by the steady increase in the temperature as the current increases, as shown in Figure 95.

It should be noted that there is uncertainty in the location of the start of the heated region within the shock tube. In the present simulations, this location was taken to be the edge of the cathode situated farthest away from the spark source (27.2 cm). If the start of the heated region were to be displaced to smaller distances, the result would be to lower the shock arrival times in the simulation. Since the electrodes

are 5 cm long and made of metal (with a relatively high thermal conductivity) the actual location of the heated region could be displaced toward the spark end of the tube, possibly starting as early as 22.2 cm. In addition, the gas is flowing toward the spark end of the tube with a velocity of the order of 1.0 m/sec. This flow would tend to transport hot gas from the plasma region toward the spark end of the tube, further complicating the precise determination of the start of the heated region. None of these effects were included in the present simulations. Thus the temperature distribution used in the simulations (Equation 93) is an idealization. Experimental measurement of the actual temperature distribution (both radially and longitudinally) within the shock tube would greatly reduce the uncertainties in assessing the influence of thermal effects on shock propagation in a plasma.

5.6.2.4 Shock Velocity. The shock front arrival times calculated previously (shown in Figures 96 and 97) were based on the temperature profile given in Equation 93. Although the radial temperature profile used in this equation was determined in a reasonable manner, a calculation of shock front arrival times admits significant uncertainties associated with the temperature field. These uncertainties were pointed out in the last section and include the effects of a long, heated cathode and the convective flow of hot gas through the shock tube, both of which were not included in Equation 93. By calculating the average shock velocity within the positive column of the glow discharge (where the radial temperature profile is independent of the x coordinate) these uncertainties can be reduced or eliminated. The average velocity in this region can be calculated from

$$V_{avg} = \frac{x_2 - x_1}{t_2 - t_1} \tag{94}$$

where t_1 is the time the shock front passes location x_1 and t_2 is the time the shock front passes location x_2.

The average shock velocity in the plasma region of an Argon discharge at pressures of 10 and 30 torr are shown in Figure 98. The data is represented by the boxes while the solid curve represents the influence of the calculated thermal profile. The comparison between the data and the prediction is generally very good. The largest relative error in the thermal predictions at 30 torr ($\approx$ 10%) occurs for the highest discharge current. The largest relative error in the thermal predictions at 10 torr is less than 4%.

The agreement between the data and the simulations (based solely on the influence of a thermally enhanced region to represent the plasma) is striking. It should be emphasized that in all the simulations of the Ganguly experiments, the values of the input parameters used in the code have been either experimentally determined or are reasonable estimates of the experimental conditions. However, it should be reiterated that experimental measurement of the radial and longitudinal temperature profile would greatly reduce the uncertainties inherent in the present thermal analysis.

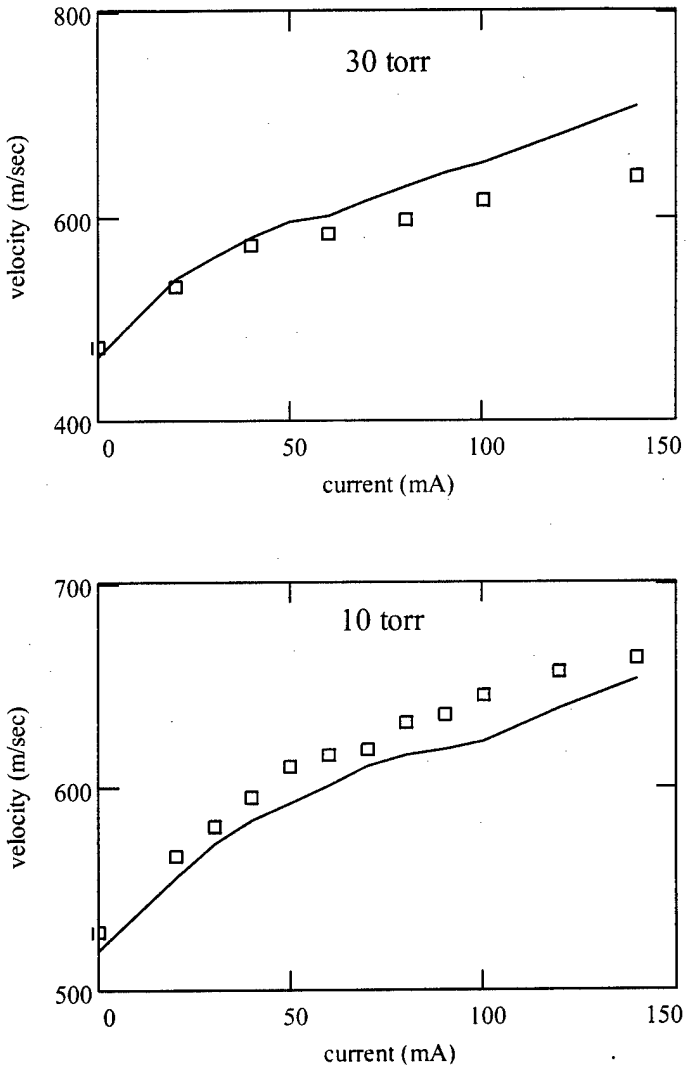

Figure 98. Average shock velocity in an Argon plasma at 30 torr (top) and 10 torr (bottom) [data (boxes) from [46], results from two-dimensional calculation (solid curve)].

5.6.2.5 Photo-Acoustic Deflection Signal: Simulation vs Data. The photo-acoustic deflection technique senses changes in density gradients along the optical path of the laser, as detailed in Appendix E. This deflection signal was numerically synthesized using densities computed at points along the shock tube corresponding to the experimental measurement locations. As in the simulations predicting arrival times and average shock velocities, these simulations used radial temperature profiles which were calculated under conditions corresponding to the experiments. The results of applying the PADS technique to the numerically determined density fields at a laser location of 42.2 cm in Argon at a pressure of 30 torr are shown in Figure 99 (left). The experimental signals as reported in [46] are shown in Figure 99 (right). The comparison is quite favorable. As the discharge current increases, both the time of arrival and the amplitude of the PADS signal decrease. In addition, the width of the signal increases with increasing current. A double-humped structure is observed in the simulation signal while two, and sometimes three, localized peaks are observed in the experimental signal.

With proper alignment of the laser and associated optics, the PADS signal voltage will be proportional to the voltage obtained under ambient conditions. The detectors used in the experiment were intentionally misaligned so as to capture only the compression portion of the shock pulse, therefore the laser beam deflection in only one direction was observed [20]. Since the ambient voltage in this case would be zero, another proportionality constant must be used in order to calibrate the PADS signal from the numerical simulation. The proportionality constant used in the present analysis was determined by taking the ratio of the peak signal amplitudes in the zero current case (experiment peak signal/simulation peak signal). The numerically determined signals shown in Figure 99 have been multiplied by this constant ratio, so that the peak amplitude of the numerical signal matches the peak amplitude of the experimental signal in the zero current case (by design).

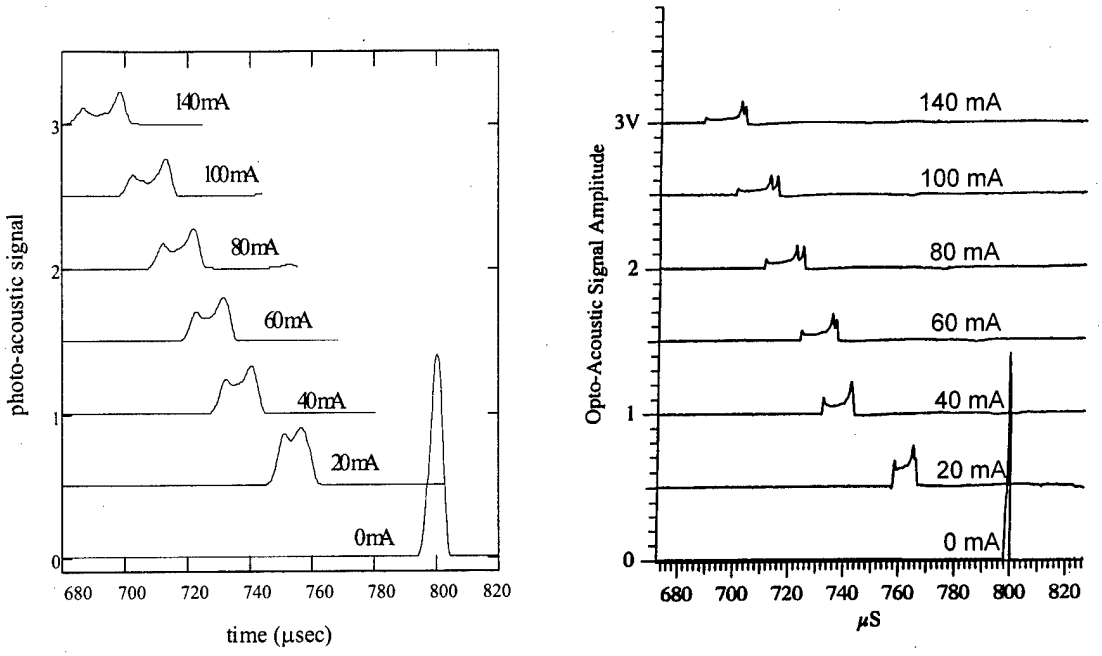

Figure 99. Photo-acoustic deflection signal at 42.2 cm in an Argon plasma at 30 torr at the indicated discharge currents [simulation (left) and experiment (right)].

5.7 Conclusion

A convincing argument can be made that thermal effects go a long way in explaining many of the observed plasma/shock phenomena. As a shock propagates into a heated region, the shock speed increases, the shock front appears to disperse (based on the transverse integrated nature of the both the interferometer and photo-acoustic deflection measurement technique) and the shock strength decreases. These observations are true for shocks in both molecular and rare gases, consistent with experimental observation. In addition, simulations of several plasma/shock

experiments based solely on thermal effects have resulted in good agreement with experimental measurements.

There are, however, several experimental observations that do not appear to be explainable based solely on thermal inhomogeneities. First, in the more recent experiments of Ganguly [45], it was observed that, under some conditions, the unique structure in the shock front region (of which the data shown in Figure 99 can be considered typical) was maintained for a length of approximately 12 cm beyond the end of the plasma region, during which time the shock essentially propagated through gas at room temperature. Numerical simulations of this experiment revealed that the predicted shock structure had essentially relaxed to its nominal state after the shock had traveled approximately 1 cm. In addition, in experiments conducted by Klimov in a pulsed discharge [77], two interesting observations are noted. First, it was observed that significant shock acceleration occurred on a time scale during which little, if any, gas heating was reportedly present. Secondly, at longer time scales, during which gas heating was reportedly present, no shock acceleration was observed. Such observations, if accurately recorded, must point to some other mechanism at work.

VI. Conclusions/Recommendations

The objective of the present research was to examine the influence of three physical processes on shock propagation. Each of these processes has been repeatedly mentioned in the literature has having some role to play in the observed plasma/shock anomalies. These processes are, in the order in which they were examined in this study:

- charged particle/neutral particle interactions
- post-shock energy release
- thermal inhomogeneities

6.1 Computational Codes

A suite of computational fluid dynamic codes was developed in order to examine each of the processes mentioned above separately. Although each of these codes used the basic explicit MacCormack algorithm [82], in conjunction with a flux corrected transport scheme [23], the particular algorithm used was selected and modified as required on the basis of the the individual specifics of each process.

To examine ion-acoustic wave damping in a weakly-ionized plasma, the plasma was modelled as a gas comprised of two fluids. The neutrals were treated as one fluid and the electrons and ions were treated together as a single fluid. This treatment is based on the assumption that the electric force strongly links the electrons and ions together, resulting in the plasma remaining quasi-neutral at all points in the flow. Ion-neutral collisions allowed for the transfer of momentum and energy between the two fluids. The numerical algorithm described by Toth [112] was modified to handle the additional source terms arising from the two-fluid treatment of the plasma. Toth's algorithm was chosen for the two-fluid plasma problem due to its reported success in handling magnetohydrodynamic processes, as well as the way it treats the

source terms. The code was validated with the aid of an analytic solution of the Riemann problem, for the case in which the two fluids were uncoupled from each other. In addition, a small-amplitude ion-acoustic wave was used to validate the code by comparing the numerically determined wave speed with the analytic expression for the ion-acoustic wave speed.

Nonequilibrium vibrational relaxation was examined with the MacCormack/FCT algorithm reported by Fletcher [44], which was modified to include a vibrational energy equation, as well as source terms coupling this equation to the conservation of energy equation for the fluid. Fletcher's algorithm was selected for this part of the research due to its streamlined design, which resulted in short computational run times. This code was validated by comparison of the numeric solution to the analytic solution of the Riemann problem. In addition, the numerically determined post-shock equilibrium flow parameters could be compared to analytic values of the same.

The effect of thermal inhomogeneities in two spatial dimensions was examined with a code which made use of both of the algorithms mentioned previously, as well as an additional algorithm used to treat source terms separately. Strang-type operators allowed splitting the multi-dimensional problem into consecutive applications of one-dimensional fluid solvers. The MacCormack/FCT algorithm of Fletcher was applied in the x (longitudinal) direction and the MacCormack/FCT algorithm of Toth was applied in the y (transverse) direction. The greater length of the shock tube in the x direction necessitated a method which was very fast at handling the large number of nodes in this direction (i.e., Fletcher's method). However, the boundary conditions in the transverse direction were better handled by a method which uses central differences (i.e., Toth's method). An implicit method (suggested by Yee [120]) was used to handle the source terms related to the spark-initiated discharge simulations. This two-dimensional code was validated for both the Riemann problem (by comparison to the analytic solution) and the spark-initiated discharge problem

(by comparison to previously reported experiments). The code was further validated by testing its ability to propagate both small and large-amplitude waves at equal speeds in all directions (analogous to the way a stone dropped into a still body of water generates ripples which propagate equally in all directions).

6.2 Charged Particle/Neutral Particle Interactions

Charged particle/neutral particle interactions were examined in both a steady-state and time-dependent approach. A two fluid approximation was used in which the neutral gas comprised one of the fluids and the electrons and ions were treated as a single fluid. The electron temperature was treated as a constant and the electric field was assumed to be proportional to the electron pressure gradient. With these restrictions, the results of both the steady and unsteady analyses were similar and essentially reconfirmed the work of Ingard [65] and Avramenko [6]. Although a precursor of charged particles in front of the neutral shock is predicted under conditions typically encountered in a weakly ionized plasma, both the spatial extent of this precursor and the particle density in it are insufficient to explain the experimental observations . The fractional ionizations in such plasmas are extremely low (10^{-6}). resulting in insignificant feedback from the charged particle precursor into the neutral component at the neutral shock front.

At higher fractional ionizations ($10^{-3} - 10^{-1}$), variations in the neutral shock parameters were evident. In these cases, the shock velocity increased, the shock front dispersed and the density and pressure jumps behind the shock decreased. Each of these is consistent with experimental observation, although these values of fractional ionization are many orders of magnitude greater than that typical of the weakly ionized glow discharges used in experiments. There has been, however, some experimental evidence that additional ionization is present in the shock front region ([50], [32], [33]). If these measurements are accurate, then it may be possible for the fractional ionization in the shock front region to be significantly greater than that

present in the quiescent plasma in front of the shock. In such a case, energy transfer from the ion-acoustic wave to the neutral shock may become a relevant process, resulting in a perturbation of the neutral flow. If some kinetic based plasma process is at work in the shock front region, it may be possible for the fractional ionization in this region to be altered. A kinetic based effect may not be predicted by a solution method which uses the fluid equations as a basis. Such is the case, for example, in the phenomena of Landau waves in plasma physics, which describes the collisionless damping of waves [36:51]. This process, in which energy is transferred between the particles and the wave, is a kinetic based effect and is not predicted when the plasma is modeled by fluid equations. However, a similar process has yet to be proposed in the study of plasma/shock interactions in weakly ionized gas.

The restriction imposed by treating the electron temperature as a constant can be relaxed by solving the electron energy equation simultaneously with the other fluid equations. Caution must be exercised, however, in any attempt to use the resulting set of equations to simulate shock propagation into an active plasma region, due to the complexities linking the external circuit to the charged particles. Unfortunately, most of the reported plasma/shock experiments involve propagating a shock into an active plasma region.

6.3 Post-Shock Energy Release

The release of energy in the post-shock region was examined based on the transfer of vibrational energy into the gas flow under nonequilibrium conditions. Two requirements were defined in order for this energy transfer to have significant influence on the shock parameters. First, the amount of energy added to the flow must be an appreciable fraction of the thermal energy already present in the flow. Second, this energy must be added to the flow on a time scale comparable to the characteristic time of the shock parameter variation on interest. For example, in order to influence the shock front region, the vibrational energy release must occur

on a time scale comparable to the transit time for a fluid element to cross the shock front (≈ 1 μsec). In order to influence the shock speed, the vibrational energy release must occur on a time scale comparable to the time required for the shock to travel a characteristic distance defined by the measurement technique. Initial estimates (Chapter II) showed that under some nonequilibrium conditions both requirements may be fulfilled. A more detailed analysis of the relaxation of vibrational energy was undertaken in two phases. In the first phase, the influence of energy transfer on shock propagation was examined for a design gas that met the requirements given above, while in the second phase the ability of a real molecular gas (N_2) to meet the given requirements was studied.

Results from the first phase of study revealed that the shock speed increases as energy is added to the post-shock region, regardless of the initial shock velocity. In addition, a "critical" shock speed (V_{crit}) was found, with V_{crit} always being less than or equal to the Chapman-Jouguet velocity (V_{CJ}). Shocks with initial velocities below V_{crit} accelerated in the nonequilibrium region, eventually converging to V_{CJ}. Shocks with initial velocities higher than V_{crit} also accelerated, with the numerically determined steady-state shock velocity converging to velocities greater than V_{CJ}. These velocities correlated closely with analytical values determined by a nonequilibrium extension to the nominal analytic Riemann solution. This effect has not been reported previously in the literature, to the knowledge of the author.

The second phase of the vibrational relaxation study focussed on the ability of a real gas (N_2) to both contain a significant amount of energy in the vibrational manifold and release it quickly into the post-shock region of the flow. These areas were analyzed with the use of a vibrational kinetics code, taking into account vibration-vibration (VV) and vibration-translation (VT) energy exchange. The results of this study indicate that it is possible, under some conditions, for a significant amount of vibrational energy to be available for release in the post-shock region. The actual amount of vibrational energy which can be released depends on the plasma

conditions in front of the shock, which define T_{vib} and T_{gas}, and the shock speed, which together define the post-shock equilibrium temperature. The characteristic time scale of this energy release is too long to explain variations in the flow parameters near the shock front region. However, under some conditions, it was found that an amount of energy approximately equivalent to 10% of the post-shock thermal energy could be released into the flow on time scales comparable to the shock transit time. This amount of energy would result in the shock speeding up, although further calculations would be required to quantify the exact effect.

6.4 Thermal Inhomogeneities

The effect of thermal inhomogeneities in the flow was explored by the numerical solution to Euler's equations in two dimensions. This analysis revealed many similarities between experimental measurements and numerical simulations of the experiments. Consistent with experimental observations of shocks entering a weakly ionized plasma, when a shock enters a heated region

- the shock speed increases
- nonmonotonic variations in the density appear
- the shock front smears
- slight curvature in the shock front appears
- the density and pressure jumps at the shock front are reduced

As a shock enters a heated region, it accelerates to a higher velocity. In simulations of the experiments of Ganguly [46] and Voinovich [115], the shock velocity in the heated region (simulating the plasma zone) agreed well with experimental measurements. In addition, the numerically determined variations in the gas density in the shock front region were in fair agreement with density measurements based on the photo-acoustic deflection method [46]. In these simulations, thermal effects caused both a nonmonotonic structure in the predicted density variation and shock

front smearing, due to slight shock front curvature in the thermal region. Slight curvature of the shock front has been reported in the literature [77], along with the claim that thermal inhomogeneities are not responsible for it. This claim appears to have been made based on the perception that thermal inhomogeneities lead to excessive curvature. The present calculations indicate that this perception is incorrect, as calculated values of shock front curvature were similar to measured values.

Thermal effects can also explain the observed decrease in the density and pressure jumps at the shock front as a shock propagates into a plasma region. This is due to the reduced Mach number in such a region. That is, although the shock velocity increases in the heated region, its Mach number decreases, resulting in a decrease in the density and pressure jumps at the shock front in such a region. For the same reason, thermal effects also predict an increase in the shock standoff distance as an object propagates into a heated region, since shock standoff distance increases with decreasing Mach number [5:189].

In spite of the many similarities between numerical simulation and experimental observation, some measurements have been made which appear to be inexplainable based solely on thermal inhomogeneities. First, in the more recent experiments of Ganguly [45], it was observed that, under some conditions, the unique structure in the shock front region (of which the data shown in Figure 99 can be considered typical) was maintained for a length of approximately 12 cm beyond the end of the plasma region, during which time the shock essentially propagated through gas at room temperature. Numerical simulations of this experiment revealed that the predicted shock structure had essentially relaxed to its nominal state after the shock had traveled approximately 1 cm. In addition, in experiments conducted by Klimov in a pulsed discharge [77], two interesting observations are noted. First, it was observed that significant shock acceleration occurred on a time scale during which little, if any, gas heating was reportedly present. Secondly, at longer time scales, during

which gas heating was reportedly present, no shock acceleration was observed. Such observations, if accurately measured, must point to some other mechanism at work.

6.5 Recommendations

It is recommended that any further study of shock/plasma interactions based on charged particle/neutral particle effects be undertaken within a kinetic framework, rather a fluid approach. This recommendation is based on the similarities between the many different studies of this effect, each of which has modeled the plasma as a fluid and each of which has led to the same conclusion: the low degree of fractional ionization present in the experiments do not allow significant coupling between the charged and neutral species. Therefore, if charged particle effects are important in shock/plasma interactions, the responsible mechanism must be tied to kinetic theory. Kinetically, it may be possible for a small group of hot electrons to be present in the flow, causing significant deviations of the distribution function from a Maxwell-Boltzmann form. These hot electrons, if present, may be able to cause additional ionization in front of the neutral shock due to their high mobility. A good starting point for such a study might be one based on the work of Lu and Huang [80]. Here, a shock in a fully ionized plasma in equilibrium was treated kinetically by solving the Boltzmann equations for both ions and electrons, with the use of the BGK collision operator [19]. An extension of their method to include neutrals in nonequilibrium plasma conditions seems to be a reasonable approach to the present problem.

Post-shock energy addition in the form of vibrational energy relaxation could be studied further, although the results of the present research indicate that the contribution of this effect to the experimental observations is minor, at best. This conclusion is based on the long time scales of the relaxation process in comparison to the much shorter gas dynamic transit time. However, if this process is studied further, it is recommended that each vibrational level be treated as a separate fluid, with the vibration-vibration and vibration-translation processes coupling the conser-

vation equations together (see [56], for example). Such an approach eliminates the need for an effective relaxation time (τ), which is difficult to accurately determine in nonequilibrium conditions.

Since thermal inhomogeneities have a significant influence on most, if not all, of the experimentally measurable parameters, knowing the gas temperature in an experiment is critical to discriminating thermal effects from other effects. Ideally, the gas temperature field throughout the experimental apparatus should be known. In this manner, it should be possible to distinguish the effects of thermal inhomogeneities on the shock parameters from the effects of other physical processes.

Appendix A. List of Symbols

Symbol	Definition
$\vec{A}$	Anti-diffusive fluxes used in flux corrected transport
C	Speed of sound
c	Shock velocity
$\vec{D}$	Diffusive fluxes in flux corrected transport
$\vec{E}$	Fluxes in the Euler equations; Electric field
E_{10}	Energy difference between the ground and first vibrational states
$\vec{F}$	Fluxes in the Euler equations
$\vec{H}$	Sources due to axisymmetric geometry in the Euler equations
$H(\xi)$	Heaviside step function
$\vec{J}$	Current density
j	Mass flux
k_B	Boltzmann's constant
L_x	x sweep Strang-type operator
L_y	y sweep Strang-type operator
L_s	Source Strang-type operator
M	Mass of a particle; Mach number
N	Number density
N_v	Number density of the vth vibrational level
n	Number density
P	Pressure
P_{in}	Rate of transfer of momentum in ion-neutral collisions
P_{en}	Rate of transfer of momentum in electron-neutral collisions
$P_{v,v+1}$	Rate at which molecules are promoted in a VT collision
$\vec{Q}$	Sources due to energy addition in the Euler equations

Symbol	Definition
$Q_{v,v+1}^{m,m-1}$	Rate at which molecules are promoted in a VV collision
Q_{in}	Rate of transfer of energy in ion-neutral collisions
Q_{en}	Rate of transfer of energy in electron-neutral collisions
Q_{ie}	Rate of transfer of energy in ion-electron collisions
q	Elementary unit of charge
R	Frequency at which molecules are promoted from the vibrational ground state
$\vec{S}$	Sources appearing in the Euler equations
T	Temperature
T^{10}	Characteristic vibrational temperature
t	Time
$\vec{U}$	Conserved variables in the Euler equations
U	Flow velocity
V	Flow velocity; Specific volume
V_{CJ}	Shock Velocity corresponding to the Chapman-Jouguet regime
V_{crit}	A critical shock velocity in a nonequilibrium vibrational gas
$\vec{V}_{drift}$	Drift velocity of electrons in a glow discharge
V_{shock}	Shock front velocity
$\hat{V}$	Flow velocity in a reference frame attached to the shock front
V_{ia}	Ion-acoustic velocity
V_{th}	Thermal velocity
v	Flow velocity
x	Longitudinal spatial coordinate
y	Transverse spatial coordinate

Symbol	Definition
α	Fractional ionization; Axisymmetric switch in the Euler equations
β	Source switch in the Euler equations
γ	Ratio of specific heat capacities (c_p/c_v)
δ	Kronecker delta function
ϵ	Specific internal energy
ϵ_{vib}	Specific vibrational energy
ϵ_{chem}	Specific chemical energy used to simulate a spark-initiated discharge
ϵ_{vib}^{eq}	Specific vibrational energy at equilibrium
ϵ_{avg}	Average specific vibrational energy
ϵ_0	Permittivity of free space
η	Fractional power into gas heating
κ	Coefficient of thermal conductivity
λ_{in}	Ion-neutral mean free path
ν	collision frequency
ξ	spatial coordinate in a reference frame attached to the shock front
ξ_0	A characteristic length in weakly ionized, nonequilibrium plasma
ρ	Mass density
σ_{in}	Ion-neutral collision cross-section
σ_{en}	Electron-neutral collision cross-section
σ_{ei}	Electron-ion collision cross-section
τ	Vibrational relaxation time
τ_{eff}	Effective vibrational relaxation time
ω^*	A characteristic frequency in weakly ionized, nonequilibrium plasma
ω_{in}	Ion-neutral collision frequency

Appendix B. Two-Dimensional Fluid Dynamics Code Description

B.1 Introduction

The influence of thermal inhomogeneities on the propagation of shocks was studied with the use of a computational fluid dynamics code. This code solves the two-dimensional Euler equations using the explicit MacCormack scheme [82]. A flux corrected transport (FCT) algorithm [23] is used in conjunction with the MacCormack scheme to reduce numerical oscillations that occur in regions of sharp gradients, such as around shocks. Strang-type splitting operators [109] are used in order to solve the differential equations in two spatial dimensions. This method is commonly used in order to extend a one-dimensional method to higher dimensions.

The MacCormack scheme (with second-order accuracy) was chosen due to both its suitability for solving nonlinear Equations [62:192] and its relative programming ease. However, the use of a second-order accurate method by itself would lead to oscillations in the solution near shocks. The FCT method was adopted as a way to get rid of these numerical oscillations by preventing them before they are allowed to grow [61:127]. Of course, other methods could be used to accomplish the same goal (Godunov method [47], artificial viscosity, etc.), however the MacCormack/FCT method offers stability and sharp resolution for a relatively small effort in coding [112]. Higher-order Gondunov schemes like the Roe method [99] produce more accurate solutions than the MacCormack/FCT scheme, however they are more complicated to code and more expensive to run [44:173]. Additionally, the FCT method is more accurate than using artificial viscosity to damp out the oscillations [44:173].

B.2 Nondimensionalization of Equations

The Euler equations describe the flow of an inviscid, compressible fluid. They are given in a compact form in Equation 95 for two-dimensional axisymmetric ($\alpha = 1$)

or planar ($\alpha = 0$) geometries, where the vectors $\vec{U}, \vec{E}, \vec{F}, \vec{H}$ and $\vec{Q}$ were defined in Chapter V by Equations 83 through 87. The vectors on the left hand side of Equation 95 are the conserved variables ($\vec{U}$) and the numerical fluxes ($\vec{E}$ and $\vec{F}$). The vectors on the right hand side are sources due to axisymmetry ($\vec{H}$) and energy addition ($\vec{Q}$). This latter source vector allows for the treatment of spark-initiated shocks (if $\beta = 1$).

$$\frac{\partial \vec{U}}{\partial t} + \frac{\partial \vec{E}}{\partial x} + \frac{\partial \vec{F}}{\partial y} = -\alpha \vec{H} + \beta \vec{Q} \tag{95}$$

These equations are nondimensionalized so that the values of the variables will be of order 1, making it convenient to analyze the results. Additionally, nondimensionalization reduces the possibility of either an underflow or overflow error.

The parameters used to nondimensionalize the variables appearing in Equation 95 are the ambient density (ρ_0), the ambient temperature (T_0), the thermal velocity at the ambient temperature ($V_{th} = \sqrt{\frac{k_B T_0}{M}}$) and the length of the shock tube (L_0). Using these parameters, the nondimensional variables can be defined as

$$\begin{aligned} x' &= \tfrac{x}{L_0}, \quad y' = \tfrac{y}{L_0}, \quad t' = t\,\tfrac{V_{th}}{L_0} \\ \rho' &= \tfrac{\rho}{\rho_0}, \quad T' = \tfrac{T}{T_0}, \quad \epsilon'_{chem} = \tfrac{\epsilon_{chem}}{V_{th}^2} \\ V'_x &= \tfrac{V_x}{V_{th}}, \quad V'_y = \tfrac{V_y}{V_{th}} \end{aligned} \tag{96}$$

where the nondimensional variables are denoted with a prime.

B.3 Model Equations (nondimensional)

Using the nondimensional variables defined in above, the dimensional Euler equations (Equation 95) can be transformed into a nondimensional system of equations:

$$\frac{\partial \vec{U}'}{\partial t'} + \frac{\partial \vec{E}'}{\partial x'} + \frac{\partial \vec{F}'}{\partial y'} = -\alpha \vec{H}' + \beta \vec{Q}' \tag{97}$$

with $\vec{U}'$ defined as

$$\vec{U}' = \begin{bmatrix} \rho' \\ \rho' V_x' \\ \rho' V_y' \\ \rho' \left\{ \frac{1}{2} \left(V_x'^2 + V_y'^2 \right) + \frac{1}{\gamma - 1} T' \right\} \\ \rho' \epsilon_{chem}' \end{bmatrix} \tag{98}$$

where ρ' is the nondimensional mass density of the gas, V_x' is the nondimensional flow velocity in the $\hat{x}$ direction, V_y' is the nondimensional flow velocity in the $\hat{y}$ direction, γ is the usual ratio of specific heats, T' is the nondimensional gas temperature and ϵ_{chem}' is the nondimensional specific chemical energy to be used in generating a shock in the spark-discharge case. Each of the variables in $\vec{U}'$ is a function of x', y' and t'; i.e., $\rho' = \rho'(x', y', t')$, $V_x' = V_x'(x', y', t')$, etc. The flux vectors $\vec{E}'$ and $\vec{F}'$ are defined as

$$\vec{E}' = \begin{bmatrix} \rho' V_x' \\ \rho' \left(V_x'^2 + T' \right) \\ \rho' V_x' V_y' \\ \rho' V_x' \left\{ \frac{1}{2} \left(V_x'^2 + V_y'^2 \right) + \frac{\gamma}{\gamma - 1} T' \right\} \\ \rho' \epsilon_{chem}' V_x' \end{bmatrix} \tag{99}$$

and

$$\vec{F}' = \begin{bmatrix} \rho' V_y' \\ \rho' V_x' V_y' \\ \rho' \left(V_y'^2 + T' \right) \\ \rho' V_y' \left\{ \frac{1}{2} \left(V_x'^2 + V_y'^2 \right) + \frac{\gamma}{\gamma - 1} T' \right\} \\ \rho' \epsilon_{chem}' V_y' \end{bmatrix}, \tag{100}$$

the axisymmetric source vector $\vec{H}'$ is defined as

$$\vec{H}' = \frac{1}{y'} \begin{bmatrix} \rho' V_y' \\ \rho' V_x' V_y' \\ \rho' V_y'^2 \\ \rho' V_y' \left\{ \frac{1}{2} \left(V_x'^2 + V_y'^2 \right) + \frac{\gamma}{\gamma - 1} T' \right\} \\ \rho' \epsilon_{chem}' V_y' \end{bmatrix} \tag{101}$$

while the vector of sources used for the spark-initiated shock problem is defined as

$$\vec{Q}' = \begin{bmatrix} 0 \\ 0 \\ 0 \\ \frac{\rho' \epsilon_{chem}'}{\tau'} \\ -\frac{\rho' \epsilon_{chem}'}{\tau'} \end{bmatrix} \tag{102}$$

where τ' governs the temporal release of the chemical energy. The first equation in 97 expresses conservation of mass, the second and third equations describe the conservation of momentum in the $\hat{x}$ and $\hat{y}$ directions, respectively. The fourth equation expresses the conservation of directed kinetic energy and thermal energy, and the fifth equation expresses the conservation of chemical energy.

Note that in the axisymmetric source vector (Equation 101) there appears to be the possibility of a singularity when y' is zero (along the centerline). By application of L'Hospital's rule to each element of the array, it can be shown that this is not the case. While the use of symmetry arguments requiring such terms as $\frac{\partial \rho'}{\partial y'}$, $\frac{\partial V_y'}{\partial y'}$, etc. to be zero are necessary to accomplish this, such arguments are entirely justifiable in the axisymmetric geometry.

Equation 97 can be modified to include viscosity and/or thermal conductivity if desired. The modifications necessary to include these processes in the present code

are straightforward, although the construction of the analytic Jacobian matrices used in the solution method can be tedious.

B.4 Strang-Splitting Operators

The temporal and spatial integration of the two-dimensional Euler equations can be written as a series of one-dimensional operations acting on the solution [120:122]. The general formulation can be written as

$$\vec{U'}^{n+2} = L_s^{\Delta t'/2} L_{y'}^{\Delta t'} L_{x'}^{\Delta t'} L_s^{\Delta t'} L_{x'}^{\Delta t'} L_{y'}^{\Delta t'} L_s^{\Delta t'/2} \vec{U'}^{n} \tag{103}$$

where time is indexed by n. The vector of conserved variables at time t_n is denoted by $\vec{U'}^{n}$ (Equation 98). The solution two time steps later is denoted by $\vec{U'}^{n+2}$. The operators $L_{x'}^{\Delta t'}$ and $L_{y'}^{\Delta t'}$ represent the temporal integration (over a time period of $\Delta t'$) and the one-dimensional spatial integration of the homogeneous fluid equations containing the x' and y' derivatives, respectively. The operator $L_s^{\Delta t'}$ represents the temporal integration (over a time period of $\Delta t'$) of the fluid equations assuming the flow to be frozen (i.e., during this integration the fluid is not convected). The symmetric sequence of operations given in Equation 103 is necessary in order to maintain the second order accuracy contained in the individual operations themselves [61]. Each of the operators will be described in detail in the sections to follow.

Yee [120:38] points out that such a method has advantages in that good algorithms already exist that can handle each part of the problem well. In other words, good numerical techniques already exist that integrate the homogeneous fluid equations and other good techniques exist which can integrate the ordinary differential equations describing the source terms. Using an operator methodology is a quick and simple way to combine the two types of problems with a reasonable hope for success, and may even give better results than an algorithm which attempts to solve both types of problems at once.

In practice, Equation 103 was split into two series of operations, with the decision of which one to use determined by whether the time step n was odd or even:

$$\vec{U'}^{n+1} = L_s^{\Delta t'/2} L_{x'}^{\Delta t'} L_{y'}^{\Delta t'} L_s^{\Delta t'/2} \vec{U'}^{n} \quad \text{for } n \text{ odd} \tag{104}$$

$$\vec{U'}^{n+1} = L_s^{\Delta t'/2} L_{y'}^{\Delta t'} L_{x'}^{\Delta t'} L_s^{\Delta t'/2} \vec{U'}^{n} \quad \text{for } n \text{ even} \tag{105}$$

This was done in order to have access to the solution after each time step, instead of after every other time step. This may not be necessary, but in the original formulation of the solution method it was thought that some parameters should be as highly resolved in time as possible (e.g., shock position, integrated density and PADS signal).

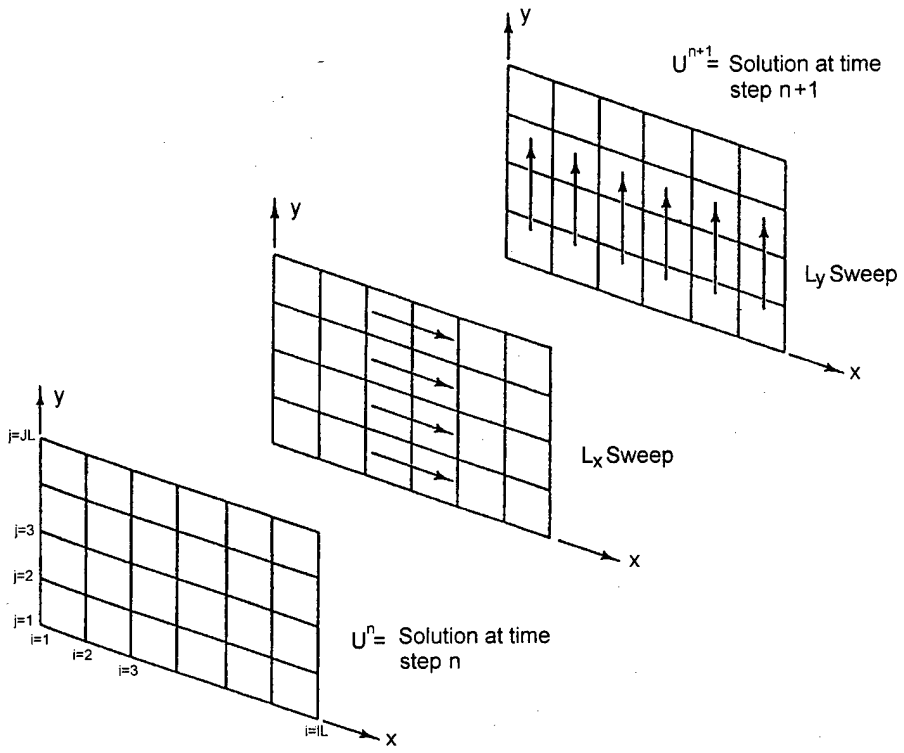

Figure 100. Application of Strang-type operators showing sequential sweeps of $L_{x'}^{\Delta t'}$ and $L_{y'}^{\Delta t'}$ through the computational domain. $L_{x'}^{\Delta t'}$ is first applied horizontally to each j line, then $L_{y'}^{\Delta t'}$ is applied vertically to each i line (adapted from [62:131]).

An illustration of the application of Strang-type operators is shown in Figure 100. Here, Equation 105 (specialized for the case in which no sources are present) is applied to a known solution. The $L_{x'}^{\Delta t'}$ operator is applied to the known solution first. A sweep of $L_{x'}^{\Delta t'}$ is made down each j line throughout the domain. Then the $L_{y'}^{\Delta t'}$ operator is applied to the intermediate solution, sweeping $L_{y'}^{\Delta t'}$ up each i line throughout the domain. On the next time cycle, the order of the x and y sweeps will be interchanged.

B.4.1 x Sweep Operator. The $L_{x'}^{\Delta t'}$ operator solves the equation

$$\frac{\partial \vec{U}'}{\partial t'} + \frac{\partial \vec{E}'}{\partial x'} = 0 \tag{106}$$

using an algorithm given by Fletcher [44:153-173]. This algorithm combines a second-order accurate MacCormack scheme with a flux corrected transport scheme. In the notation that follows, primes will be dropped from the variables, with nondimensional quantities implicitly assumed. Cell interfaces are located at $x_{i+1/2,j}$ and $x_{i-1/2,j}$, with $x_{i+1/2,j} = (x_{i,j} + x_{i+1,j})/2$. The subscript $i + 1/2$ refers to a quantity centered on the cell interface at $x_{i+1/2,j}$. The difference of conserved variables in adjacent cells is given by $\Delta\vec{U}_{i+1/2,j} = \vec{U}_{i+1,j} - \vec{U}_{i,j}$. Both steps of the MacCormack predictor-corrector method are first accomplished before applying the FCT algorithm:

$$\vec{U}_{i,j}^{t} = \vec{U}_{i,j}^{n} - \frac{\Delta t}{\Delta x}(\vec{E}_{i+1,j}^{n} - \vec{E}_{i,j}^{n}) \tag{107}$$

$$\vec{U}_{i,j}^{T} = \frac{1}{2}(\vec{U}_{i,j}^{n} + \vec{U}_{i,j}^{t}) - \frac{1}{2}\frac{\Delta t}{\Delta x}(\vec{E}_{i,j}^{t} - \vec{E}_{i-1,j}^{t}) \tag{108}$$

where a forward difference is used in the predictor (Equation 107) and a backward difference is used in the corrector (Equation 108). This is consistent with the general usage of the MacCormack method in which the flux $\vec{E}$ is differenced in the direction of shock propagation in the predictor, and in the opposite direction in the corrector;

i.e., in the problems investigated using this algorithm the shock always propagated in the positive x direction, which was the direction in which the i index increased. In Equations 107 and 108 the superscripts t and T refer to the time at the half step and full step, respectively. Note that the calculation of $\vec{E}^t$ requires the half-step solution $\vec{U}^t$ be decoded in order to determine the primitive variables, then constructed using Equation 99.

The trademark of the FCT method is the use of diffusive and anti-diffusive fluxes. The former is used to add numerical diffusion to the solution in order to ensure stability and monotonicity, while the latter is used to eliminate the excessive numerical diffusion where possible [112:84]. Following the predictor and corrector steps, the FCT algorithm is applied to the solution in the following format:

$$\vec{U}^d_{i,j} = \vec{U}^T_{i,j} + \vec{D}^n_{i+1/2,j} - \vec{D}^n_{i-1/2,j} \tag{109}$$

$$\vec{U}^{n+1}_{i,j} = \vec{U}^d_{i,j} - \vec{A}^{n+1/2}_{i+1/2,j} + \vec{A}^{n+1/2}_{i-1/2,j} \tag{110}$$

where the superscript d denotes the diffused solution and $\vec{D}$ and $\vec{A}$ are the diffusive and corrected anti-diffusive fluxes, respectively.

The diffusive flux is defined as

$$\vec{D}^n_{i+1/2,j} = \nu^n_{i+1/2,j} \Delta\vec{U}^n_{i+1/2,j} \tag{111}$$

where ν is defined as

$$\nu^n_{i+1/2,j} = \frac{1}{6} + \frac{1}{3}(\epsilon^n_{i+1/2,j})^2 \tag{112}$$

with ϵ given by

$$\epsilon^n_{i+1/2,j} = \frac{\Delta t}{\Delta x}\left(\frac{V^n_{x_{i+1,j}} + V^n_{x_{i,j}}}{2}\right) \tag{113}$$

and $\Delta\vec{U}^n$ is given by

$$\Delta\vec{U}^n_{i+1/2,j} = \vec{U}^n_{i+1,j} - \vec{U}^n_{i,j}. \tag{114}$$

The value of the anti-diffusive flux is controlled by a limiter, with the intent to prevent the appearance of new maxima or minima in the solution [112:85]. The flux limiter is the key to the FCT method, as it "effectively allows the diffusion introduced in the predictor stage to selectively annihilate the dispersive 'ripples"' generated by the second-order accurate MacCormack algorithm [44:165]. The corrected (or limited) anti-diffusive flux is defined as

$$\vec{A}^{n+1/2}_{i+1/2,j} = s^{n+1/2}_{i+1/2,j} max\left[0, min\left(|\vec{\tilde{A}}^{n+1/2}_{i+1/2,j}|, s^{n+1/2}_{i+1/2,j}\Delta\vec{U}^{d}_{i-1/2,j}, s^{n+1/2}_{i+1/2,j}\Delta\vec{U}^{d}_{i+3/2,j}\right)\right] \tag{115}$$

where $\Delta\vec{U}^{d}$ is given by

$$\Delta\vec{U}^{d}_{i+1/2,j} = \vec{U}^{d}_{i+1,j} - \vec{U}^{d}_{i,j}, \tag{116}$$

$s^{n+1/2}$ is defined as

$$s^{n+1/2}_{i+1/2,j} = sgn(\vec{\tilde{A}}^{n+1/2}_{i+1/2,j}). \tag{117}$$

The uncorrected anti-diffusive flux $\vec{\tilde{A}}$ is defined as

$$\vec{\tilde{A}}^{n+/2}_{i+1/2,j} = \mu^{n+1/2}_{i+1/2,j}\Delta\vec{U}^{T}_{i+1/2,j} \tag{118}$$

with μ defined as

$$\mu^{n}_{i+1/2,j} = \frac{1}{6} - \frac{1}{6}(\epsilon^{n}_{i+1/2,j})^2 \tag{119}$$

and with ϵ given by Equation 113. The term $\Delta\vec{U}^{T}$ is given by

$$\Delta\vec{U}^{T}_{i+1/2,j} = \vec{U}^{T}_{i+1,j} - \vec{U}^{T}_{i,j}. \tag{120}$$

The description of the $L^{\Delta t'}_{x'}$ operator is now complete.

B.4.2 y Sweep Operator. The $L^{\Delta t'}_{y'}$ operator solves the equation

$$\frac{\partial\vec{U}'}{\partial t'} + \frac{\partial\vec{F}'}{\partial y'} = 0 \tag{121}$$

using a MacCormack predictor-corrector scheme in combination with a flux corrected transport algorithm, as reported by Toth [112]. This method is different than the algorithm represented by the $L_{x'}^{\Delta t'}$ operator discussed previously. It was found that the algorithm presented here for $L_{y'}^{\Delta t'}$ gave better results along the centerline and wall of the shock tube than Fletcher's algorithm. Specifically, it was found that the value of V_y' in these locations was not zero (or very close to zero, as compared to values of V_y' in adjacent bins) when the $L_{x'}^{\Delta t'}$ operator discussed previously was adapted to the $\hat{y}$ direction. With the use of the algorithm reported by Toth however, V_y' was zero (or very close to zero) for all points along the centerline and wall. More on this subject can be found in the section on boundary conditions, contained in this appendix.

Consistent with Toth's method, the flux vector $\vec{F}'$ (Equation 100) is rearranged slightly, putting Equation 121 in strict conservation law form. Equation 121 is thus transformed into

$$\frac{\partial \vec{U}'}{\partial t'} + \frac{\partial \vec{F}_1'}{\partial y'} = \vec{S}' \tag{122}$$

where $\vec{U}'$ remains unchanged, $\vec{F}_1'$ is given by

$$\vec{F}_1' = \begin{bmatrix} \rho' V_y' \\ \rho' V_x' V_y' \\ \rho' V_y'^2 \\ \rho' V_y' \left\{ \frac{1}{2} \left(V_x'^2 + V_y'^2 \right) + \frac{1}{\gamma - 1} T' \right\} \\ \rho' e'_{h,m} V_y' \end{bmatrix} . \tag{123}$$

and the new source vector $\vec{S}'$ is given by

$$\vec{S}' = \frac{\partial}{\partial y'} \begin{bmatrix} 0 \\ 0 \\ -\rho' T' \\ -\rho' T' V_y' \\ 0 \end{bmatrix}. \tag{124}$$

In the notation that follows, primes will be dropped with nondimensional quantities implicitly assumed. Cell interfaces are located at $y_{i,j-1/2}$ and $y_{i,j+1/2}$, with $y_{i,j+1/2} = (y_{i,j} + y_{i,j+1})/2$. The subscript j+1/2 will refer to a quantity centered on the cell interface at $y_{i,j+1/2}$. The difference of conserved variables in adjacent cells is given by $\Delta\vec{U}_{i,j+1/2} = \vec{U}_{i,j+1} - \vec{U}_{i,j}$.

Toth's algorithm advances the solution from time n to time $n+1$ in two steps: a half step and a full step:

The half step:

$$\vec{U}^t_{i,j} = \vec{U}^n_{i,j} - \frac{\Delta t}{2\Delta y}(\vec{f}^n_{i,j+1/2} - \vec{f}^n_{i,j-1/2}) + \frac{\Delta t}{2}\vec{S}^n_{i,j} \tag{125}$$

$$\vec{U}^d_{i,j} = \vec{U}^t_{i,j} + \vec{D}^n_{i,j+1/2} - \vec{D}^n_{i,j-1/2} \tag{126}$$

$$\vec{U}^{n+1/2}_{i,j} = \vec{U}^d_{i,j} - \vec{A}^n_{i,j+1/2} + \vec{A}^n_{i,j-1/2} \tag{127}$$

The full step:

$$\vec{U}^T_{i,j} = \vec{U}^n_{i,j} - \frac{\Delta t}{\Delta y}(\vec{f}^{n+1/2}_{i,j+1/2} - \vec{f}^{n+1/2}_{i,j-1/2}) + \Delta t\vec{S}^{n+1/2}_{i,j} \tag{128}$$

$$\vec{U}^D_{i,j} = \vec{U}^T_{i,j} + \vec{D}^{n+1/2}_{i,j+1/2} - \vec{D}^{n+1/2}_{i,j-1/2} \tag{129}$$

$$\vec{U}^{n+1}_{i,j} = \vec{U}^D_{i,j} - \vec{A}^{n+1/2}_{i,j+1/2} + \vec{A}^{n+1/2}_{i,j-1/2} \tag{130}$$

where $\vec{D}$ and $\vec{A}$ refer to the diffusive flux and corrected anti-diffusive flux, respectively, which are trademarks of the FCT method. The flux $\vec{f}$ used in Equations 125 and 128 is given by

$$\begin{aligned} \vec{f}^{n}_{i,j+1/2} &= \vec{U}^{n}_{i,j+1/2} V^{n}_{y_{i,j+1/2}} \\ \vec{f}^{n+1/2}_{i,j+1/2} &= \vec{U}^{n}_{i,j+1/2} V^{n+1/2}_{y_{i,j+1/2}} \end{aligned} \tag{131}$$

where $\vec{U}^{n}_{i,j+1/2} = (\vec{U}_{i,j+1} + \vec{U}_{i,j})/2$ and $V_{y_{i,j+1/2}} = (V_{y_{i,j+1}} + V_{y_{i,j}})/2$. Note that $\vec{U}^{n}$ is used to compute the flux at time $n + 1/2$. The use of fluxes centered at the cell interfaces in Equations 125 and 128 ensures the conservation property of the Equations [112:84]. The source terms $\vec{S}$ appearing in Equations 125 and 128, are second-order finite-differenced representations of those defined in equation 124.

The diffusive and anti-diffusive fluxes are defined in a manner analogous to those given for the $L^{\Delta t'}_{x'}$ operator. The diffusive fluxes are defined as

$$\begin{aligned} \vec{D}^{n}_{i,j+1/2} &= \nu^{n}_{i,j+1/2} \Delta \vec{U}^{n}_{i,j+1/2} \\ \vec{D}^{n+1/2}_{i,j+1/2} &= \nu^{n+1/2}_{i,j+1/2} \Delta \vec{U}^{n}_{i,j+1/2} \end{aligned} \tag{132}$$

where $\vec{U}^{n}$ is used in computing the diffusion flux at time $n + 1/2$.

The value of the anti-diffusive flux is controlled by a limiter, with the intent to prevent the appearance of new maxima or minima in the solution [112:85]. This flux, called the corrected anti-diffusive flux, is defined as

$$\begin{aligned} \vec{A}^{n}_{i,j+1/2} &= s^{n}_{i,j+1/2} max\left[0, min(|\vec{\tilde{A}}^{n}_{i,j+1/2}|, s^{n}_{i,j+1/2} \Delta \vec{U}^{d}_{i,j-1/2}, s^{n}_{i,j+1/2} \Delta \vec{U}^{d}_{i,j+3/2})\right] \\ \vec{A}^{n+1/2}_{i,j+1/2} &= s^{n+1/2}_{i,j+1/2} max\left[0, min(|\vec{\tilde{A}}^{n+1/2}_{i,j+1/2}|, s^{n+1/2}_{i,j+1/2} \Delta \vec{U}^{D}_{i,j-1/2}, s^{n+1/2}_{i,j+1/2} \Delta \vec{U}^{D}_{i,j+3/2})\right] \end{aligned} \tag{133}$$

where $s^n_{i,j+1/2} = sgn(\Delta\vec{U}^d_{i,j+1/2})$ and $s^{n+1/2}_{i,j+1/2} = sgn(\Delta\vec{U}^D_{i,j+1/2})$. The term $\vec{\tilde{A}}^n_{i,j+/2}$ is labeled the uncorrected anti-diffusive flux and is defined as

$$\begin{aligned}\vec{\tilde{A}}^n_{i,j+/2} &= \mu^n_{i,j+1/2}\Delta\vec{U}^t_{i,j+1/2} \\ \vec{\tilde{A}}^{n+1/2}_{i,j+/2} &= \mu^{n+1/2}_{i,j+1/2}\Delta\vec{U}^T_{i,j+1/2}.\end{aligned} \tag{134}$$

The terms ν and μ appearing in equations 132 and 134 are defined as

$$\begin{aligned}\nu^n_{i,j+1/2} &= \frac{1}{6} + \frac{1}{3}(\epsilon^n_{i,j+1/2})^2, \quad \nu^{n+1/2}_{i,j+1/2} = \tfrac{1}{6} + \tfrac{1}{3}(\epsilon^{n+1/2}_{i,j+1/2})^2 \\ \mu^n_{i,j+1/2} &= \frac{1}{6} - \frac{1}{6}(\epsilon^n_{i,j+1/2})^2, \quad \mu^{n+1/2}_{i,j+1/2} = \tfrac{1}{6} - \tfrac{1}{6}(\epsilon^{n+1/2}_{i,j+1/2})^2\end{aligned} \tag{135}$$

where

$$\epsilon^n_{i,j+1/2} = \frac{1}{2}\frac{\Delta t}{\Delta y}V^n_{y_{i,j+1/2}}, \quad \epsilon^{n+1/2}_{i,j+1/2} = \frac{\Delta t}{\Delta y}V^{n+1/2}_{y_{i,j+1/2}}. \tag{136}$$

With these definitions the formulation of the $L^{\Delta t'}_{y'}$ operator is complete.

B.4.3 Source Operator. The $L^{\Delta t'/2}_s$ operator solves the equation

$$\frac{\partial\vec{U}'}{\partial t'} = \alpha\vec{H}' + \beta\vec{Q}' \tag{137}$$

using an implicit method suggested by Yee [120:38]. First, however, remember that $\vec{Q}'$ describes the energy density per unit time that is either lost or gained by the fluid during the detonation process for a spark-initiated shock. For a Riemann shock, this term will be zero. The axisymmetric source terms are contained in $\vec{H}'$, which will be nonzero only in the axisymmetric geometry. Therefore, the $L^{\Delta t'/2}_s$ operator will need to be used only if a spark-initiated shock problem is to be solved and/or the geometry is axisymmetric. To start, rewrite Equation 137 using finite-difference notation in which a half-time step is used on the left hand side and the right hand

side is represented by an average of the sources at each time:

$$\frac{\vec{U'}^{n+\frac{1}{2}} - \vec{U'}^{n}}{\Delta t'/2} = \frac{Q'(\vec{U'}^{n}) + Q(\vec{U'}^{n+\frac{1}{2}})}{2} + \frac{H'(\vec{U'}^{n}) + H'(\vec{U'}^{n+\frac{1}{2}})}{2} \tag{138}$$

This can be rewritten as

$$\vec{U'}^{n+\frac{1}{2}} - \vec{U'}^{n} = \frac{\Delta t'}{4}\left[H'(\vec{U'}^{n}) + H'(\vec{U'}^{n+\frac{1}{2}}) + Q'(\vec{U'}^{n}) + Q'(\vec{U'}^{n+\frac{1}{2}})\right]. \tag{139}$$

The terms $H'(\vec{U'}^{n+\frac{1}{2}})$ and $Q'(\vec{U'}^{n+\frac{1}{2}})$ are functions of the conserved variables at the $1/2$ time step and are thus unknown. In order to solve the equation, these terms are linearized, using

$$\vec{H'}(\vec{U'}^{n+\frac{1}{2}}) \approx \vec{H'}(\vec{U'}^{n}) + \left(\frac{\partial \vec{H'}}{\partial \vec{U'}}\right)^{n} (\vec{U'}^{n+\frac{1}{2}} - \vec{U'}^{n}) \tag{140}$$

and

$$\vec{Q'}(\vec{U'}^{n+\frac{1}{2}}) \approx \vec{Q'}(\vec{U'}^{n}) + \left(\frac{\partial \vec{Q'}}{\partial \vec{U'}}\right)^{n} (\vec{U'}^{n+\frac{1}{2}} - \vec{U'}^{n}). \tag{141}$$

In these equations, the terms $\left(\frac{\partial \vec{H'}}{\partial \vec{U'}}\right)^{n}$ and $\left(\frac{\partial \vec{Q'}}{\partial \vec{U'}}\right)^{n}$ are 5x5 Jacobian matrices, to be evaluated at time step n. These Jacobians are of the usual form, i.e.

$$\frac{\partial \vec{Q'}}{\partial \vec{U'}} = \begin{bmatrix} \frac{\partial Q'_1}{\partial U'_1} & \frac{\partial Q'_1}{\partial U'_2} & \frac{\partial Q'_1}{\partial U'_3} & \frac{\partial Q'_1}{\partial U'_4} & \frac{\partial Q'_1}{\partial U'_5} \\ \frac{\partial Q'_2}{\partial U'_1} & \frac{\partial Q'_2}{\partial U'_2} & \frac{\partial Q'_2}{\partial U'_3} & \frac{\partial Q'_2}{\partial U'_4} & \frac{\partial Q'_2}{\partial U'_5} \\ \frac{\partial Q'_3}{\partial U'_1} & \frac{\partial Q'_3}{\partial U'_2} & \frac{\partial Q'_3}{\partial U'_3} & \frac{\partial Q'_3}{\partial U'_4} & \frac{\partial Q'_3}{\partial U'_5} \\ \frac{\partial Q'_4}{\partial U'_1} & \frac{\partial Q'_4}{\partial U'_2} & \frac{\partial Q'_4}{\partial U'_3} & \frac{\partial Q'_4}{\partial U'_4} & \frac{\partial Q'_4}{\partial U'_5} \\ \frac{\partial Q'_5}{\partial U'_1} & \frac{\partial Q'_5}{\partial U'_2} & \frac{\partial Q'_5}{\partial U'_3} & \frac{\partial Q'_5}{\partial U'_4} & \frac{\partial Q'_5}{\partial U'_5} \end{bmatrix}. \tag{142}$$

Carrying out the operations required in Equation 142 results in

$$\frac{\partial \vec{Q}'}{\partial \vec{U}'} = \begin{bmatrix} 0 & 0 & 0 & 0 & 0 \\ 0 & 0 & 0 & 0 & 0 \\ 0 & 0 & 0 & 0 & 0 \\ 0 & 0 & 0 & 0 & \frac{1}{\tau'} \\ 0 & 0 & 0 & 0 & -\frac{1}{\tau'} \end{bmatrix} \tag{143}$$

and

$$\frac{\partial \vec{H}'}{\partial \vec{U}'} = \frac{1}{y'} \begin{bmatrix} 0 & 0 & 1 & 0 & 0 \\ -V_x' V_y' & V_y' & V_x' & 0 & 0 \\ -V_y'^2 & 0 & 2V_y' & 0 & 0 \\ A_{41} & A_{42} & A_{43} & \gamma V_y' & 0 \\ -\epsilon_{chem}' V_y' & 0 & \epsilon_{chem}' & 0 & V_y' \end{bmatrix} \tag{144}$$

where

$$A_{41} = V_y' \left[(\gamma - 1)(V_x'^2 + V_y'^2) - \gamma \epsilon_t' \right] \tag{145}$$

$$A_{42} = -(\gamma - 1) V_y' V_x' \tag{146}$$

$$A_{43} = \gamma e_t' - (\frac{\gamma - 1}{2})(V_x'^2 + 3V_y'^2) \tag{147}$$

with $\epsilon_t' = \frac{1}{2}(V_x'^2 + V_y'^2) + \frac{1}{\gamma - 1} T'$. The derivations of these Jacobians are straightforward, but can be tedious. Note, again, the apparent possibility of a singularity in Equation 144 along the centerline ($y' = 0$) in the axisymmetric geometry. However, it must be remembered that the axisymmetric sources are zero along the centerline, therefore the use of this Jacobian is limited to points away from the centerline.

Combining Equations 140 and 141 with Equation 139 results in

$$\left[\overleftrightarrow{I} - \frac{\Delta t'}{4} \left\{ \left(\frac{\partial \vec{H}'}{\partial \vec{U}'} \right)^n + \left(\frac{\partial \vec{Q}'}{\partial \vec{U}'} \right)^n \right\} \right] \Delta \vec{U}'^{n+\frac{1}{2}} = \frac{\Delta t'}{2} \left(\vec{H}'(\vec{U}'^n) + \vec{Q}'(\vec{U}'^n) \right) \tag{148}$$

where

$$\Delta \vec{U'}^{n+\frac{1}{2}} = \vec{U'}^{n+\frac{1}{2}} - \vec{U'}^{n} \tag{149}$$

and $\overleftrightarrow{I}$ is the 5x5 identity matrix. Equation 148 is the chief result of this section and is the equation to which the $L_s^{\Delta t'/2}$ operator is applied. With the solution $\vec{U'}^{n}$ known at time step n, all terms in equation 148 are known except $\Delta \vec{U'}^{n+\frac{1}{2}}$, putting this equation in the familiar form $\overleftrightarrow{A}\,\vec{X} = \vec{B}$ (where $\overleftrightarrow{A}$ and $\vec{B}$ are known). Equation 148 is solved for $\Delta \vec{U'}^{n+\frac{1}{2}}$ at each interior grid node at every time step, using an LU decomposition method with back substitution. Once $\Delta \vec{U'}^{n+\frac{1}{2}}$ is known, $\vec{U'}^{n+\frac{1}{2}}$ can be found by use of Equation 149.

B.5 Initial Conditions

The initial conditions used in the code depend on the type of problem to be solved (Riemann or spark-initiated). In general, however, the initial values of the primitive variables ($\rho, T, V_x, V_y, \epsilon_{chem}$) are defined in two stages. The first stage defines the values of the variables for the nominal case, while the second stage modifies the density and temperature to account for a heated region in the flow.

In the Riemann problem, the first stage amounts to specifying the values of the variables on both sides of the diaphragm. In this case, all velocities and the chemical energy at each grid node are specified to be zero, and the density and temperature on the low and higher pressure sides of the shock tube are set equal to the values determined from the input conditions. In the spark-initiated shock problem, the first stage sets the density and temperature at each grid node to their ambient values, and all velocities are set to zero. The chemical energy at each grid node throughout the domain is set to zero, except for the grid points along the left edge of the shock tube. These are set equal to the value determined from the input conditions. The chemical energy along this edge of the shock tube simulates the explosive release of energy from a spark discharge and leads to the development of a shock.

If no changes were made to these input conditions the computer would solve the typical Riemann problem or generate and propagate a spark-initiated shock through a homogeneous gas. To account for a heated region in the flow, the temperature is adjusted at each grid point to the desired level. Since the pressure is assumed to be a constant throughout the heated region, the density must also be adjusted by the appropriate amount at each nodal point.

B.6 Boundary Conditions

Application of the correct boundary conditions is an important part of the solution method used in the code. The boundary conditions applied to the model equations are

$$\begin{aligned}
&\text{along the wall } (y = 0) \text{ and centerline } (y = y_{wall}): \\
&\frac{\partial \rho}{\partial y} = 0 \quad \frac{\partial T}{\partial y} = 0 \quad \frac{\partial V_x}{\partial y} = 0 \quad V_y = 0 \qquad \frac{\partial \epsilon_{chem}}{\partial y} = 0 \\
&\text{along the left } (x = x_{left}) \text{ and right ends } (x = x_{right}): \\
&\frac{\partial \rho}{\partial x} = 0 \quad \frac{\partial T}{\partial x} = 0 \quad V_x = 0 \quad \frac{\partial V_y}{\partial x} = 0 \qquad \frac{\partial \epsilon_{chem}}{\partial x} = 0
\end{aligned} \tag{150}$$

where y is the transverse coordinate in the $\hat{r}$ or $\hat{y}$ direction, depending on whether the geometry is axisymmetric or planar, respectively.

Since the solution to the problem is assumed to be independent of either the θ (in the cylindrical case) or z (in the planar case) coordinate we can take advantage of the symmetry and solve only half of the problem. The physical layout of the shock tube (shown in Figure 101) illustrates how the geometry of the problem is represented within the computer. The shock tube's centerline, wall and left and right ends are shown. The x and y coordinates are indexed by i and j, respectively. The physical boundaries of the shock tube within the grid are $i = 2$ (left edge), $i = IL - 1$ (right edge), $j = 2$ (centerline) and $j = JL - 1$ (wall). Notice that the physical boundaries of the shock tube do not lie at the edge of the computational boundaries. A row of 'ghost' nodes lies beyond the centerline and wall of the shock tube, while a column

of 'ghost' nodes lies to the left of the left edge of the tube and to the right of the right edge of the tube. The use of ghost nodes at the boundaries was necessary in order to incorporate the reflection boundary conditions [3:284], which are used in the code. The flow parameters are defined at the grid nodes (indicated by the dots at the intersections of the i and j lines) in the finite-difference form of the governing equations.

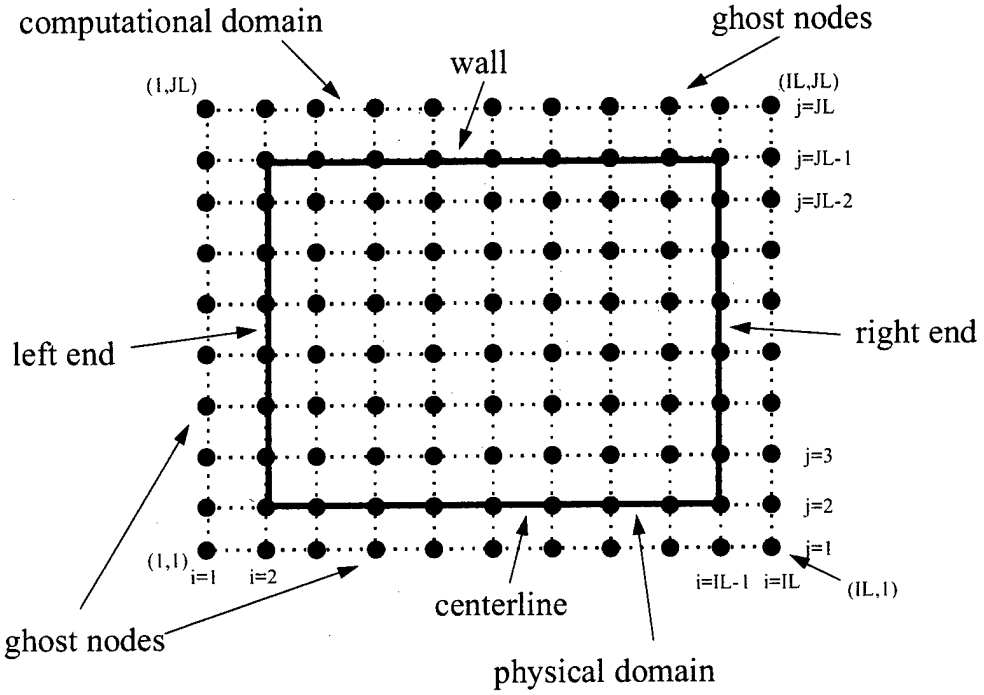

Figure 101. Representation of the shock tube geometry used in the code.

When applied to the grid shown in Figure 101, the boundary conditions specified by Equation 150 become

Along tube wall: (i=2, IL-1)

$$\rho_{i,JL} = \rho_{i,JL-2} \quad V_{x_{i,JL}} = V_{x_{i,JL-2}} \quad \epsilon_{chem_{i,JL}} = \epsilon_{chem_{i,JL-2}}$$
$$T_{i,JL} = T_{i,JL-2} \quad V_{y_{i,JL}} = -V_{y_{i,JL-2}}$$

Along tube centerline: (i=2, IL-1)

$$\rho_{i,1} = \rho_{i,3} \qquad V_{x_{i,1}} = V_{x_{i,3}} \qquad \epsilon_{chem_{i,1}} = \epsilon_{chem_{i,3}}$$
$$T_{i,1} = T_{i,3} \qquad V_{y_{i,1}} = -V_{y_{i,3}}$$

Along left end: (j=1, IL)

$$\rho_{1,j} = \rho_{3,j} \qquad V_{x_{1,j}} = -V_{x_{3,j}} \qquad \epsilon_{chem_{1,j}} = \epsilon_{chem_{3,j}}$$
$$T_{1,j} = T_{3,j} \qquad V_{y_{1,j}} = V_{y_{3,j}}$$

Along right end: (j=1, IL)

$$\rho_{IL,j} = \rho_{IL-2,j} \quad V_{x_{IL,j}} = -V_{x_{IL-2,j}} \quad \epsilon_{chem_{IL,j}} = \epsilon_{chem_{IL-2,j}}$$
$$T_{IL,j} = T_{IL-2,j} \quad V_{y_{IL,j}} = V_{y_{IL-2,j}}$$

These boundary conditions were applied to the solution each time a Strang-type operator ($L_{x'}^{\Delta t'}$, $L_{y'}^{\Delta t'}$, $L_{x}^{\Delta t'/2}$) was used, as well as at different points within the algorithm represented by each operator.

B.7 Determination of Time Step

In explicit integration schemes the time step is limited by the Courant-Friedrichs-Levy (CFL) criteria, which in one-dimensional takes the form (assuming a constant grid spacing of Δx):

$$\Delta t \leq \frac{(CFL)\Delta x}{(|V_x| + C_s)_{max}} \tag{151}$$

where CFL is a number less than unity and C_s is the sound speed. Transforming this equation to the nondimensional form required by the code and taking into account both the discrete nature of the grid and the dimensional splitting of the integration

results in

$$(\Delta t')_x \leq min_{i,j} \frac{(CFL)\Delta x'}{(|V'_{x_{i,j}}| + C'_{s_{i,j}})}, \qquad (\Delta t')_y \leq min_{i,j} \frac{(CFL)\Delta y'}{(|V'_{y_{i,j}}| + C'_{s_{i,j}})} \tag{152}$$

where $C'_s = \sqrt{\gamma T'}$.

Consistent with the algorithms represented by the $L_{x'}^{\Delta t'}$ and $L_{y'}^{\Delta t'}$ operators, a CFL number of 0.4 was used [44:166], [112:85], resulting in a global time step $\Delta t'$ determined by

$$\Delta t' = 0.4\ [(\Delta t')_x,\ (\Delta t')_y]_{min} \tag{153}$$

The time step given by Equation 153 was determined based only on the CFL criteria. The computation of flows in which physical processes like energy transfer occur may require one to take into account the time scale of the process. In the spark-initiated shock problem the variable τ' determines the time scale associated with the energy release used to generate the shock. Taking into account this time scale, the calculation time step should be modified to be

$$\Delta t' \leq [(\Delta t')_{CFL}, (\tau')]_{min}. \tag{154}$$

In practice, τ' was hardwired to be equal to 20 to 100 times the value of $\Delta t'$, thus $\Delta t'$ was always determined by the CFL limit.

B.8 Code Flowchart

A brief flowchart of the main features of the code is shown in Figure 102. The input file defines the problem to be solved, specifying whether the Riemann-type problem or the spark-initiated shock problem is to be run. It also defines the geometry (two-dimensional planar or axisymmetric), physical size of the shock tube (length and width), type of gas, as well as the ambient pressure and temperature. In addition, the size of the computational grid to be used is also specified. Finally,

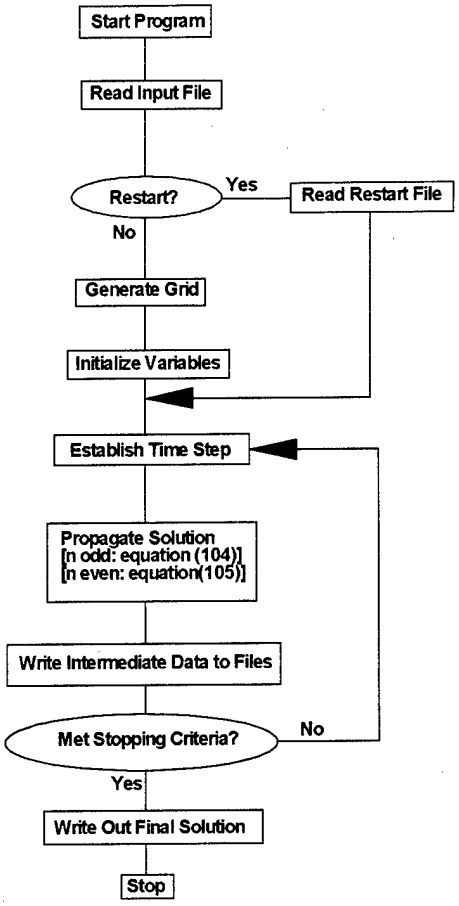

Figure 102. Two-dimensional fluid dynamics code flowchart.

the input file determines whether the problem is to be run from scratch or initiated from a restart file. If a restart file is not used, the code generates the geometric grid and initializes all variables according to the input parameters. If a restart is used, these actions are accomplished by reading in the appropriate values from a previous simulation.

After the computational time step is determined (using Equation 154), the solution at a known point in time is propagated according to either equation 104 or 105, depending on whether the value of the iteration counter is odd or even. After each time step, some data is written to external files for post-processing and/or flow visualization. If the stopping criteria is not met, the code increments the iteration

counter and loops back to establish a new computational time step, propagates the solution to a new time, writes intermediate data and then rechecks the stopping criteria. The stopping criteria is based on one of three different conditions and is determined by the input file. The code can either run for a certain number of iterations, or until a certain physical time is reached, or until the shock front along the centerline reaches a particular location. These choices allow the user to select the type of stopping criteria most useful for the particular problem at hand. In any case, if the stopping criteria is met the code exits the propagation loop, writes out the final solution and stops.

B.9 Determination of Shock Velocity

Although not calculated directly by the code, the determination of the shock velocity is such an important parameter in the analysis of shock propagation that a description of its calculation is warranted. While the code determines V_x and V_y, these are average fluid velocities, not shock velocities. The determination of the shock velocity is determined by an analysis of the position of the shock front as a function of time.

After each time step, the location of the shock front along the centerline of the shock tube is determined. This is accomplished by finding the first spatial bin in which the nondimensional pressure, which is always initialized to unity, has a value greater than 1.01. The search for this particular bin always starts from the right end of the shock tube and proceeds to the left, which is the direction opposite of the shock velocity. The value of 1.01 was found to be a good compromise between a lower number (which would be subject to small numerical oscillations in front of the shock and could place the computed shock front location slightly to the right of the actual shock front location) and a larger number (which would place the computed shock front location slightly to the left of the actual shock front location). Once this bin was found, the x position corresponding to it and the time corresponding to

the calculation were written to an external file. The process of searching for the bin containing the shock front was accomplished every time step. The data was written to the external file only if the location of the shock front changed between consecutive time steps. Thus, as the program runs, a temporal history is built describing the location of the shock front. This file is post-processed to determine the shock velocity by computing the slope of the position vs time curve ($V_{shock} = \frac{dx}{dt}$).

Care must be exercised in the calculation of this slope as the effects of a finite sized grid lead to some noise in the data. Through considerable effort a satisfactorily method was found that was quite accurate in validation tests against analytic (Riemann) solutions. The method consists of finding the slope of a line defined by a linear least squares fit to a group of data points centered around the time level of interest. For example, say that the shock velocity at a time level of n (corresponding to a physical time of t_n) is to be computed. From the external data file, the values of the shock positions at ten data points before through ten data points after the interested time level are extracted. These x locations are labeled as $x_{n-10}, x_{n-9}, x_{n-8} \ldots x_n \ldots x_{n+8}, x_{n+9}, x_{n+10}$, where the shock position at time t_n is x_n. The times corresponding to these shock locations are labeled as $t_{n-10}, t_{n-9}, t_{n-8} \ldots t_n \ldots t_{n+8}, t_{n+9}, t_{n+10}$. With these ordered pairs of data, a linear least squares fitting routine is used to draw a line through these points, from which the slope can be determined, which defines the shock velocity at time t_n. The shock velocities at times t_{n+1}, t_{n+2}, etc. are determined similarly. Notice that shock velocities cannot be determined for times that correspond to either the first or last ten data points within the data set. In practice, this is a small restriction and is of little consequence.

Appendix C. Two-Fluid Plasma Code Description

This appendix offers a short description of the plasma fluid code used in the time-dependent calculations of Chapter III. The code, based on the MacCormack method with flux corrected transport (FCT) as given by Toth, et al. [112], solves the one-dimensional equations for a plasma in the two fluid approximation. The assumptions upon which the two fluid approximation is based have already been given in Chapter III and will not be repeated here.

The two fluid plasma equations (given by Equations 52 to 62) were nondimensionalized so that the value of all variables was of the order of one. The density and temperature of each component were nondimensionalized with respect to the respective upstream ambient values. For example, the ion density was normalized with respect to the upstream ambient ion density, while the neutral density was normalized with respect to the upstream ambient neutral density. Thus, although the fractional ionization of the plasma may be very low (10^{-6}, for example), the computed density of both fluid components will be of order one. The flow velocities of each component were normalized with respect to the upstream ambient thermal velocity. Since the ions and neutrals were assumed to be in thermal equilibrium in the upstream ambient conditions, the thermal velocity was the same in both cases.

The inputs to the code are divided into computational parameters and physical parameters. The physical parameters are

- T_0 - ambient heavy particle temperature (K)
- P_0 - ambient heavy particle pressure (torr)
- γ - heavy particle specific heat ratio (unitless)
- T_e - electron temperature (K)
- α - fractional ionization (unitless)

- σ_{in} - ion/neutral collision cross-section (m^2)
- σ_{en} - electron/neutral collision cross-section (m^2)
- σ_{ei} - electron/ion collision cross-section (m^2)
- L - physical length of the shock tube (m)
- P_4/P_1 - ratio of the high pressure to the low pressure for the shock tube
- T_4/T_1 - ratio of the heavy particle temperature in the high pressure side to the heavy particle temperature in the low pressure side
- x_{dia} - location of the diaphragm (m)

These parameters are all self-explanatory. In all the calculations performed, σ_{en} and σ_{ei} were set to zero. Thus, only ion-neutral interactions were allowed to play a role in the shock dynamics. Since a Riemann problem was used to generate the shock, the parameters P_4/P_1 and T_4/T_1 determined the neutral shock speed for a given γ (in the absence of ion/neutral interactions). while the computational parameters are

- NX - number of bins
- stopping criteria
- restart (Y/N)
- computer system (PC/UNIX)

The stopping criteria determined when the calculation would end, and could be defined in one of three ways. The total number of time steps for the calculation could be specified, or the time (in seconds) at which the calculation should end could be specified or the final position of the shock front could be specified. The restart capability allows the program to pick up the calculation at a previous point.

Once the inputs to the code were read in, all variables were initialized and the code entered the main program loop. Here, the following steps were performed each time iteration:

- calculate the time step
- calculate the source terms
- propagate the solution one time step

The time step was determined based on the usual Courant-Friedrichs-Lewy (CFL) criteria used in explicit computational fluid dynamics codes [3:76]. For the neutral fluid, this amounts to

$$(\Delta t)_n \leq \frac{(\mathrm{CFL})\Delta x}{(C_n + \mid V_n \mid)\max}, \tag{155}$$

where C_n is the neutral sound speed and V_n is the neutral flow speed. The CFL number is determined by the numerical algorithm. For the present choice of algorithms, Toth [112] recommends CFL < 0.5. In all calculations using the present code, CFL was equal to 0.4. Whereas the sound speed (C_n) was used in determining Δt in the neutral component, the ion-acoustic sound speed (C_{ia}) is used in determining Δt in the plasma component. Thus, the time step for the plasma component is

$$(\Delta t)_i \leq \frac{(\mathrm{CFL})\Delta x}{(C_{ia} + \mid V_i \mid)\max}. \tag{156}$$

When transformed to a computational grid, these become

$$(\Delta t)_n \leq \min_j \frac{(\mathrm{CFL})\Delta x}{(C_{n_j} + \mid V_{n_j} \mid)}, \qquad (\Delta t)_i \leq \min_j \frac{(\mathrm{CFL})\Delta x}{(C_{ia_j} + \mid V_{i_j} \mid)} \tag{157}$$

where j indexes the spatial grid. The time step for the calculation was determined by choosing the smallest time step meeting both criteria above. Thus,

$$\Delta t = [(\Delta t)_n,\ (\Delta t)_i]_{\min} \tag{158}$$

determines the computational time step for both components.

The source terms were calculated by use of Equations 55 through 62. These source terms are divided into three types. Some source terms are a result of the form of the Euler equations used in the calculation and are not connected with the plasma in any way (Equation 55). Some source terms are due to the ion/neutral collisions (Equation 56), while others are a result of the presence of an electric field (Equation 62). Note that the last of these source terms affects only the ion fluid, as required.

With the time step and source terms determined, the solution is propagated one time step using the algorithm reported by Toth [112], and previously reported in Appendix B as the $L_y^{\Delta t}$ operator. A detailed description of this operator was given there and will not be repeated here. However, a brief comment on the application of the FCT will be made. Since there are two flow velocities in the plasma code, the FCT scheme must be applied to each fluid separately, based on the flow velocity of the appropriate component.

In practice, extensive use of the restart capability of the code was required. Transients in the flow parameters near the diaphragm were observed at very early times. With large values of the electron temperature and ion/neutral interaction cross-section, these transients became very large and forced the calculation to end prematurely due to numerical oscillations. Allowing the shock to form and begin to propagate away from the diaphragm before turning on the source terms due to the ion/neutral interaction and the electric field eliminated this problem.

Appendix D. Self-Consistent Model of Gas Heating in a Glow Discharge

One of the difficulties in assessing the influence of thermal effects on shock propagation in a plasma is the determination of the gas temperature at each point in the shock tube. This is particularly true when experimental data of various shock wave parameters (density, pressure, velocity, etc) are reported, with no accompanying gas temperature data. In the absence of such thermal data, the temperature profiles must be calculated. In the general case, the time dependent energy equation should be solved, which requires the simultaneous solution of a coupled set of equations (conservation of mass, momentum and energy) in addition to a detailed knowledge of the form of the heat source term. This level of detail is generally lacking in the case of transient gas discharges. However, in the case of steady-state gas discharges the problem is simplified considerably, and, generally speaking, enough experimental data is available for a calculation to be carried out.

D.1 Problem Statement

The steady-state heat conduction equation for a neutral gas heated by a gas discharge is

$$\vec{\nabla} \cdot (\kappa \vec{\nabla} T) = -\eta \, (\vec{J} \cdot \vec{E}) \tag{159}$$

where κ is the thermal conductivity (and is a function of temperature), T is the neutral gas temperature, $\vec{J}$ is the current density and $\vec{E}$ is the electric field. The objective is to solve this equation for the neutral gas temperature (as a function of radial position) given the experimentally determined values of the electric field and total current in the discharge. The difficulty lies in the treatment of the source term, which is itself a function of the temperature. This difficulty will be addressed in the next section. $\vec{J} \cdot \vec{E}$ represents the total power input to the electrons from the external circuit. Some of this power is used to ionize the neutral gas to sustain the discharge,

some is used to excite bound electrons into higher energy states (thereby producing radiation) and some is used to heat the gas through electron-neutral. The fraction of the total power that goes into gas heating (η), is a function of the E/N ratio (ratio of the electric field to neutral number density) in the positive column of a gas discharge. For rare gases, η can be considered to be the fraction of the power that goes into momentum transfer collisions [66]. For molecular gases, η can be estimated as the fraction of the total power that does not go into either ionization or electronic excitation.

Anticipating the cylindrical geometry of the experimental arrangement, Equation 159 is cast in cylindrical coordinates, resulting in

$$\frac{d^2T}{dr^2} = -\frac{1}{r}\frac{dT}{dr} - \frac{Q(r)}{\kappa} - \frac{1}{\kappa}\frac{d\kappa}{dT}\left(\frac{dT}{dr}\right)^2 \tag{160}$$

where $Q(r) = \eta[\vec{J}\cdot\vec{E}]$. Note that the possibility of a singularity exists in the first term on the right hand side. By application of L'Hospital's rule and by assuming cylindrical symmetry, this term limits to $-\frac{d^2T}{dr^2}$ at small r. Therefore, two forms of Equation 160 result, one valid for points very near the origin and the other valid for points further removed from the origin:

$$\frac{d^2T}{dr^2} = \frac{1}{2}\left[-\frac{Q(r)}{\kappa} - \frac{1}{\kappa}\frac{d\kappa}{dT}\left(\frac{dT}{dr}\right)^2\right] \quad \text{for } r \approx 0 \tag{161}$$

$$\frac{d^2T}{dr^2} = -\frac{1}{r}\frac{dT}{dr} - \frac{Q(r)}{\kappa} - \frac{1}{\kappa}\frac{d\kappa}{dT}\left(\frac{dT}{dr}\right)^2 \quad \text{for } r \not\approx 0 \tag{162}$$

Computationally, Equation 161 is solved at the origin, while Equation 162 is solved at every other point in the r domain. A standard Runga-Kutta fourth order technique is used to integrate the differential equation in space.

D.2 Source Term

As mentioned previously, the difficulty in solving Equation 159 lies in the source term. For a given temperature profile ($T(r)$) the source term is known, however $T(r)$ is not known a priori. Therefore an iterative computational scheme is used in which an initial $T(r)$ profile is assumed. Using this initial (or guess) $T(r)$ profile to define the source term, Equation 160 is solved for a new $T(r)$ profile. This new $T(r)$ profile is then used to define a new source term, and the process is repeated until convergence is achieved. Therefore, although the final temperature profile is not known in the beginning, the functional form of the source term for a given $T(r)$ is known, and is used to determine the steady-state solution in a self-consistent manner which conserves the total current in the discharge. The source term $Q(r)$ is defined as

$$Q(r) = \eta(E/N)\ [\vec{J}(r) \cdot \vec{E}] \tag{163}$$

where η (the fraction of the total power that goes into gas heating) has been written explicitly as a function of the E/N ratio and the current density ($\vec{J}$) is a function of position.

The current density in the positive column (where the electrons are the majority charge carrier) can be defined as

$$\vec{J}(r) = n_e(r)\ q_e\ \vec{V}_{drift}\left(\frac{E}{N(r)}\right) \tag{164}$$

where n_e is the number density of electrons, q_e is the charge on an electron and $\vec{V}_{drift}$ is the drift velocity of the electron in the applied $\vec{E}$ field. $\vec{V}_{drift}$ is a function only of E/N within the positive column of the discharge for a given gas (Figure 106). E/N is a function of the electric field, (which is assumed to be constant over the discharge tube radius [83]) and the neutral number density, which is a function of pressure and

temperature given the equation of state $P = Nk_BT$. Thus,

$$\frac{E}{N}(r) = \frac{E}{P}k_BT(r) \tag{165}$$

where P has been assumed to be constant over the discharge tube radius. In the shock tube experiments of [46], constant pressure was maintained in the shock tube, thus this assumption is justified in steady-state numerical simulations of these experiments. A zeroth order Bessel function is used as the functional form for $n_e(0)$, in accordance with the standard theory of diffusion-dominated discharges in cylindrical geometry [31]. Thus

$$n_e(r) = n_e(0)\ J_0\left(\frac{r}{R}2.405\right) \tag{166}$$

where $n_e(0)$ is the on-axis electron number density and 2.405 is the first zero of J_0.

Experimentally, the discharge current is measured, not the current density. Therefore, the current density must be determined from the measured total current:

$$I = \int_0^{2\pi}\int_0^R J(r)\ r\ drd\theta \tag{167}$$

where R is the discharge tube radius and I is the total discharge current. Since the current density is a field quantity and the experimentally known parameter (total current) is an integrated quantity, the determination of $\vec{J}$ must be done carefully. Using Equations 164 through 166, Equation 167 can be written as

$$I = \int_0^{2\pi}\int_0^R n_e(0)J_0\left(\frac{r}{R}2.405\right) q_e\vec{V}_{drift}\left(\frac{E}{P}k_BT(r)\right)\ r\ drd\theta. \tag{168}$$

Solving this equation for $n_e(0)$ results in

$$n_e(0) = \frac{I}{\int_0^{2\pi}\int_0^R J_0\left(\frac{r}{R}2.405\right) q_eV_{drift}\left(\frac{E}{P}k_BT(r)\right) rdrd\theta}. \tag{169}$$

For a given experimental condition (current and pressure assigned) $n_\epsilon(0)$ is a function only of the temperature profile $T(r)$, which is the object of the calculation. Thus once a $T(r)$ profile is defined (either as an initial guess or as an intermediate solution in the iterative computational process) the on-axis electron number density is determined in a manner which ensures that the total current in the discharge remains a constant (Equation 167 being used as a constraint). This value of $n_\epsilon(0)$ is then used in the definition of the source term $Q(r)$ and Equation 163 can be written as

$$Q(r) = \eta\left(\frac{E}{P}k_B T(r)\right)\left[n_\epsilon(0) J_0\left(\frac{r}{R}2.405\right) q_e \vec{V}\left(\frac{E}{P}k_B T(r)\right)\cdot\vec{E}\right] \tag{170}$$

where the source is a function of only the temperature profile $T(r)$.

D.3 Boundary Conditions

The boundary conditions applied to the solution of Equation 160 are

$$\begin{aligned} \frac{dT(r)}{dr} &= 0 \quad \text{at } r = 0 \\ T(r) &= T_{wall} \quad \text{at } r = R \end{aligned} \tag{171}$$

The first condition is due to symmetry while the second condition assumes that the wall temperature (T_{wall}) is fixed.

D.4 Solution Method

Equation 160 is solved for the temperature $T(r)$, together with the use of Equation 170 describing the source term $Q(r)$ and the boundary conditions as given by Equation 171. The user supplied inputs to the calculation are divided into experimentally determined parameters and computational parameters. Included in the former are gas type, electric field in the positive column, discharge current, wall temperature and tube radius, while the latter include the number of spatial bins used to define the radial axis and the peak temperature to be used as the initial

guess of $T(0)$. Specifying the gas type defines the thermal conductivity to be used in the calculation, and a zeroth order Bessel function is used to define the initial guess profile $T(r)$ such that

$$T_{guess}(r) = T_{wall} + [T_{guess}(0) - T_{wall}]\, J_0\left(\frac{r}{R}2.405\right) \tag{172}$$

The use of J_0 as an approximation to the temperature profile is consistent with [39] in which an analytic solution was determined for the case in which the current density was assumed to follow a zeroth order Bessel function dependence. Once the initial temperature profile is defined the source term (Equation 170) is specified at all r values and Equation 160 is solved as a boundary value problem using a fourth order Runga-Kutta scheme, with the integration proceeding from $r = 0$ to $r = R$. The exact value of the initial on-axis temperature $T(0)$ which satisfies the boundary condition at $r = R$ is not known a priori, therefore a shooting method is used to adjust $T(0)$ until $T(R)$ is within a small epsilon of T_{wall} (typically 100 μK). During the solution of the boundary value problem, the $T(r)$ profile used to define the source term $Q(r)$ remains unchanged. After each solution of the boundary value problem has been obtained, it is used in Equation 169 to determine a new value for the on-axis electron number density (n_0) and in equation 170 to determine the subsequent source term. Equation 160 is re-solved with the updated source term as a boundary value problem, again ensuring that $T(R)$ is within a small epsilon of T_{wall}. This process is repeated until the $T(r)$ profiles determined from consecutive iterations are very nearly unchanged. In the present solution method, convergence is achieved when

$$T_m^N - T_m^{N-1} < 0.01, \tag{173}$$

where N denotes the Nth iteration in the cycle and T_m^N is defined as

$$T_m^N = \frac{R^2}{2}\left[\int_0^R \frac{rdr}{T^N(r)}\right]^{-1} \tag{174}$$

where $T^N(r)$ is the Nth solution to the boundary value problem. T_m is a density weighted mean temperature, the use of which was motivated by its utility as reported in the Russian literature ([41], [115]).

A summary of the solution algorithm is shown in Figure 103. In practice, the method typically requires between 5 and 40 iterations to converge and generally takes about 30 seconds to run on a 486 PC.

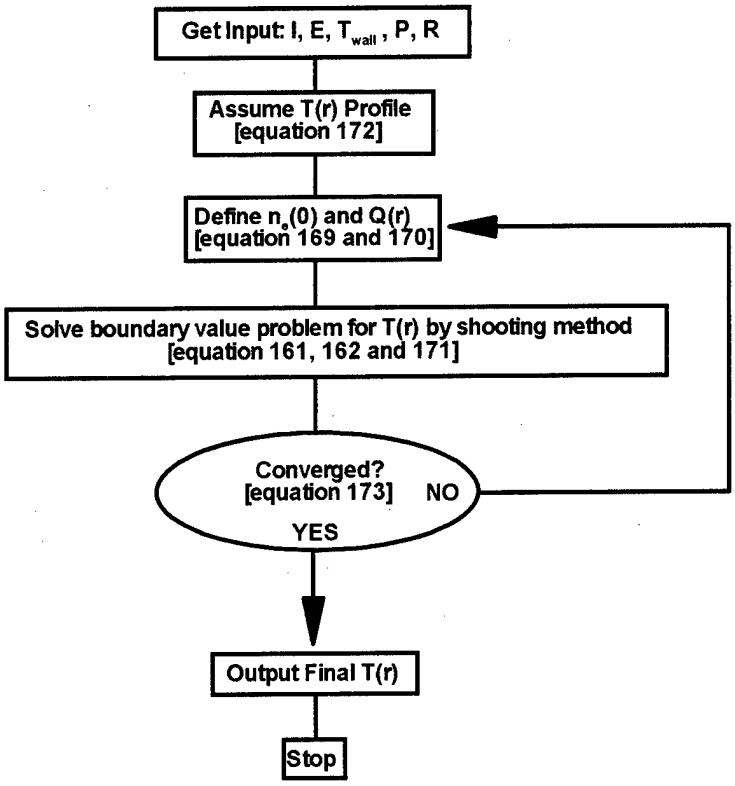

Figure 103. Thermal model solution algorithm

D.5 Input Parameters

The model used to determine the radial gas temperature profile requires a number of input parameters. These input parameters can be divided into two groups:

inputs which are an easily measurable quantity and remain fixed throughout the calculation and those which have an established functional form, but may vary throughout the calculation. The fixed input parameters are current (I), electric field (E), wall temperature (T_{wall}), pressure (P) and tube radius (R). The input parameters which are allowed to vary, but which have an established form, can be supplied to the program in the form of lookup tables. These inputs are the fractional power that goes into gas heating (η), electron drift velocity (V_{drift}), and the neutral gas thermal conductivity (κ). The first two are functions of only E/N, while the last is a function of only the neutral gas temperature.

The electric field and current in the positive column of a glow discharge are not independent parameters, but are related through the discharge characteristic. The experimentally measured variation in the electric field in an Argon discharge is

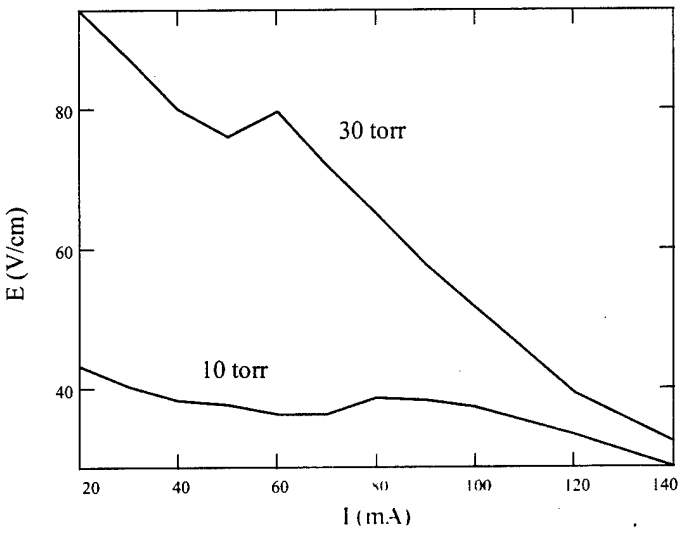

Figure 104. Electric Field in the positive column of a DC Argon Discharge as a function of discharge current [Data from [46]]

shown in Figure 104. This data was used in calculating the radial gas temperature profile for the shock simulations reported in Chapter 5.

The data that can be supplied to the model in terms of lookup tables are η (the fraction of the total power going into gas heating), V_{drift} (drift velocity of the electrons in the positive column due to the axial electric field) and κ (thermal conductivity of the neutral gas). The former two are shown in Figures 105 and

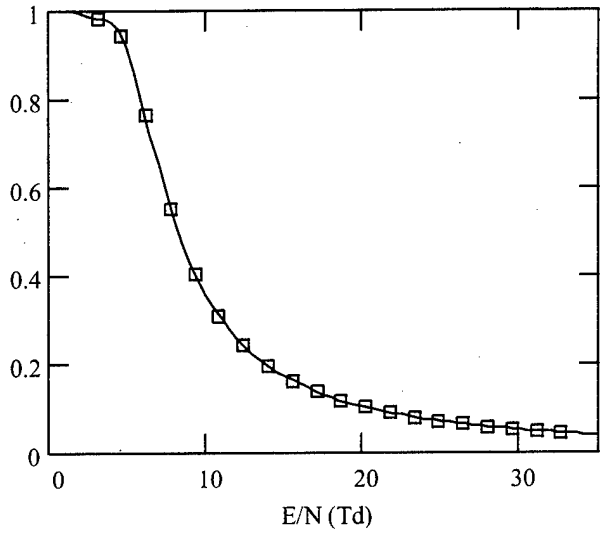

Figure 105. η (fractional power into gas heating) vs E/N in Argon (points were determined from numerical solution to Boltzmann's equation [97]; solid curve is a cubic spline fit to points)

106 as functions of E/N in Argon (E/N is in units of Townsend, where 1 Td = 1.0 $\times 10^{-17}$ Volt-cm^2). The data points in these figures were extracted from a numerical solution to the Boltzmann equation, using the Bolsig code [97]. Bolsig was run for a broad E/N range (1-100 Td), with the resulting transport coefficients cross-checked using an independent Boltzmann solver [17] to ensure accuracy. The solid curves in these figures represent a cubic spline fit to the data points and were used in the thermal model.

The thermal conductivity of Argon as a function of temperature is shown in Figure 107. The points in this figure were taken from tables in [5] while the solid curve is used in the thermal model to represent the thermal conductivity.

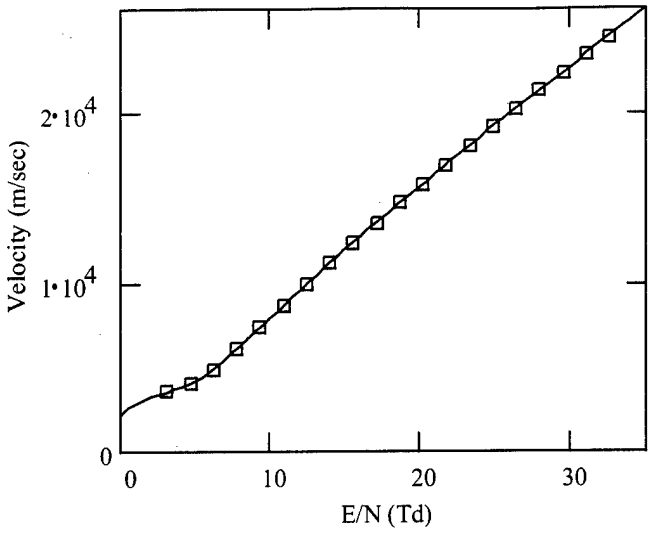

Figure 106. V_{drift} (electron drift velocity) vs E/N in Argon (points were determined from numerical solution to Boltzmann's equation [97]; solid curve is a cubic spline fit to points)

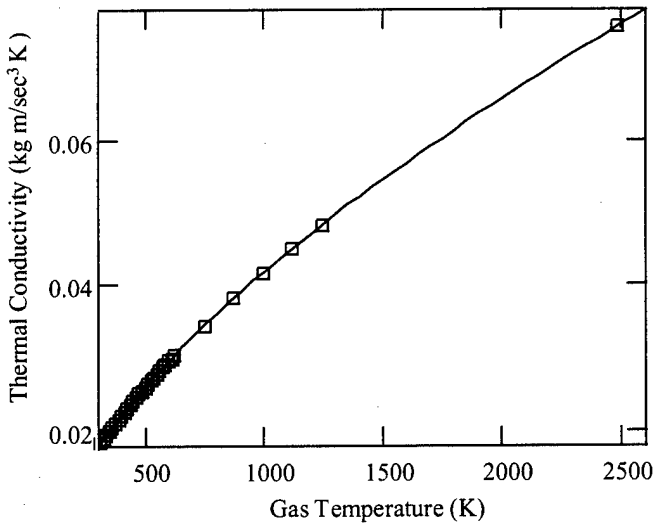

Figure 107. Thermal Conductivity in Argon [kg m/sec^3/K]

D.6 Test Cases and Typical Results

Results of the thermal model were compared to peak temperatures from previous calculations as reported in the literature. These comparisons are summarized in Table 1, where the peak temperatures from the present model are listed in the last column and the peak temperatures from previous calculations are listed in the next to last column. The agreement between the two is quite good, with less than 1% relative difference. The other entries in this table define the parameters of the calculation and are inputs into the present model (shown for clarity).

Table 1. Test Cases: Results of thermal model in Argon

Source	I (mA)	E (V/cm)	R (cm)	P (torr)	T_{wall} (K)	T_{peak}^{old} (K)	T_{peak}^{new} (K)
[39]	250	1.377	0.4	10	340	**525**	**529**
[39]	250	1.50	0.4	5	344	**543**	**547**

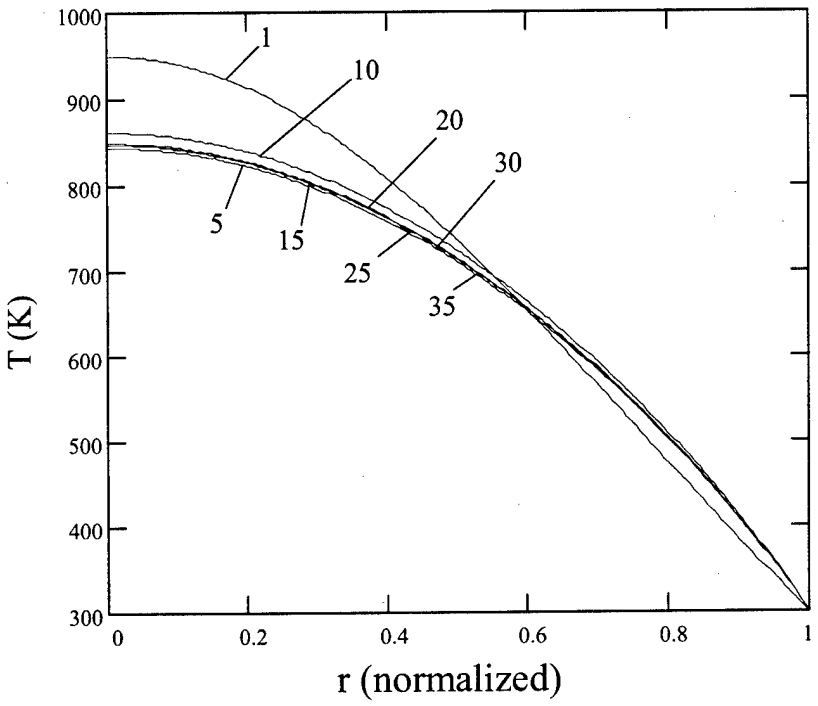

Figure 108. Intermediate T(r) profiles corresponding to the I=100 mA case in [46].

A typical sequence of intermediate T(r) profiles is shown in Figure 108 calculated for the I=100 mA case in [46] (Argon, $I = 100$ mA, $E = 51.5$ V/cm, $R = 2.5$ cm, $P = 30$ torr). This case took 35 iterations through the algorithm to converge, with the numbers shown in the figure corresponding to the iteration number. The curve labeled 1 is the initial guess (a J_0 Bessel function with a peak temperature of 950 K). The curve labeled 35 is the final converged solution. It is apparent there is little deviation between the solutions of successive iterations as the converged solution is approached.

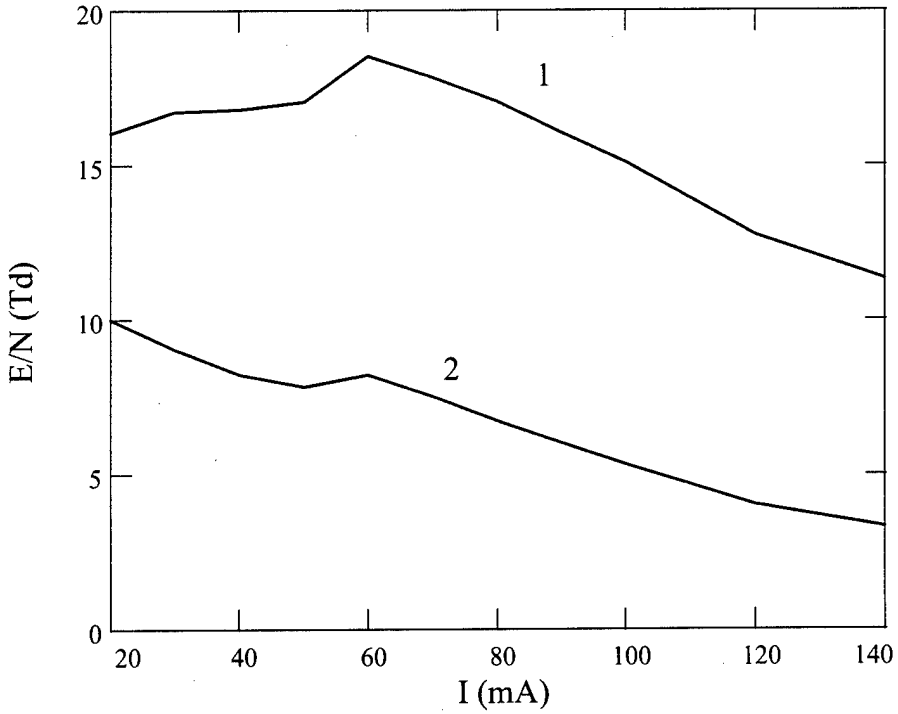

Figure 109. Calculated E/N ratios along centerline (curve 1) and along the tube wall (curve 2) for an Argon discharge at 30 torr (input parameters from [46]).

Using the electric field values determined experimentally for an Argon discharge at 30 torr (Figure 104) and the temperatures as determined by the thermal model, the E/N ratios along the centerline and tube wall can be calculated (see Equation 165). The result is shown in Figure 109, where curve 1 represents the E/N ratio (in

units of Td) along the centerline and curve 2 the same quantity along the tube wall. The E/N ratio is not a constant, but can vary from a maximum of approximately 18 Td (on the centerline for a current of 60 mA) to a minimum of approximately 4 Td (at the wall for a current of 140 mA): a factor of more than 4. Since the wall temperature in these calculations was assumed to be a constant ($300K$), the E/N ratio along the wall simply reflects the discharge characteristic as given in Figure 104. The calculation of the E/N ratio along the centerline, however, takes into account both the discharge characteristic and the centerline temperature, each of which varies with current.

The strength of the present thermal model is that all its inputs are parameters which are either readily controlled or measured by the experimenter. Other thermal models [[39], [41]] require the user to specify parameters over which the experimenter has no control, such as the fraction of the total power going into gas heating (η). In the present model, η is determined at each radial location by the local value of the E/N ratio, using the results from a Boltzmann equation solver in the process. Additionally, the source term used in the calculation (RHS of equation 159) is consistent at all times with the total discharge current. The algorithm upon which the present thermal code is based should be applicable in cases in which the local (or 0-D Boltzmann) model of the plasma holds and in which the wall temperature (T_{wall}) of the discharge tube can be specified as a constant. While T_{wall} may continue to rise over time until a true steady-state is achieved, it can be considered to be constant over the time in which a shock propagates through the discharge. Therefore, it should be applicable in the positive column of the discharge. Finally, the effect of the convective flow of gas has not been included in this gas heating model.

Appendix E. Optical Diagnostics in Shock Tubes: A Short Tutorial

Optical measurements are frequently made in shock tubes due to their non-intrusive nature. That is, measurements can be made without inserting probes into the shock tube that would otherwise interfere with the gaseous flow. Both density and density gradient measurement techniques have been used in investigating plasma/shock interactions and each relies on a different physical principle. Understanding these principles is essential in order to compare the results of numerical simulations to the measured data.

Although optical measurement techniques applied to shock waves are probably well known in certain settings, it was a new field to the author, and as such provided some difficulty in understanding the data reported in the literature. Accordingly, a good measure of time was spent in researching the various techniques in an effort to determine the manner in which the simulated data should be sampled in order to provide a meaningful comparison to experimental results. The purpose of the present appendix is not to replace the existing volumes of literature on the subject of optical shock diagnostics, rather, the intent is to provide a short tutorial of two optical techniques commonly employed and to provide enough references to send the interested reader in the proper direction to get more information.

Although many optical methods are available for shock tube diagnostics, only those methods used in experiments which were numerically simulated in the present research will be discussed. These methods are optical interferometry and photoacoustic deflection spectroscopy (PADS). Using a Riemann problem as a basis, both of these techniques will be addressed and a sample of the simulated data provided by each will be shown.

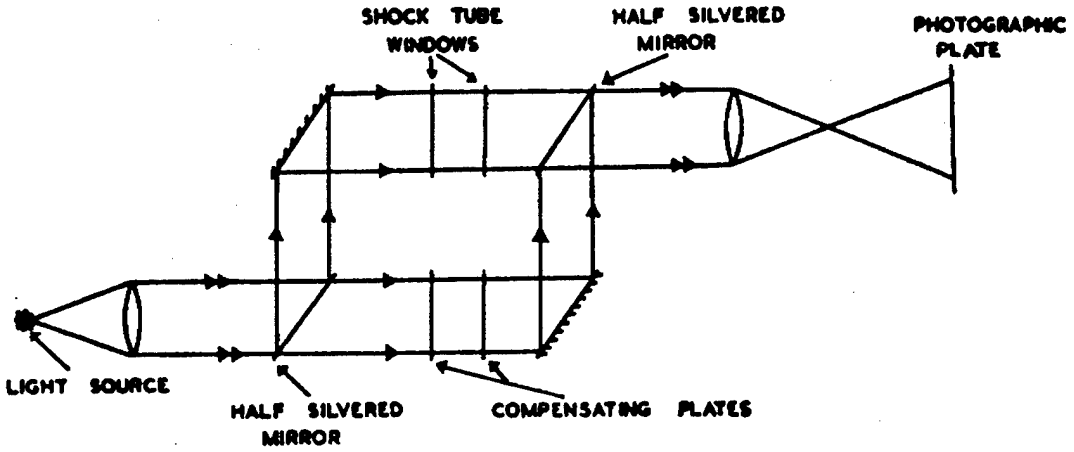

Figure 110. Typical Mach Zehnder interferometer used in shock tube diagnostics [118].

According to Wright [118:49], the interferometer is 'undoubtably the best method of obtaining quantitative information about the density profile of the flow in a shock tube.' A Mach Zehnder interferometer is shown in Figure 110. A monochromatic light source of wavelength λ is split into two legs, only one of which traverses the shock tube. The other leg is designed to have the same optical path as the first, using glass plates to compensate for the optical path difference and dispersion introduced by the shock tube windows. Any density change from ambient ($\Delta\rho$) in the shock tube portion of the path causes a change in the refractive index (Δn) at the same location. That is, since the density and refractive index are related through

$$n = 1 + K\rho, \tag{175}$$

where K is known as the Gladstone Dale constant (see [118:41] for typical values), the changes are also related, in that

$$\Delta n = K\Delta\rho. \tag{176}$$

The optical path length is increased by $Y\Delta n$ (where Y is the width of the shock tube), which can be equated to an integral number of wavelengths ($N\lambda$). Thus, the change in density can be determined by the number of fringes which are observed as the shock passes, according to

$$N = \frac{KY}{\lambda}\Delta\rho. \tag{177}$$

In general, the density change across the shock tube can be a function of position, that is, $\Delta\rho = \Delta\rho(y)$, where y is the transverse coordinate. Such would be the case if a transverse thermal gradient were present, for example. In this case, the number of fringes observed would be determined by the integrated value of the density change at each transverse position, given by

$$N = \frac{K}{\lambda}\int_0^Y \Delta\rho(y)dy. \tag{178}$$

Thus, one sees a difficulty emerging in that while the number of fringes can be measured, the density change inferred from this measurement is a quantity averaged over the width of the shock tube. Accordingly, the density that is reported in the literature using this technique can be described as an average density, defined as

$$\rho(t) = \frac{1}{Y}\int_0^Y \rho(y,t)dy \tag{179}$$

where t denotes time. In the two-dimensional numerical simulations of experiments using the interferometry technique, Equation 179 was used to sample the computed density field at each time step of the calculation.

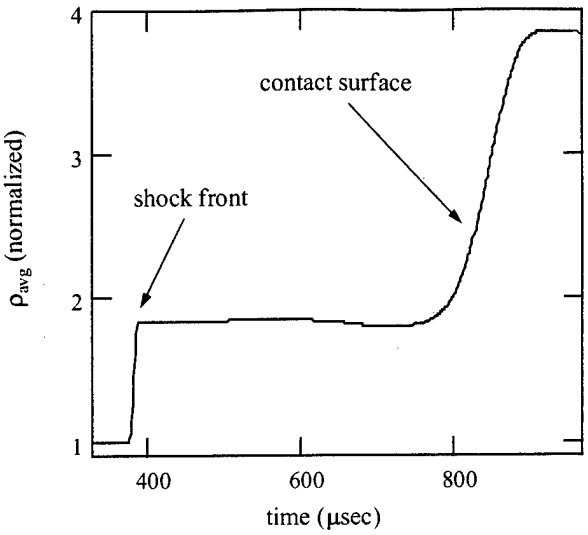

Figure 111. Typical simulated signal resulting from the application of the interferometer measurement technique (equation 179) to a two-dimensional Riemann problem for a shock in gas at $300K$.

Using the Riemann problem as a basis, the temporal variation of the transverse-averaged density (according to Equation 179) is shown in Figure 111. The shock tube used in this example is 100 cm long with a width of 5 cm. The diaphragm is initially located at 40 cm and Equation 179 was applied transversely at a longitudinal location of 60 cm. The initial pressure and temperature ratios in the shock tube were 10.0 and 1.25, respectively, resulting in a Mach 1.6 shock in Argon. The temperature on the low pressure side of the diaphragm is $300K$. The sharp initial rise in the curve is due to the passage of the shock wave front. The average density (normalized by the upstream ambient density) rises to a level of 1.84, consistent with the Rankine-Hugoniot relations under the given conditions. The density remains relatively constant at this level until the passage of the contact surface. Ideally, the rise associated with the contact surface would also be very steep, however numerical dissipation from the computational algorithm causes this region to be diffuse. This is typical of many computational algorithms in the contact surface region.

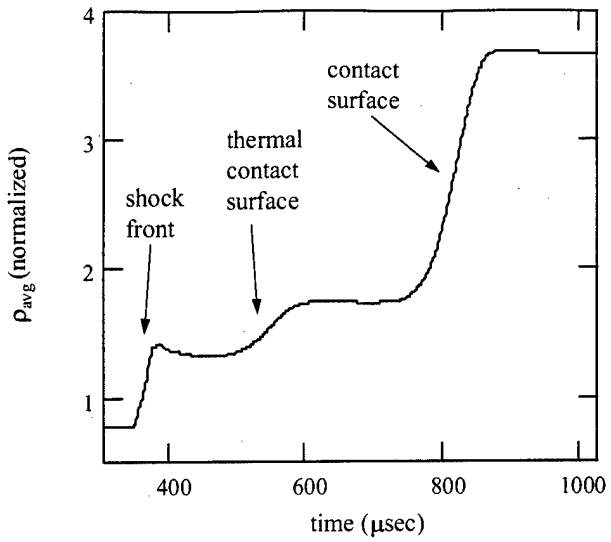

Figure 112. Typical simulated signal resulting from the application of the interferometer measurement technique (equation 179) to a two-dimensional Riemann problem for a shock in gas with a radial thermal inhomogeneity.

As another example, the case in which a radial thermal inhomogeneity is present will be considered. Here, the conditions are exactly the same as in the previous example, except a heated region is present, starting 10 cm from the diaphragm on the low pressure side. The region is heated according to Equation 88 with $T_0 = 300K$ and $T_1 = 200K$. The temporal variation in the average density is shown in Figure 112. The rise in the density at the shock front is not as sharp as in the previous example. This is due to the curvature of the shock front resulting from the transverse thermal inhomogeneity. The density reaches a localized maximum, then decreases until passage of the thermal contact surface (see Chapter V). Another steady rise in the density is associated with the passage of the contact surface.

E.2 Photo-Acoustic Deflection Spectroscopy

The photo-acoustic deflection spectroscopy (PADS) technique also relies on the principle of an index of refraction change caused by the passage of a shock wave, but in a completely different way from the interferometer. In the PADS technique, laser light traverses the shock tube at normal incidence to the tube walls, as shown in Figure 113. A passing shock wave produces density gradients in the x direction resulting in gradients in the index of refraction in the x direction as well. For

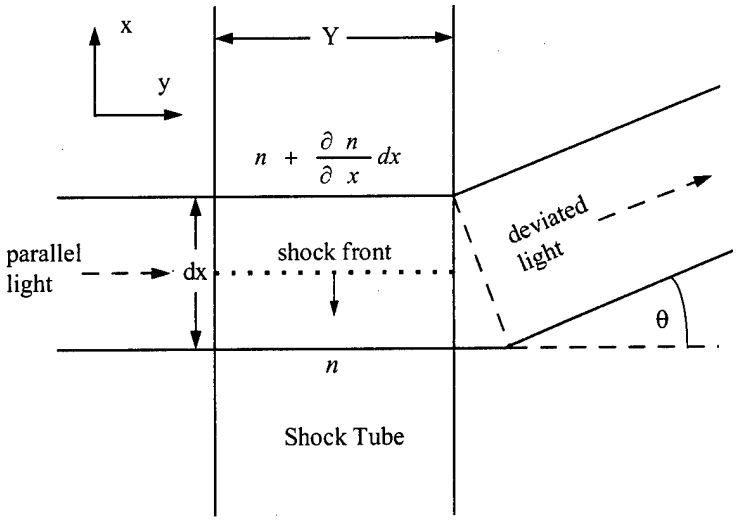

Figure 113. Deviation of a light beam by a refractive index gradient, as used by photo-acoustic deflection spectroscopy (adapted from [118]).

example, behind the shock the density is higher than in front of the shock, thus the optical path length is greater in this region than in front of the shock. This larger path length results in the wavefront being deflected from the normal. This deflection is not limited to the wave front only, as the Poynting vector of the wave is also deflected. Thus, the laser beam is deflected from the normal. The amount by which the optical path length is changed can be expressed as [118:46]

$$dy = Y \frac{dn}{dx} dx, \tag{180}$$

thus small angular deflections ($\approx dy/dx$)can be expressed as

$$\theta = Y\frac{dn}{dx}. \tag{181}$$

In general, the longitudinal gradient of the index of refraction can be a function of position, thus $\nabla_\perp n = \nabla_\perp n(y)$, where the symbol $\perp$ indicates the gradient is to be computed in the x direction, which is perpendicular to the initial direction of the laser beam. This would happen in the case of a shock propagating through a transverse thermal inhomogeneity, for example. In this case, Equation 181 would become

$$\theta = \int_0^Y \nabla_\perp n(y)dy, \tag{182}$$

which is, to within a constant of the order of unity, equivalent to the expression given in [96:507]. Making use of the relationship between index of refraction and density (Equation 175), Equation 182 becomes

$$\theta = K\int_0^Y \nabla_\perp \rho(y)dy, \tag{183}$$

indicating the linear relationship between angular deflection and the integrated value of the transverse density gradient.

Experimentally, it is common practice to use a single detector to measure the laser beam deflection ([96], [46], [95], for example). This is made possible by use of either a knife edge (as in [96]) or a slit (as in [46] and [95]), which blocks a portion of the beam from the detector. According to [96], the voltage from the photodetector in such an arrangement will be according to

$$\Delta V = V_0 \,\mathrm{erf}\,(\sqrt{2}\phi/\theta), \tag{184}$$

where erf is the error function, V_0 is the signal from the photodetector under ambient conditions and ϕ is the divergence angle from the laser, given as $\phi = \lambda/(\pi w_0)$,

where w_0 is the beam waist. For small deflection angles, the photodetector signal is proportional to the deflection angle, as given by Equation 183. Notice, however, that the beam deflection can be either positive or negative, according to whether the integrated density gradient is either positive or negative. More information on the photo-acoustic deflection technique can be found by in [7], [30], [67], [95], [100], [104], [107] and [122].

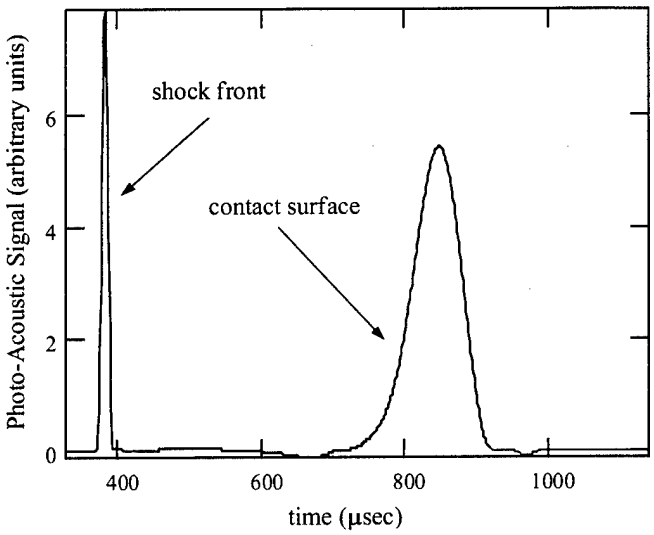

Figure 114. Typical simulated signal resulting from the application of the photo-acoustic deflection measurement technique (equation 184) to a two-dimensional Riemann problem for a shock in gas at $300K$.

As an example of this technique, consider a Riemann problem in which the shock propagates into Argon at a uniform temperature of $300K$. The shock tube configuration is the same as given previously. The temporal variation of the photo-acoustic signal, which has been assumed to be proportional to the laser deflection angle given by Equation 183, is shown in Figure 114. The sharp spike at approximately 400 μsec is due to passage of the shock wave front. The width of this signal is an indication of the width of the shock front. Behind the shock front, the density is relatively constant, as shown in Figure 111. The passage of the contact surface results in another signal, starting at approximately 800 μsec. This signal is broader

in time than that associated with the shock front. This is a result of the numerical dissipation in the contact surface region mentioned previously in this appendix.

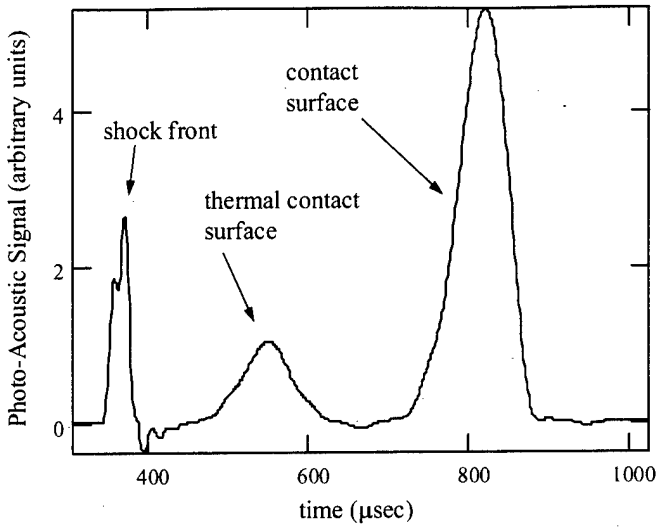

Figure 115. Typical simulated signal resulting from the application of the photo-acoustic deflection measurement technique (equation 184) to a two-dimensional Riemann problem for a shock in gas with a radial thermal inhomogeneity.

As a final example, consider the case in which the shock propagates into a region with a transverse thermal inhomogeneity, defined exactly as before. The temporal variation of the photo-acoustic signal in this case is shown in Figure 115. Again, a sharp spike is present in the signal which is associated with passage of the shock front. However, the structure of this spike is different in this case, due to the curvature of the shock front in the presence of a thermal inhomogeneity. Broader signals associated with the thermal contact surface and contact surface are also shown.

Bibliography

1. Abe, Kanji and Gyo Sakaguchi. "Linear and Nonlinear Evolution of Double-humped Ion Distributions in Strong Unmagnetized Shock Structures," *The Physics of Fluids*, *28*(12):3581–3589 (December 1985).
2. Aleksandrov, A.F., et al. "A possible mechanism for interaction of a shock wave with a decaying plasma in air," *Sov. Phys. Tech. Phys.*, *31*(4):468–469 (April 1986).
3. Anderson, Dale A., et al. *Computational Fluid Mechanics and Heat Transfer*. Hemisphere Publishing Corporation, 1984.
4. Anderson, Jr., John D. *Introduction to Flight*. New York: McGraw-Hill, Inc., 1978.
5. Anderson, Jr., John D. *Hypersonic and High-Temperature Gas Dynamics*. New York: McGraw-Hill, Inc., 1989.
6. Avramenko, R.F., et al. "Structure of a shock wave in a weakly ionized non-isothermal plasma," *JETP Lett.*, *34*(9):463–466 (1981).
7. Azzeer, A.M., et al. "Optical probing of laser-induced shock waves in air," *Appl. Phys. B*, *63*:307–310 (1996).
8. Bailey, William F. *Collision induced dissociation of diatomic molecules*. PhD dissertation, Air Force Institute of Technology, Wright-Patterson AFB, OH, 1978.
9. Baksht, F.G. and G.I. Mishin. "Effects of vibrational relaxation on the parameters of shock waves in a molecular gas plasma," *Sov. Phys. Tech. Phys.*, *28*(5):547–549 (May 1983).
10. Barkhudarov, E.M., et al. "Dissipation of a weak shock wave in a laser spark in air," *Sov. Tech. Phys. Lett.*, *10*(10):498–499 (October 1984).
11. Basargin, I.V. and G.I. Mishin. "Probe studies of shock waves in the plasma of a transverse glow discharge," *Sov. Tech. Phys. Lett.*, *11*(11):535–538 (1985).
12. Basargin, I.V. and G.I. Mishin. "Shock-wave propagation in the plasma of a transverse glow discharge in argon," *Sov. Tech. Phys. Lett.*, *11*(2):85–87 (1985).
13. Basargin, I.V. and G.I. Mishin. "Precursor of shock wave in glow-discharge plasma," *Sov. Tech. Phys. Lett.*, *15*(4):311–313 (1989).
14. Basargin, I.V. and G.I. Mishin. "Evolution of anomalous dynamic properties of a decaying glow-discharge plasma," *Tech. Phys.*, *41*(7):742–744 (1996).
15. Beam, R.M. and R.F. Warming. "An Implicit Finite-Difference Algorithm for Hyperbolic Systems in Conservation Law Form," *J. Comp. Phys.*, *22*:87–110 (1976).

16. Bedin, A.P. and G.I. Mishin. "Ballistic studies of the aerodynamic drag on a sphere in ionized air," *Tech. Phys. Lett.*, *21*(1):5–7 (January 1995).

17. Bennett, Eric, "Bolt — A Time - Dependent Bolzmann Solver." Unpublished, July 1996. Air Force Institute of Technology, Wright-Patterson AFB, OH.

18. Beran, Philip S., "Aero752 Lecture Notes." 1997. AERO 752 - Computational Aerodynamics, Air Force Institute of Technology, Wright-Patterson AFB, OH.

19. Bhatnagar, P.L., et al. "A Model for Collision Processes in Gases. I. Small Amplitude Processes in Charged and Neutral One-Component Systems," *Physical Review*, *94*:511 (1954).

20. Bletzinger, Peter. Private Communication, 1997. Wright Laboratory (WL/POO), Wright-Patterson AFB, OH.

21. Bond, Jr., John W., et al. *Atomic Theory of Gas Dynamics*. Reading, Mass.: Addison-Wesley, 1965.

22. Bond, Jr., J.W. "Plasma Physics and Hypersonic Flight," *Jet Propulsion*, 228–235 (April 1958).

23. Boris, J.P. and D.L. Book. "Flux Corrected Transport I, SHASTA, a Fluid Transport Algorithm that Works," *Journal of Computational Physics*, *11*:38–69 (1973).

24. Bray, K.N.C. "Vibrational relaxation of anharmonic oscillator molecules: relaxation unber isothermal conditions," *J. Phys. B (Proc. Phys. Soc.)*, *1*:705 (1968).

25. Brown, Garry, "Hypersonic Flow Control." Plasma-Based Hypersonic Drag Reduction Workshop, Wright-Patterson AFB, OH, May 1996.

26. Buyanova, E.A., et al. "Stationary Shock Waves in a Nonequilibrium Diatomic Gas," *Sov. J. Chem. Phys.*, *1*(12):2856–2860 (1984).

27. Bystrov, S.A., et al. "Propagation of Plane Shock Wave in Weakly Ionized Plasma," *Sov. J. Plasma Phys.*, *15*(5):324–326 (1989).

28. Bystrov, S.A., et al. "Precursor ahead of a shock front in an rf discharge plasma," *Sov. Phys. Dokl.*, *35*(1):39–40 (1990).

29. Cambel, Ali Bulent. *Plasma Physics and Magnetofluiddynamics*. New York: McGraw-Hill Book Co., 1963.

30. Casperson, Lee W. "Gaussian Light Beams in Inhomogeneous Media," *Applied Optics*, *12*(10):2434–2441 (1973).

31. Cherrington, B.E. *Gaseous Electronics and Gas Lasers*. New York: Pergamon Press, 1979.

32. Chutov, Yu.I. "Experimental Investigation of Shock Waves in a Partially Ionized Discharge Plasma," *Zhurnal Prikladnoi Mekhaniki i Tekhnicheskoi Fiziki*, *11*(1):124–130 (1970).

33. Chutov, Yu.I. and V.N. Podolskii. "Shock Waves in a Gas-Discharge Plasma," *Journal of Engineering Physics and Thermophysics*, *62*(5):504–509 (May 1992).

34. Chutov, Yu.I., et al. "Explosive waves in an evolving gas discharge," *Sov. Tech. Phys. Lett.*, *17*(2):101–102 (February 1991).

35. DeJoseph, Jr., C.A., "N2 Kinetic Vibration Code." Private Communication, 1997. Wright Laboratory (WL/POO), Wright-Patterson AFB, OH.

36. Dendy, Richard. *Plasma Physics: An Introductory Course*. Cambridge: Cambridge University Press, 1993.

37. Dolgov, G.G. and S.L. Mandel'shtam. "Density and temperature of a gas in a spark discharge," *Zh. Eksperim. i Teor. Fiz.*, *24*:691–700 (1953).

38. Drabkina, S.I. "The theory of the development of a spark discharge column," *Zh. Eksperim. i Teor. Fiz.*, *21*:473–483 (1951).

39. Eden, J.G. and B.E. Cherrington. "Radial neutral gas temperature and density profiles in low-pressure argon discharges," *J. Appl. Phys.*, *44*(11):4920–4926 (November 1973).

40. Emanuel, G. *Gasdynamics: Theory and Applications*. New York: American Institute of Aeronautics and Astronautics, 1986.

41. Evtyukhin, N.V., et al. "On the Nature of Shock Wave Acceleration in Glow Discharge Plasma," *Sov. J. Chem. Phys.*, *3*(9):2080–2089 (1986).

42. Evtyukhin, N.V., et al. "Shock Waves in a Vibrationally Excited Gas," *Sov. J. Chem. Phys.*, *4*(9):2100–2108 (1987).

43. Feynman, Richard P., et al. *The Feynman Lectures on Physics, II*. Reading, Massachusettes: Addison-Wesley Publishing Company, Inc., 1964.

44. Fletcher, C.A.J. *Computational Techniques for Fluid Dynamics*. Berlin: Springer-Verlag, 1991.

45. Ganguly, B.N., "Private Communication," 1997. Wright Laboratory (WL/POO), Wright-Patterson AFB, OH.

46. Ganguly, B.N. and P. Bletzinger. "Shock Wave Dispersion in Nonequilibrium Plasmas," *AIAA Paper 96-4607* (1996).

47. Godunov, S.K., "A difference scheme for numerical computation of discontinuous solution of hydrodynamic equations." Math. Sbornik, 47:271-306 (in Russian). Translated in US Joint Publ. Res. Service, JPRS 7226 (1969).

48. Gordeev, V.P., et al. "Experimental Study of the Possibility of Reducing Supersonic Drag by Employing Plasma Technology," *Fluid Dynamics*, *31*(2):313–317 (1996).

49. Gordiets, Boris F., et al. *Kinetic Processes in Gases and Molecular Lasers*. New York: Gordon and Breach Science Publishers, 1988.

50. Gorshkov, V.A., et al. "Behavior of electron density in a wakly ionized nonequilibrium plasma with a propagating shock wave," *Sov. Phys. Tech. Phys.*, *32*(10):1138–1141 (October 1987).

51. Grachev, L.P., et al. "Interaction of a shock wave with a decaying plasma in an electrodeless microwave discharge," *Sov. Phys. Tech. Phys.*, *30*(5):586–588 (1985).

52. Gridin, A.Yu., et al. "Propagation of Shock Waves in a Nonuniform Transverse Pulsed Discharge," *High Temperature*, *32*(4):454–457 (1994).

53. Gridin, A.Yu., et al. "Two-Dimensional Simulation of Shock Wave Propagation in a Transverse Pulse Glow Discharge with a Heated Cathode Layer," *High Temperature*, *32*(6):755–758 (1994).

54. Gridin, A.Yu., et al. "Structure of a shock wave in the plasma of a nonsteady-state glow discharge with ultraviolet irradiation," *Sov. Tech. Phys. Lett.*, *16*(4):295–297 (1990).

55. Gridin, A.Yu., et al. "Propagation of shock waves in the plasma of a glow discharge," *Technical Physics*, *38*(3):238–240 (March 1993).

56. Gureev, K.G. and V.O. Zolotarev. "Evolution of the molecular vibrational distribution function and the structure of the flow in the relaxation zone behind a stationary shock front in a vibrationally excited molecular gas," *Sov. Phys. Tech. Phys.*, *35*(2):149 (February 1990).

57. Gurijanov, Evgeniy P. and Philip T. Harsha. "AJAX: New Directions in Hypersonic Technology," *AIAA Paper 96-4609* (November 1996).

58. Harsha, Philip T. Private Communication, August 1997. Hypersonics Division, North American/Boeing.

59. Harten, A. "High Resolution Schemes for Hyperbolic Conservation Laws," *Journal of Computational Physics*, *9*:357–393 (1983).

60. Hasegawa, Masaaki. "Amplification of Sound Waves in Partially Ionized Gases," *Journal of the Physical Society of Japan*, *37*(1):193–199 (July 1974).

61. Hirsch, Charles. *Numerical Computation of Internal and External Flows*. New York: John Wiley and Sons, 1990.

62. Hoffmann, Klaus A. and Steve T. Chiang. *Computational Fluid Dynamics for Engineers*. Wichita, Kansas: Engineering Education System, 1993.

63. Ingard, Uno and Kenneth W. Gentle. "Longitudinal Waves in a Weakly Ionized Gas," *The Physics of Fluids*, *8*:1396–1397 (1965).

64. Ingard, Uno and Michael Schulz. "Acoustic Wave Mode in a Weakly Ionized Gas," *Physical Review*, *158*(1):106–111 (1967).

65. Ingard, Uno and Michael Schulz. "Ion Density and Electric-Field Perturbations Caused by an Acoustic-Wave Pulse in a Weakly Ionized Gas," *Phys. Fluids*, *11*:106–111 (June 1967).

66. Ingold, John. Private Communication, 1997.

67. Jackson, W.B., et al. "Photothermal deflection spectroscopy and detection," *Applied Optics*, *20*(8):1333–1344 (1981).

68. Jaffrin, Michel Y. "Shock Structure in a Partially Ionized Gas," *The Physics of Fluids*, *8*(4):606–625 (1965).

69. Jaffrin, Michel Y. and Ronald F. Probstein. "Structure of a Plasma Shock Wave," *The Physics of Fluids*, *7*(10):1658–1674 (October 1964).

70. Jones, W.D., et al. *An Introduction to the Linear Theories and Methods of Electrostatic Waves in Plasmas*. New York: Plenum Press, 1985.

71. Kandebo, Stanley W. "'Air Spike' Could Ease Hypersonic Flight Problems," *Aviation Week and Space Technology*, *142*:66–67 (May 1995).

72. Keck, J.C. and G. Carrier. "Diffusion Theory of Nonequilibrium Dissociation and Recombination," *Journal of Chemical Physics*, *43*:2284 (1965).

73. Klimov, A.I. Private Communication, April 1996. Flow Control Through Plasma Effects, Windows on Science Lecture, Wright-Patterson AFB, OH.

74. Klimov, A.I., et al. "Shock wave propagation in a decaying plasma," *Sov. Tech. Phys. Lett.*, *8*(5):240–241 (1982).

75. Klimov, A.I., et al. "Shock wave propagation in a glow discharge," *Sov. Tech. Phys. Lett.*, *8*(4):192–194 (1982).

76. Klimov, A.I. and G.I. Mishin. "Interferometric studies of shock waves in a gas-discharge plasma," *Sov. Tech. Phys. Lett.*, *16*(12):960–962 (1990).

77. Klimov, A.I., et al. "Propagation of shock waves in a non-steady-state discharge," *Sov. Tech. Phys. Lett.*, *15*(10):800–802 (1989).

78. Landau, L. and E. Teller. "Zur Theorie der Schalldispersion," *Physik Z. Sowjetunion*, *b. 10*(h. 1):34 (1936).

79. Landau, L.D. and E.M. Lifshits. *Fluid Mechanics*. London: Pergamon Press, 1959.

80. Lu, C.S. and A.B. Huang. "Shock-Wave Structure in a Partially Ionized Gas," *The Physics of Fluids*, *17*(8):1527–1534 (August 1974).

81. Lusczek, Jr., Joseph J., et al., editors. *Proceedings of the Hypersonics: The New Physics Conference*, *ASC-TR-97-5013*, 1997.

82. MacCormack, R.W. "The Effect of Viscosity in Hypervelocity Impact Cratering," *AIAA Paper 69-354* (1969).

83. Maksimov, A.I., et al. "Thermocouple measurements of the gas temperature in a glow discharge," *Sov. J. Plasma Phys.*, *4*(2):194–197 (1978).

84. Millikan, Roger C. and Donald R. White. "Systematics of Vibrational Relaxation," *The Journal of Chemical Physics*, *39*(12):3209–3213 (December 1963).

85. Mishin, G.I. "Shock waves in a weakly ionized nonisothermal plasma," *Sov. Tech. Phys. Lett.*, *11*(3):112–114 (1985).

86. Mishin, G.I. *Gas Dynamics*, chapter Sonic and Shock Wave Propagation in Weakly Ionized Plasma. Commack, New York: Nova Science Publishers, Inc., 1992.

87. Mishin, G.I. "Total pressure behind a shock wave in weakly ionized air," *Sov. Tech. Phys. Lett.*, *20*(11):857–859 (1994).

88. Mishin, G.I., et al. "Anomalous relaxation and instability of shock waves in gases," *Sov. Tech. Phys. Lett.*, *26*(11):1363–1368 (1981).

89. Mishin, G.I., et al. "Measurements of the pressure and density in shock waves in a gas discharge plasma," *Sov. Tech. Phys. Lett.*, *17*(8):602–604 (1991).

90. Mishin, G.I., et al. "Flow around a sphere moving supersonically in a gas-discharge plasma," *Sov. Tech. Phys. Lett.*, *17*(6):413–416 (1991).

91. Mott-Smith, H.M. "The Solution of the Boltzmann Equation for a Shock Wave," *The Physical Review*, *82*(6):885–892 (June 1951).

92. Newell, Alan C., et al., "Can One Use A Plasma Sheath Around Hypersonic Vehicles to Improve Flight Characteristics?." Plasma-Based Hypersonic Drag Reduction Workshop, Wright-Patterson AFB, OH, May 1996.

93. Osipov, A.I. and A.V. Uvarov. "Kinetic and Gasdynamic Processes in Nonequilibrium Molecular Physics," *Sov. Phys. Usp.*, *35*(11):903–923 (November 1992).

94. Peterkin, Jr., Robert E. and Captain Dennis E. Lileikis, "Simulating Plasma-Magnetic Field Interactions for Boundary Layer Control in Hypersonic Flight." Plasma-Based Hypersonic Drag Reduction Workshop, Wright-Patterson AFB, OH, May 1996.

95. Petzoldt, S., et al. "Surface laser damage thresholds determined by photacoustic deflection," *Appl. Phys. Lett.*, *53*(21):2005–2007 (1988).

96. Pini, R., et al. "Probe-beam deflection diagnostics of shock waves generated during laser drilling," *Appl. Phys. B*, *61*:505–510 (1995).

97. Pitchford, L.C. and W.L. Morgan, "Bolsig Version 1.05 Electron Boltzmann Equation Solver," 1996. Freeware.

98. Raizer, Yu. P. *Gas Discharge Physics*. Berlin: Springer-Verlag, 1991.

99. Roe, P.L. "Approximate Riemann solvers, parameter vectors and difference schemes," *Journal of Computational Physics*, *43*:357–72 (1981).

100. Rose, A. and R. Gupta. "Application of photothermal deflection technique to flow-velocity measurements in a flame," *Optics Letters*, *10*(11):532–534 (1985).

101. Rukhadze, A.A., et al. "Propagation of Nonstationary Shock Waves in Vibrationally Excited Nitrogen," *Soviet Physics Lebedev Institute Report*, (6):18–23 (1983).

102. Sato, Masumi and Satoshi Arima. "Measurements of gas temperature in an argon positive column using acoustic wave propagation," *J. Phys. D: Appl. Phys.*, *23*:1302–1306 (1990).

103. Schwartz, R.N., et al. "Calculation of Vibrational Relaxation Times in Gases," *J. Chem. Phys.*, *20*(10):1591 (October 1952).

104. Sell, Jeffrey A., et al. "Laser beam deflection as a probe of laser ablation materials," *Appl. Phys. Lett.*, *55*(23):2435–2002437 (1989).

105. Serov, Yu.L. and I.P. Yavor. "Ablation during supersonic motion of an object in a plasma," *Tech. Phys.*, *40*(3):248–251 (March 1995).

106. Sessler, G.M. "Propagation of Longitudinal Waves in a Weakly Ionized Gas," *The Physics of Fluids*, *7*(1):90–95 (January 1964).

107. Sigrist, Markus W. "Laser generation of acoustic waves in liquids and gases," *J. Appl. Phys.*, *60*(7):R83–R90 (1986).

108. Strang, G. *Linear Algebra and Its Applications*. New York: Academic Press, 1968.

109. Strang, G. "On the construction and comparison of difference schemes," *SIAM J. Numer. Anal.*, *5*(3):506–517 (1968).

110. Sutton, George W. and Arthur Sherman. *Engineering Magnetohydrodynamics*. McGraw-Hill Book Company, 1965.

111. Tidman, D.A. "Structure of a Shock Wave in Fully Ionized Hydrogen," *The Physical Review*, *111*(6):1439–1446 (September 1958).

112. Toth, Gabor and Dusan Odstrcil. "Comparison of Some Flux Corrected Transport and Total Variation Diminishing Numerical Schemes for Hydrodynamic and Magnetohydrodynamic Problems," *Journal of Computational Physics*, *128*:82–100 (1996).

113. Vidal, F., et al. "Ion Kinetic Simulations of the Formation and Propagation of a Planar Collisional Shock Wave in a Plasma," *The Physics of Fluids*, *5*(9):3182–31190 (September 1993).

114. Vincenti, Walter G. and Jr. Charles H. Kruger. *Introduction of Physical Gas Dynamics*. Malabar, Florida: Robert E. Krieger Publishing Company, 1965.

115. Voinovich, P.A., et al. "Propagation of Weak Shock Waves in Plasma of Longitudinal Flow Discharge in Air," *High Temperature*, *29*:468–475 (1991).

116. Vstovskii, G.V. and G.I. Kozlov. "Propagation of weak shock waves in a vibrationally excited gas," *Sov. Phys. Tech. Phys.*, *31*(8):911–914 (1986).

117. Wood, 2nd Lt, Brandon, "AEDC Tests." Unpublished, 1997. WL/POP (HyTech), Wright-Patterson AFB, OH.

118. Wright, John Keith. *Shock Tubes*. London: Methuen, 1961.

119. Yeager, General Chuck and Leo Janos. *Yeager*. New York: Bantam Books, 1985.

120. Yee, H.C. NASA TM-101088, 1989.

121. Yuschenkova, N.I., et al. "Mechanism for anomalous relaxation in shock waves in inert gases," *Sov. Tech. Phys. Lett.*, *11*(5):215–217 (May 1985).

122. Zapka, W. and A.C. Tam. "Noncontact optoacoustic determination of gas flow velocity and temperature simultaneously," *Appl. Phys. Lett.*, *40*(12):1015–1017 (1982).

123. Zel'dovich, Ya. B. and Yu. P. Raizer. *Physics of Shock Waves and High-Temperature Hydrodynamic Phyenomena, I*. New York: Academic Press, 1966.

124. Zel'dovich, Ya. B. and Yu. P. Raizer. *Physics of Shock Waves and High-Temperature Hydrodynamic Phyenomena, II*. New York: Academic Press, 1966.

Vita

Major William M. Hilbun was born at Columbus AFB, MS on 12 SEP 62, spending his youth among the rich farmlands of Mississippi. He graduated from Tupelo High School in May 81 and entered the U.S. Air Force Academy as part of the twenty-seventh class in June of the same year. He was graduated in May 85 with a B.S. degree in physics and a commission as a 2nd Lieutenant in the U.S. Air Force. His first tour of duty was with the 3246 Test Wing, Eglin AFB, FL as an infrared (IR) test engineer, where he worked on the test and evaluation of IR guided missiles. In May 89, he was reassigned to the Air Force Institute of Technology (AFIT) for post-graduate studies in engineering physics. He graduated with a M.S. degree 18 months later, with his thesis work being in the area of numerical solutions to the Boltzmann equation. Reassigned to the (then) Foreign Technology Division, Wright-Patterson AFB, OH, Major Hilbun worked on designing, building and flight-testing realistic re-entry vehicle decoys in support of the Strategic Defense Initiative. In June 94, Major Hilbun entered AFIT to begin his doctoral studies in the field of plasma aerodynamics. In October 97, he was reassigned to the Air Force Technical Applications Center, Patrick AFB, FL. Major Hilbun is married to the former Kathi Babbel, of Seattle, WA, and they have four children: Houston (7), Travis (5), Poiette (4) and Tyler Davis (2).

Permanent address: 3630 Manassas Ave
Melbourne, FL 32934

REPORT DOCUMENTATION PAGE			Form Approved OMB No. 0704-0188

1. AGENCY USE ONLY *(Leave blank)*	2. REPORT DATE	3. REPORT TYPE AND DATES COVERED
	October 1997	Final

4. TITLE AND SUBTITLE
Shock Waves in Nonequilibrium Gases and Plasmas

5. FUNDING NUMBERS

6. AUTHOR(S)
William M. Hilbun, Major, USAF

7. PERFORMING ORGANIZATION NAME(S) AND ADDRESS(ES)
Department of Engineering Physics
Air Force Institute of Technology
Wright-Patterson AFB, OH, 45433-7542

8. PERFORMING ORGANIZATION REPORT NUMBER
AFIT/DS/ENP/97D-08

9. SPONSORING/MONITORING AGENCY NAME(S) AND ADDRESS(ES)
Wright Laboratory
2130 Eighth St., Ste. 1
Wright-Patterson AFB, OH, 45433-7542

10. SPONSORING/MONITORING AGENCY REPORT NUMBER

11. SUPPLEMENTARY NOTES

12a. DISTRIBUTION AVAILABILITY STATEMENT
Distribution Unlimited

12b. DISTRIBUTION CODE

13. ABSTRACT *(Maximum 200 words)*

An analysis and assessment of three mechanisms describing plasma/shock wave interactions was conducted under conditions typically encountered in a weakly ionized glow discharge. The mechanisms of ion-acoustic wave damping, post-shock energy addition and thermal inhomogeneities were examined by numerically solving the Euler equations with appropriate source terms adapted for each mechanism. Ion-acoustic wave damping was examined by modelling the partially ionized plasma as two fluids in one spatial dimension using the Riemann problem as a basis. Post-shock energy addition in the form of nonequilibrium vibrational energy relaxation was also examined in one spatial dimension using the Riemann problem as a basis. The influence of thermal inhomogeneities on shock wave propagation was examined in two spatial dimensions for both a Riemann shock and a shock generated by a spark discharge. Shocks were propagated through realistic thermal profiles with the resulting shock structure examined through the numerical application of various optical diagnostic techniques. Results from shock simulations indicate that ion-acoustic wave damping has an insignificant effect on the neutral flow at fractional ionization levels typical of glow discharges. Post-shock vibrational energy relaxation is also unable to effect the shock structure on the time scales of interest. An analysis of the effects of thermal inhomogeneities reveals that many of the observed plasma/shock anomalies can be explained based solely on this mechanism.

14. SUBJECT TERMS
shocks, weakly ionized plasma, ion-acoustic waves, vibrational relaxation, thermal inhomogeneities, fluid equations

15. NUMBER OF PAGES
274

16. PRICE CODE

17. SECURITY CLASSIFICATION OF REPORT	18. SECURITY CLASSIFICATION OF THIS PAGE	19. SECURITY CLASSIFICATION OF ABSTRACT	20. LIMITATION OF ABSTRACT
Unclassified	Unclassified	Unclassified	UL